DEVELOPMENT OF IMAGING FOURIER-TRANSFORM SPECTROSCOPY

FOR THE CHARACTERIZATION OF TURBULENT JET FLAMES

DISSERTATION

Jacob L. Harley, Captain, USAF

AFIT-ENP-DS-14-S-13

DEPARTMENT OF THE AIR FORCE
AIR UNIVERSITY

AIR FORCE INSTITUTE OF TECHNOLOGY

Wright-Patterson Air Force Base, Ohio

AFIT-ENP-DS-14-S-13

DEVELOPMENT OF IMAGING FOURIER-TRANSFORM SPECTROSCOPY FOR THE CHARACTERIZATION OF TURBULENT JET FLAMES

DISSERTATION

Presented to the Faculty

Graduate School of Engineering and Management

Air Force Institute of Technology

Air University

Air Education and Training Command

in Partial Fulfillment of the Requirements for the

Degree of Doctor of Philosophy in Applied Physics

Jacob L. Harley, B.S., M.S.

Captain, USAF

September 2014

AFIT-ENP-DS-14-S-13

DEVELOPMENT OF IMAGING FOURIER-TRANSFORM SPECTROSCOPY FOR

THE CHARACTERIZATION OF TURBULENT JET FLAMES

Jacob L. Harley, B.S., M.S.
Captain, USAF

Approved:

//signed//	12 Sep 2014
Kevin C. Gross, PhD (Chairman)	Date
//signed//	12 Sep 2014
Glen P. Perram, PhD (Member)	Date
//signed//	18 Aug 2014
David L. Blunck, PhD (Member)	Date
//signed//	12 Sep 2014
Marc D. Polanka, PhD (Member)	Date

Accepted:

ADEDEJI B. BADIRU, PhD, PE   Date
Dean, Graduate School of Engineering
and Management

Abstract

The global proliferation of combustion systems has driven a need for improvements in combustion efficiency to reduce the financial and environmental impact associated with this growth. Combustion diagnostics is a vast field of research dedicated to that effort, and turbulence is one of the fundamental problems. The nature of turbulence and its influence on chemistry, radiation, and flow dynamics makes its study important for practical and academic reasons, yet also highly challenging. Recent advances in computational models to simulate turbulent, reactive flow fields have outpaced the ability to collect highly constraining data—throughout the entire flow field—for validating and improving such models. In particular, the ability to quantify in three dimensions both the mean scalar fields (i.e. temperature & species concentrations) and their respective fluctuation statistics via hyperspectral imaging would be a game-changing advancement in combustion diagnostics, with high impact in both validation and improvement efforts for computational combustion models. This research effort establishes imaging Fourier-transform spectrometry (IFTS) as a valuable tool (which complements laser diagnostics) for the study of turbulent combustion. Specifically, this effort (1) demonstrates that IFTS can be used to quantitatively measure spatially resolved spectra from a canonical turbulent flame; (2) establishes the utility of quantile spectra in first-ever quantitative comparisons between measured and modeled turbulent radiation interaction (TRI); (3) develops a simple onion-peeling-like spectral inversion methodology suitable for estimating radial scalar distributions in axisymmetric, optically-thick flames; (4) builds understanding of quantile spectra and demonstrates proof of concept for their use in estimating scalar fluctuation statistics.

Measurements of a $CH_4/H_2/N_2$ turbulent non-premixed jet flame (Purdue Flame A) were acquired using a mid-IR IFTS. Spatially-resolved (128×192 pixels, $0.72\,\text{mm/pixel}$)

mean radiance spectra were collected between $1800\,\text{cm}^{-1} \leq \tilde{\nu} \leq 4500\,\text{cm}^{-1}$ ($2.22\,\mu\text{m} \leq \lambda \leq 5.55\,\mu\text{m}$) at moderate spectral resolution ($\delta\tilde{\nu} = 16\,\text{cm}^{-1}$, $\overline{\delta\lambda} = 20\,\text{nm}$), spanning the visible flame. Higher spectral resolution measurements ($\delta\tilde{\nu} = 0.25\,\text{cm}^{-1}$, $\overline{\delta\lambda} = 0.3\,\text{nm}$) were also captured on a smaller window (8×192) at 20, 40, and 60 diameters (D) above the jet exit and reveal the rotational fine structure associated with various vibrational transitions in CH_4, CO_2, CO, and H_2O. The high-resolution spectra represent a 64-fold increase in resolution compared to existing (non-imaged) point spectral measurements. Low-resolution $16\,\text{cm}^{-1}$ mean spectra are validated against previously published point spectral measurements at 20 D, 40 D and 60 D with agreement to within 10 % at 40 D and 60 D, and a two-fold larger discrepancy at 20 D. IFTS-measured turbulence integral length scales of 5.7 mm, 11.7 mm and 15.7 mm are reported at 20 D, 40 D and 60 D, respectively, and are within 14 % of published narrowband infrared (IR) values. Low-resolution quantile spectra are used to estimate the root mean square (RMS) spectrum which compares favorably to directly-measured RMS point spectral measurements.

An existing time and space series (TASS) flame model is implemented and expanded to preserve correlations between multiple species which produce emissions within the IFTS bandpass. A multi-layer radiance model is developed—which incorporates the latest high-temperature spectroscopic databases—for simulating instantaneous flame emissions via TASS model outputs. High-resolution, on-axis comparisons between the simulated and IFTS measured time-averaged spectra are excellent. The mean relative error between data and simulation is 17.4 %, 18.6 % and 13.5 % at 20 D, 40 D and 60 D, respectively. A simple onion-peeling-inspired inversion method which removes optically-thin requirements is developed to handle scalar retrievals from broadband spectra. With no *a priori* knowledge of the flame scalar field, the inversion algorithm successfully retrieves temperature and CO_2 profiles for stationary (i.e., non-turbulent) simulated spectra with mean relative errors (RMS/peak) of 2.4 % and 10.4 % for temperature and CO_2, respectively.

Quantile spectra from an ensemble of simulated turbulent flame emissions are inverted at 20 D, 40 D and 60 D with relative fit errors (RMS/mean) between 1.5 % to 2.5 % for the diametric path, and between 2.3 % to 4.0 % for a representative off axis path ($r/x = 0.0625$). Temperatures retrieved from the $q = 0.25$, 0.50, and 0.75 quantiles afford estimates of the non-dimensional quantity, (T_{RMS}/T_{mean}), which are within 18 %, 8 % and 7 % of simulation inputs at 20 D, 40 D and 60 D, respectively. Spectral fits of measured Purdue Flame A exhibited larger systematic errors, with RMS fit residuals between 10-15 $\mu W/(cm^2 srcm^{-1})$ at the three heights, which are 3-5 times larger than the measurement noise. Retrieved quantile temperature profiles are near 1900 K and indistinguishable from $r = 0$ to $r = 3.6$ cm, but show an increase in separation from $r = 3.6$ cm to flame edge, consistent with the turbulent behavior expected in this region. Retrieved CO_2 quantile concentrations are well separated across all radii. Systematic errors and flame opacity limited the accuracy of spectral retrievals near flame center. Inversions on simulated turbulent spectra suggest radial estimation of scalar fluctuation statistics may be possible using quantile spectra and justify a full-scale research effort to explore this exciting possibility.

This work is dedicated entirely to my wife and children. They are my single greatest achievement. This work is a distant second.

Acknowledgements

I would like to thank the institution of AFIT for providing me the opportunity to earn this degree. Through the many ups and downs I have never felt anything but support. The bar is high, as it should be, and I appreciate the faculty making me earn it, albeit with some gentle nudges along the way. Specifically, I would like to thank Dr. William Bailey for his consistently high academic and moral standards coupled with a true concern for my success as an academic, Air Force officer, and individual.

I would also like to thank my committee. Each of them have been a major source of support and encouragement at different points along the way, and I truly appreciate it. Outside of my committee I have received a great deal of assistance as well. Dr. Brent Rankin was instrumental in helping me obtain the experimental data so vital to this work, and he has been an active advisor and coauthor of various works along the way. More importantly he has become a friend, and I am fortunate for that. I also appreciate the help of Dr. Cameron Keenan and the amazing speed improvements he made to the code used in my analysis. I must thank Jake Martin—not for attending my defense—but for helping to make sure I was prepared for it. I have to acknowledge Mike Rhoby for sharing this entire journey with me. We have walked much of the same path, and we have shared many tasks, experiences, and pain. I am glad I was not alone.

Finally, and most importantly, I give my sincerest thanks to my advisor, Dr. Kevin Gross. The most profound endorsement I can provide is this: I agreed to undertake this monumental task only because I knew he would be my advisor and with me every step of the way. Now that the journey is complete, I would only do it again with that same guarantee.

Jacob L. Harley

Table of Contents

List of Figures

List of Tables

List of Symbols

Symbol	Definition
L	Spectral radiant intensity
L_k	Radiance at instant k
L_{BB}/B	Planckian blackbody equation
L_0	Background radiance
L^S	Scene/source radiance
L^I	Instrument radiance
α	Optical thickness
τ	Transmittance or integral time scale
ILS	Instrument line shape function
$S(\alpha, \hat{s})$	Source function
ω	Single scattering albedo
Φ	Scattering phase function
h	Planck's constant
c	Speed of light
$\tilde{\nu}$	Wavenumber
k_b	Boltsmann's constant
T	Temperature
$\vec{T}$	Profile of temperatures across multiple layers
ε	Emissivity
ξ	Single species concentration
$\vec{\xi}$	Vector of relevant species concentrations in a layer
$\boldsymbol{\xi}$	Matrix of species vectors for multiple layers
N	Total gas density

Symbol	Definition
q	Column density or quantile
I	Interferogram
I^{AC}	Modulated component
I^{DC}	Constant (spectrally integrated) component
I^{DC}_{LPF}	Low frequency intensity fluctuations
l	Pathlength or integral length scale
σ	Absorption cross-section or standard deviation
$S(T)$	Spectral line intensity
f	Line shape function or frequency
P	Probability distribution or pressure
t	Time
v	Velocity
G	Instrument gain
I	Intensity response
a	Random shock
ζ	Gaussian variable
ρ	Temporal or spatial autocorrelation function
ϕ	Intermediate correlation model parameter
σ_a	Random shock distribution
$\Phi(\zeta)$	Gaussian cumulative probability distribution function
$F(T)$	Non-gaussian cumulative probability distribution function
S	Matrix of scalars at each line-of-sight
L	Matrix of spectra at each line-of-sight
χ	Species mole fraction

List of Acronyms

Acronym	Definition
2D	two-dimensional
3D	three-dimensional
AC	alternating current (modulated signal)
CARS	coherent anti-Stokes Raman spectroscopy
CPDF	cumulative probability distribution function
CRF	Combustion Research Facility
DC	direct current (constant signal)
DLR	Deutsches Zentrum für Luft und Raumfahrt (German Aerospace Center)
FBP	filtered back projection
FFT	fast Fourier-transform
FIAS	fast infrared array spectrometer
FPA	focal plane array
FTIR	Fourier-transform infrared
FTS	Fourier-transform spectrometry
HITEMP	High-Temperature
HITRAN	High-Resolution Transmission
HPF	high pass filter
IFTS	imaging Fourier-transform spectrometry
IR	infrared
IRPIV	infrared particle imaging velocimetry
LAS	laser absorption spectrometry
LIF	laser-induced fluorescence
LOS	line-of-sight

Acronym	Definition
LPF	low pass filter
LTE	local thermodynamic equilibrium
OPD	optical path difference
PDF	probability distribution function
PLIF	planar laser-induced fluorescence
PSD	power spectral density
RMS	root mean square
SNR	signal-to-noise ratio
TASS	time and space series
TFP	thin filament pyrometry
TNF	turbulent nonpremixed flame
TRI	turbulence-radiation interaction

DEVELOPMENT OF IMAGING FOURIER-TRANSFORM SPECTROSCOPY FOR THE CHARACTERIZATION OF TURBULENT JET FLAMES

I. Introduction

Wɪᴛʜ an ever-expanding population and a global reliance on combustion systems for energy, transportation, and military needs it is now, more than ever, vital to maximize the efficiency of these systems. From the global effects of pollution due to the propagation of combustion to the massive costs of developing more advanced propulsion systems, diagnostic tools capable of understanding and interpreting combustion behavior are vital to the community. Combustion diagnostics is a field of long-standing interest with many resources continually dedicated to its study. Techniques such as Raman scattering, laser-induced fluorescence (LIF), planar laser-induced fluorescence (PLIF), Fourier-transform spectrometry (FTS), and traditional IR imaging have all been brought to bear on the subject [20, 38]. Turbulence has significant effects on combustion processes such as turbulence-chemistry interactions, turbulence-radiation interaction (TRI), scalar dissipation, transport, and mixing.

IFTS have recently become commercially available, and their ability to capture images with high spectral resolution across a wide band-pass makes them particularly attractive for combustion diagnostics since hyperspectral images contain information about the three-dimensional (3D) temperature and species scalar fields. However, these systems are designed for studying static scenes, and the impact of turbulent intensity fluctuations must be understood in order to make them useful for combustion diagnostics. This work adapts the unique strengths of IFTS to the characterization of combustion flames

1

by understanding the impact of—and benefiting from—the intensity fluctuations which encode key information about the turbulence.

1.1 Historical perspective

The following summary of the various Symposia on Combustion conducted by the Combustion Institute is presented to fully appreciate the study of combustion, combustion diagnostics, and turbulent flames (and the various methods applied to their study) as they have evolved since the foundation of the Institute. A more complete and technical literature review is found in Chapter 2.

The now recognized first and second Symposia on Combustion occurred in 1928 and 1937 respectively, prior to the incorporation of the Combustion Institute. These early meetings focused on radiant energy from flames, temperature measurement, diffusion flames, ignition, and the mechanisms of combustion. It was not until after the Second World War that a third symposium would occur, the first to dedicate a full week to combustion and to be published in a single volume. The World War greatly emphasized the practical significance of combustion research and it could easily be claimed the field of combustion diagnostics was already underway. Published in 1948, the proceedings from this third meeting already contained a session dedicated to Flame Spectroscopy and Radiation, emphasizing the applicability of spectroscopy to combustion study from the outset. Techniques and topics such as sodium line reversal, IR brightness thermometry, and temperature dependence of the intensity distribution of ro-vibrational lines were already being presented. By the fourth symposium in 1952, attendance was well above 700 with 14 countries from around the world in attendance. The universal desire to study and understand the various aspects of combustion could not be denied. This symposium was the first to contain a session on turbulent flames and even hosted a round table discussion specifically about combustion in turbulent flames.

Two years later, in 1954, The Combustion Institute was incorporated as a non-profit professional society. The fifth symposium that same year focused on combustion in engines and combustion kinetics, but did contain a session dedicated to flame spectra. It is worth noting the foundation of The Combustion Institute—laid in the first four symposiums prior to the official formation of the Institute itself—contains the topics still heavily studied and emphasized today: the interaction of combustion and turbulence, and turbulent flames. It is also no coincidence spectroscopic methods are present in that same foundation, and—as the techniques mature through the years to come—spectroscopy remains a major contributor to combustion diagnostics.

The symposia continued over the next ten years, with a stress on combustion theory as it pertained to propulsion development and high speed flight into the 1960s. Both laminar and turbulent flames continued to be of interest as they related to combustion and were heavily studied. Spectroscopic study was represented well with separated sessions on spectroscopy of flames, combustion spectroscopy, and high temperature spectroscopy containing topics such as: emission and absorption spectra of flat flames (from a quartz spectrograph), chemiluminescence in hydrogen flames, and mass spectrometry. As the 1970's began, pollution was an influential topic with regard to the study and understanding of combustion, but the study of turbulence as it pertained to flames and the combustion process continued. While pollution is an obvious area of study even today, the greatest influence to emerge from that decade was the arrival of the laser as a diagnostic tool.

Transitioning from the 1970s into the mid-1980s, the various forms of laser driven spectroscopy began to become more prevalent. While this laser driven focus remained through the 1980s (and truly the decades to follow), there are other items of specific interest which occured in that decade. In 1984, at the 20th Symposium (International) on Combustion, a session entitled Combustion Diagnostics was convened for the first time. Truly the study of combustion and flames via various methods over the previous decades

can be considered combustion diagnostics, but it is of interesting historical note to see a session specific to the topic not occur until the 20th Symposium. At the next symposium another combustion diagnostics session was convened where an emission and transmission Fourier-transform infrared (FTIR) spectroscopic method for *in situ* combustion diagnostics was presented. This work, done by Solomon *et al.* at a time when the laser had taken center stage, did an excellent job of applying FTIR to a method previously applied using dispersive infrared. It stands out as a reminder of the applicability of FTIR to combustion diagnostics [65].

The next decade was influenced by laser-based diagnostic methods as they continue to impress with their utility and results well into the 1990s. However, the 26th Symposium in 1996 was not focused on methods but on a specific challenge. After twenty-six symposia spanning nearly sixty years, combustion was the primary topic for the first time. While it was consistently a topic of various sessions and papers, the "elephant in the room" was not truly confronted until the mid-1990s. In his plenary lecture at that symposium, Bray described turbulence as "the most serious bottleneck between combustion science and its application" [10]. It is likely not a coincidence the International Workshop on Measurement and Computation of Turbulent Nonpremixed Flames met for the first time that same year with a goal of establishing experimental datasets on turbulent flames for the purpose of validating state-of-the-art combustion models [75]. The emphasis on the study of turbulent combustion from that point forward is evident in the various symposia, with the various flames and datasets established by the International Workshop surfacing frequently.

Through the 2000s, the success and availability of laser methods and equipment ensure the laser remained prevalent. During this decade the once single session on combustion diagnostics branched out into several different sessions specific to the particular type of diagnostic method. Separate diagnostic sessions dedicated to subtopics such as absorption, emission, nonlinear, LIF, Raman and coherent anti-Stokes Raman spectroscopy (CARS),

and scattering were now the norm. In this time, a few non-laser based combustion diagnostic techniques did emerge. Of particular note was the work accomplished by Purdue University in a series of studies (reviewed in detail later in this document) using an IR imager and a non-imaging fast IR array spectrometer (FIAS) [54, 55, 78–81] to study various flames of interest. These more recent works did much to demonstrate the role such nonintrusive, passive methods still have in the current field of turbulent combustion study.

A historical understanding of the topics presented at the various Combustion Institute symposia cannot be considered an all inclusive account of combustion and all of the techniques available for its study in general. However, it reveals the overarching areas of greatest (or least) development and common techniques. This understanding allows one to get a "finger on the pulse" of the combustion community. Several fundamental conclusions can be drawn from this historical perspective: combustion research has always been, and remains, a staple scientific field; the "serious bottleneck" that is turbulence presents drastic challenges to the community to this day; combustion diagnostics itself has emerged as a stand-alone area of interest; and the laser has largely dominated the last thirty years of diagnostic methods. Combined, these ideas speak to the relevance and novelty of this research effort.

1.2 Research objectives and methodology

A method for turbulent flow field analysis which uses a portable, nonintrusive instrument, while still achieving accurate scalar estimates (to include the relevant turbulent statistics) would prove to be extraordinarily useful. Due to the spatial information provided by the focal plane array (FPA), IFTS can go beyond the normal FTS result of temperature and species identification (and concentration estimation) in a small subsection of a plume. The FPA provides a spatial analysis capability which lends itself well to flow field visualization. The generation of an interferogram at every pixel allows for

5

analysis across a wide spectral band throughout a large area of the flow field. The corresponding spatially-resolved spectra can be used in conjunction with appropriate inversion methods to understand two-dimensional (2D) (or 3D when symmetry and/or tomographic methods are used) variations in the underlying scalar fields (i.e., temperature and species concentrations). In addition, the combination of interferometer and IR imager ensures the fluctuations in intensity occurring during the capture of an interferogram–information lost using a traditional FTS–are retained. This unique characteristic of IFTS ensures information about the turbulent intensity fluctuations and their spatial and temporal correlations are captured. This research effort leverages this unique information to estimate key turbulent length and time scales. Moreover, it permits sorting an ensemble of IFTS measurements into quantile interferograms, and this work demonstrates that the corresponding quantile spectra can be used to estimate temperature fluctuation statistics throughout the flame.

While individual efforts have been made to remotely analyze these types of sources via either high-speed IR cameras or non-imaging spectrometers [54, 70, 78], IFTS joins both technologies within a single instrument, thereby providing a unique means of studying combustion. The major goal of this work leverages this unique capability and is two-fold: (1) to demonstrate the utility of IFTS as a viable passive combustion diagnostic which is complementary to the suite of laser-based methods in current use; (2) explore the possibility of estimating scalar fields and their associated fluctuation statistics via quantile spectra. To realize this goal, the following research objectives are identified and pursued in this dissertation effort:

1. *Enable the forward spectral modeling of an inhomogeneous flame*. This will be accomplished by developing a multilayer spectral model which incorporates the latest high-temperature spectroscopy databases.

2. *Simulate realistic instantaneous scalar fields of an inhomogeneous turbulent flame*. This will entail implementing and extending TASS, and coupling it with existing simultaneous scalar measurements.

3. *Gain an understanding of the information content in quantile spectra*. This will be achieved by simulating an ensemble of instantaneous, LOS spectra for various locations in the modeled flame.

4. *Estimate scalar profiles from LOS spectra of a non-optically-thick axisymmetric flame*. This will require the development of a spectral inversion method unencumbered by optically-thin requirements.

5. *Explore the possibility of estimating the fluctuation statistics of the scalar fields*. This will be accomplished by applying the spectral inversion method to both simulated and measured quantile spectra.

The experimental measurements in this work were taken at the Purdue combustion research laboratory. The turbulent nonpremixed flame (TNF) source was intended to replicate canonical Flame DLR_A (Flame A) from the International Workshop on Measurement and Computation of TNF (described in more detail in Chapters 2 and 3). Planned on-site measurements of the Workshop Flame A housed at the Sandia Laboratories Combustion Research Facility (CRF) were later cancelled by the CRF, and the Purdue dataset became the only experimental measurements available. Despite its intention of being a "preliminary" data set, validation efforts using existing point spectral and narrow-band IR camera measurements demonstrate that it is a high-quality dataset. However, there were some issues with the data acquisition computer during the experiment (see Chapter 3 and Appendix A) which precluded the capture of an ideal number of datasets for the statistical nature of this study. The limited availability of experimental IFTS Flame A measurements dictated a very pragmatic approach be taken toward the timely

accomplishment of this work. The methodology was centered around four phases of research:

- Validate: IFTS measurements of Purdue Flame A are compared to previous spectral and IR imagery measurements of Sandia Flame A. This provides an experimental link between the two flames and validates the Purdue Flame A measurements.

- Simulate: A forward multilayer radiance model is developed and combined with a stochastic TASS model of turbulent flames to allow for the simulation of instantaneous radiances. Simulated Flame A spectra are important to this work for two reasons. First, a larger number of samples is desirable to properly capture the statistics associated with the turbulence and simulating spectra allows control of the sample size. Second—and more importantly—this is a first-ever attempt to apply IFTS to turbulent flames. As such, simulations can be used to understand the influence of TRI as they pertain to IFTS measurements and the interpretation of quantile spectra. Simulated spectra provide an avenue for analysis which is completely verifiable against the input results. In addition, leveraging simulations removes the possibility of any systematic error, allowing for complete focus on the analysis method and results.

- Analyze: Two methods of analysis are uniquely applied in this work: quantile interferometric analysis and an onion-peeling inspired inversion method for turbulent flames. The two are developed and improved upon via analysis of simulated spectra until suitable comparisons with the known input data is reached.

- Apply: Finally, the simulation verified turbulent flame analysis methods are applied to the experimental IFTS measurements of Purdue Flame A.

It should be pointed out the computational effort involved with the spectral simulations and inversions is very high. Care had to be taken in the scoping of parametric studies as

8

they pertained to this work. In some cases, additional simulations and inversions of spectral data were impractical to perform. For example, while inversions of the $16\,\mathrm{cm}^{-1}$ data at a single quantile and single flame height could be achieved in approximately $6\,\mathrm{hrs}$, it would take approximately 16 days to perform the same inversion using the $0.25\,\mathrm{cm}^{-1}$ data due to the 64-fold increase in spectral resolution.

1.3 Document outline

Each chapter in this dissertation contains an introductory paragraph which outlines the particular sections and goals of each. A broad overview of the entire work is provided here to paint a complete picture of the document and an understanding of the manner in which it is organized.

A background chapter follows this introductory chapter, containing both a literature review and discussion of theory. The review focuses on various works as they apply to diagnostic techniques, Flame A diagnostics, quantile analysis, and the available inversion methods. The theory discussion lays out the relevant theory in regards to radiative transfer, interferometric behavior, modeling and simulation of a turbulent flame, quantile interferogram analysis for turbulent flames, and a unique inversion method developed for this work.

The primary results of this work are presented in Chapters 3 through 5. Chapter 3 presents a journal article in its entirety as published in Optics Letters (Volume 39, Issue 8, Page 2350). This article supports the validation phase of the methodology and contains the published description of the Purdue Flame A experiment, describes the impact of turbulence on interferogram formation, and favorably compares time-averaged results of IFTS measured spectra and imagery to previously published FIAS Flame A measurements. Chapter 4 contains a manuscript draft being prepared for submission to the Journal of Quantitative Spectroscopy and Heat Transfer. The article is presented in its entirety to include the supporting theory and results, and it supports both validation and simulation

methodology components. It reports IFTS measured flame characteristics, demonstrates the utility of high-resolution IFTS spectra for spectral model and database validation, and compares low-resolution quantile spectra for several cases. Chapter 5 is written in the more traditional style of a dissertation chapter. It is a results driven chapter which focuses on analysis and application. Here, a straightforward inversion method developed for this work is applied to simulated and IFTS acquired spectra. Scalar profiles are first retrieved for a simulated stationary (i.e., non-turbulent) flame to test the inversion method. Then, inversions are performed on quantile-sorted spectra from a simulated turbulent flame, and this is repeated on the measured Flame A quantile spectra. In addition, a method for linking quantile scalar fit results to the scalar statistics is demonstrated.

After the conclusion in Chapter 6, several supporting appendices are included. Each of the three primary results chapters have a complementary appendix with additional figures and discussion. In particular, the choice to present Chapters 3 and 4 in article format forced a precise selection of figures, and the excluded—but applicable—material is found in their respective appendices. Appendix D is a published journal article in the International Journal of Energetic Materials and Chemical Propulsion (Volume 12, 2013, Issue 1, pages 15-26) [59], which presents the first demonstration of IFTS for turbulent flow field diagnostics and introduces the quantile spectra concept. As a coauthor for this paper I acted as an editor and contributed experimental data and analysis. Finally, Appendix E contains a conference proceeding in its entirety [32]. This proceeding summarizes analysis of a turbofan engine exhaust via the Hyper-Cam and further supports the validation component of the methodology. The effort was an early attempt to demonstrate the feasibility of IFTS as a combustion diagnostics tool. It presents temperature estimates and species volume mixing fractions (computed assuming a homogeneous flow) and leverages interferometric imagery to estimate the velocity of a turbulent feature.

II. Background

I̲ɴ this chapter a review of relevant literature with regard to general combustion diagnostic techniques and those specific to Flame A are presented. A complete discussion of the applicable theory behind this work then follows. The radiative transfer, interferometric behavior, modeling and simulation of Flame A, and methods of spectral analysis are described in detail.

2.1 Literature Review

2.1.1 Diagnostic techniques.

Turbulence is an inherent part of combustion, and a viable diagnostic method must account for the associated analytical complications it introduces. The different strengths and weaknesses of the various diagnostic methods typically dictate when they are viable.

The laser, under various experimental configurations, is capable of estimating scalars and turbulent statistics, and it is capable of imaging as well [20, 38, 74]. Both LIF and PLIF have met great success and grown in popularity. They are capable of point and planar imaging of trace species with high spectral resolution and high signal to noise. However, multiple laser sources are typically required and the methods can result in higher than desirable uncertainty [15, 37, 38, 56]. The application of laser absorption spectrometry (LAS) has had success and it is an extremely capable method. Trace species are detectable via LAS at a high temporal and spectral resolution, although the technique offers no spatial capability without moving the flame or laser, or using multiple lasers in an experiment [41, 47]. While complicated, CARS is also a common and well proven laser-based technique. As an active interrogation technique, CARS is also able to interrogate trace species, and is capable of highly accurate temperature estimations. This technique requires the application of three lasers in a given experiment, which complicates setup

and limits portability considerably [21, 38]. The complexities of these various laser-based methods may not be desirable in some diagnostic situations, and perhaps presents a reason to pursue other complementary methods which may–at times–offer advantages otherwise not available. Portability and fast experimental setup are not two attributes typically associated with laser diagnostics. They most often involve a large experimental footprint, a need for careful alignment of optics, and the use of hazardous chemicals. In addition, the source itself may have limited optical ports which inhibit any active interrogation.

Less complex, nonintrusive radiant emission diagnostic methods have also been shown to be capable options [38]. Flow fields have been well studied with infrared particle imaging velocimetry (IRPIV) [13], but the reach of IR imaging techniques extends well beyond only flow field imaging. Various IR studies have been accomplished using the popular IR imaging diagnostic method, several of which are discussed in much detail in the Flame A diagnostics review to follow [6, 18, 35, 53–55]. The long standing presence of FTIR spectroscopy in the combustion diagnostics literature indicates the soundness of the technique [11, 26, 65], and its presence in more recent works demonstrates a method which is highly desirable even today. Several of these recent works are also described in more detail in the Flame A diagnostics review [5, 78–81]. Similarly, due to its wide spectral band and high spectral resolution, FTS is an effective remote optical sensing technique [65, 76, 78]. Clearly a less experimentally complex diagnostic option to the laser-based techniques has a place. But individually, the various radiant emission diagnostic methods may not produce the complete description desired (or required) of the source. In the case of traditional FTS, the spectrum can divulge useful temperature and species information, but the narrow field of view can make a description of the entire source difficult. The spatial component of an IR imager obviously overcomes that limitation and provides an excellent map of a plume and the turbulent statistics, but is then hampered by the lack of in-depth spectral information.

IFTS is a powerful combination of these passive techniques and the combination of interferometer and IR FPA overcomes some of their individual inherent weaknesses. A highly resolved spectrum at a given pixel provides the opportunity for the strengths of traditional FTS or FTIR to be applied, while the FPA provides this analysis across an entire image. In addition, this entire process is enhanced by the capture of the turbulent fluctuations in each interferogram. The emerging technology of IFTS has been successfully applied in a number of experiments [27, 28, 30, 43, 57, 71]. However, until now the sources were assumed homogeneous, and in several cases optically thin [28, 30, 43].

2.1.2 Flame A diagnostics.

The International Workshop on Measurement and Computation of TNF was established to promote collaborative study of well documented and repeatable flames. The primary focus of this work (Flame A) is a product of this collaboration. The flame conditions were repeated and measured via IFTS at the Purdue University Turbulent Combustion Laboratory, and simulations were generated using data from the Workshop flame internet library [75]. This review focuses on works which study Flame A, but includes studies across the flame series.

The Flame A temperature and species data available for testing and validation is initially presented by Bergmann *et al.* (Deutsches Zentrum für Luft und Raumfahrt (German Aerospace Center) (DLR) Stuttgart) in their application of several techniques to characterize the flame [2]. The flame is investigated with single-pulse pointwise spontaneous Raman/Raleigh scattering for temperature and major species determination, 2D Rayleigh scattering for instantaneous temperature distributions and 2D LIF measurements of OH, CH_4, and NO for flame structure visualization. Raman radial profile measurements were performed at $5\,D$, $10\,D$, $20\,D$, $40\,D$, $60\,D$ and $80\,D$, where D is the flame exit tube diameter. An axial profile was also measured for $2.5\,D \leq x \leq 100\,D$. At each location, joint probability distribution function (PDF)s of temperature and species concentrations were

13

deduced based on 400 single-pulse measurements. The maximum mean flame temperature was found to be 1926 K, which was at the flame axis at 60 D. Near nozzle exit (5 D) the reaction zone is cylindrical with a center axial temperature near ambient and a maximum mean temperature of 1634 K approximately 8 mm off axis. The effects of differential diffusion are discussed, which specifically describe the behavior of H_2 and CH_4 and their impact on burnt gas composition. In addition, measured temperature and H_2O, CO_2, and CO mole fractions (data is also available for CH_4, H_2O, N_2, and O_2) versus mixing fraction at 5 D and 40 D are presented (data for the additional heights is also available). These results are compared to calculated adiabatic equilibrium values, a strained laminar counterflow diffusion flame calculation including differential diffusion, and a calculation without diffusion. The results of H_2O compare best with the calculation which includes diffusion, while the CO_2 measured values lie somewhere between the calculations with and without diffusion. The CO data exhibits a great deal of scatter which the authors attribute to low signal intensities and the correction of cross talk (between Raman channels). Although not presented, the additional species are described as being in good agreement with both strained laminar counterflow diffusion flame calculations, with and without diffusion. The dataset from this work is intended to be a reliable basis for mathematical flame calculations and has been made available for this purpose. This data is used as the foundation for the spectral simulations presented in this work.

The complementary Sandia study of Flame A by Barlow *et al.* is presented in an additional paper [46]. The joint PDFs of temperature, mixture fraction, and major (CH_4, H_2, O_2, N_2, H_2O, CO_2, CO) and minor (OH, NO) species mass fractions are calculated. The experimental methods and results between Sandia and DLR are compared and evaluated. The two datasets agree well and any deviations are within experimental errors. While not completely quantified, the observed deviations were attributed to non-identical flame and environmental conditions. Ultimately, the redundant measurements from different facilities

compared in this paper provide a useful check on the repeatability of flame conditions and scalar measurements.

The available Flame A flow field velocity data is documented by Schneider *et al.* in their study of hydrocarbon-fueled jet flames which vary in gas composition and jet exit Reynolds number (Flame A is referred to as DLR flame in their work) [64]. A two-component fiber-optic laser Doppler anemometer is used to characterize the flow field. The paper itself is brief and is only representative of the results available in their entirety upon download. The complete dataset contains radial distributions of mean axial and radial velocity components, Reynolds stress components, and turbulent kinetic energies. Measurements are taken in areas complementary to the scalar measurements: 0.125 D, 5 D, 10 D, 20 D, 40 D, 60 D and 80 D. Only an example of radial distributions in the far field at 40 D is presented. The flame exhibits the expected self-similar behavior at this location, and the authors indicate this behavior is observed downstream as well. Although the data is not shown in the paper, the mean radial velocities are discussed and described as 7 % below the corresponding axial velocities.

Frank *et al.* study a range of fuel mixtures in their work on radiation and NO formation in TNF, and Flame A is included in the analysis [25]. The work is intended to provide a basis for developing a realistic radiation submodel that incorporates absorption by CO_2 as it pertains to the formation of NO. Radiant fractions (ratio of total radiated power to power released in the combustion reaction) were measured for 12 different flames. Calculations of radiant fraction were then computed and compared for several of the flames: the pure H_2 flames, the helium-diluted H_2 flames, and Flame D of the CH_4/air series. The calculations were based on an optically thin assumption. Results were good for the diluted hydrogen flames and fairly reasonable for the pure hydrogen flames. In the CH_4/air flame radiant fractions were over predicted by more than a factor of 2. The authors assert that absorption by CO_2 is the driving factor for this discrepancy. Additional calculations using RADCAL

were performed to compare emission/absorption to emission-only predictions. Results showed the optically thin assumption as being adequate for hydrogen flames, but not in the case of the methane flame. The emission only model predicts 39 % higher total radiated power than the emission/absorption model, indicating the importance of absorption with the CH_4/air flame.

The Sandia flame series is investigated by Zheng *et al.* (Purdue University) using FIAS in a number of papers. The FIAS has a spectral resolution which varies from 20 nm to 44 nm (a resolution on the order of the 16 cm^{-1} seen in this work), a spatial resolution between 2 mm and 4 mm, and a sampling rate of 6250 Hz [78–81]. This group investigates the spectral radiation intensities of Flame A at three heights (20 D, 40 D and 60 D) for diametric and chord-like paths at various distances off axis [81]. They employ stochastic TASS analysis to simulate the instantaneous scalar properties for the radiation paths and to compute the RMS spectral radiation intensities (using integration of the equation of radiation transfer for non-homogeneous paths and arbitrary optical thickness). In addition, they examine three different interpretations of integral length scale to include one involving a tomography-like determination. The TASS analysis give excellent estimates of mean and RMS spectral radiation intensities, and the group emphasize the importance of investigating LOS radiation from paths off axis for TRI understanding. The TASS method is described in more detail within the theory discussion below.

Zheng *et al.* examine the entire TNF Workshop flame series in a separate work [78]. Similar methods of analysis are applied as with the initial Flame A experiment, but additional flames are now studied and at three additional heights. In this study it is found the effects of TRI are not significant for regions near flame axis, and it is asserted a mean property approach for loss calculations is adequate. In the regions off axis, where TRI effects are significant, the TASS analysis method again proves successful. A follow-up study of the partially premixed methane/air turbulent flames seeks to provide

16

deeper information regarding the influence of TRI [79]. In this work the mean, RMS, PDF, power spectral density (PSD), and autocorrelation coefficient (ρ) are derived from previous measured and simulated LOS intensities. The PDFs of the intensity fluctuations of all three flames provide similar results. The diametric paths result in symmetric PDFs nearly Gaussian in shape; however, away from flame axis the PDFs are skewed due to intermittency.

In his dissertation entitled *Quantitative Experimental and Model-Based Imaging of Infrared Radiation Intensity from Turbulent Reacting Flows*, Rankin (Purdue University) builds on the TNF analysis accomplished by Zheng [53, 54]. Rankin uses an imaging IR camera (FLIR Phoenix) with an InSb detector to capture data from two of the Sandia flames (to include Flame A) for comparison with simulation and PDF method results. The high speed imagery is acquired using three bandpass filters (2.58 ± 0.03, 2.77 ± 0.12, 4.34 ± 0.10 μm). The results are compared with the measurements acquired at Purdue where an experimental arrangement was established to duplicate the Sandia flame configuration (without the slow coflow) and are found to be in excellent quantitative agreement. The good agreement between Purdue and Sandia flame configurations is important to the study in this work as spectral measurements of the Purdue Flame A via IFTS are compared to Sandia-based spectra.

2.1.3 Quantile analysis.

The quantile analysis approach to overcoming scene change artifacts has been used previously with IFTS studies of turbulent sources [43, 71]. This statistics-based method leverages the direct current (constant signal) (DC) component of the intensity and statistically sorts the interferograms prior to the Fourier transform. By considering a temperature-fluctuating blackbody as a simple model for a turbulent plume, Tremblay et al define quantile interferograms and demonstrate that their corresponding spectra preserve the underlying temperature statistics. The approach relies on the fact that increases in

temperature produce corresponding increases in spectral radiance at all frequencies. This ensures that the interferogram (AC+DC) for a higher temperature blackbody will be greater than the interferogram for a lower temperature blackbody *at all OPDs*. Collecting an ensemble of measurements at each OPD permits sorting into various quantiles and constructing the corresponding quantile interferograms, with the DC level ensuring that higher quantiles map to higher temperatures. This relation only holds for an ensemble of interferometric measurements consisting of both the unmodulated (DC) and modulated (AC) components, like those recorded by IFTS and not like most traditional, AC-coupled FTS systems. Evaluating the median ($q = 0.5$) at each optical path difference (OPD) allows for construction of a "median" interferogram, and a similar procedure can be used to construct interferograms corresponding to arbitrary quantiles. These interferograms lead to spectra which represent the true initial temperature conditions [43, 71].

2.1.4   *Inversion methods.*

The terms tomography, tomographic reconstruction, deconvolution, and inversion are used nearly interchangeably in much of the literature. For the sake of continuity and to simplify discussion, this review will use the term inversion as it applies to any technique or method referenced in the cited source. The different inversion techniques have been applied to both simulated and experimental data with varying levels of success. The review of the inversion techniques to follow does not provide the details of performing each method, but instead focuses on the strengths and weaknesses of each, and some results of their application. The straight-forward onion-peeling inspired method employed in this work (and described in the Theory section to follow) was specifically implemented to avoid many of the complications found in this review. Most of the methods found in this review rely on the requirement for an optically source. When a source is not optically thin, photons at certain wavelengths can get trapped within the source and do not reach the detector. This

18

complicates the inversion of LOS intensity data, and makes understand behavior near the center of the source difficult.

In his review of one-dimensional inversion techniques, Dasch compares Abel, onion-peeling, and filtered back projection (FBP) methods [16]. These are deemed applicable to LOS absorption, beam deflection, or emission (with negligible absorption) data. Specifically, they are applicable to the diagnostics of flames where there is cylindrical symmetry, but the requirement for an optically thin source is significant. The methods were found to be very similar when the projection data were sampled at equal spacing. Onion-peeling was found to be very similar to an Abel inversion using a two-point interpolation, and the FBP methods were similar to a three-point Abel inversion. All three methods seemed susceptible to noise, with the onion-peeling method being twice as noisy as the three-point Abel inversion. The FBP methods (both Ramachandran-Lakshminarayanan and Shepp-Logan) were much more computationally constly than the three-point Abel inversion while still generating slightly more noise. Based on ease of calculation, robustness, and noise, Dasch recommends the three-point Abel inversion; however, he does cite instances in which the onion-peeling method may provide an exact solution.

Posner *et al.* used an Abel inversion technique to perform temperature field measurements of small, nonpremixed flames [52]. They investigated both an electric field controlled capillary flame and a burning droplet stream. The three-point Abel inversion method was first verified using an arbitrary radial field distribution (a combination of step, Gaussian, and Lorentzian functions). The original function, simulated LOS integration, and final inversion were all presented. The final inversion compared very well to the original (simulated) distribution, with some expected error near the step function (due to discontinuous derivatives). The group went on to apply the Abel method to their holographic interferometry technique and compared their results with CARS data, with

19

good agreement away from the flame front in the case of the capillary flame, but not with the burning droplet stream. The very small droplet stream geometry posed problems specifically for the holographic interferometry technique. The three-point Abel inversion method itself properly inverted the LOS data and seemed appropriate for the small (optically thin) source and interferometric function.

Hall *et al.* used an emission-absorption method in their temperature measurement of a sooting flame [29]. The authors fully recognized the use of inversion in temperature measurements as being based on optically thin sources, but they proposed corrections for the method provided the thickness not become too extreme. It should be pointed out their work primarily focused on spatially uniform absorption coefficient profiles. To account for the self-absorption factor in a less than optically thin flame the group used a heuristic method which they openly admitted may or may not have a rigorous basis, but it gave good results in reconstruction of synthetic spectra. As with Posner *et al.*, Hall *et al.* performed a number of computer-based experiments to test the reconstruction algorithm, and they highly recommended such inversions of synthetic spectra be carried out by anyone interested in applying the technique. The group ultimately used the FBP method discussed by Dasch, and they noted the onion-peeling method was found to definitely amplify experimental errors.

Solomon *et al.* applied an IR emission/transmission spectroscopy technique to measure concentration and temperature of gases and soot particles in reacting flows [4]. They presented several examples to include a coannular laminar ethylene diffusion flame. Experimentally they measured both transmissivity and emissivity with a non-imaging FTIR spectrometer. The group did not specify what inversion technique was used to reconstruct the spatially resolved data, but their method of analysis which used a quantity called the normalized radiance is of interest. A Planck blackbody function was fit to the normalized radiance for determination of temperature with excellent results. Hall *et al.* referenced

20

this Planck function technique in the paper discussed above. Deriving temperature by measuring the Planck function is highly desirable due to the sensitive dependence of the function on temperature (T^4) [29].

In their paper on IR band model techniques Brewer *et al.* look at a radiating combustion source which is inhomogeneous (but cylindrically symmetric) and not optically thin [11]. They specifically cited the Abel inversion technique as being applicable only when self-absorption was negligible or, when self-absorption did occur, both radiance and transmittance measurements were made with the transmittances expressed by the Beer-Lambert absorption law. The IR band model technique required the measurement of both radiance and transmittance at a fixed wavelength in an IR band over adjacent paths through the source. The model consisted of a random band model with constant line widths and a delta function distribution for line strengths. No *a priori* knowledge of the temperature profile or concentration profile was required using this technique. However, in their experiment absorption measurements were made by observing the attenuation of the modulated source located behind the burner. A significant point made by the group was to emphasize the behavior of the band radiation transmission. They specifically asserted the transmission through combustion gases does not obey Beers law, which was what removed the option to scan laterally and invert to radial positions (as with the Abel method).

Blunck *et al.* employed an onion-peeling inversion combined with thin filament pyrometry (TFP) and the RADCAL narrow-band model to achieve good estimates of temperature and water vapor mole fractions in an unsteady nonpremixed hydrogen flame [6]. Ma *et al.* used LAS and a hyperspectral laser source to interrogate a H_2/air flame [41]. The measurements were inverted and compared reasonably well with previous CARS measurements.

2.2 Theory

The following section is a pedagogical discussion of the fundamental theory underpinning the turbulent flame analysis found in this work. The primary topics are radiative transfer, interferometric measurements of turbulent flames, TASS analysis, modeling flame spectral radiance, quantile interferogram analysis, and an onion-peeling inspired inversion technique. Radiative transfer theory is described first from homogeneous participating media and then considered in the presence of a multilayer flame. The equation for the instantaneous radiance generated by a multilayer flame is then considered in a time-averaged sense. The issue of instantaneous versus time-averaged radiance leads to the discussion of the interferogram, its response to the stochastically fluctuating radiance, and the turbulent statistics inherent within a single interferogram, as well as an ensemble of interferograms. The discussion then turns to the modeling of the flame and subsequent simulations of instrument response to be used in analysis. The TASS model was developed elsewhere but is leveraged in this work, therefore a succinct description of the model—and the modifications made—is warranted. The TASS model is driven by the temporal and spatial correlations found in the high-speed imagery. The calculation of these correlations is presented with the TASS model description. The TASS flame realizations drive the simulation of instantaneous radiances. In turn, these spectra are the foundation of the interferogram simulations. Thus, the TASS description leads to a discussion on the method used in generating the interferograms for analysis. The quantile analysis method for leveraging interferometric turbulent effects is then described, with a final description of the complete method when combined with a straight-forward onion peeling inspired inversion technique.

2.2.1 Radiative transfer.

Following Modest [48], the equation of transfer in participating media (to include emission, absorption, and scattering) is

$$\frac{dL}{d\alpha} + L = S(\alpha, \hat{s}), \tag{2.1}$$

where L is the spectral radiant intensity, α is the optical thickness (called τ in Modest, but that term is reserved for transmittance, $\tau = e^{-\alpha}$, in this document), and $S(\alpha, \hat{s})$ is the source function for spectral radiant intensity from the $\hat{s}$ direction. All three of these components are wavelength dependent. The source function is a combination of two terms which account for the augmentation due to emission (under conditions of local thermodynamic equilibrium (LTE)) and scattering:

$$S(\alpha, \hat{s}) = (1 - \omega) L_{BB} + \frac{\omega}{4\pi} \int_{4\pi} L(\hat{s}_i) \, \Phi(\hat{s}_i, \hat{s}) \, d\Omega_i, \tag{2.2}$$

where ω is the single scattering albedo, and $\Phi(\hat{s}_i, \hat{s})$ is the scattering phase function. Scattering is often ignored with combustion sources [48], and in this study of a non-sooting flame, where $\omega \ll 1$, it is as well. The source function then reduces to the equation for a blackbody, $L_{BB}(T) = \frac{2 h c^2 \tilde{\nu}^3}{\exp[\frac{h c \tilde{\nu}}{k_b T}] - 1}$, at a specific temperature (where h is Planck's constant, c is the speed of light, $\tilde{\nu}$ is wavenumber, and k_b is Boltzmann's constant). Equation 2.1 then becomes

$$\frac{dL}{d\alpha} + L = L_{BB}(T), \tag{2.3}$$

and can be solved by using the integrating factor $e^{-\alpha}$, with solution (for a homogeneous layer):

$$L(\alpha) = L_0 \, e^{-\alpha} + (1 - e^{-\alpha}) L_{BB}(T). \tag{2.4}$$

The first term on the right side of Equation 2.4 represents the spectral radiance due to the background, which decays as it transmits through the medium and is the expected Beer's law behavior. The second term is the contribution from the local emission which upon

inspection is simply the emissivity, ε, when expressed as one minus the transmissivity $(1 - e^{-\alpha} = 1 - \tau = \varepsilon)$ and the equivalent Planckian blackbody radiation distribution at a given temperature. This allows Equation 2.4 to be re-expressed as

$$L(\tilde{\nu}) \;=\; L_0 \, e^{-\alpha} + \varepsilon \, L_{BB}(T), \tag{2.5}$$

where the the radiance is now intentionally described as a function of wavenumber and not α. The α term in the exponent of the transmissivity is itself a function of wavenumber, pathlength, species concentration, and temperature. In addition, this term incorporates the molecular properties of the gas which allows for species and temperature estimation (via spectral analysis) as described in the following discussion.

From the perspective of any given pixel in the IFTS, the radiance integrated over all wavenumbers is interpreted as

$$L(\tilde{\nu}) = \int \tau(\tilde{\nu}') \, L^S(\tilde{\nu}) \, ILS \, (\tilde{\nu} - \tilde{\nu}') \, d\tilde{\nu}' \tag{2.6}$$

where τ is the LOS transmittance through the atmosphere, $ILS \, (\tilde{\nu} - \tilde{\nu}')$ is the convolution with the instrument's line shape function and accounts for the instrument spectral resolution, and $L^S(\tilde{\nu})$ is the apparent radiance from the source. When the source is homogenous the radiance can typically be described in the manner of Equation 2.5, which includes the assumptions of LTE and negligible scattering. The model is simplified further by also assuming background radiation and atmospheric self-emission can be ignored [27]. This removes the L_0 term and reduces the source radiance to a product of the atmospheric transmittance, the emissivity of the source, and a Planck function, $L^S(\tilde{\nu}) = \tau(\tilde{\nu}) \, \varepsilon(\tilde{\nu}) \, L_{BB}(T)$. As already described, the emissivity may be expressed as

$$\varepsilon(\tilde{\nu}) = 1 - \exp\left(-\alpha\left(\tilde{\nu}, l, \vec{\xi}, T\right)\right) = 1 - \exp\left(-Nl \sum_i q(\vec{\xi})_i \, \sigma_i(\tilde{\nu}, T)\right) \tau_p, \tag{2.7}$$

where α is now explicitly represented as a function of plume geometry, l, species concentration (expressed as volume mixing fraction), ξ, and temperature, T. Here, species

24

concentration is expressed as a vector to emphasize there are a number of relevant species represented. The right side of the equation, completely expresses α as a sum over the relevant species. The total gas density, N, is given by $\frac{P}{k_B T}$ via the ideal gas law, $q(\xi)_i$ is the column density (a function of the ith species concentration, ξ_i), σ_i is the absorption cross-section, and τ_p is the transmittance of the particulate matter (if applicable). The absorption cross-section is the spectroscopic term which ties in the molecular properties of the gas. The physical interpretation is that of the "effective area" presented by a molecule to a stream of photons [3], but when expressed as the product of the spectral line intensity and line shape function,

$$\sigma_{i,j}(\tilde{\nu}, T) = \sum_j S_{i,j}(T) f_{i,j}(\tilde{\nu} - \tilde{\nu}_j, T), \tag{2.8}$$

it is more spectroscopically applicable. The spectral lines represent transitions between specific energy levels within a molecule. Due to the spacing between levels, spectral lines in the IR typically correspond to vibrational or ro-vibrational transitions. No transition is measured exactly, and the line shape function, $f_{i,j}(\tilde{\nu} - \tilde{\nu}_j, T)$, accounts for the shifting and broadening of spectral lines due to collisions and other physical processes. The spectral line intensity term, $S_{i,j}$, contains the spectral properties as they relate to the various molecular energy level transitions. It is driven by the population of the upper state and the probability of transition between the upper and lower state. The state populations are a function of temperature and governed by Boltzmann statistics (and non-linear), while the probability of transition is related to the Einstein coefficients and the transition-moment [3, 48].

In the present work, Equation 2.8 is computed directly in accordance with Rothman *et al.* [63]. LTE is assumed for the population Boltzmann statistics. The Voigt profile is used for the line shape, and a constant pressure is assumed throughout the flame. In computing the profile, only broadening rates for dry air are used, and the line mixing and continuum effects on the line shape are ignored. To reduce spectral simulation and fit computation time, cross-sections for each species are pre-computed between 300 K and 3000 K at 50 K

intervals. A quadratic interpolation is used to account for temperatures between those pre-computed points. The High-Temperature (HITEMP) spectroscopic database provides parameters for the computation of the H_2O and CO cross-sections, the High-Resolution Transmission (HITRAN) database provides for the CH_4, and the CDSD-4000 database provides for the CO_2. The HITEMP database incorporates CO_2 lines from the more dated CDSD-1000 database[68], therefore the more recent CDSD-4000 with additional lines is used [61, 67]. This database has shown some discrepancies at higher temperatures, but is still an improvement when compared to purely HITEMP generated spectra [1]. The HITRAN database used to provide the CH_4 parameters is not ideal for Flame A temperature conditions and does not contain the necessary hot bands to predict lines above 600 K [50, 60]. An expanded database (up to 2000 K) more suitable for this work has been found in the literature [50], but attempts to contact the authors have been unsuccessful. Therefore, the HITRAN database is used in this work despite the known disparity.

The flame observed in this work is both turbulent and inhomogenous. Both of which can complicate the interpretation of the spectrum and thus the three-dimensional temperature and species estimation from two-dimensional imagery. Figure 2.1, Panel A depicts the path of photons as they are born and pass through the additional layers of an arbitrary axisymmetric flame. A photon born at the rear of the flame in layer i is impacted by the transmissivity of the remaining layers between it and the detector. The representation of the instantaneous radiance due to these photons at time, k, is

$$L_k(\tilde{\nu}) = \sum_{i=1}^{n} \left[\left(1 - \tau\left(\tilde{\nu}, T_{i,k}, \vec{\xi}_{i,k}\right)\right) L_{BB}(\tilde{\nu}, T_{i,k}) \times \prod_{j=i+1}^{n} \tau\left(\tilde{\nu}, T_{j,k}, \vec{\xi}_{j,k}\right) \right], \qquad (2.9)$$

where, at instant k, the radiance of the ith layer is a product of the emissivity and the Planckian function at that layer. Where, as with Equation 2.7, the species concentration, $\vec{\xi}_{i,k}$, is again expressed as a vector to designate all the relevant species in the ith layer. As it passes through the flame, the radiance contribution from the ith layer is then attenuated
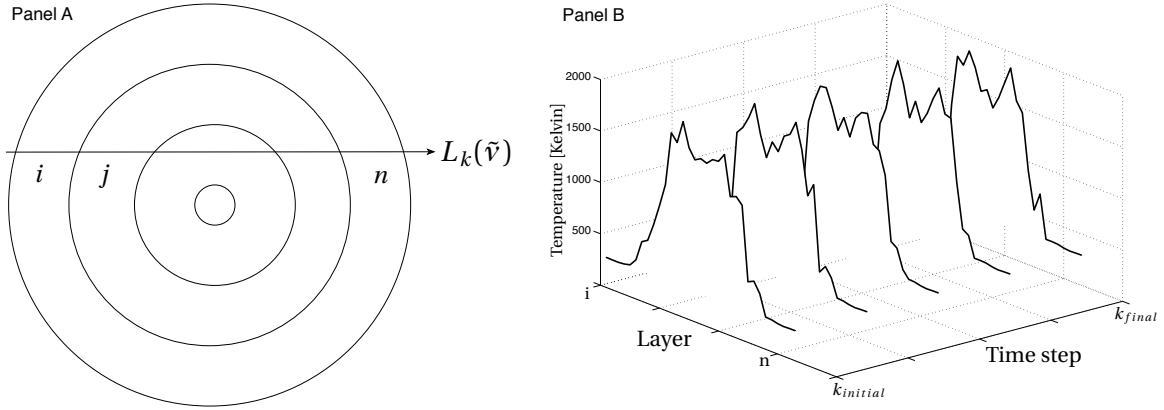
Figure 2.1: *Panel A*: Simple overhead rendering of an axisymmetric inhomogeneous flame in which each layer contains a unique temperature and species concentration. *Panel B*: Sample spatial and temporal turbulent flame temperature profiles for diametric paths.

by the remaining $n - i$ layers, each with its own unique instantaneous temperature and species values. The radiance at each layer is generated, attenuated and summed in this manner until the radiance contribution from all photons at all n layers is accounted for at instant k. Clearly the radiance is dependent upon the particular instantaneous profiles of the temperature and species across the layers of the flame, and these scalar profiles are impacted by turbulence.

To take any arbitrary time step, t, and interpret the radiance contribution from $L_{k+t}(\tilde{v})$ a new series of temperature and species profiles must now be considered. Figure 2.1, Panel B presents a series of sample instantaneous temperature profiles across the flame. At time k the temperature at any given layer has some degree of spatial dependence upon the temperature in neighboring layers, driven by the turbulent length scales inherent in the flame. At time $k + 1$ the temperature profile is subject to the same spatial constraints as well as some degree of temporal dependence upon the profile from time k, driven by the flames turbulent temporal scales. The calculation of these time and length scales is presented in the TASS analysis discussion further below, but an appreciation for the link between the

27

stochastic turbulent fluctuations, the scalar profiles, and the flame's radiance is essential to now consider an averaged flame radiance.

The instantaneous radiance is itself a path-integrated quantity, the corresponding mean radiance, $\overline{L(\tilde{\nu})}$, from N flame configurations is then both path-integrated and time-averaged and described as,

$$\overline{L(\tilde{\nu})} = \sum_{k=1}^{N} L_k(\tilde{\nu}) \, P\left(\vec{T}_k, \boldsymbol{\xi}_k\right).\tag{2.10}$$

Here, $P\!\left(\vec{T}_k, \boldsymbol{\xi}_k\right)$ is a normalized joint probability distribution which weights the likelihood of scalar profiles in the flame and thus the associated $L_k(\tilde{\nu})$. Temperature is a vector representing a single temperature for each layer, and concentration is a matrix representing the vector of relevant species for each layer. Recall the non-linearity of radiance in response to temperature and species. This ensures the mean radiance is not simply the radiance of the mean scalar values, i.e. $\overline{L(\tilde{\nu})} \neq L_k\left(\tilde{\nu}, \overline{T}, \overline{\xi}\right)$. Therefore, estimations of scalar quantities and the extraction of any turbulent statistics are complicated by both the inhomogeneous path and the averaging over the fluctuations in the radiance. With a firm grasp of the radiance generated at the flame, a discussion of the interferometric response to the scene radiance now follows.

2.2.2 Interferometric behavior.

Fourier-transform spectroscopy is the study of spectra resulting from detected source rays after they have been passed through an interferometer and mathematically manipulated via Fourier-transform. Figure 2.2, Panel A depicts a Michelson interferometer and the standard path a beam would take to the detector. The incident source ray is split at a beamsplitter; the two rays of equal intensity travel separate paths and are then recombined and measured at the detector. Due to the movable reflector, Ray 2 encounters an OPD and is forced in and out of phase with Ray 1. This results in an interference pattern at the detector and an interferogram of the type seen at the top of Panel B (gray).

28
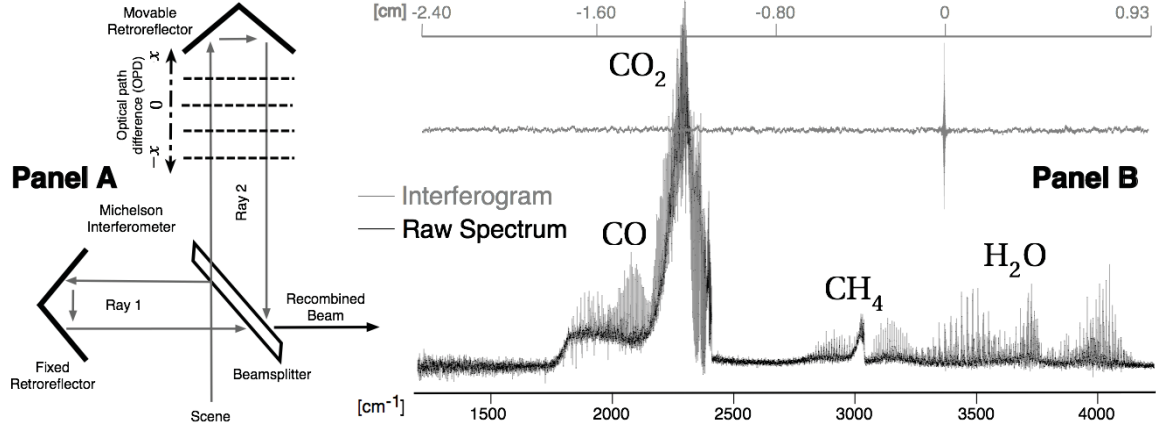
Figure 2.2: *Left*: The FPA captures broadband infrared images at regular OPDs as the Michelson sweeps, generating an interference pattern. *Right*: The interferogram (gray)—upon Fourier-transform—produces a recognizable source spectrum (black).

For a source with many frequencies, the interferogram is a superposition of interfering cosine waves of different wavelengths. The signal spike seen at the center of the interferogram corresponds to the point of zero OPD, where the movable mirror is at a location which has Rays 1 and 2 traveling the same pathlength—constructively interfering. A traditional FTS would obtain a single interferogram (and thus, a single spectrum) upon a complete scan of the mirror. An imaging FTS disperses the scene onto a FPA which results in an interferogram at each pixel. This combination of traditional IR camera and spectrometer provides a spatially resolved spectral understanding of a scene and opens doors to analysis traditionally not available. The complete equation for an interferogram $I(x)$ produced at pixel i, j by a Michelson-based IFTS is

$$I_{i,j}(x) = \int_0^\infty \left(1 + \cos\left(2\pi\tilde{v}vt\right)\right) G_{i,j}(\tilde{v}) \left(L_{i,j}^S(\tilde{v}, t) + L_{i,j}^I(\tilde{v})\right) d\tilde{v}, \qquad (2.11)$$

where x is the OPD (determined by $x = vt$, with mirror scan velocity, v, and time, t), $G_{i,j}(\tilde{v})$ is the spectrally-dependent response of the instrument, $L_{i,j}^S$ is the spectral radiance from the scene, and $L_{i,j}^I$ is the spectral radiance from the instrument's thermally generated photons.

The Fourier-transform of Equation 2.11 leads to the spectral representation of the intensity seen in Figure 2.2, Panel B (black) with the expected spectral features from any associated species.

In non-imaging FTS, the detector is typically AC-coupled. For a stationary scene, only the alternating current (modulated signal) (AC) (modulated) piece offers any useful information about the scene and the DC (constant) offset can be subtracted out. However, if the source is unsteady the fluctuations in the DC offset can cause significant fluctuations during the formation of the interferograms. To emphasize this point, Equation 2.11 can be alternately expressed as (ignoring instrument effects since they are accounted for during calibration):

$$I(x_k) = \int_0^\infty \left(1 + \cos\left(2\pi\tilde{\nu}x_k\right)\right) L_k(\tilde{\nu}, T, \vec{\xi}) \, d\tilde{\nu} = I_k^{\text{DC}} + I^{\text{AC}}(x_k), \tag{2.12}$$

where k now designates time-changing components, I_k^{DC} is the constant, spectrally-integrated signal, and $I^{\text{AC}}(x_k)$ is the modulated component associated with the change in OPD. Stochastic fluctuations in L_k^s drive variations in the I_k^{DC} offset.

This can be seen in Panel A of Figure 2.3, where the gray interferogram has been formed via a single sweep of the Michelson mirror. The stochastic fluctuations in the turbulent scene have severely disrupted the interferogram, and the resultant gray spectrum (the fast Fourier-transform (FFT) of the absolute value of the single interferogram) in Panel B appears to be difficult—if not impossible—to interpret. These fluctuations due to I_k^{DC} cannot simply be subtracted (as in the steady source case), but the impact of the fluctuations can be reduced by averaging over a number of interferograms. This is evidenced by the "cleaner" overlaid black interferogram and spectrum, here presented as the absolute value of the FFT of the mean interferogram. An expression for this time-averaged interferogram, $\overline{I(x_k)}$, will be of the same form as Equation 2.12, but now with a dependence on a time-averaged scene radiance, $\overline{L^S(\tilde{\nu})}$, and a now constant I^{DC} term with no k dependence.
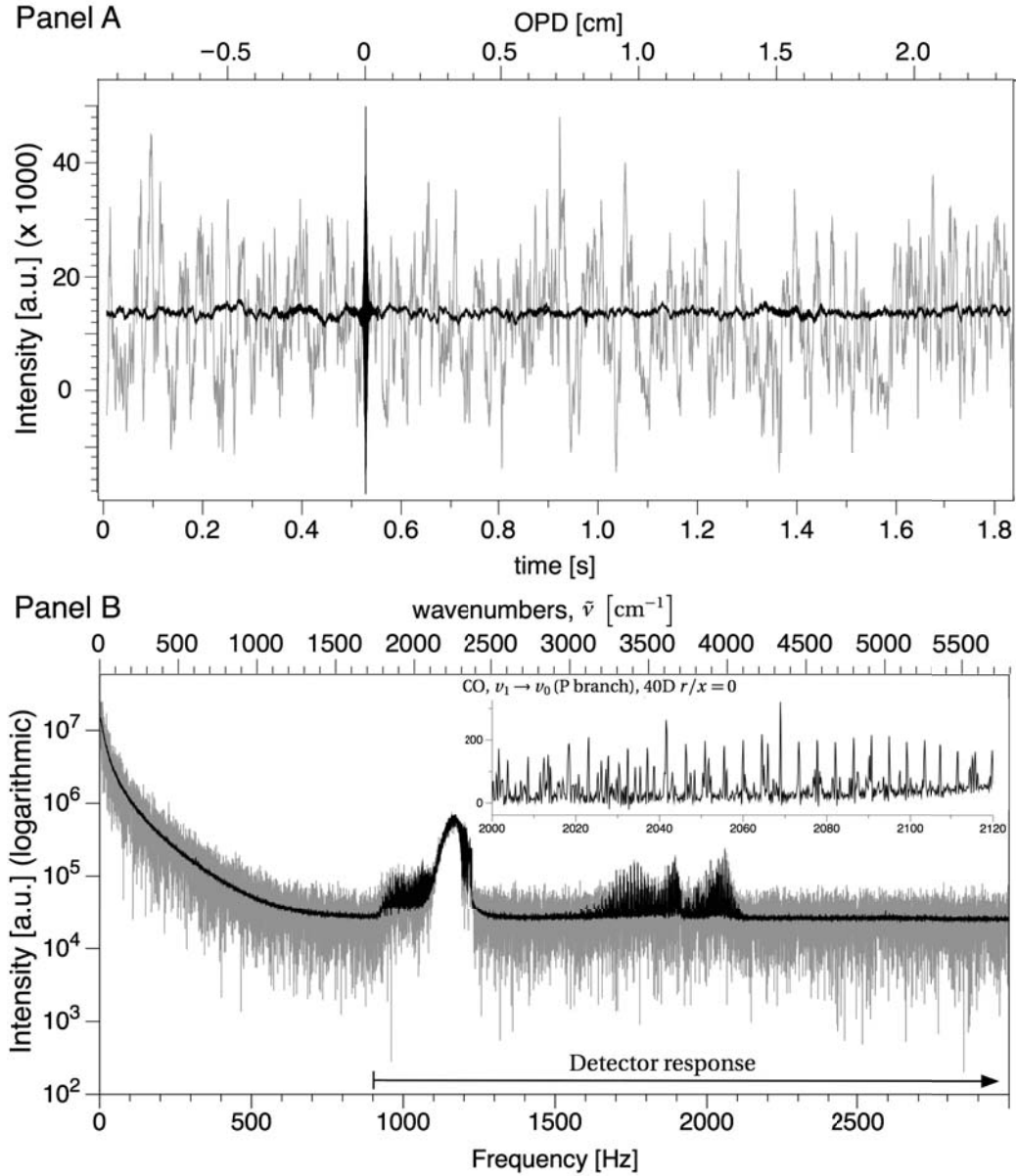
Figure 2.3: *Top*: A single interferogram (gray) impacted by fluctuations in L_k^S. Mean interferogram (black) averaged over many sweeps of the Michelson mirror. *Bottom*: The associated spectra with the single (gray) and mean (black) interferograms.

This time-averaging is useful when it is necessary to interpret a well resolved spectrum (as demonstrated by the expanded inset CO spectrum seen in Figure 2.3, Panel B), and in

the case of a steady source it can greatly increase the signal to noise, but in the case of the turbulent scene information is lost in this averaging. Notice the fluctuations in the single scan spectrum that are found below the start of the detector's spectral response near $1800\,\mathrm{cm^{-1}}$. Wavenumber and frequency are related via the Michelson mirror sweep speed, $f = v\tilde{v}$. Those fluctuations at frequencies below $1800\,\mathrm{cm^{-1}}$ are equivalent to radiant intensity fluctuations at frequencies unassociated with the spectral information encoded by the Michelson. These fluctuations contain information about $P\left(\vec{T}_k, \xi_k\right)$ and therefore the associated scalar profiles found in the flame. The heart of this work is to isolate the method to best detangle this turbulent "noise" and recover the scalar estimates and their associated statistics.

To best achieve this, an appropriate model of the scene radiance is required. The following discussion describes the theory behind the modeling and simulation of Flame A and the techniques used in the analysis of those simulations.

2.2.3   Modeling and simulation of a turbulent flame.

Instantaneous flame profiles are modeled following the TASS method described by Box, *et al.* [8] and applied to turbulent flames by Zheng [81] and Rankin [53]. In those works, all scalars were modeled following the TASS method; however, in the present work the TASS method is used solely to model the temperature profiles in the flame. The associated species concentrations are then selected based upon their individual correlation with temperature as determined by the DLR experimental data. The legacy and merits of TASS have been discussed in the literature review above, here the focus is on the modeling method itself.

As an overview, TASS employs Gaussian statistics to determine spatially and temporally correlated values while allowing for a weighted randomness to influence each successive selection. The Gaussian values are then mapped back to the non-Gaussian scalars and an instantaneous flame profile is realized [53, 81]. Two pieces are of primary

input to the model: the legacy DLR experimental data (and the inherent statistics) provide the foundation for the mapped values at each point, and the imagery from the current work provides the spatial and temporal length scales needed to properly correlate each selection.

For a normalized Gaussian variable—with a mean of zero and standard deviation of one—the realization at location, i, and instant, k, is described as

$$\zeta(i,k) = \phi_1 \, \zeta(i, k - \Delta k) + \phi_2 \, \zeta(i - \Delta i, k) + a(i,k), \tag{2.13}$$

where $a(i,k)$ is a random shock, $\zeta(i, k - \Delta k)$ and $\zeta(i - \Delta i, k)$ are the most recent temporal and closest spatial values of ζ respectively. ϕ_1 and ϕ_2 are intermediate model parameters which weight the influence of the two nearest temporal and spatial values relative to the random shock. The weighting is based on the correlation length and time scales, l and τ, respectively, and given by:

$$\phi_1 = \frac{\rho(\Delta k) - \rho(\Delta i)\rho(\Delta i, \Delta k)}{1 - \rho^2(\Delta i, \Delta k)} \tag{2.14}$$

and

$$\phi_2 = \frac{\rho(\Delta i) - \rho(\Delta k)\rho(\Delta i, \Delta k)}{1 - \rho^2(\Delta i, \Delta k)}. \tag{2.15}$$

The temporal $\rho(\Delta k)$ and spatial $\rho(\Delta i)$ autocorrelations are treated as functions of exponential decay and modeled as

$$\rho(\Delta i) = \exp\left(\frac{-\Delta i}{l}\right), \tag{2.16}$$

and

$$\rho(\Delta k) = \exp\left(\frac{-\Delta k}{\tau}\right). \tag{2.17}$$

The integral length and time scales are calculated from the imagery (described further below). Instances of high spatial correlation occur when l is greater than Δi, and equivalently high temporal correlation occurs when τ is greater than Δk. The cross-correlation function, $\rho(\Delta i, \Delta k)$ is simply modeled as the product of the two autocorrelation

33

functions. The random perturbation from Equation 2.13 is from a Gaussian distribution with a mean of zero and a standard deviation of

$$\sigma_a = 1 - \phi_1 \rho(\Delta k) - \phi_2 \rho(\Delta i). \tag{2.18}$$

A brief discussion of these equations and their behavior under certain conditions is warranted. The intermediate model parameters (ϕ_1, ϕ_2, and a) drive Equation 2.13 and are themselves influenced by the autocorrelation functions. When there is high spatial correlation ($\Delta i \ll l$) but little temporal correlation ($\Delta k \gg \tau$) Equation 2.14 goes to zero and Equation 2.15 goes to one. This then removes the impact of ϕ_1 in Equation 2.18, and the "randomness" impact of variable a—described by the spread of σ_a—while still reduced by ϕ_2 is greater than it would be if the system were both spatially and temporally correlated. The absence of ϕ_1 in Equation 2.13 removes the influence of the most recent temporal value of ζ, leaving only the spatial neighbor—weighted by ϕ_2—and the spatially influenced random shock. A reversal of these example correlation conditions results in a reversal of the impact to Equation 2.13: A large temporal correlation ($\Delta k \ll \tau$) and small spatial correlation ($\Delta i \gg l$) removes ϕ_2 and thus any influence from spatial neighbors. A physical flame will no doubt have some sort of combined spatial and temporal correlation, but examination of each extreme provides clarity to the behavior of the model parameters.

After a Gaussian variable has been assigned via Equation 2.13 at location, i, and instant, k, it is then mapped to the scalar realization (in this case, temperature). This simple mapping procedure occurs between the TASS generated Gaussian cumulative probability distribution function (CPDF) and the experimentally determined non-Gaussian scalar CPDF as seen in Figure 2.4, Panel A. Here, the Gaussian value, ζ, is specific to a location on the continuous interval $(0, 1)$ CPDF, $\Phi(\zeta)$. The mapping between the Gaussian CPDF to the non-Gaussian CPDF (continuous on the same interval), $F(T)$, is straightforward and provides a realization of a temperature, T, at location, i, and instant, k [33, 81]. The temperature CPDF comes directly from the Flame A measurements available in the DLR

experimental archive [75]. A value for ζ is generated and mapped at each location in the flame, forming a complete temperature instantaneous profile. This process is repeated for additional time steps until the desired number of flame profile realizations is met. Figure 2.1, Panel B, is a TASS generated model of n layers of Flame A at 40 D from arbitrary times $k_{initial}$ to k_{final}. To complete the flame model the species concentrations associated with each temperature at a given i,k must be chosen.
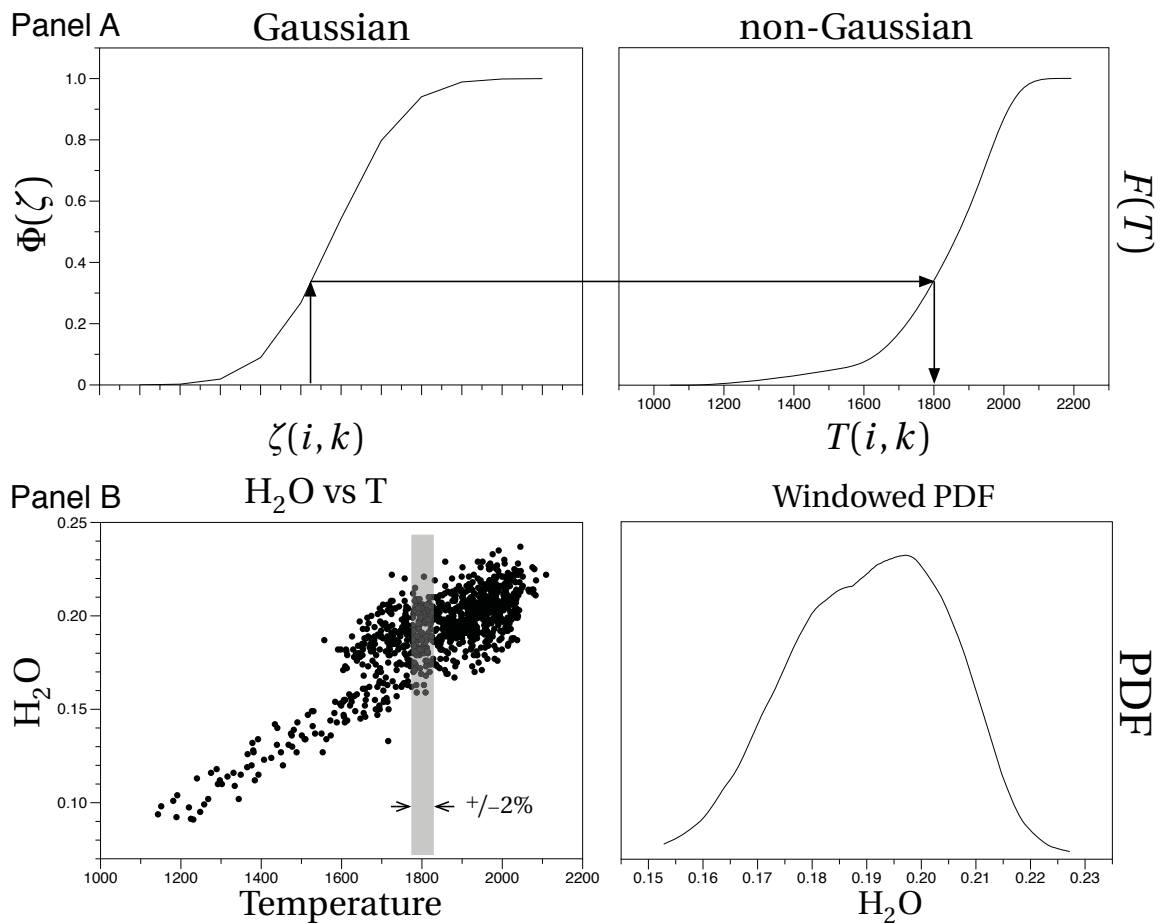
Figure 2.4: *Pane A:* Mapping of the non-Gaussian realization, $T(i,k)$ [75], from the Gaussian random variable, $\zeta(i,k)$. *Panel B:* (left) Sample of correlation between temperature and H_2O at 60 D, $r = 0$. (right) A species concentration is randomly selected from a narrow subset about the TASS generated temperature realization.

The DLR archive data contains simultaneous scalar measurements. This library—and the strong correlation between temperature and species—provides a simple method to generate physically viable concentration values for a given TASS generated temperature. Figure 2.4, Panel B, is a sample scatter plot of temperature versus H_2O (40 D, $r = 0$) from the DLR data [75]. After down-selecting the range of available species to a smaller window ($\Delta T = 2\%$) about the TASS generated temperature, an experimentally determined concentration is randomly chosen from the smaller subset of species concentration values. This pairing is accomplished for each species for all layers and time steps, effectively assembling a complete scalar model of Flame A stemming from the archived DLR data and driven by the integral time and length scales derived from the imagery acquired in this work. This method is a simplification brought about by the requirement to efficiently manage computational time and resources, but it is believed to be a reasonable approximation to the flame and suitable for analysis.

Turbulence at higher Reynolds number is typically separated into three main scales. It can be viewed as a cascade of the energy from the larger integral length scales, down to the mid-range Taylor microscale, and finally to the smallest Kolmogorov scale. The integral length scale is associated with the turbulent mixing and transport, and it is strongly influenced by the geometry of the flow [51]. The integral length and time scales used as inputs to the TASS model and reported in Chapter 4 and Appendix B of this work were calculated in the following manner [51]:

$$l = \int_0^\infty \rho(\Delta i)\, di, \tag{2.19}$$

and

$$\tau = \int_0^\infty \rho(\Delta k)\, dk, \tag{2.20}$$

where the autocorrelation functions ($\rho(\Delta i)$ and $\rho(\Delta k)$) are experimentally determined directly from the broadband intensity fluctuations in the DC imagery. These fluctuations are isolated by low-pass filtering the interferograms to remove any signal above the spectral

response beginning near $1800\,\mathrm{cm}^{-1}$, essentially converting the signal to that of a broadband IR camera. The exact methods and equations used to calculate $\rho(\Delta i)$, $\rho(\Delta k)$, and other flame properties (PDF and PSD) are described in more detail in Chapter 4. Here it is important to emphasize the link between the IFTS imagery and the TASS model. The degrees of spatial and temporal correlation defined by Equations 2.16 and 2.17 form the foundation of the TASS model and the integral length and time scales driving those equations are derived directly from the IFTS experimental data.
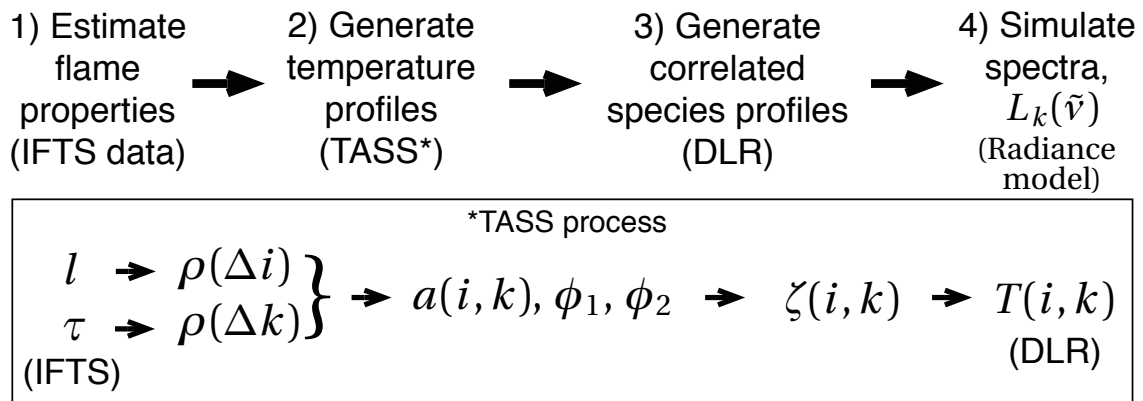
Figure 2.5: The flame modeling and spectral simulation process. *Inset:* The TASS modeling process.

The complete process for modeling Flame A and simulating the associated spectra is summarized in Figure 2.5. First, the autocorrelation functions are estimated from the IFTS data. These are then converted to integral time and length scales via Equations 2.19 and 2.20. Second, these results are input into the TASS model, as seen in the Figure 2.5 inset box. Equations 2.16 and 2.17 are used to calculate the intermediate TASS parameters ϕ_1, ϕ_2, and $a(i,k)$ at each location, i, and instant, k. These parameters yield Gaussian variables via Equation 2.13 that map to temperature values found in the non-Gaussian DLR measurement data. A complete spatial and temporal flame temperature model exists after

37

step two. Third, each temperature is associated with the remaining species scalars using the simple correlation method described above. At this point a temporally and spatially correlated profile of Flame A exists for any chosen number of time steps. Finally, the instantaneous profiles are are used to simulate an instantaneous LOS flame spectrum via Equations 2.8 and 2.9. A unique spectrum will exist at each LOS for each instantaneous configuration of the flame.

2.2.4   *Quantile interferogram analysis for turbulent flames.*

Tremblay's work in establishing quantile interferograms considered a blackbody radiator with a fluctuating temperature as a simple model of a turbulent source. While this model is unrealistic for quantitative plume modeling, the concept of quantile interferograms is still useful. When averaging over all interferograms—or equivalently all spectra—every instantaneous flame configuration is weighted in accordance with its likelihood. In a quantile interferogram, only those flame configurations which produce the same integrated quantile intensity (I_q^{DC}) are "averaged". In this section, this idea will be made more precise, and additional complications associated with LOS averaging will be discussed. For a TNF source, a single spectrally integrated intensity value can be achieved by more than one configuration of $L_k(\tilde{\nu}, T, \vec{\xi})$. This is driven by two primary factors. First, the various layers and different pathlengths through each of those layers (driven by the radial plume geometry) impact the spectral contribution from any scalar along a given LOS. For example, a higher temperature at one location, but with little pathlength contribution along the LOS, can contribute less to the total intensity than a lower temperature but a larger pathlength. The 2D imaging of a 3D source introduces such unavoidable complications. Second, even for a single layer source, the scalars can be combined in more than one manner to produce distinct spectra which share the same spectrally integrated value. This is ensured by the $2\,\mu$m to $5\,\mu$m range of the IFTS and the number of species with a spectral presence in that band.

Despite this break down in the monotonic response of intensity, the spirit of the quantile sorting method remains intact and may have utility in the analysis of turbulent flames. A major effort of this dissertation is exploring this utility. Several observations make this a reasonable approach. Temperature remains the most dominant driver of radiance, and as such remains highly correlated to integrated intensity even in these flame conditions. While not a monotonic relationship, the intensity response is still directly linked to the temperature profile along any LOS. As will be illustrated, the positive correlation between the two implies the fundamental concept of sorting by intensity to obtain quantile spectra which describe the scalar field remains viable.

For a TNF, the equation for the radiance, $L_q(\tilde{v})$, due to a particular integrated intensity quantile, I_q^{DC} (the quantile equivalent of I_k^{DC} from Equation 2.12), is treated as

$$L_q(\tilde{v}) = \sum_{k=1}^{N} L_k(\tilde{v}) \, P\left(\vec{T}_k, \xi_k \mid I_q^{DC}\right), \tag{2.21}$$

where the joint probability distribution governing the scalar profiles—which weighs the likelihood of the associated $L_k(\tilde{v})$—is now a conditional event. Only the configurations that give rise to I_q^{DC} are a part of this conditional distribution. This will be a much smaller subset of $L_k(\tilde{v})$ than the complete set giving rise to $\overline{L(\tilde{v})}$ in Equation 2.10.

In the present work, the integrated intensity will be sorted in the manner described by Tremblay *el al*. [71]. However, it will not be assumed a single point can be drawn from the sorted intensity and treated as a quantile spectra representative of the associated quantile temperature (or concentrations). Here, a sampling of interferograms about the intensity quantile will be drawn, and an $L_q(\tilde{v})$—an average over that smaller subset of flame configurations—will be determined to represent a particular quantile. Figure 2.6 depicts a random distribution of (simulated) integrated intensity values (upper left) and the equivalent sorted intensity profile (upper right). The 0.25, 0.50, and 0.75 quantiles are annotated on the sorted line where the dashed boxes represent a region over which spectra would be drawn. The resultant $\overline{L_q(\tilde{v})}$ will be the spectra used to retrieve scalar profiles.
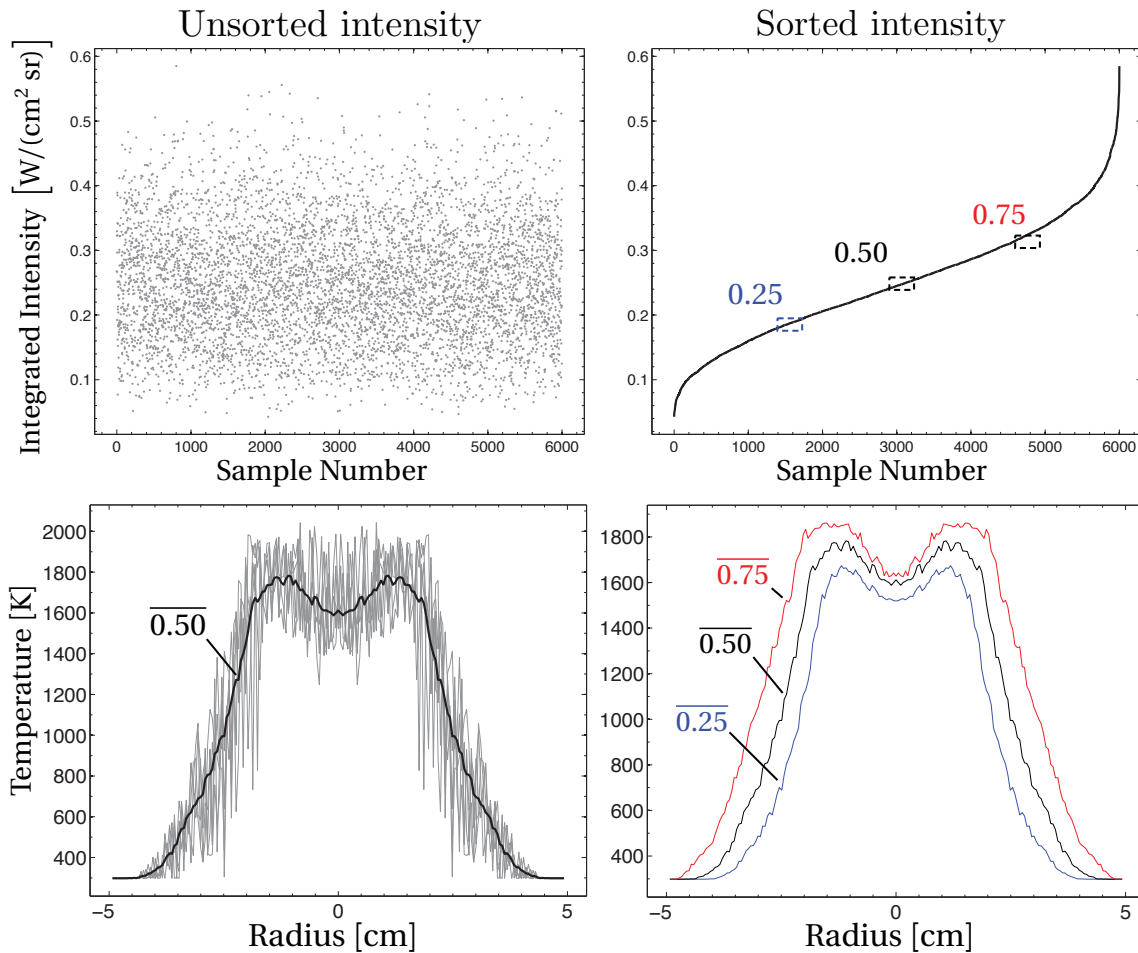
Figure 2.6: *Top*: Unsorted (left) and sorted (right) intensity values along a given LOS. Quantile locations are regions over which a spectral averaging would occur (dashed boxes). *Bottom*: (left, gray) Instantaneous temperature profiles associated with flame conditions leading to LOS found within the $q = 0.50$ bin. (left, black) Average temperature profile from within the $q = 0.50$ bin. (right) Average temperature profiles from the separate intensity sorted quantile bins.

The temperature profiles associated with the sorted intensities are shown in the lower half of Figure 2.6. The mean 0.50 temperature profile (black, lower left) is shown with a sampling of various instantaneous temperature profiles (gray) which—when combined

with the additional scalar profiles—give rise to the integrated LOS intensities found within the smaller 0.50 sort window. While fluctuations about the mean are evident, the standard deviation within this smaller sorted window is much smaller than what would be found from the deviations about the mean of the entire 6000 sample set. The comparison between the mean temperature profiles from each intensity sorted quantile window (lower right) establishes confidence in the fundamental concept of quantile spectra describing the scalar fields. A clear separation between temperatures can be seen across the entire profile, a direct result of the intensity quantile sort.

The complications introduced by a TNF such as inhomogeneity through multiple layers and fluctuating scalar statistics along each LOS disrupt the pure monotonic relationship between intensity and temperature exploited in Tremblay's analysis. However, since temperature is highly correlated with the major flame species concentration and with the LOS integrated intensity, the quantile spectra will be used—with the radiative transfer model—to explore their utility in the analysis of turbulent flames. First, the TASS flame model just described will be assessed to quantify its agreement with both mean spectra and with various quantile spectra. In principle, the quantile spectra provide a sensitive measure of how well a given flame model represents TRI. Flame measurements and TASS models will be compared to demonstrate the utility of quantile spectra for this purpose. Second, quantile spectra will be directly interrogated with a spectral fitting model—described in the next section—to assess the degree to which the fitted scalars at various quantiles are correlated with their known statistical distributions.

2.2.5 *Inversion method for a non-optically thin source.*

The inversion method developed in this work is inspired by a standard onion-peeling type method [16]. However, the implementation is iterative and removes the requirement for an optically thin source. The method leverages the multiple LOS provided by IFTS,
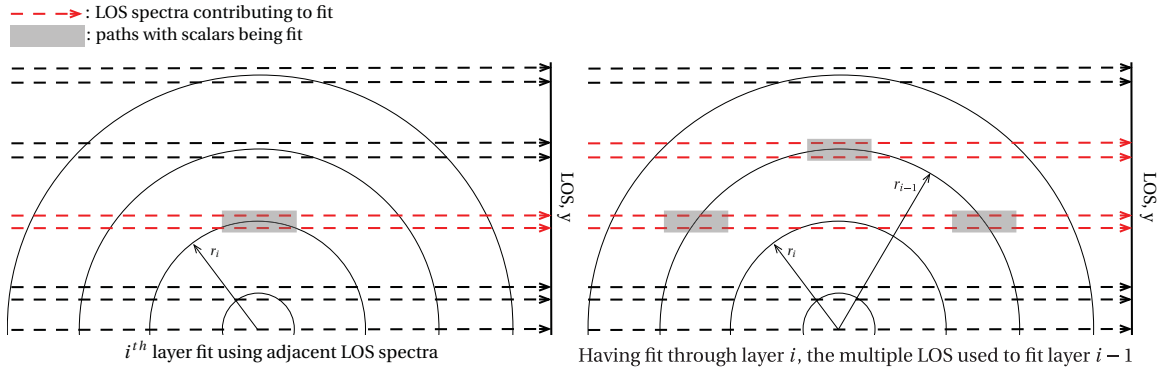
Figure 2.7: *left*: Geometry of the flame and LOS for a fit at an arbitrary layer, *i*. Fitting began at the outer most layer and those results are used along the LOS. The adjacent LOS spectra (red) are fit to the model and scalar estimates for layer *i* are acquired. *right*: Layer *i* results are then used to refine estimates from layer *i* − 1. Here, multiple LOS (red) are used in the refinement.

fits the entire spectrum to estimate scalars at each layer in the flame, and only requires atmospheric parameters as a starting estimate of scalars.

The inversion algorithm begins at a LOS well outside the flame. The exact location is determined by examining a radial plot of integrated intensity and selecting a point beyond where the signal is obviously only due to background and/or noise. A starting guess of atmospheric parameters is reasonable at this point, and no knowledge of the flame conditions is required to begin. The algorithm fits a layer then moves inward to the next, applying the results of that previous fit along the appropriate pathlength in the LOS at the new location. With the exception of the center most layer, at least two LOS are fit to retrieve scalar estimates. Initially, only the two adjacent LOS are simultaneously fit at a layer. Multiple LOS are fit when the algorithm works back outward to refine previous estimates. Figure 2.7 describes the geometry and the retrieval process for an arbitrary layer, *i*. The left side of the figure depicts layer *i* being fit for the first time. Initial scalar estimates

for the outer layers have been acquired as the process began at the outer edge and moved inward. The red arrows designate the two LOS spectra fit for the initial scalar estimates at layer i. Prior to moving inward to layer $i + 1$, the algorithm refines the results from layer $i - 1$ by applying the newly acquired estimates from i. Notice this now provides additional LOS for use in the fitting. The algorithm will continue this process of fitting, refining, and moving outward until all of the layers from $i - 1$ to outer most layer have been refined. It then steps to fitting $i + 1$. The initial guess passed into the model is either the scalar estimates from the previous layer, or—if it is a refinement step—the estimates from the previous fit at that layer.

The logic of the process is described more succinctly in Algorithm 1. Here, the inputs are a matrix, $\mathbf{S}$, of layers and atmospheric scalars, a vector, $\vec{r}$, which contains the radial sample points (equal to the number of layers in $\mathbf{S}$), a vector, $\vec{y}$, containing the LOS axis, and the matrix, $\mathbf{L}$, which contains the accompanying IFTS acquired (or simulated) spectra at each LOS. The algorithm returns an $\mathbf{S}$ which contains retrieved scalar estimates at each layer. The logic begins at line 1, where the fitting is declared to start at the outer most layer and move inward to center. The number of iterations to perform a given fit loop are defined in line 2. The fitting should continue for six iterations unless there is no change (from the previous iteration) in any estimated temperature value greater than 5 K. The refinement process—equivalent to the right side Figure 2.7—is handled by the loop over j at line 3. This moves from the current inner layer, i, to the outer most. The scalar fit results are retrieved at line 4. They are a result of fitting the multilayer radiative transfer model simultaneously to the various LOS spectra applicable at this stage of the algorithm. This process continues until the initial $\mathbf{S}$ has been filled with spectrally fit scalars from the outer layer to center.

Algorithm 1: INVERSION Onion-peeling inspired inversion method

    Input: $\mathbf{S}$ (*layers* × scalars), $\vec{r}$ (*layers*), $\vec{y}$ (LOS axis), $\mathbf{L}$ (LOS spectra)

    Output: An $\mathbf{S}$ matrix with spectrally fit scalar results at each layer

1 **for** $i \leftarrow$ *layers* ***down to*** 1 **do**

2   **while** *any* $\Delta T > 5\,\mathrm{K}$ ***and*** *iter* ≤ 6 **do**

          `// Fit current, inner most layer (i) then use results to`

             `refine previous estimates at outer layers`

3   **for** $j \leftarrow i$ ***up to*** *layers* **do**

             `// Fit applicable multiple LOS to retrieve or refine`

                `scalar estimates at layer j`

4             $\mathbf{S}(j) \leftarrow MultiLayerFit(\mathbf{S}, \vec{r}, \vec{y}, \mathbf{L})$

5 **return** S

III. Imaging Fourier-transform spectrometer measurements of a turbulent non-premixed jet flame

THE following is a published submission to Optics Letters presented in its entirety [31]. The focus is on documenting and summarizing the Purdue Flame A experiment, describing the impact of turbulence on interferogram formation, and presenting time-averaged imagery and spectra. The work is significant for the following reasons:

- It presents the first-ever high-resolution mid-infrared IFTS measurements of a turbulent jet flame.

- It provides unprecedented spectral and spatial resolution of a well-studied, canonical flame suitable for the verification and validation of combustion and radiation models.

- It presents a simple framework for understanding dynamic-scene interferometric measurements. This is necessary as it may seem counter-intuitive to some combustion diagnostics scientists that IFTS can be used to study turbulent flames.

- It compares IFTS measurements with existing non-imaging spectral measurements of a similar flame, and the excellent agreement validates the use of IFTS for this and future turbulent flame measurements.

This paper provides the foundation for the additional work found in Chapters 4 and 5 which examine the turbulent statistics and inhomogeneity of the flame. This brief article establishes the experiment and links the Purdue Flame A results to those found in the Sandia Flame A studies.

As the first author I was the primary contributor responsible for data capture, data reduction and analysis, and the initial draft of the article. Dr. Kevin Gross contributed as the primary editor and assisted with planning and organization. Dr. David Blunck acted as a

secondary editor and provided guidance from the standpoint of the combustion community. Dr. Brent Rankin acted as a secondary editor, but was also vital to the success of the experiment. He was the point of contact at the Purdue University Turbulent Combustion Laboratory and managed all the experimental set up and control of the flame being studied. Finally, Dr. Jay Gore acted as a secondary editor and recommended reviewers for the article upon submission. He also provided the personnel, materials, and funding for operation of the flame during the experiment.

3.1 Abstract

This work presents recent measurements of a $CH_4/H_2/N_2$ turbulent non-premixed jet flame using an IFTS. Spatially-resolved (128×192 pixels, $0.72\,mm/pixel$) mean radiance spectra were collected between $1800\,cm^{-1} \leq \tilde{\nu} \leq 4500\,cm^{-1}$ ($2.22\,\mu m \leq \lambda \leq 5.55\,\mu m$) at moderate spectral resolution ($\delta\tilde{\nu} = 16\,cm^{-1}$, $\overline{\delta\lambda} = 20\,nm$), spanning the visible flame. Higher spectral resolution measurements ($\delta\tilde{\nu} = 0.25\,cm^{-1}$, $\overline{\delta\lambda} = 0.3\,nm$) were also captured on a smaller window (8×192) at 20, 40, and 60 diameters above the jet exit and reveal the rotational fine structure associated with various vibrational transitions in CH_4, CO_2, CO, and H_2O. These new imaging measurements compare favorably with existing spectra acquired at select flame locations, demonstrating the capability of IFTS for turbulent combustion studies.

3.2 Introduction

Combustion diagnostics is a field of long standing interest with many resources continually dedicated to its study. Turbulence has significant effects on combustion processes such as turbulence-chemistry interactions, turbulence-radiation interactions, scalar dissipation, transport, and mixing. Non-intrusive optical diagnostic methods have been used to study combustion and all must consider the effects of turbulence. Laser-based methods are highly effective and widely used due to their high spectral and temporal

resolution [38]. Dispersive instruments [78, 79] and Fourier-transform spectrometers [65] have been used with optical scanners to tomographically deconvolve temperature and species concentrations. High-speed infrared cameras with various band-pass filters have been used to map spatial variations in radiant intensity and relate these to various measures of turbulence (e.g. integral length and time scales) [54] as well as the spatial distribution of scalar values (e.g. temperature and mole fraction) [6].

An IFTS is a hyperspectral imager that combines a Michelson interferometer with a staring infrared focal-plane array (FPA). There are several potential advantages of this instrumentation for combustion diagnostics. High spectral resolution across a wide bandpass enables identification of multiple species. Proper interpretation of the spectrum can permit simultaneous determination of temperature and species concentrations [28]. High spectral resolution is also beneficial to tomographic reconstruction techniques [41]. High-speed broadband infrared imagery is collected during each interferometric scan. This captures turbulence information and enables similar types of analysis already performed using infrared cameras. IFTS provides a useful passive and non-intrusive technique for studying combustion, and is particularly useful when (1) both high-speed imagery and spatially-resolved spectra are required; (2) characterization of high-pressure systems is required and collisional broadening effects become important; (3) more than one optical port is not available, limiting the types of laser-based methods available for interrogation. The present work presents the first IFTS measurements of a canonical turbulent jet flame. The scope of this work includes a qualitative discussion of the spectral imagery and a quantitative comparison with existing spectral measurements acquired at select locations in a similar flame. The impact of turbulent intensity fluctuations on interferogram formation is also described. Quantitative interpretation of flame spectra is the ultimate goal of this effort. However, it requires scalar field fluctuation statistics, and this important topic will be considered in future work.

47

3.3 Experimental

The experiment consisted of the Telops Hyper-Cam IFTS, two calibration blackbodies, and the flame. The flame tube is 480 mm long with an 8 mm exit diameter (D), mounted vertically, and moveable via unislide to allow combined imaging of the entire visible flame length without camera tilt. The flame replicates Flame DLR_A from the International Workshop on Measurement and Computation of Turbulent Nonpremixed Flames (TNF Workshop) with a jet exit Reynolds number of 15,200 and exit velocity of 42.2 m/s. Mass flow rates were 313 mg/s, 59 mg/s and 1105 mg/s for CH_4, H_2, and N_2 respectively. Flow rates were calibrated using a dry turbine meter and controlled by setting the pressure upstream of three choked orifice plates [54].

The TNF Workshop flames are well characterized and designed for collaborative comparisons of measurements and models. A library of local velocities and scalar values (temperature, species mole fractions) measured simultaneously using laser doppler velocimetry, Raman, Rayleigh, and LIF techniques is available for download [46, 75].

The IFTS is based on a traditional Michelson interferometer coupled to a high-speed $320{\times}256$ Indium Antimonide staring focal-plane array (FPA) via $f/\# = 2.5$ imaging optics [23, 28]. The spectral range covers $1800\,cm^{-1}$ to $6667\,cm^{-1}$, and the spectral resolution can be selected between $0.25\,cm^{-1}$ to $150\,cm^{-1}$. An interferometric "datacube" is a collection of snapshot images taken at equally-spaced OPD, and Fourier-transformation along this dimension produces a spectrum at each pixel.

An external 0.25 X telescope expanded the field-of-view and reduced the minimum working distance to the flame. A 45% transmission neutral density filter, used to prevent saturation, limited the short-wavelength response to $2.22\,\mu m$ ($4500\,cm^{-1}$). The IFTS was located 47.5(10) cm from the flame. The imaging system has an effective focal length of 19.7 mm at this working distance. The $30\,\mu m$ pixel pitch of the FPA yields an instantaneous field-of-view (IFOV) of 1.52 mrad which translates to 0.72±0.02 mm at the flame and is

constant across the array. The mean RMS spot size radius is 13.7 μm, and increases from 11.2 μm to 21.1 μm moving from center to corner of a 128×192 window. Mapping the Rayleigh $\lambda/4$ wavefront error depth-of-focus criterion, $\delta f = \pm 2\lambda (f/\#)^2$, to object space produces a conservative estimate of the depth-of-field of ± 2 cm when computed at 2.5 μm, the shortest wavelength with appreciable energy arriving at the FPA. Throughout much of the flame, the spectral imagery can thus be interpreted as integrated along the line-of-sight (LOS). However, the widest part of the flame is ~ 15 cm, indicating some blurring will occur along the LOS. A detailed Zemax [77] optical model of our system indicates that more than 75% of the energy (relative to the diffraction-limited case, 86.4%) comes from the LOS for a pixel viewing the center of the widest (± 7.5 cm) flame region.

The IFTS was mounted to a gimbal with preset locations for intermittent calibration measurements. A standard two-point calibration using the wide-area blackbodies set to 595 °C and 200 °C was performed pixel-wise to determine the system response (gain, $G_i(\tilde{\nu})$) and instrument self-emission (offset, $L_i^I(\tilde{\nu})$). The higher blackbody temperature produced a peak signal at ˜90% of the detector's dynamic range and slightly exceeding that from the brightest part of the flame. At 595 °C, the Planckian distribution monotonically decreases with frequency across the detector bandpass. This resulted in a nominal signal-to-noise ratio (SNR) in $G(\tilde{\nu})$ which decreased nearly linearly from 15 to 1 between 3000 cm^{-1} to 5000 cm^{-1}. Since the system response is known to vary smoothly and slowly with $\tilde{\nu}$, a spline was fit to each pixel's gain curve to mitigate the impact of low gain SNR on the calibrated spectrum.

Two sets of flame measurements were made. The first set was collected with high spectral resolution (0.25 cm^{-1}) in a small window (8×192) traversing the flame at 20 D, 40 D and 60 D above the burner to facilitate identification of various chemical species. Interferometric datacubes consisted of 52,742 images and were collected at a rate of 0.55 Hz. 512 cubes were averaged to produce a mean, calibrated image of the flame

radiance. The second set increased the FPA window height (128 × 192) to facilitate measurement of the entire flame and decreased spectral resolution ($16\,\text{cm}^{-1}$) to simplify data reduction. Datacubes consisted of 1,186 images and the acquisition rate increased to 4.2 Hz. Seven separate regions of the flame were imaged to produce a composite image of the entire flame. In each set, the camera's integration time was $20\,\mu\text{s}$, and imaging frame rates exceeded 5 kHz. Ambient temperature, pressure, and humidity were monitored with a Kestrel 4500 Weather Meter with averages of $25\,^{\circ}\text{C}$, 989 hPa, and 44% respectively.

3.4 Dynamic Scene Interferometry

Fourier-transform spectrometry is typically used to study stationary scenes, so we briefly review interferogram formation so that the impact of stochastic intensity variations from the turbulent flame can be properly understood. The formation of an interferometric datacube is depicted in Panel A of Fig. 3.1. Light enters the Michelson producing an interference pattern at the FPA which encodes the spectral radiance at each pixel in the image. This interferogram is a function of the optical path difference, x, or time, t, (the two being related by the constant mirror sweep speed v):

$$I_i(x) = \int_0^\infty \left(1 + \cos\left(2\pi\tilde{\nu}x\right)\right) G_i(\tilde{\nu}) \left(L_i^S(\tilde{\nu}) + L_i^I(\tilde{\nu})\right) d\tilde{\nu} \tag{3.1}$$

$$= I_i^{\text{DC}} + I_i^{\text{AC}}(x). \tag{3.2}$$

Here, $L_i^S(\tilde{\nu})$ is the scene spectrum at pixel i, $L_i^I(\tilde{\nu})$ represents the instrument's thermal self-emission, and $G_i(\tilde{\nu})$ is the system response. A two-point calibration determines $G_i(\tilde{\nu})$ and $L_i^I(\tilde{\nu})$. The I_i^{DC} term represents the spectrally-integrated intensity and $I_i^{\text{AC}}(x)$ is the cosine transform of the spectrum produced by the Michelson. In a non-imaging FTS, the detector is often AC-coupled, dedicating the full range of the analogue-to-digital converter to the more useful AC piece. This is not possible with a FPA, so each pixel has a modulation signal riding on top of the DC offset.
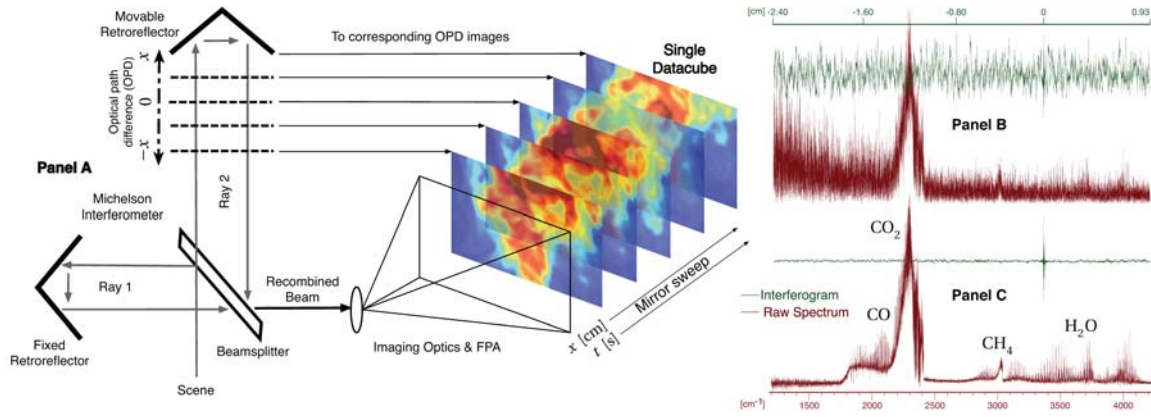
Figure 3.1: *Panel A*: Schematic illustrating the FPA capturing infrared images at fixed OPDs as the Michelson sweeps, generating an interferometric datacube. *Panel B*: Single interferogram (green, upper curve) and corresponding raw spectrum (red, lower curve) at flame center 20D above exit. *Panel C*: Time-averaged interferogram (green, upper curve) and corresponding mean flame spectrum (red, lower curve).

For a turbulent jet, the scene radiance is stochastically fluctuating on a timescale much shorter than the interferometer's acquisition rate. Thus, the "DC" term is now time-dependent and the AC term has no simple interpretation as it is the cosine transformation of a stochastically-varying signal. This is illustrated in Panel B of Fig. 3.1 showing a single interferogram and corresponding raw magnitude spectrum. The fluctuations in integrated intensity dominate the signal and obscure the zero-path difference (ZPD) where all wavelengths constructively interfere. The corresponding spectrum is dominated by the frequencies associated with turbulent radiation fluctuation, although a feature near $2300 \, \mathrm{cm}^{-1}$ resembling emission from the asymmetric stretching mode (ν_3) of CO_2 is recognizable. Large intensities below the detector cut-off ($\tilde{\nu} \leq 1800 \, \mathrm{cm}^{-1}$) are due to turbulent fluctuations.

For an ergodic system, an ensemble of measurements will produce a mean interferogram corresponding to the mean spectral radiance since Eq. 3.1 is a linear

transformation. Panel C presents the same pixel's mean interferogram from 512 measurements, demonstrating that the turbulent fluctuations are suppressed. The resulting spectrum is now recognizable with rotational fine structure associated with vibrational transitions in H_2O, CH_4, CO, and CO_2.

3.5 Results and Discussion

Fig. 3.2 presents uncalibrated broadband imagery in Panels A and B, dividing the flame along the axis of symmetry into single-snapshot and time-averaged quantities. Each segment is temporally independent from the others. In Panels A and B, the images were acquired at a common OPD near $x = 370\,\mu m$. Away from ZPD, the imagery is similar to what an infrared camera would measure ($I_i(x) \simeq I_i^{DC}$) since the broadband nature of radiation ensures $\left|I_i^{AC}(x)\right| \ll I_i^{DC}$. At the burner tip, the distance traveled by the jet during the FPA's integration time is 0.84 mm, exceeding the IFOV by approximately 12%, a conservative estimate of blurring due to the rapid deceleration of the jet. Moreover, the turbulence integral length scales for this flame between 20 D to 60 D are within 9.1 mm to 24 mm [54]. Thus, the turbulent structures exceed the spatial resolution by an order of magnitude. The time between repeated observations at a particular OPD is 240 ms, greatly exceeding the turbulence integral time scales (2.3 ms to 5 ms between 20 D to 60 D). Repeated observations at each OPD are statistically independent.

Also shown in Fig. 3.2 are calibrated images (via the time-averaged interferometric cubes) resulting from integration over spectral bands corresponding to CO_2 (Panel C) and CH_4 (Panel D). The imagery provides a qualitative impression of the distribution of these species throughout the flame. For example, CO_2 emission is low near the burner tip but increases axially as air is entrained to fuel the combustion reaction. The CO_2 band radiance peaks at 55 D, in agreement with previous narrowband 4.34(10) μm measurements of the same flame [54]. Temperature, species concentration, and the LOS distance through the flame all affect the band-integrated radiance. For example, the initial increase in CH_4
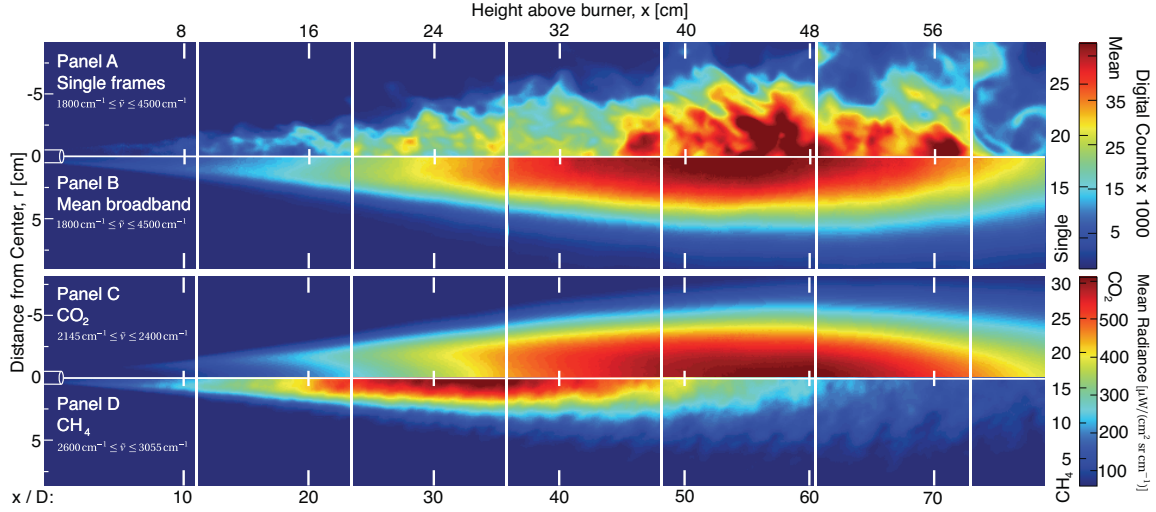
Figure 3.2: *Panel A*: Single broadband images from the lower spectral resolution ($16\,\mathrm{cm}^{-1}$) datasets with 128×192 FPA window. *Panel B*: Corresponding time-averaged broadband images. *Panel C*: Time-averaged radiance spectrally-averaged over a prominent CO_2 band. *Panel D*: Time-averaged radiance spectrally-averaged over a prominent CH_4 band. (Last spatial region limited due to unislide range.)

intensity with distance from the tip is due to increasing temperature and despite decreasing concentration. Proper interpretation of the spectrum will enable the deconvolution of these interdependencies.

The mean high-resolution spectrum acquired from a diametric path at $20\,\mathrm{D}$ is presented in Panel A of Fig. 3.3. Emissions from CH_4, CO, CO_2, and H_2O are resolved, and major vibrational transitions are annotated using common spectroscopic notation [60]. Individual lines associated with the P-branch of CO are visible between $2000\,\mathrm{cm}^{-1}$ to $2150\,\mathrm{cm}^{-1}$; lines from the R-branch overlap with the strong CO_2 emission band associated with the asymmetric stretching mode.

The mean low-resolution spectra from diametric paths at $20\,\mathrm{D}$, $40\,\mathrm{D}$ and $60\,\mathrm{D}$ are compared with previous (non-imaged) LOS measurements of Flame A by Zheng *et al.* [78]

in Panel B of Fig. 3.3. A spatial average over a 3×3 window was performed to approximate the 2 mm resolution of Zheng's data. The solid lines represent the apparent (i.e. at-sensor) radiance. For proper comparison, atmospheric correction was performed (dashed lines) using measured lab conditions and assuming 500 ppm CO_2 concentration. Agreement is excellent at 40 D and 60 D. However, the CO_2 peak near 2300 cm^{-1} is 20 % below the previously reported value at 20 D. Radiance uncertainties (95% confidence interval) are shown and include the effects of both systematic errors in calibration and noise. Noise is estimated as the root-mean-square value of the imaginary component of the time-averaged spectrum. Turbulent fluctuations are minimized in the time-averaged interferogram, so the error band does not quantify the large variance in flame radiance. At 20 D and 60 D, the mean uncertainty between 2200 cm^{-1} to 2350 cm^{-1} is 5% and 4%, respectively. Between 3000 cm^{-1} to 4000 cm^{-1}, the uncertainty increases to 20% and 10%, respectively, at 20 D and 60 D.

3.6   Conclusions

This work makes two key contributions. First, it validates the use of IFTS for studying turbulent flames and provides complete time-averaged hyperspectral imagery of Flame A. Segments of the flame were imaged with spectral resolution an order-of-magnitude better than previous measurements, and this data could be used to evaluate and improve narrowband radiation models. Second, it demonstrates the potential of IFTS for combustion diagnostics. Mean hyperspectral images contain information about the distribution of both temperature and many major gas species throughout the flame. Additionally, the high-speed broadband imagery comprising each interferometric measurement contains information about the fluctuation statistics. High resolution in all three domains — spectral, spatial, and temporal — is extremely valuable in the study of turbulent combustion, and is captured in IFTS measurements. Having demonstrated the validity of time-averaged spectra in this
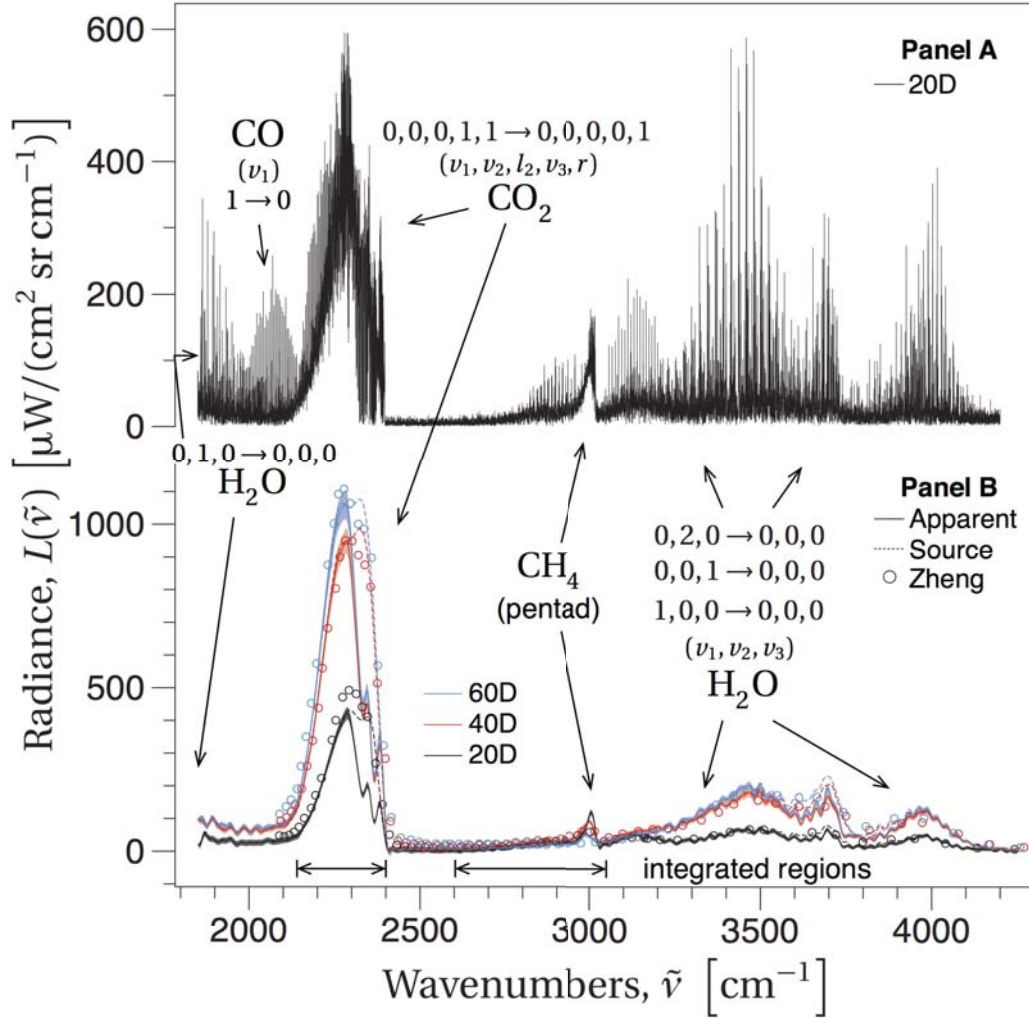
Figure 3.3: *Panel A*: Diametric, high-resolution ($\delta\tilde{\nu} = 0.25\,\text{cm}^{-1}$) apparent flame spectrum at 20 D with spectroscopic transitions annotated. *Panel B*: Apparent (—) and atmospheric-corrected ($\cdots$) low-resolution diametric flame spectra ($\delta\tilde{\nu} = 16\,\text{cm}^{-1}$) at 20 D, 40 D and 60 D (black, red, blue) compared with previous measurements ($\circ$). Radiance uncertainty (95% confidence interval) presented as a translucent band around each apparent spectrum. The CO_2 and CH_4 bands used in Fig. 3.2 are identified.

work, our efforts will now turn to leveraging the high-speed imagery contained within

IFTS measurements to understand scalar fluctuation statistics, a key step in the quantitative interpretation of turbulent flame hyperspectral imagery.

IV. Forward modeling and simulation of a turbulent, multilayer source

T HE following is a draft manuscript prepared for submission to the Journal of Quantitative Spectroscopy and Radiative Transfer presented in its entirety. The focus is on describing flame radiance and interferogram formation in the absence of time-averaging, deriving flame properties via IFTS for TASS analysis and simulation, and it introduces the quantile analysis method for turbulent flames. The work is significant for the following reasons:

- It presents the first-ever IFTS acquired flame properties (PDF, PSD, spatial and temporal auto-correlation coefficients, and integral time and length scales) validated against published narrowband IR results.

- It provides unprecedented high-resolution ($0.25\,\text{cm}^{-1}$) on axis spectral comparisons between IFTS acquired and TASS simulated spectra. This demonstrates the utility of IFTS for the verification and validation of combustion and radiation models.

- It introduces and demonstrates the quantile interferogram analysis method for turbulent flames. Successful demonstration of the sorting method is necessary to establish quantile spectra as suitable for future inversion and scalar retrieval.

- It compares on-axis, quantile-sorted IFTS acquired and TASS simulated spectra.

- It demonstrates that RMS spectra can be estimated from quantile spectra with favorable comparison to directly-measured RMS spectra from FIAS.

This paper is important to the inversion and scalar retrievals performed in Chapter 5. The TASS simulated spectra are anchored to experimentally acquired spectra, and the viability of the quantile method is established.

As the first author and primary contributor I was responsible for data capture, data reduction and analysis, and the initial draft of the article. Dr. Kevin Gross is a contributor and will be the primary editor. Dr. Brent Rankin is an ongoing source of collaboration and will be a secondary editor.

4.1 Background

Turbulent fluctuations introduce many complications in combustion radiation modeling, and experimental diagnostic methods for the evaluation and improvement of narrowband radiation models are extremely valuable. A diagnostic method is even more useful if scalar statistics—beyond simply the mean values—can be reported throughout the flame. Infrared (IR) imaging, Fourier-transform spectroscopy (FTS), and a litany of laser based methods have been applied to the study of turbulent flames, all with success [6, 38, 54, 65, 74, 80]. Imaging Fourier-transform spectroscopy (IFTS) is a relatively recent option and has previously achieved good results reporting lower resolution $16\,\mathrm{cm}^{-1}$ mean spectra [31]. Here, the diagnostic method is advanced significantly further: (1) IFTS derived flame properties are calculated and compared to previously reported IR imagery results; (2) an established stochastic TASS method and a line-by-line radiative transfer model featuring the latest high-temperature spectroscopy databases are used to simulate LOS spectra which are compared with measurements at $0.25\,\mathrm{cm}^{-1}$ resolution; (3) quantile spectra are introduced as means of quantifying turbulence-radiation interaction (TRI) and measured and TASS-modeled quantile spectra are compared. This sorting method demonstrates a powerful link between stochastic interferometric fluctuations and the associated scalar fluctuations driving the turbulence. The intensity sorted quantile spectra are sensitive to the non-linearities driven by the turbulence and are excellent descriptors of the turbulence-radiance interaction (TRI). Stochastic fluctuations would initially seem to make IFTS a futile diagnostic method for the analysis of turbulent flames [40]. However, the cou-

pling of these intensity fluctuations with the interferograms at each pixel presents a dataset rich in the spectral, spatial, and temporal regimes.

4.2 Experimental

A complete experimental description has been documented previously [31], therefore only a brief description of the flame, instrument, and calibration procedures will be provided here. The flame is a reproduction of Flame DLR_A (Flame A) from the International Workshop on Measurement and Computation of Turbulent Nonpremixed Flames (TNF Workshop) with a jet exit Reynolds number of 15,200 and exit velocity of 42.2 m/s. There is good agreement between IFTS spectral measurements from this experiment with previously published Flame A on-axis measurements [31, 78]. The flames are not experimentally identical, and some spread in the Purdue flame (likely due to the lack of outer coflowing air) has been noted [53], therefore comparisons made here are only for the diametric path.

The TNF Workshop flames are ideal for the verification and improvement of mathematical models and collaborative comparisons of measurements. The flames have been shown to be reproducible through independent measurements at separate laboratories and are extremely well characterized [2, 46, 64]. An internet library of experimental results characterizing each flame in the series is available for download [75].

The IFTS disperses the signal from a traditional Michelson interferometer onto an Indium Antimonide (InSb) 320×256 focal-plane array (FPA). It has a spectral range from $1800\,\mathrm{cm^{-1}}$ to $6667\,\mathrm{cm^{-1}}$, and a selectable spectral resolution between $0.25\,\mathrm{cm^{-1}}$ to $150\,\mathrm{cm^{-1}}$. An interferometric "datacube" is a collection of images taken at equally-spaced optical path differences (OPDs). The Fourier-transform of the datacube along the OPD produces a spectrum at each pixel.

The two sets of measurements emphasized either spectral or spatial resolution. The first set was collected at $20\,\mathrm{D}$, $40\,\mathrm{D}$ and $60\,\mathrm{D}$ above the burner with high spectral resolution

$(0.25\,\text{cm}^{-1})$ but small window $(8 \times 192,\ \text{H}\times\text{W})$ size. The 512 datacubes at each pixel consisted of 52,742 images and were collected at a spectral acquisition rate of $0.55\,\text{Hz}$. The second set increased the FPA window height (128×192) to increase the amount of flame imaged and decreased spectral resolution $(16\,\text{cm}^{-1})$ to simplify data transfer, storage, and reduction. The 512 datacubes at each pixel consisted of 1,186 images and the spectral acquisition rate increased to $4.2\,\text{Hz}$. Seven separate regions of the flame were imaged to capture the entire flame, which was moveable via unislide. Imaging frame rates exceeded $5\,\text{kHz}$ throughout, and the camera's integration time $(20\,\mu\text{s})$ was the same for both sets. A standard two-point calibration using two wide-area blackbodies set to $595\,^{\circ}\text{C}$ and $200\,^{\circ}\text{C}$ was performed to determine the system response and instrument self-emission at each pixel. A complete description of calibration procedures is documented elsewhere [31, 57].

4.3 Theory

4.3.1 *Turbulent multilayer flame radiance.*

The LOS radiance due to a turbulent flame of n layers at instant k is represented as

$$L_k(\tilde{v}) = \sum_{i=1}^{n} \left[\left(1 - \tau\left(\tilde{v}, T_{i,k}, \vec{\xi}_{i,k}\right) \right) L_{BB}(\tilde{v}, T_{i,k}) \times \prod_{j=i+1}^{n} \tau\left(\tilde{v}, T_{j,k}, \vec{\xi}_{j,k}\right) \right]. \qquad (4.1)$$

Here, the photons born at layer i are expressed as the product of the emissivity (shown as one minus the transmittance, $\tau(\tilde{v}, T, \vec{\xi})$), and Planck's blackbody function, $L_{BB}(\tilde{v}, T)$. The transmittance is expressed via

$$\tau\left(\tilde{v}, T, \vec{\xi}\right) = \exp\left(-lN \sum_{m} \xi_m \sigma_m\right), \qquad (4.2)$$

where l is the pathlength through layer i, N is the number density, ξ_m is the mth species mole fraction at layer i, and σ_m is the corresponding absorption cross-section. As they travel, the photons from layer i are then attenuated by the transmittance in the remaining $n - i$ layers of the flame. Both τ and L_{BB} are wavenumber dependent and non-linear functions of temperature, T, while τ has an additional non-linear dependence on species concentration,

$\vec{\xi}$, where species concentration is expressed as a vector representing all the relevant species at a given layer. Accordingly, the radiance has a non-linear response to changes in the unique temperature and species profiles across the flame at each instant, k. The expression for the time-averaged radiance due to this flame is

$$\overline{L(\tilde{\nu})} = \sum_{k=1}^{N} L_k(\tilde{\nu}) \, P\left(\vec{T}_k, \vec{\xi}_k\right), \qquad (4.3)$$

where each of the N total instantaneous configurations of $L_k(\tilde{\nu})$ are weighted appropriately by the joint scalar probability distribution, $P\left(\vec{T}_k, \vec{\xi}_k\right)$. This distribution weights the instantaneous radiance profiles, L_k, by the likelihood of the flame configuration which produced it. Here, temperature is now expressed as a vector representing the profile across the multiple layers, and species concentration as a matrix representing the profiles of the relevant species. The non-linear relationship between the scalar field values and the instantaneous radiance ensures the mean radiance is not equal to the radiance generated by the mean scalar values, i.e. $\overline{L(\tilde{\nu})} \neq L_k\left(\tilde{\nu}, \overline{T}, \overline{\xi}\right)$. Properly interpreting or modeling the radiance due to a turbulent flame is highly dependent on a reasonable model for the scalar profiles and their probability.

4.3.2 Instantaneous flame profile modeling.

It has been shown a turbulent flame's scalar profiles can be reasonably represented via TASS analysis [53, 81]. The complete details of the method are fully described in the literature and will only be briefly summarized here. This technique employs Gaussian statistics to model flame behavior while accounting for spatial and temporal correlations between scalars and allowing for a (turbulent) random shock. A simple mapping procedure is then employed to determine the non-Gaussian scalar flame realizations from the model results.

Here, the TASS model is driven by two primary inputs: the multipoint scalar measurements from the DLR experimental archive and the turbulent time and length scales measured in this work. The DLR data provides the mapped non-Gaussian scalar statistics

61

and anchors the modeled flame profiles to experimentally validated data. The integral time and length scales measured in this work drive the Gaussian statistics at the front end of the model and influence the degree of temporal and spatial correlation throughout. The integral values are determined by the expressions [51],

$$\tau = \int_0^\infty \rho(\Delta k)\, dk, \tag{4.4}$$

and

$$l = \int_0^\infty \rho(\Delta i)\, di. \tag{4.5}$$

Here, the autocorrelation coefficients, $\rho(\Delta k)$ and $\rho(\Delta i)$, are measured directly from the interferometric imagery (described in more detail in the Measured flame characteristics section below).

It should be pointed out the method for building the complete scalar profile used in this work is modified from that of the literature. Here, the documented TASS method is used to determine only the flame's temperature profile realizations, and the remaining concentration values are chosen based on their correlation with temperature. The temporally correlated scalar measurements found in the DLR archive data show a strong correlation between temperature and species, providing a simple method to generate physically viable concentration values for a given TASS generated temperature. Temperature correlated species profiles were assembled by leveraging this relationship.

Instantaneous scalar profiles were modeled using this modified TASS method and combined with Equation 4.1 to simulate the instantaneous radiance due to Flame A. Spectra are modeled by computing cross-sections directly in accordance with Rothman *et al.* [63]. LTE is assumed for the population Boltzmann statistics. The Voigt profile is used for the line shape, and a constant pressure is assumed throughout the flame. In computing the profile, only broadening rates for dry air are used, and the line mixing and continuum effects on the line shape are ignored. To reduce spectral simulation and fit computation time, cross-sections for each species are pre-computed between 300 K and 3000 K at 50 K intervals. A

quadratic interpolation is used to account for temperatures between those pre-computed points. The HITEMP spectroscopic database provides parameters for the computation of the H_2O and CO cross-sections, the HITRAN database provides for the CH_4, and the CDSD-4000 database provides for the CO_2. The HITEMP database incorporates CO_2 lines from the more dated CDSD-1000 database[68], therefore the more recent CDSD-4000 with additional lines is used [61, 67]. This database has shown some discrepancies at higher temperatures but is still an improvement when compared to purely HITEMP generated spectra [1]. It is known the HITRAN database used to provide the CH_4 parameters is not ideal for Flame A temperature conditions and does not contain the necessary hot bands to predict lines above $600\,\text{K}$ [50, 60]. Various comparisons between the simulated and experimentally captured spectra are provided in the results below. The interpretation of the scene radiance and the response at the detector is now provided.

4.3.3 *Interferometric analysis.*

A brief description of a Michelson interferometer-based IFTS is beneficial. Light enters the Michelson and is split—one beam encounters a movable reflector, the other follows a fixed path. As the moveable reflector is scanned the light is forced in and out of phase, resulting in an interference pattern dispersed onto the detector. The resultant interferogram encodes the spectral radiance at each pixel in the image.

This interferogram at a given pixel is described by the equation:

$$I(x_k) = \int_0^\infty \left(1 + \cos\left(2\pi\tilde{\nu}x_k\right)\right) L_k(\tilde{\nu}, T, \vec{\xi})\, \mathrm{d}\tilde{\nu} = I_k^{\mathrm{DC}} + I^{\mathrm{AC}}(x_k), \qquad (4.6)$$

where the optical path difference (OPD), x_k, is related to time, t_k, via the constant mirror sweep speed, v. To simplify discussion of Equation 4.6 the instrument's thermal self-emission is omitted and the system response is treated as unity. $L_k^S(\tilde{\nu}, T, \vec{\xi})$ is the scene spectrum described by Equation 4.1 and is itself a dynamic quantity subject to the stochastic fluctuations in the flame's scalar profiles. The I_k^{DC} term on the right side of Equation 4.6 represents the spectrally-integrated total intensity (a quantity which varies with L_k),

and $I^{AC}(x_k)$ is the cosine transform of the total spectrum produced by the action of the Michelson. In a non-imaging FTS the DC term is filtered out. Here the FPA makes this separation impossible, therefore each pixel contains both the modulated signal and the offset. This outcome proves to be advantageous for flame study, as demonstrated in Figure 4.1.

In Panel A of Figure 4.1, a high pass filter (HPF) and low pass filter (LPF) have been applied at $1600\,\mathrm{cm}^{-1}$ to a single interferogram at $60\,\mathrm{D}$ (center pixel). The lower frequency broadband intensity fluctuations due to turbulence, I^{DC}_{LPF}, are clearly seen in the upper LPF interferogram centered near 30,000 counts. The filtering has removed the high-frequency signal content due to the scanning Michelson and isolated the lower frequency turbulence, essentially converting the signal to that of a kHz frame rate IR imager. The HPF interferogram centered about zero is the modulated signal encoded by the Michelson—the $I^{AC}(x_k)$ term from Equation 4.6—which contains the spectrum upon Fourier-transform.

In Panel B, the unfiltered instantaneous (grey) spectrum is the absolute value of the FFT of a single interferogram to frequency space. Here, the impact of the turbulence on the spectrum is obvious. Only the most prominent spectral features are discernible amongst the "noise" of the intensity fluctuations. The improved (black and inset) spectrum is the absolute value of the FFT of the mean interferogram from 256 measurements. The lower frequency response due to the turbulence has mostly dissipated prior to the start of the detector response near $900\,\mathrm{Hz}$ ($1800\,\mathrm{cm}^{-1}$), and the uncorrelated fluctuations in the spectral region is suppressed. The inset CO spectrum demonstrates the precision of species identification via hi-resolution ($0.25\,\mathrm{cm}^{-1}$) mean spectra, where individual rovibrational transitions within the fundamental $v_1 \to v_0$ P branch have been isolated.

Panel C of Figure 4.1 demonstrates the utility of recording an interferogram at each pixel. The left image is a spatial map of the coefficient of variation (I_σ/I_μ) generated from the broadband intensity fluctuations—of the type shown in Panel A—found in each
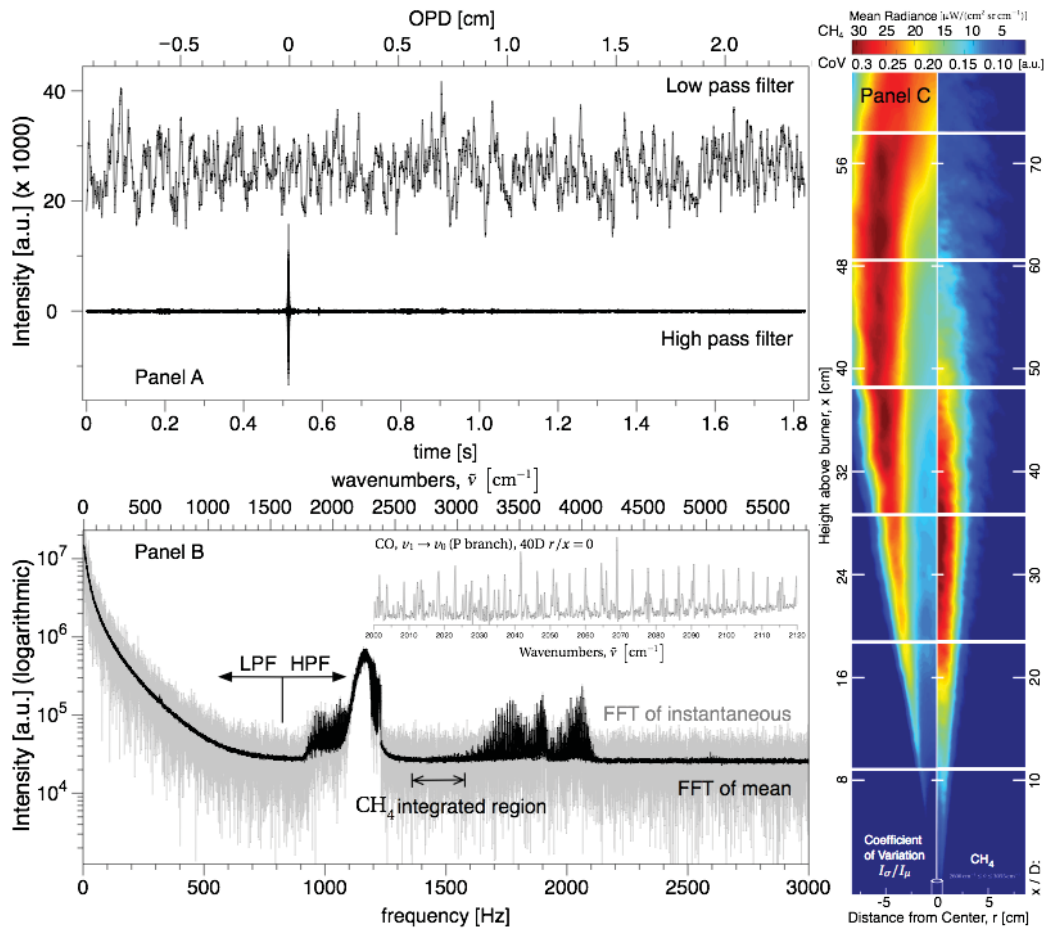
64

Figure 4.1: Interferometric behavior in the presence of turbulence *Panel A*: A high and low pass filter (HPF and LPF) applied at $1600\,\mathrm{cm}^{-1}$ to a single interferogram. *Panel B*: Absolute value of instantaneous (grey) and mean (black) spectra after fast Fourier-transform (FFT) of a single interferogram and a mean interferogram, respectively. Inset is an expanded view of the CO fundamental ($v_1 \rightarrow v_0$) P branch from the $0.25\,\mathrm{cm}^{-1}$ mean spectrum. *Panel C*: Left is a map of the coefficient of variation (I_σ/I_μ) captured from the interferometric statistics at each pixel. Right is a time-averaged intensity map of a prominent CH_4 spectral band.

interferogram after low pass filtering. The right image is a map of the time-averaged integrated intensity from the CH_4 spectral pentad. The integrated region is annotated in

Panel B—although few CH_4 spectral features remain at 60 D above exit. The broadband spectrum at each pixel opens the door to the imaging of select species as desired, while the high-speed imaging associated with the capture of each interferogram complements the spectral information with rich statistical data to further characterize the flame.

Broadband fluctuations captured by LPF interferograms of the type seen in Panel A are an integrated response to $L_k(\tilde{\nu})$ as the scene changes with each instant, k. As such, these fluctuations contain information about $P\left(\vec{T}_k, \xi_k\right)$ from Equation 4.3. As demonstrated by the imagery in Panel C, this information is contained at each pixel, providing statistical information for the entire flame. The joint nature of $P\left(\vec{T}_k, \xi_k\right)$ and the nonlinear response of $L_k(\tilde{\nu})$ to concentration and temperature make the detangling of the statistics problematic and requires a unique method of analysis.

4.3.4 *Quantile interferogram analysis for turbulent flames.*

The method of quantile sorting by I_{LPF}^{DC} has previously been applied with some success [43, 71]. The previous efforts relied on the monotonically increasing nature of $L_k(\tilde{\nu})$ with T. In the present work, the joint distributions of scalars at different layers of the flame and the associated various pathlengths no longer guarantee that monotonic relationship. However, temperature along the LOS remains the dominant driver of intensity, and it is believed the quantile sorting method remains applicable to turbulent flames.

In this work the experimentally captured scene radiance is first sorted by DC component at each OPD in interferogram space. The quantile-sorted interferograms are then Fourier-transformed to quantile spectra. The simulated spectra are sorted by their integrated intensity—essentially the DC component—and the equivalent quantile spectra are selected from that sort.
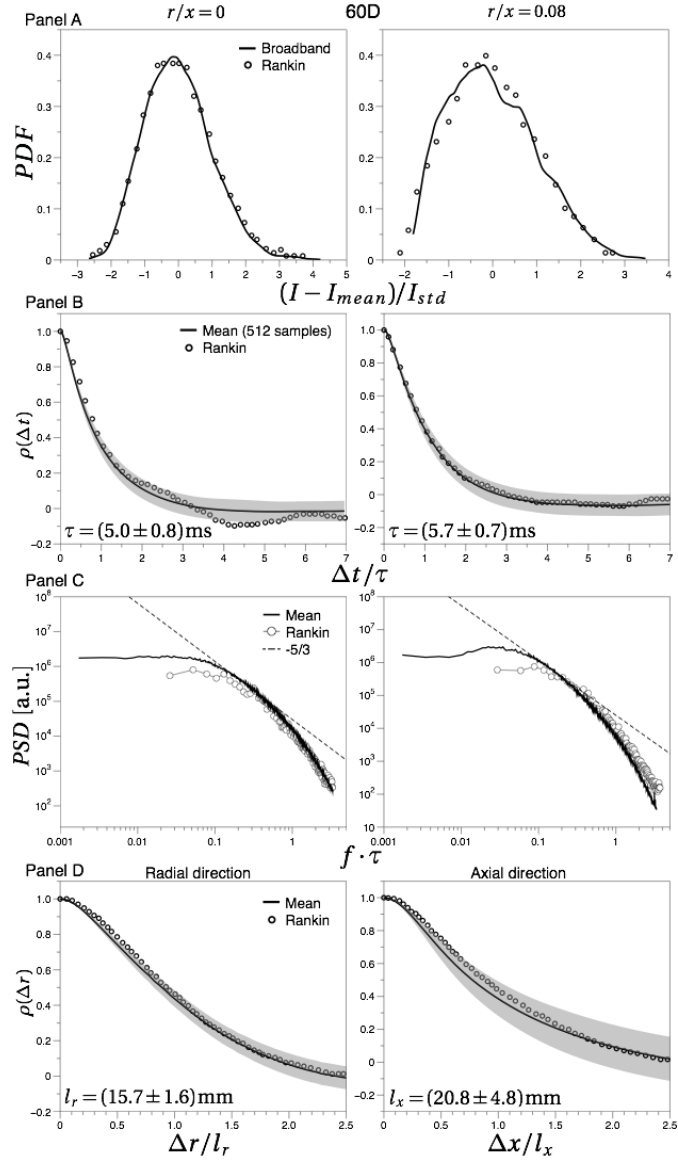
Figure 4.2: Broadband (solid line) and narrowband (points) [54] flame property comparisons at 60 D for representative diametric ($r/x = 0$, left) and chord-like ($r/x = 0.08$, right) paths. *Panel A*: Probability density functions of the radiation intensity. *Panel B*: Temporal auto-correlation coefficients. *Panel C*: Power spectral density functions of the radiation intensity. *Panel D*: Spatial auto-correlation coefficients for the radial (left) and axial (right) directions.

4.4 Results and Discussion

4.4.1 *Measured flame characteristics.*

Various Flame A properties derived from I_{LPF}^{DC} at 60 D are compared with narrowband IR imagery data previously reported by Rankin *et al.* [54] in Figure 4.2 and Table 4.1. The narrowband measurements were acquired using an IR camera (InSb detector) with a narrowband 4.34±0.1 µm filter to measure the radiation emitted by carbon dioxide. The broadband autocorrelation and PSD functions were computed in the same manner as the narrowband measurements described by Rankin *et al.* [53, 54]. Comparisons solely at 60 D are presented here, but additional comparisons have also been made at 20 D and 40 D with similar results.

The normalized PDFs in Panel A of Figure 4.2 compare well for both diametric ($r/x = 0$) and chord-like ($r/x = 0.08$) paths. The broadband PDFs were generated from the stochastic fluctuations in a single hi-resolution raw interferogram. After low pass filtering at 1600 cm^{-1} each 52,000+ point interferogram was then cropped by 3,000 points on each end to remove any artifacts from the filtering. There is little skewness for the diametric path, while the chord-like path produces a perceptibly skewed PDF. This is a result of intermittency off axis [22] and in agreement with previous studies of turbulent flames [79]. The PDFs at additional heights (not shown) confirm the increase of skewness with r.

Temporal autocorrelation functions are compared in Panel B. The narrowband points were generated from 6,400 measurements while the broadband data is the mean of the 512 separate high-resolution interferograms, each filtered and cropped in the manner described above. The band of grey is the standard deviation about the mean results. For comparison, the separation time (Δt) is normalized by the integral time scales (τ) of the radiation intensity fluctuations calculated via Equation 4.4 and reported in the lower left of each plot. The broadband computed time scales exactly match the narrowband results for both the diametric and chord-like paths at 60 D, and the autocorrelation plots are in good

agreement. Table 4.1 contains the additional time scale comparisons at 20 D and the IFTS measurements at 40 D (IR measurements at that height were not reported). The excellent agreement (at or below 4 %) between IFTS and IR at both 20 D and 60 D indicates the IFTS measurement at 40 D is likely accurate. The IFTS measured values for τ from Table 4.1 are used in the TASS simulated spectra found below.

The broadband PSD plots in Panel C have been scaled to overlap the narrowband, allowing for a comparative emphasis on functional behavior. The logarithmic y-axis is therefore an arbitrary, unitless scale. The shape of the plots agree well and the broadband PSD confirm the steady energy-containing region at low-frequencies, the normalized break frequency near 0.1, and the $(f \cdot \tau)^{-5/3}$ normalized decay behavior in the inertial-like region at intermediate frequencies [51, 54].

Spatial autocorrelation functions and integral length scales calculated via Equation 4.5 for the radial (left) and axial (right) directions are presented in Panel D. As with the temporal results, the x-axis has been normalized by the computed integral scale. To calculate l_x a larger window height was needed than that provided by the high-spectral resolution dataset. Therefore, the broadband axial data was computed from the 512 low-resolution interferograms, each with less than 1,200 measurements, and the standard deviation is much larger for these results. The autocorrelation functions for both paths are in excellent agreement, but the computed length scales for the narrowband differ more than expected. Table 4.1 contains the IFTS and IR comparisons between length scales at 20 D and 60 D. The IFTS results agree with the IR results within 14 % and 12 % for 20, and 60, respectively. The FIAS measurements of l_r at 40 D are reported by Zheng *et al.* [81]. These values stem from varying l_r radially within the TASS model until good agreement between FIAS and simulated spectra for both mean and RMS spectral radiation intensities was reached. The 2.4 mm to 11 mm reported in Table 4.1 span from $r/x = 0$ to $r/x = 0.14$, with the peak 10.8 mm occurring at $r/x = 0.12$. Varying l_r had little affect on the mean

spectra, but the RMS spectral values for the chord-like paths greater than $r/x = 0.3$ were very sensitive to the length scale. In the present work the single IFTS measured l_r value for each height is used in the TASS computation, therefore spectral comparisons are made at $r/x = 0$ to avoid complications due to off axis l_r sensitivity.

Table 4.1: Comparison of computed Flame A integral length and time scales at 20 D, 40 D and 60 D. Properties computed from broadband IFTS measurements made in this work, narrowband IR measurements made by Rankin *et al*. [54], or FIAS/TASS comparisons made by Zheng *et al*. [81]. Narrowband IR results were not reported at 40 D, IFTS l_x measurements were not possible at 20 D and 40 D due to the alignment of the flame and FPA at those heights, and radial variations of l were only carried out at 40 D.

Property	τ [ms]				l [mm]				
	$r/x = 0$		$r/x = 0.08$		Radial (l_r)			Axial (l_x)	
x/D	IFTS	IR	IFTS	IR	IFTS	IR	FIAS	IFTS	IR
20	2.2 ± 0.2	2.3	2.3 ± 0.3	2.4	5.7 ± 0.4	5.0	N/A	N/A	9.1
40	4.2 ± 0.6	N/A	3.6 ± 0.3	N/A	11.7 ± 1.0	N/A	$2.4 - 11$	N/A	N/A
60	5.0 ± 0.8	5.0	5.7 ± 0.7	5.7	15.7 ± 1.6	17.8	N/A	20.8 ± 4.8	24

4.4.2   *Mean high-resolution spectral comparisons.*

Figure 4.3 presents a comparison between high-resolution ($0.25\,\text{cm}^{-1}$) mean experimental (black) and TASS simulated (red) spectra through the diametric path at 20 D, 40 D and 60 D. The residuals from data and model and the imaginary part of the data— representative of the instrument noise—are included at each height (gray). Previous comparisons between TASS simulated spectra and Flame A did not exceed $16\,\text{cm}^{-1}$, therefore this comparison examines the simulation's performance at a much higher fidelity. The spectral comparison is excellent at all three heights with only one expected exception. The sim-
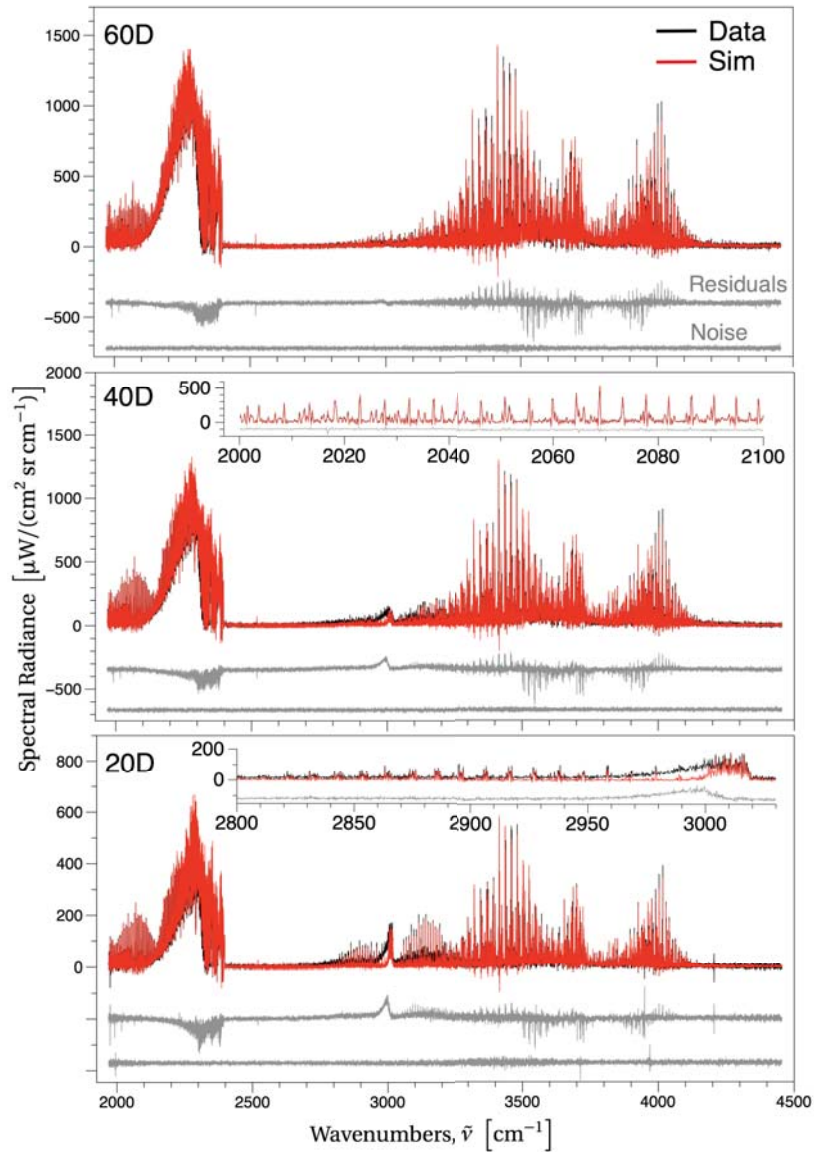
Figure 4.3: High-resolution $(0.25\,\mathrm{cm}^{-1})$ comparison of experimental (black) and TASS simulated (red) spectra through the diametric path at $20\,\mathrm{D}$, $40\,\mathrm{D}$ and $60\,\mathrm{D}$. Residuals (grey) at each height have been offset for easier interpretation.

ulated spectrum underpredicts the intensity of the CH_4 pentad seen near $3000\,\mathrm{cm}^{-1}$. This is likely due to the lack of high temperature CH_4 lines available in the spectral database, and an effort is being made to supplement the CH_4 lines accordingly. The CH_4 disparity

is more evident within the inset plot from $2800\,cm^{-1}$ to $3300\,cm^{-1}$ at 20 D. The dominant species in the midwave spectral region are CO_2 and H_2O, both of which compare very well. There is some structure in the CO_2 residuals near $2400\,cm^{-1}$ and throughout the H_2O region from $3300\,cm^{-1}$ to $4100\,cm^{-1}$ at all three heights. This is possibly due to inaccuracies with the parameters used to compute the contribution from the atmospheric pathlength between sensor and flame. Atmospheric measurements were taken near the instrument but may not have accurately reflected the warmer conditions between sensor and flame. The P and R branches of the CO fundamental transition are in excellent agreement. The inset spectrum at 40 D is an expanded region of the P branch near $2100\,cm^{-1}$ and provided to emphasize the good agreement. Upon closer inspection, individual rovibrational transitions are resolved and compare very well. The mean relative error between data and simulation is 17.4 %, 18.6 % and 13.5 % at 20 D, 40 D and 60 D respectively. This was computed using only lines at or above ten times the RMS of the instrument noise (at or above $50\,\mu W/(cm^2 srcm^{-1})$ in all three cases).

4.4.3 Quantile spectral comparisons.

In Figure 4.4 (left), comparisons between the 0.25, 0.50, and 0.75 quantiles from the DC sorted experimental (solid) and simulated (dashed) spectra through the same diametric path at 20 D, 40 D and 60 D are presented. The experimental spectra are intentionally chosen from the lower resolution ($16\,cm^{-1}$) data to ease plotting and interpretation, and the simulated spectra have been convolved to match. At 20 D and 40 D the median (0.50) quantiles match particularly well in the CO_2 region near $2300\,cm^{-1}$, while the peak 0.75 and 0.25 simulated quantiles are both within approximately 10 % of the data. At 60 D the simulated 0.50 and data 0.75 lines nearly overlap, while the 0.25 match quite well. It is unclear why the simulation overpredicts the upper two quantiles, but given the sensitivity of TASS to the choice of l_r, the use of a single length scale in the present work could be impacting the comparison. This was shown to have little effect on the mean spectrum
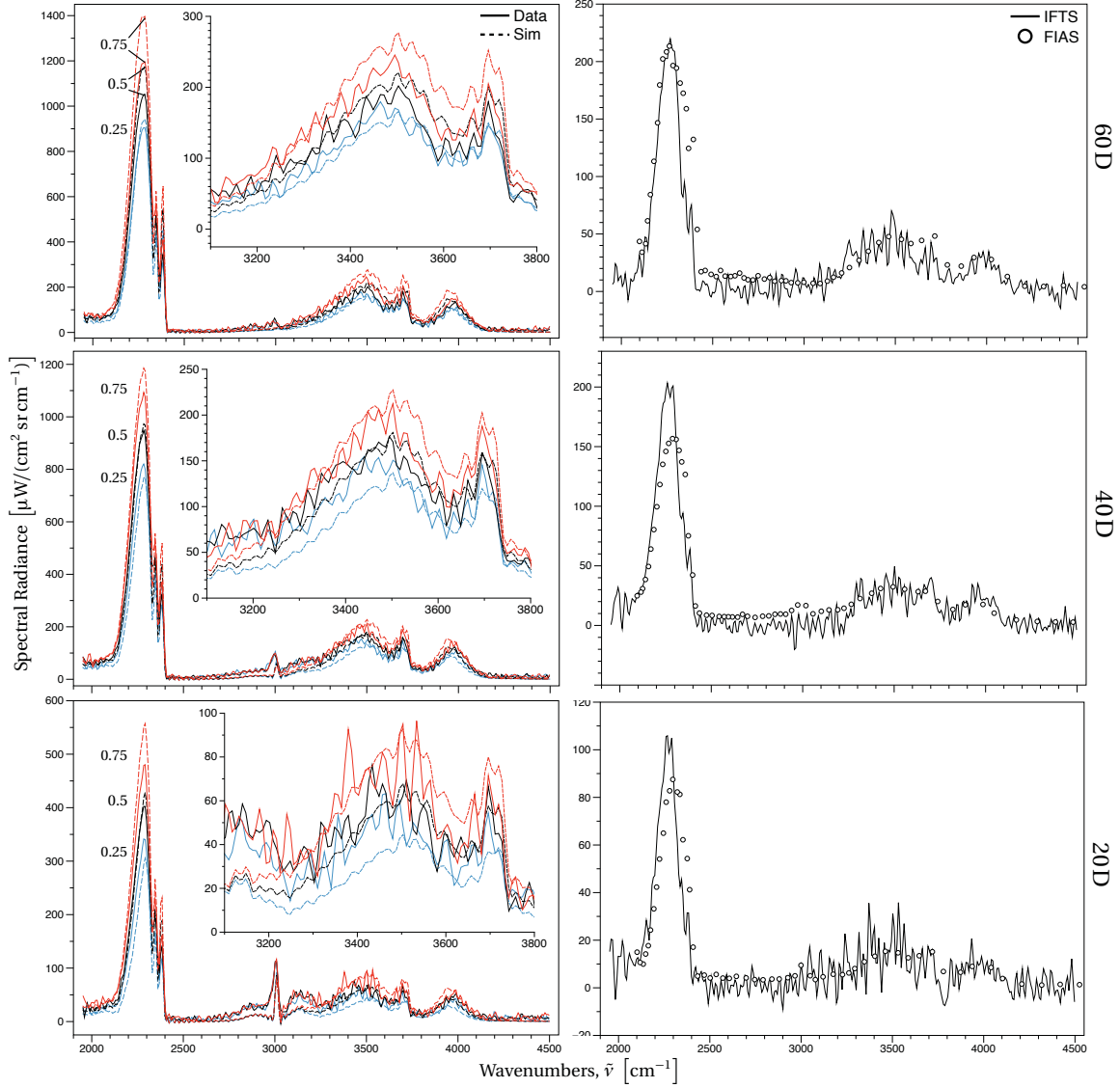
Figure 4.4: *Left*: Comparison of quartile measured (—) and simulated (- - -) $16\,\text{cm}^{-1}$ spectra selected after a sort by integrated (DC) intensity for the diametric path at 20 D, 40 D and 60 D. The water region about $3100\,\text{cm}^{-1}$ to $3800\,\text{cm}^{-1}$ is expanded at each height for better interpretation. *Right*: Comparison between IFTS and FIAS generated RMS spectra at 20 D, 40 D and 60 D, $r/x = 0$. IFTS RMS values were derived from the 0.75 and 0.25 quantile spectra while the FIAS RMS values were directly measured.

[81], but the quantile spectra are responsive to the nonlinearities driven by the turbulence, and the impact of l_r on RMS values would likely show up in the quantile sorts. In the H_2O region near $3500\,cm^{-1}$ (expanded inset plots) the comparison is not ideal at $20\,D$. However, at this convolved lower resolution the impact of the reduced number of CH_4 spectral lines will be more pronounced causing the model to underpredict intensity near $3300\,cm^{-1}$, a conclusion reinforced by the improved comparison in that region at $60\,D$ where the CH_4 footprint is greatly reduced. The comparison across the entire spectrum does indicate reasonable agreement between TASS and experimental spectra in all three quantiles at the three heights.

It is known the nonlinear relationship between temperature and radiance makes the spectra sensitive to TRI driven changes in the scalar field. The quantile-sorted spectra are thus assumed to be indicative of the TRI and the governing scalar statistics. Figure 4.4 (right) is a comparison between the FIAS acquired RMS spectra and IFTS RMS spectra derived from the quantile sorting approach. The 0.75 and 0.25 quantile difference is related to the standard deviation of the distribution simply by a scaling factor. Here, the upper and lower quantiles were converted at each spectral channel to produce an equivalent RMS spectrum. The results demonstrate a useful application of the quantile sorting method. It should be pointed out the FIAS measurements were taken with a well established prism spectrometer capable of sampling a given wavelength at up to $6250\,Hz$, but only at a single LOS. Comparable RMS spectra via quantile sorting of IFTS spectra produce those spectral statistics at every pixel and provide a map of the TRI in the flame.

The axial integrated intensity profiles in Figure 4.5 are presented to provide additional comparison between simulated and experimental spectra. Any disparities found within the spectral comparisons from Figure 4.4 are obvious here. The integrated results at $20\,D$ are, in fact, misleading as the reasonable agreement is mostly due to the offset CO_2 (overpredicted) and CH_4 (underpredicted) comparisons at that height. These results further reinforce the

74

utility of spectral information at each pixel to prevent any misinterpretation of a spectrally integrated signal.
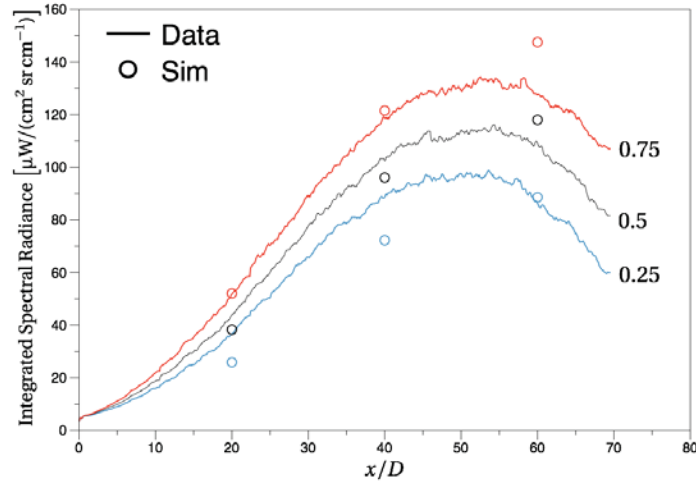

Figure 4.5: Comparison of experimental and TASS axial integrated intensity profiles at the three quartiles.

4.5 Conclusions

The present work further establishes IFTS as a viable passive combustion diagnostics tool. Comparisons have been made between IFTS measured flame properties and previously reported narrowband results. These measured flame properties indicate the utility of the high-speed broadband imaging capability of IFTS. The spectral comparisons between TASS modeled spectra and experimental data at $0.25\,\mathrm{cm^{-1}}$ resolution were not previously available, and the enhanced spectral fidelity allows a window into the performance of the TASS model as it pertains to each species across a broad spectrum. In addition, the higher spectral resolution provides insight into the performance of various spectroscopic databases at elevated temperatures. The lower resolution quantile

comparison reveals an opportunity to leverage the stochastic fluctuations in the I_{LPF}^{DC} component to describe the scalar statistics driven by TRI at every pixel.

Nonintrusive diagnostic methods are valuable and highly desirable techniques in the realm of turbulent combustion study. The combined capabilities of IFTS to capture both high-speed imagery based flame characteristics and high-resolution spectra at each pixel make it an extremely versatile option. The added possibility of quantile spectra describing scalar statistics greatly expand that versatility.

V.   Retrieval of scalar statistics from a multilayer turbulent flame via imaging Fourier-transform spectrometry

T‍‍HE results in this chapter are presented in a more traditional manner and not as a document prepared for journal submission. It is anticipated the results will warrant a submission to a reputable combustion journal in the future. As such, the analysis and results in this chapter are not preceded by the fundamental theory describing the quantile sorting method and the inversion algorithm. The applicable theory is presented in its entirety in Chapter 2. The focus is on presenting a successful inversion method for a stationary LOS, framing the complications brought about by integrated intensity sorting, and reporting retrieved scalar profiles and statistics from TASS simulated and IFTS experimental spectra. The work is significant for the following reasons:

- It demonstrates an onion-peeling inspired inversion method for IFTS which does not require an optically thin source or *a priori* knowledge of the source, and is suitable for both laminar and turbulent study.

- It firmly establishes the correlated link between LOS intensity sorting and temperature. The understanding of which is vital to the interpretation of scalars retrieved from quantile sorted spectra.

- Scalar profiles are retrieved and presented from a TASS simulated flame and quantile-based statistical temperature profiles are compared to published DLR Flame A data.

- Scalar profiles retrieved from first-ever IFTS measurements of Purdue Flame A are presented and discussed.

Building upon Chapters 3 and 4, this chapter fully validates the use of IFTS for combustion diagnostics. These results warrant the additional study of TNF type sources via IFTS.

5.1 Understanding the flame

Prior to examining any retrieval results, it is important to become oriented with the flame. Therefore, the DLR measured median radial profiles for temperature, CO_2 and CH_4 at 20 D, 40 D and 60 D are presented and discussed. The equivalent LOS spectra due to those stationary profiles are then presented at several locations with a discussion of the spectral behavior.

5.1.1 Median scalar distributions.

Figure 5.1 contains the medial radial DLR sample point profiles for temperature, CO_2 and CH_4 at 20 D, 40 D and 60 D. The temperature profile at 20 D suggests the chemical interactions are occurring near 1.5 cm, where the temperature peaks. This is to be expected at this height in a TNF where oxygen is just beginning to be entrained into the flame. The plots of CO_2 and CH_4 at this height are consistent with this view of the flame chemistry. As a product of the combustion, the profile for CO_2 is very similar to that of temperature. The CH_4 profile, as expected, has a strong presence near center at this height, where the oxygen has not yet been entrained to allow for combustion. At 40 D the turbulence has entrained much more oxygen and the profiles have changed. The peak temperature is still off axis, but is much closer to center temperature. The CO_2 profile shape is again similar to that of temperature, and the CO_2 concentration is clearly increasing. With the increase in CO_2, the CH_4 profile decreases in both peak and width. Finally, at 60 D there is complete mixing and the temperature and CO_2 profiles indicate peaks near center while the CH_4 is nearly depleted.

5.1.2 Stationary spectra.

The simulated LOS spectra for the stationary median scalar profiles are presented in Figure 5.2. The left column is the LOS through flame center, the middle column is an off axis LOS dominated by turbulence at $r/x = 0.0625$ ($r = 1$ cm, 2 cm and 3 cm for 20 D,
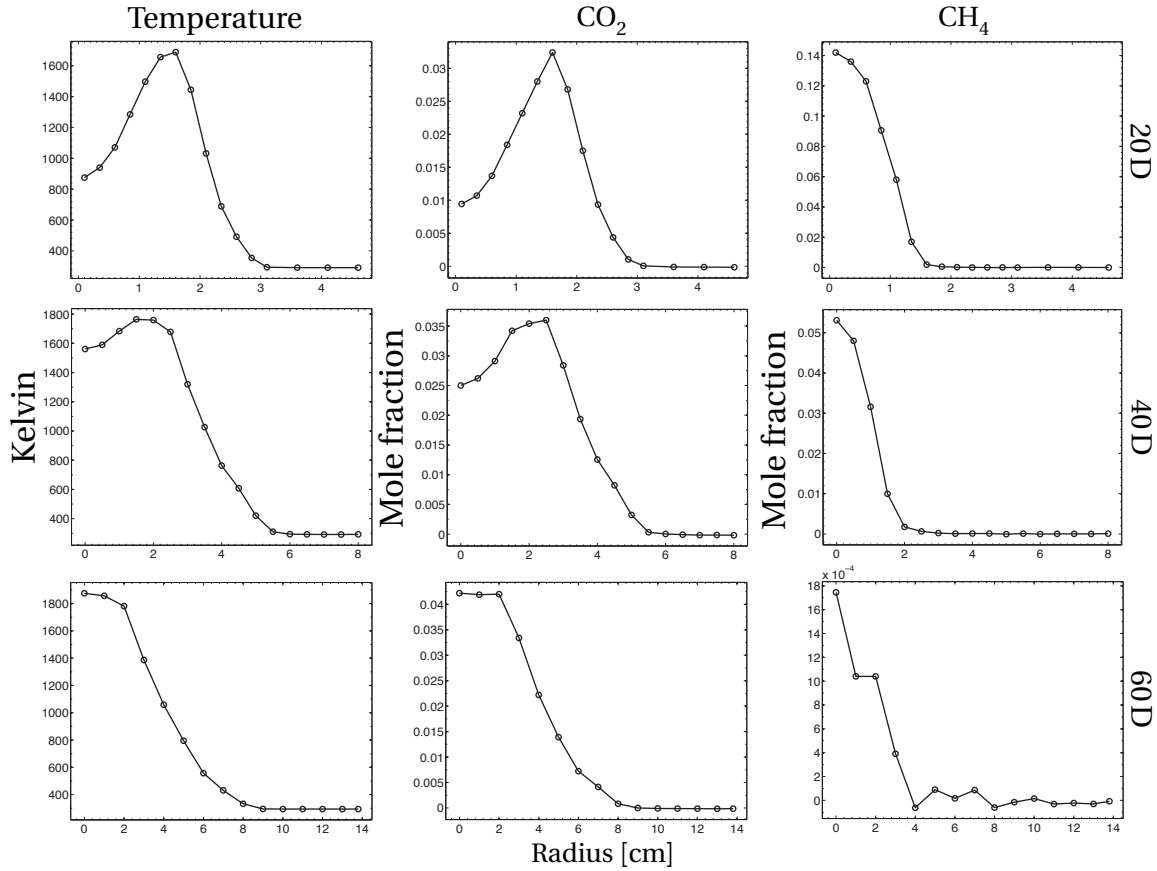
Figure 5.1: Median radial scalar profiles for temperature, CO_2, and CH_4 at 20 D, 40 D and 60 D as found in the DLR archive [75].

40 D and 60 D, respectively), and the right column is further off axis at $r/x = 0.125$ ($r = 2$ cm, 4 cm and 6 cm for 20 D, 40 D and 60 D, respectively).

The CH_4 spectral feature at 3000 cm^{-1} has been highlighted as a function of flame height at $r/x = 0$ and as a function of radius at 20 D. Both radially and axially the CH_4 spectrum is representative of the CH_4 concentration profiles seen in Figure 5.1. Radially, at 20 D, the CH_4 spectral feature is strongest at $r/x = 0$, still evident off axis at $r/x = 0.0625$ ($r = 1$ cm), and not present at $r/x = 0.0125$ ($r = 2$ cm). Axially, at $r/x = 0$, the spectral feature falls off with height and is not evident at 60 D, where species concentrations are on the order of 10^{-4}.
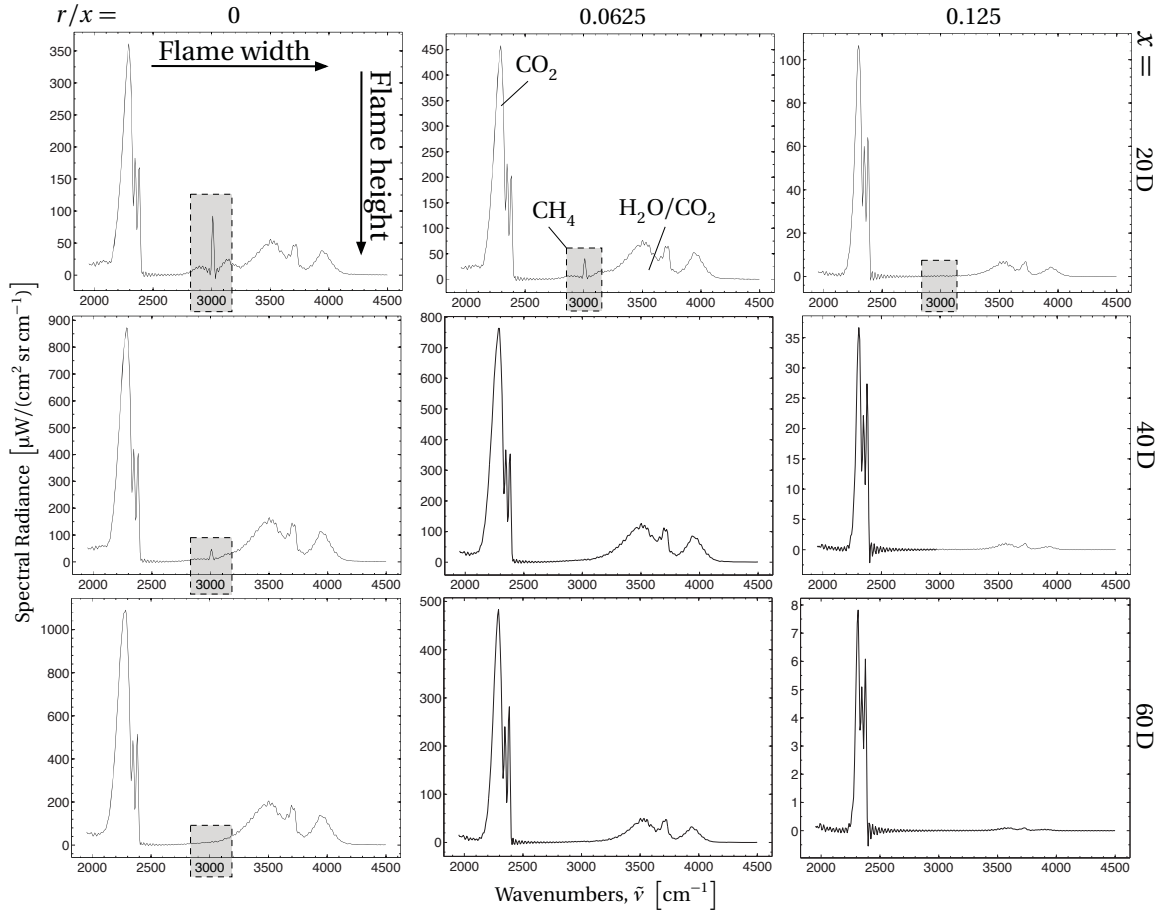
Figure 5.2: Simulated stationary LOS spectra (from median scalar profiles) at $20\,D$, $40\,D$ and $60\,D$, $r/x = 0$, 0.0625, 0.125

The CO_2 spectral feature centered near $2300\,cm^{-1}$, evident in all panels, is not as obviously representative of the CO_2 concentration profiles. The LOS spectra are path integrated, and as such are impacted not only by the off axis peak behavior of the CO_2 (and temperature) profiles but also the total path through the flame. This is most evident at $40\,D$ where the peak CO_2 intensity falls off radially. The off axis $r/x = 0.0625$ spectrum has passed through the peak of both the CO_2 and temperature profiles at $r = 2\,cm$, but the CO_2 spectral feature is approximately $100\,\mu W/(cm^2\,sr\,cm^{-1})$ less than that of the CO_2 feature at $r/x = 0$. The center LOS passes through the entire diameter of the flame and

includes radiance not just from the $r = 0$ configuration but from the entire scalar profile, to include the off axis peak temperature and CO_2 concentrations. This results in a center LOS CO_2 radiance larger than any of those off axis. Effects of the path integration are also seen at 20 D, $r/x = 0$ and 0.0625, where now the off axis LOS is passing predominantly through the temperature and CO_2 peaks near $r = 1.5$ cm and the resultant CO_2 spectral feature is more intense than that of the diametric path.

5.2 Inversion of non-turbulent multilayer profiles

The intensity sorting and selection of quantile spectra introduce several unique complications and unknowns of their own. Therefore, prior to the retrieval of scalars from quantile spectra associated with a turbulent flame, the inversion method is validated against less complicated stationary LOS spectra. Good comparison between retrieved scalars and the known input scalar profiles from several stationary flame configurations will alleviate any concerns with regard to the performance of the algorithm when retrieving from the more complicated quantile spectra.

Here, scalars from 6000 radial flame configurations generated via TASS analysis at 40 D were sorted individually at each radial location (every 0.5 cm to coincide with the DLR sample locations at that height). The three quantile scalar profiles were used to generate three quantile flame profiles along each LOS. These flame conditions would only occur if every scalar in the flame were to be at the same particular quantile at a given instant. The unlikelihood of this scenario is irrelevant as this was merely a check of the inversion algorithm in the absence of turbulence, therefore any instantaneous flame profile would suffice. These three were chosen due to their relevance in the present work.

The quantile flame profiles were combined with the multilayer radiative transfer model to generate three spectra at each LOS. These spectra were then fit in accordance with the inversion method described in Chapter 2. Comparisons between retrieved temperature and CO_2 profiles are presented in Figure 5.3. Radial plot points are bounded by temperature
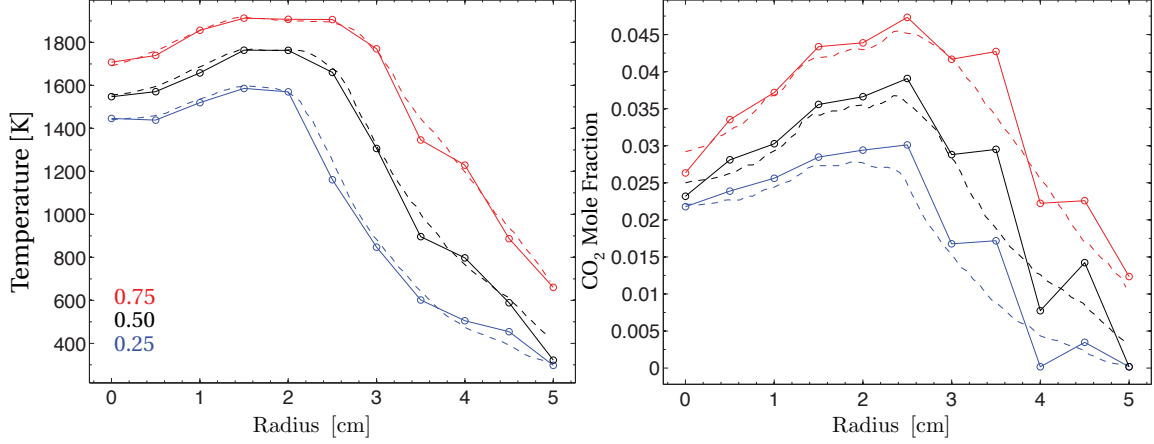
81

Figure 5.3: Scalar sorted temperature (left) and CO_2 (right) retrieval results at 40 D for 0.25 (blue), 0.50 (black), and 0.75 (red) stationary profiles. Dashed lines are the profiles resulting from a sort of the TASS generated scalars at each radial sample location. Retrieved profiles from the stationary LOS spectra are marked with the points and solid lines.

and intensity constraints described in more detail in the turbulent retrievals discussion immediately to follow. The remaining concentration profiles are found in Appendix C. Retrieved temperatures are in excellent agreement with the input profiles at all three quantiles. The RMS of the residuals between retrieved and measured in the 0 cm to 5 cm range are 40.2 K, 45.7 K and 37.2 K for the 0.25, 0.50, and 0.75 profiles, respectively. In relation to profile peak temperatures, this is an average error (T_{RMS}/T_{peak}) of 2.4 % between the three profiles. The retrieved CO_2 profiles are not as ideal as the temperature, but the input profiles are nevertheless well represented in the results. The RMS of the residuals for these profiles are 0.0033, 0.0042, and 0.0036 for the 0.25, 0.50, and 0.75 profiles, respectively. These values give an average error (χ_{RMS}/χ_{peak}) of 10.4 % between profiles.

It bears mentioning this inversion algorithm was developed as a simple, straightforward method to retrieve scalar profiles for the present work (the intended focus of the effort

being on the intensity sorting and management of turbulent effects). Therefore, these results are indicative of a suitable inversion method. With such excellent agreement between input and retrieved temperature profiles this method may be applicable in other IFTS analysis where inversion of the source is required. Future development with properly chosen optimization techniques can improve the algorithm, but this stationary LOS study demonstrates it is suitable for the inversion of the quantile spectra.

5.3 Retrievals from a simulated turbulent flame

5.3.1 Intensity sorted scalar profiles.

Prior to examining results of the quantile spectra fits, the intensity sorting method is revisited. As described in Chapter 2, quantile spectra are averages over a small (relative to the total) subset centered about a particular quantile. This idea is presented again in the upper half of Figure 5.4. The lower half of the figure extends the sorting to the corresponding temperatures from the TASS generated instantaneous profiles used in modeling the integrated spectra. The gray points are the unsorted temperature samples, the red line is the result of sorting those points directly, and the black line is the result of applying the sort index from the corresponding LOS intensity sort. The black line has been smoothed via moving average with a width equivalent to the quantile bins (4 % of the total sample number). If intensity and temperature were perfectly correlated, the black and red lines would match. The left plot contains the TASS generated temperature points from flame center, $r/x = 0$. Sorting these values by the intensity index from the LOS spectra for the diametric path does not produce an ideal match. Further off axis, at $r/x = 0.11$, the plot on the right produces a much closer match between the two sorted plots. This would indicate LOS intensity and temperature are more correlated off axis, a concept explored further in Figure 5.5.

The left side of Figure 5.5 depicts the plume geometry and relationship between radial location and LOS. The colored rays representing the various LOS coincide with the plot on
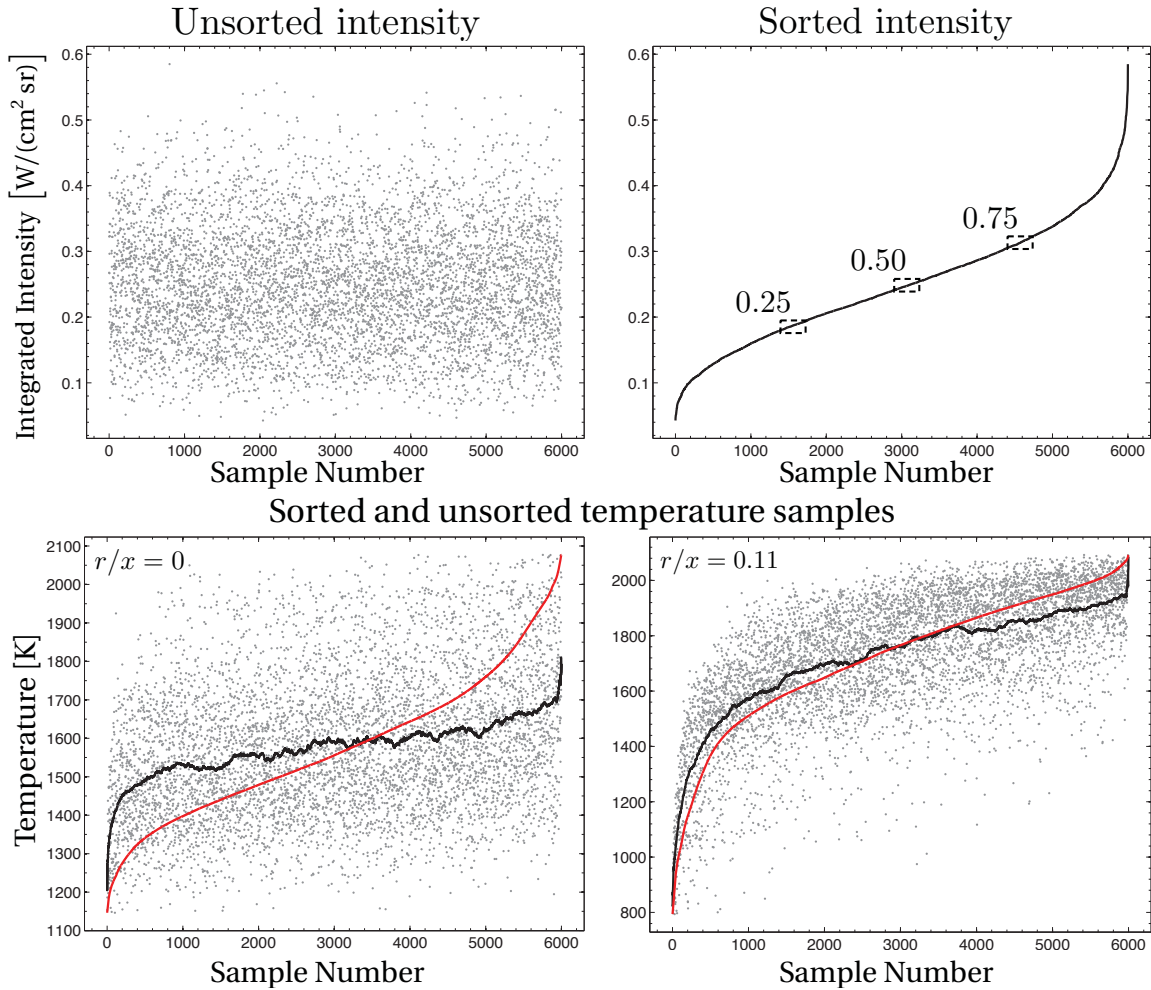
Figure 5.4: *Upper*: Unsorted (left) and sorted (right) intensity values at the $r/x = 0$ LOS. Quantile locations are annotated with 4 % bin width. *Lower*: Unsorted (gray), intensity sorted (black), and temperature sorted (red) plots of temperature samples at $r/x = 0$ (left) and $r/x = 0.11$ (right). Intensity sorted lines were smoothed within a 4 % width consistent with the quantile bins.

the right side of the same figure, where the degree of correlation between temperature and intensity at multiple locations is presented. The points on the plot designate the correlation between the intensity at that LOS and the temperature at that radial location in the flame (i.e. the red dot at $r = 0$ is the temperatures from center flame correlated with the intensity
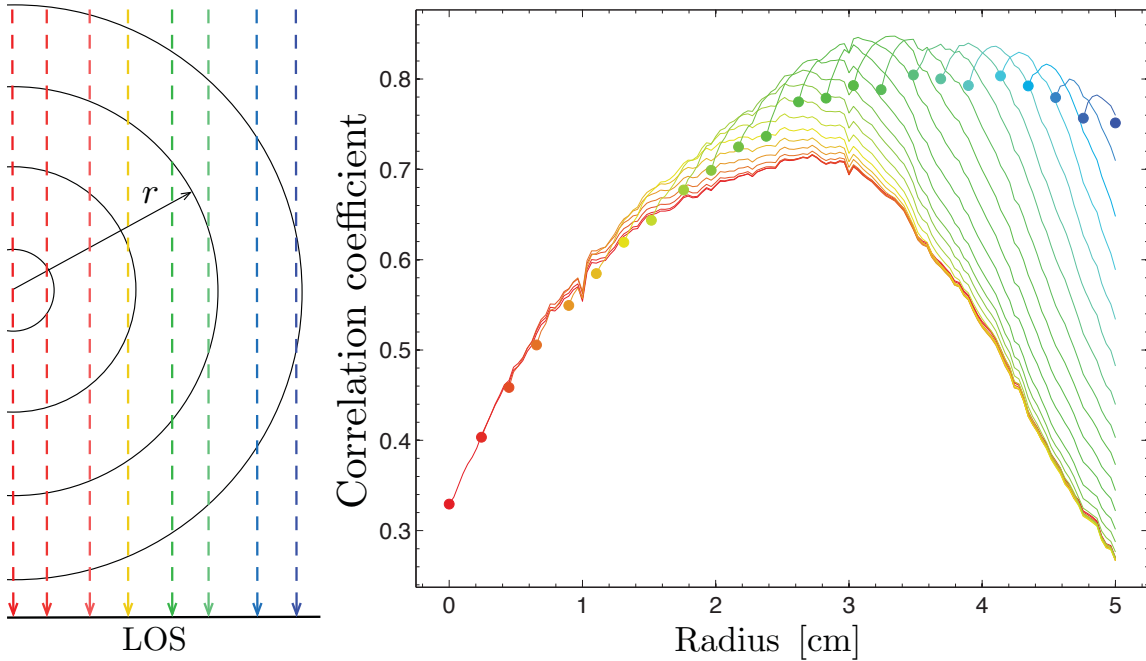
Figure 5.5: *Left*: Flame geometry. *Right*: Radial temperature versus LOS intensity correlation plot at 40 D.

from the diametric LOS). The lines of equivalent color drawn to the right of the points are the correlation of the intensities from the initial LOS with the temperatures at the radial location where the line is drawn. The results indicate the LOS intensities near the diametric path are far more correlated with those at approximately 2.5 cm ($r/x = 0.08$). This explains the disagreement between the red and black sorted plots in the lower half of Figure 5.4. The temperature and intensity have a correlation coefficient of approximately 0.33 at $r/x = 0$, and this limited correlation is shown when temperature is sorted with the LOS intensity index. Whereas, intensity and temperature have a correlation coefficient of nearly 0.8 at $r/x = 0.11$ (3.5 cm), and the sorted plots at that location are in much better agreement.

Considering the nature of the TNF, these results are not surprising. The greatest temperature fluctuations are going to occur in the more turbulent off axis regions, and the intensities from the LOS that look primarily through these regions will thus be well

correlated with the temperature. The diametric path, however, looks through all layers of the flame. The smaller fluctuations at flame center are thus dominated by the fluctuations in the turbulence still being probed along that LOS. This will have an impact on the retrieved scalars and the inversion process near flame center.

5.3.2   *Spectral fits.*

The 6000 instantaneous spectra were modeled and sorted in the manner described in Chapters 2 and 4, combining the TASS generated profiles, the multilayer radiative transfer model, and the quantile analysis method. The onion-peeling inspired inversion method described in Chapter 2 was then used to fit the appropriate LOS spectra and return the estimated scalar profiles. Prior to fitting, artificial noise was added to the spectra to test the robustness of the method. A noise parameter was generated by dividing the RMS of the simulated spectrum by 250. The noise parameter was then multiplied by a vector of psuedorandom numbers drawn from a standard normal distribution and added to the radiance. A more complete parametric study of noise effects on the inversion method is presented in Appendix C for reference. As an example of the magnitude of the noise in this instance, the RMS of the artificial noise at 40 D, $r/x = 0$, was 0.432 for the 0.50 quantile, or 0.5 % of the mean spectrum. It should be pointed out the simulated spectra were initially generated at width equivalent to that of the data, but early model results indicated the width needed to be extended. The fit was sensitive to starting well out in the noise where the initial atmospheric input was accurate. This point becomes relevant in the retrieval of scalars from the data presented in the next section.

Results of the spectral fits from the inversion are reported at 20 D, 40 D and 60 D for three LOS in Figure 5.6. Only the input and modeled spectra for the 0.50 quantile are shown, but residuals (the difference between input and modeled spectra) are shown for the 0.25, 0.50, and 0.75. RMS values were computed for the residuals and are presented in corresponding color. Agreement is, in general, excellent. The RMS of the residuals for the
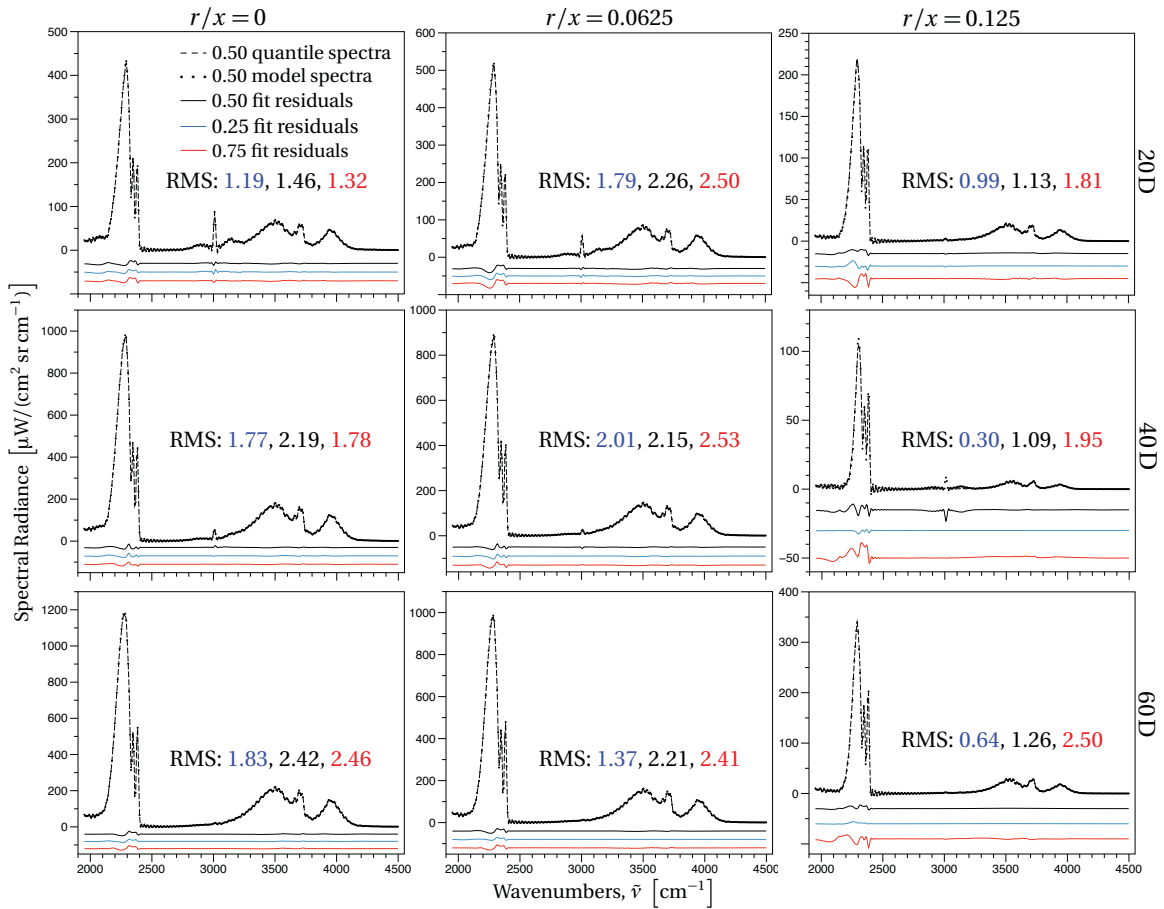
Figure 5.6: Spectral fit results at 20 D, 40 D and 60 D for $r/x = 0$, $r/x = 0.0625$, and $r/x = 0.125$. Data and model comparisons are only for the 0.50 quantile with residuals for all fits presented and colored accordingly. Residuals are offset for comparison and on the same scale as the spectra. The RMS of the residuals (in y axis units) are reported and colored to match the appropriate quantile.

0.50 quantile at 40 D, $r/x = 0$, is approximately 5 times that of the simulated instrument noise detailed above. Comparison locations were selected using the integrated intensity profile. The $r/x = 0.125$ LOS was chosen to examine the performance of the fit off axis where little spectral signal is available. Integrated intensity profiles as a function of r/x for the three heights and the three quantiles are provided in Figure 5.7.
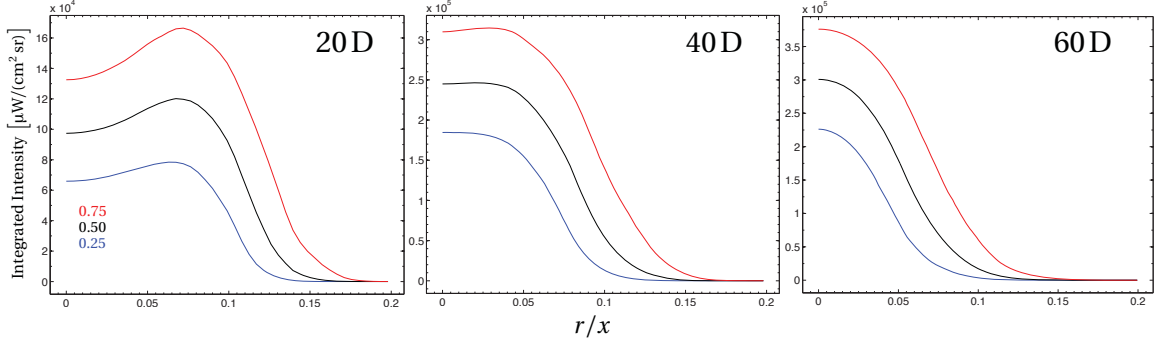
Figure 5.7: Integrated intensity as a function of r/x at 20 D, 40 D and 60 D for the 0.25 (blue), 0.50 (black), and 0.75 (red) quantiles.

The relative error (RMS/mean) at 40 D is presented in Table 5.1 and is indicative of the performance of the model at other heights and LOS. The extremely high error for the $r/x = 0.125$ fit is the result of very little spectral signal at this location (4 cm off axis). This is verified in Figure 5.7, where it can be seen the integrated intensity is almost zero for the 0.25 quantile at 40 D. As the intensity increases with the 0.50 and 0.75 quantiles at that same location, the error is reduced significantly. It is also worth noting the residuals contain the most structure in the $2150 \, \text{cm}^{-1}$ to $2400 \, \text{cm}^{-1}$ range, and in that same spectral range at $r/x = 0.125$ the relative error is only 6 %, 1 % and 0.3 % for the 0.25, 0.50, and

Table 5.1: Relative error (RMS/mean) from spectral fits at 40 D, $r/x = 0$, $r/x = 0.0625$, and $r/x = 0.125$ for the three quantiles.

	$r/x = 0$	$r/x = 0.0625$	$r/x = 0.125$
0.25	2.5 %	4.0 %	56 %
0.50	2.3 %	2.7 %	23 %
0.75	1.5 %	2.3 %	9.1 %

0.75 quantiles, respectively. This indicates the fits are reasonable (as the spectral plots indicate), and the majority of the RMS error is in regions where there is little to no actual spectral activity.

5.3.3 *Retrieval of scalar profile statistics.*

Retrieved temperature profiles and their associated RMS values are reported in Figure 5.8. Plots are presented from $r = 0$ to a temperature and intensity driven cutoff unique to each height and quantile. The entire $2\,\mu$m to $5\,\mu$m band was fit during inversion, and considering the impact to spectral fit results in regions of low intensity, points below $500\,$K and $1000\,\mu$W/(cm^{2}sr) were considered unreliable and omitted from the plots. Fit point spacing was in general consistent with the same sampling accomplished in the DLR Flame A diagnostics (0.25 cm at 20 D, 0.50 cm at 40 D, and 1.0 cm at 60 D) with the exception of 60 D, where the sampling was increased for ease comparison with the upsampled TASS plots. The dashed comparison profiles are the individually sorted TASS scalar profiles used in the stationary LOS study above.

The temperature profile comparisons in Figure 5.8 demonstrate the inversion method has captured the functional behavior of temperature in all cases. As expected, the diametric LOS is problematic at 40, and—to a much greater extent—20 D. This is consistent with the intensity and temperature correlation study above. For the diametric path, the model is attempting to estimate temperatures at flame center which are dominated by temperatures in the turbulent layers along the LOS. At 20 D this is extremely evident due to the large difference between center and off axis flame temperatures. The effect is less evident at 40 D, where off axis temperatures are not as dominant, and at 60 D there is good agreement at center as temperature mostly drops with radius at that height. For nearly all points the retrieved temperature slightly overpredicts that of the sorted scalars. This is likely due to the combination of the averaging over the subset of spectra to determine $L_q(\tilde{v})$ and the LOS profile effects already described. As pointed out in Chapter 2, the nonlinear relationship
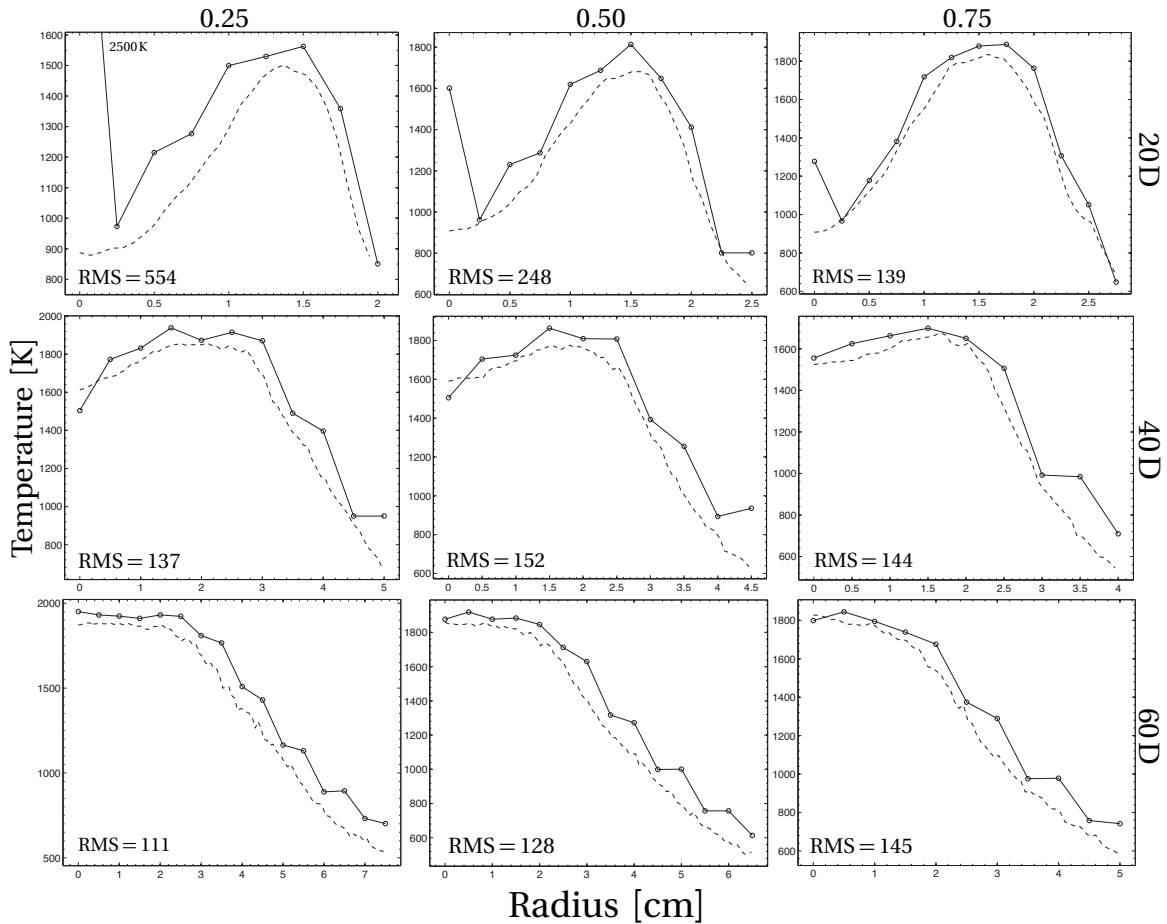
89

Figure 5.8: Comparison of radial quantile temperature profiles at 20 D, 40 D and 60 D. Dashed lines are the profiles resulting from a sort of the TASS generated scalars at each radial sample location. Points with solid lines are inversion retrieved profiles from the intensity sorted quantile spectra. (RMS values in y axis units)

between $L(\tilde{\nu})$ and scalars (particularly temperature) does not allow for an averaged $L(\tilde{\nu})$ to represent the the averaged scalars. This relationship could be driving temperature estimates up, despite the smaller bin width used in the selection of the quantile scalars. The LOS profile effects impact what is being interpreted as "truth" in these comparisons. The dashed lines representing the sorted temperatures are the results desired from this study, but do not represent the actual profiles seen along the various LOS after intensity sorting
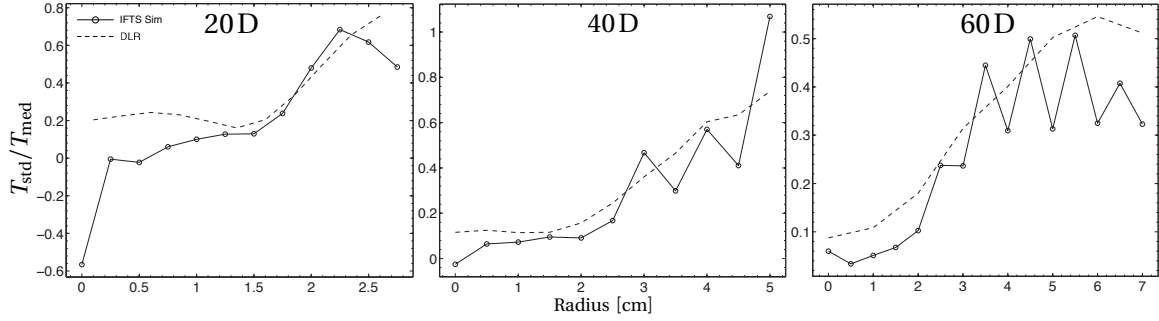
Figure 5.9: Radial profiles of DLR and IFTS measured T_{std}/T_{med} at 20 D, 40 D and 60 D. The IFTS standard deviation was converted from the retrieved 0.25 and 0.75 temperatures.

and selection of quantile spectra. Certainly the retrieved profiles appear indicative of the statistics describing the scalars, but the exact relationship between the retrieved quantiles and pure sorted quantiles is not known. Despite these complexities, the RMS values are mostly excellent. The largest disparities are found in the 0.25 and 0.50 quantiles at 20 D, but these are driven by the highly over estimated temperatures at center. The RMS of the residuals at 0.25 from 0.25 cm to 2 cm, for instance, is 122 K. Average peak relative error (T_{RMS}/T_{peak}) for the three heights is 20 %, 8 % and 7 % for 20 D, 40 D and 60 D, respectively. The 20 D calculation includes the entire plotted range.

The utility of having statistically based quantile estimates of scalars is demonstrated in Figure 5.9. Here, the upper and lower temperature quantiles have been converted to a standard deviation as in the manner used to generate the RMS spectra in Chapter 4, and the ratio of the standard deviation to the median is plotted for all three heights. The dashed lines are the statistics from the experimentally gathered DLR points and compare very well to the statistics retrieved from the simulated data. The disagreement near center at 20 D is, again, driven by the elevated estimates in that region. Qualitatively, these plots indicate IFTS retrieved scalars and scalar statistics may provide results comparable to more well established and verified methods.
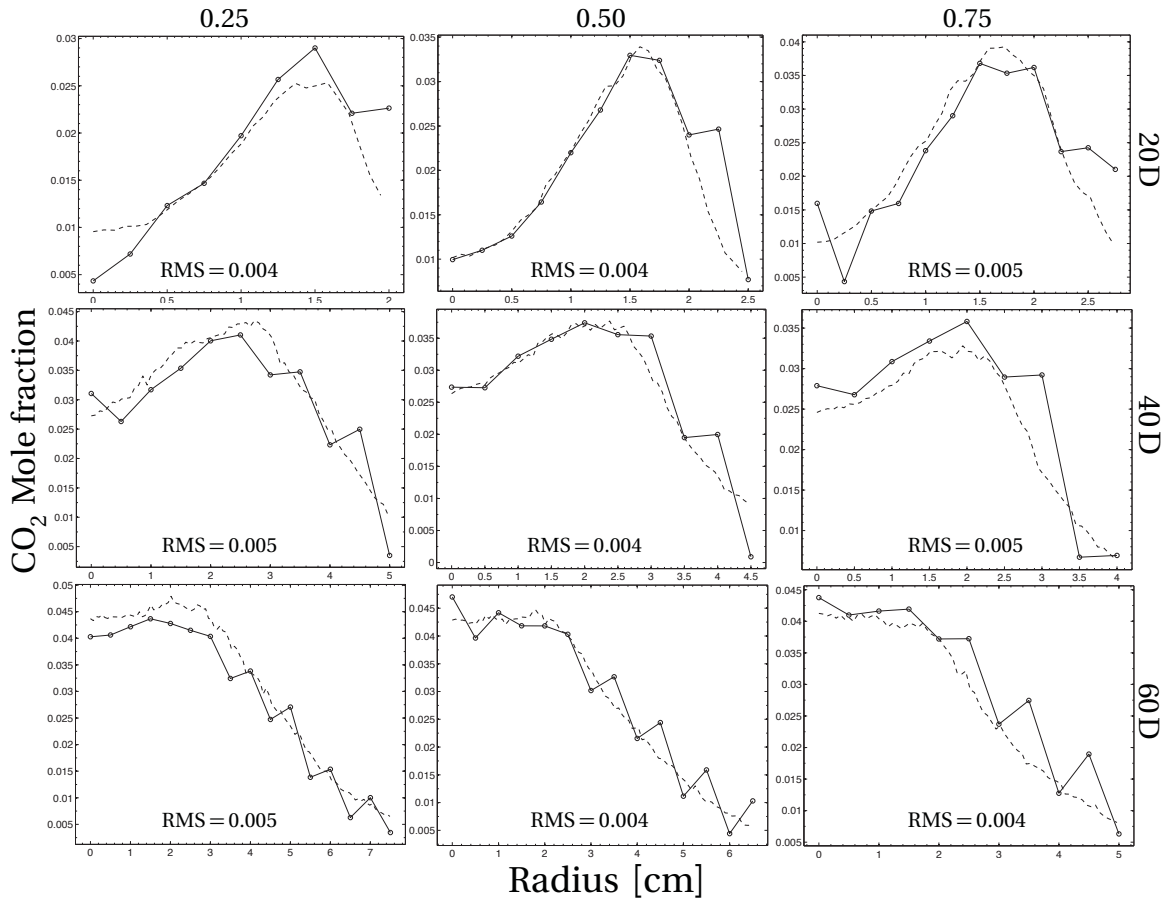
Figure 5.10: Comparison of radial quantile CO_2 concentration profiles at $20\,D$, $40\,D$ and $60\,D$. Dashed lines are the profiles resulting from a sort of the TASS generated scalars at each radial sample location. Points with solid lines are inversion retrieved profiles from the intensity sorted quantile spectra. (RMS values in y axis units)

Species concentration profile comparisons for CO_2 are presented with their RMS values in Figure 5.10. The remaining concentration profiles can be found in Appendix C, but considering the large footprint in the spectral band, it is reasonable to assume CO_2 will have the greatest correlation with integrated intensity. The radial plot constraints from the temperature profiles have been applied, and—as with the temperatures—comparisons are against the radially sorted scalar values from the TASS generated set. The inversion

once again captures the behavior of the scalar as a function of radius. The median quantiles compare particularly well at all three heights. Average peak relative errors (χ_{RMS}/χ_{peak}) of 14 %, 12 % and 10 % from 20 D to 60 D are not ideal, but are not unreasonable for an initial application of both the unique inversion method and quantile analysis approach. It can be expected advancements in both techniques will improve on this error.

5.4   IFTS measurements

5.4.1   *Examination of the data.*

Prior to reporting retrieved scalars from the IFTS measured spectra, the data is first examined and described. The spectra presented in Figure 5.11 are from the 0.50 quantile at 40 D, and are indicative of the behavior at all three heights and quantiles. To depict the spectral behavior moving radially away from flame center (top to bottom in the figure), the red lines indicate the spectra from the LOS at the current r location, while the gray are the previous spectra from $r = 0$ to the current location. The left plots are the spectra isolated at specific radial locations. The right plots are the equivalent spectra peak normalized by the CO_2 feature near $2300\,cm^{-1}$. The behavior of the CO_2 feature in both indicate optical trapping between $r = 0\,cm$ and $2.0\,cm$. At these inner LOS there is more pathlength through the flame which should coincide with more integrated signal. However, in the median spectra on the left there is very little change to the peak intensity, which should be dropping with the reduced pathlength through the flame off center axis. Concurrently, the peak normalized spectra show no change in the spectral shape of the CO_2 feature through that same region, where changes in temperature along the LOS should be impacting the width of the feature. This indicates their are photons at these wavelengths being trapped near flame center and not reaching the detector. Additionally, the H_2O feature near $3500\,cm^{-1}$ shows little change in shape from $r = 0\,cm$ and $2.0\,cm$. At $r = 3.6\,cm$ the median spectrum has dropped significantly in intensity, but the normalized relative spectral shape is only starting to change. Only at $r = 5.0\,cm$ is there observable change in the width of the normalized

CO_2 peak. The final plots at $r = 6.5$ cm indicate little to no spectral features remain, but the equivalent normalized spectrum shows significant systematic error. There is a strange non-zero mean noise pattern about the baseline which appears to vary with wavelength. This is perhaps not unexpected at lower wavenumber, but not at higher wavenumber since this is at flame edge and the spectrum is due mostly to atmospheric background. In addition, there is an unexplained baseline increase at both ends of the spectrum, and the width of the CO_2 feature is at or beyond the width found at $r = 0$ cm. The effects are explored further in Figure 5.12.

The mean radiance plots in Figure 5.12 capture the integrated behavior of the CO_2 feature across all LOS, from center pixel to edge. The left plot of the mean radiance in the CO_2 band (1950 cm^{-1} to 2450 cm^{-1}) roll off to nearly zero at the wing. In contrast, the right plot of the peak normalized mean spectra reveals the otherwise unnoticed systematic error seen in the $r = 6.5$ cm plot in Figure 5.11. Some systematic error and measurement noise is to be expected, and the model and inversion method must be robust enough to overcome them, but the behavior beyond $r = 5$ cm is excessive. The model and algorithm were proven capable of overcoming some artificial noise against simulated spectra in the previous section, but the levels of systematic error seen here affected the implementation of the scalar retrieval method for the IFTS measured data, and the simulated data did not test for such conditions. The effects seen beyond $r = 5$ cm in Figure 5.12 are likely due to a combination of low signal-to-noise ratio (SNR) and systematic errors in that region. Certainly there was a substantial statistical under-sampling which impacted the SNR across all LOS. After sorting the 256 interferograms, a quantile bin width (sample size) of 4% was used. This resulted in approximately 10 samples at each quantile, which is going to have a negative effect on the SNR. In addition, the impact of non-Gaussian noise sources on quantile sorting have not been explored. This, too, could impact the spectra and is expected to be improved if the SNR is much higher than both the measured and systematic noise.
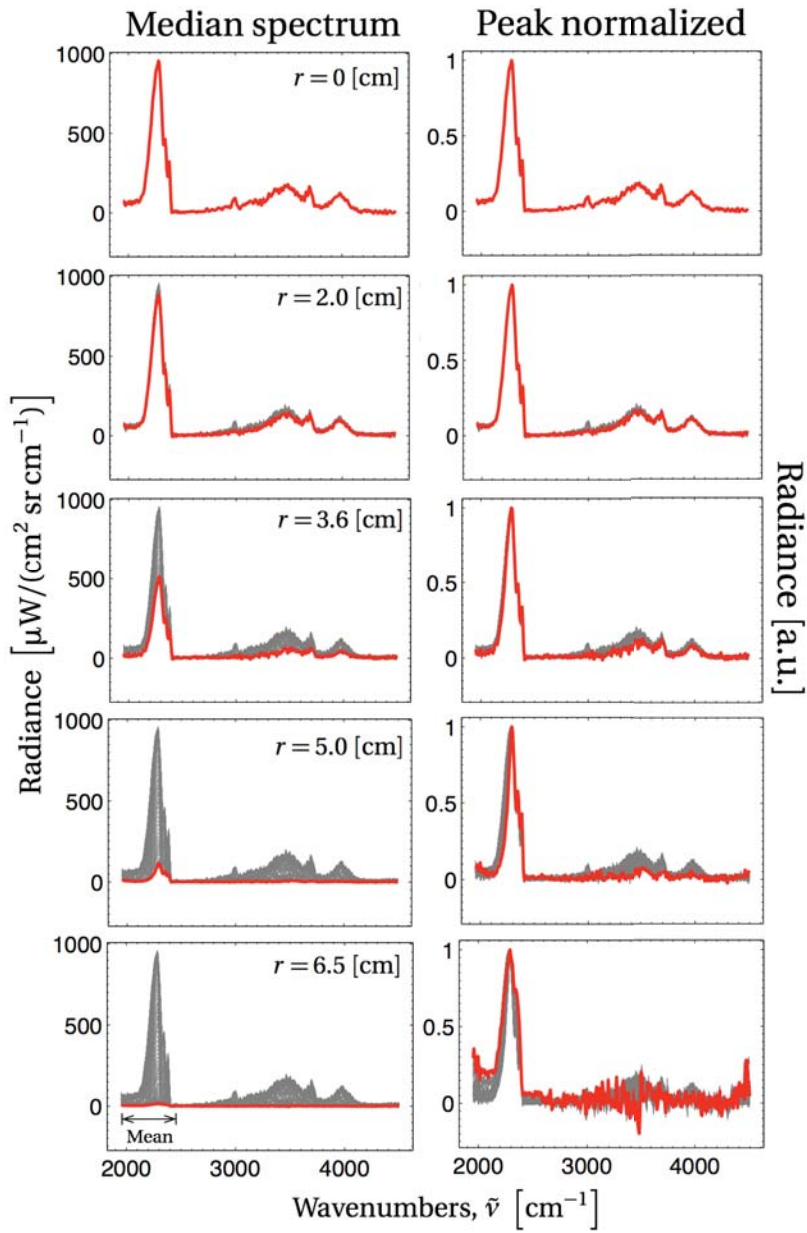
Figure 5.11: *Left*: Median (0.50) spectra at 40 D for various radial locations (red) and spectra from zero to current location (gray). *Right*: Median (0.50) CO_2 peak normalized spectra at 40 D for various radial locations (red) and spectra from zero to current location (gray).
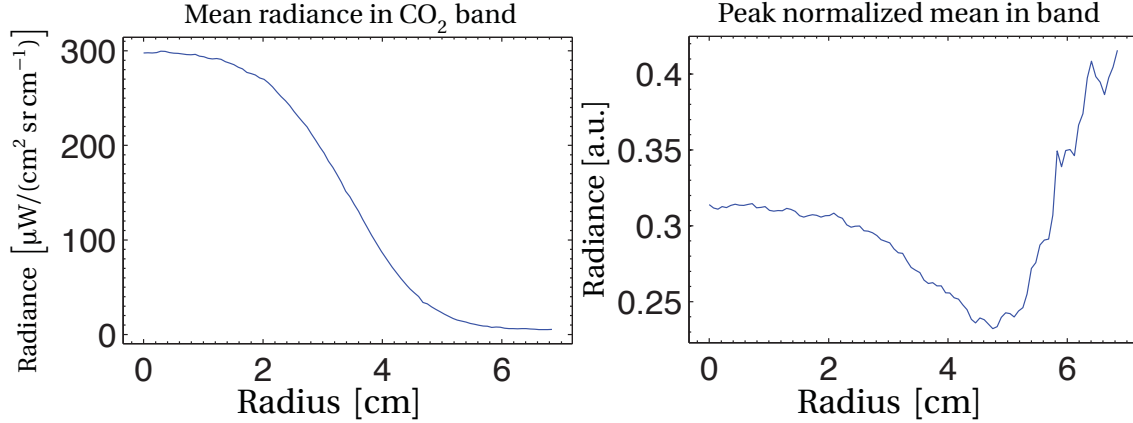
Figure 5.12: *Left*: Mean radiance of the median (0.50) quantile (40 D) in the CO_2 band
$(1950\,\text{cm}^{-1}$ to $2450\,\text{cm}^{-1})$ as a function of radius. *Right*: Mean radiance of the median
(0.50) CO_2 peak normalized quantile (40 D) in the same band. The peak normalized plot
indicates strong systematic error beyond $r = 5$ cm.

5.4.2 *Retrievals from IFTS data.*

The results of the spectral fits from the inversion at 40 D, $q = 0.5$, are presented in
Figure 5.13, with the residuals between data and model shown offset but on the same scale.
As has been discussed in the previous figures, random and systematic errors were much
larger, and the resultant RMS fit errors seen here are an order of magnitude greater than
those seen in the simulated spectral fits. The relative error (RMS/mean) is 20 %, 23 % and
64 % for $r/x = 0$, 0.0625, and 0.156, respectively. The absorption region of CO_2 around
$2350\,\text{cm}^{-1}$ shows much structure in the residuals, but the emission region below $2350\,\text{cm}^{-1}$
does not.

The inversion algorithm's sensitivity to radial starting position was known from the
analysis of the simulated spectra. Initial fits of the IFTS data were performed using the
halfwidth of the centered data window (97 pixels, 7 cm). Considering the additional width
needed for the simulations, this was already less than ideal. The early retrieval results were
poor. They indicated little separation of quantiles and were erratic throughout. However,
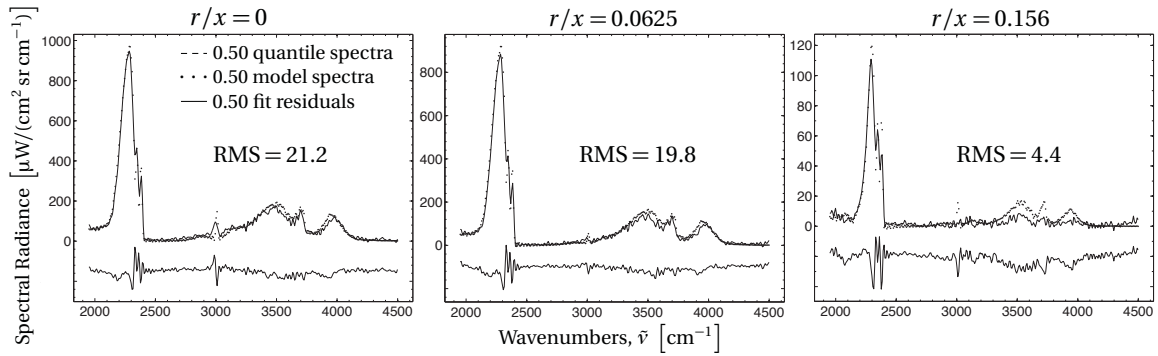
Figure 5.13: Spectral fit results for IFTS data at 40 D, $q = 0.50$. (RMS values in y axis units)

analysis of simulations indicated error at low signal could cause significant problems as well. The spectral behavior at the edges of the flame (beyond $r = 5$ cm) seen in Figure 5.12 indicated the algorithm may be more adversely affected by the systematic error than the ideal starting location. Thus, the retrieved profiles reported here are the results of fits which began well inside the available radial range at $r = 5$ cm, where the normalized plot indicates the systematic error has not yet begun to creep into the spectrum.

Retrieval results for temperature and CO_2 at 40 D are presented in Figure 5.14. As expected from the observations of the experimental data, temperature results are impacted at flame center and flame edge. The temperature results from 0–2 cm show no noticeable separation between quantiles. This is consistent with the unchanging spectral shape of the normalized CO_2 feature seen in Figure 5.12. That width is driven by the rotational population and as the dominant spectral feature should be indicative of flame temperature. Notice beyond $r = 3.6$ cm—where the CO_2 feature begins to contract—the temperature profiles display the separation expected between quantiles. The dashed line indicates the 0.5 quantile from the individually sorted TASS data. Ideally, this line would coincide with the black 0.50 retrieved scalars, but the gross overprediction seen here is likely driven by
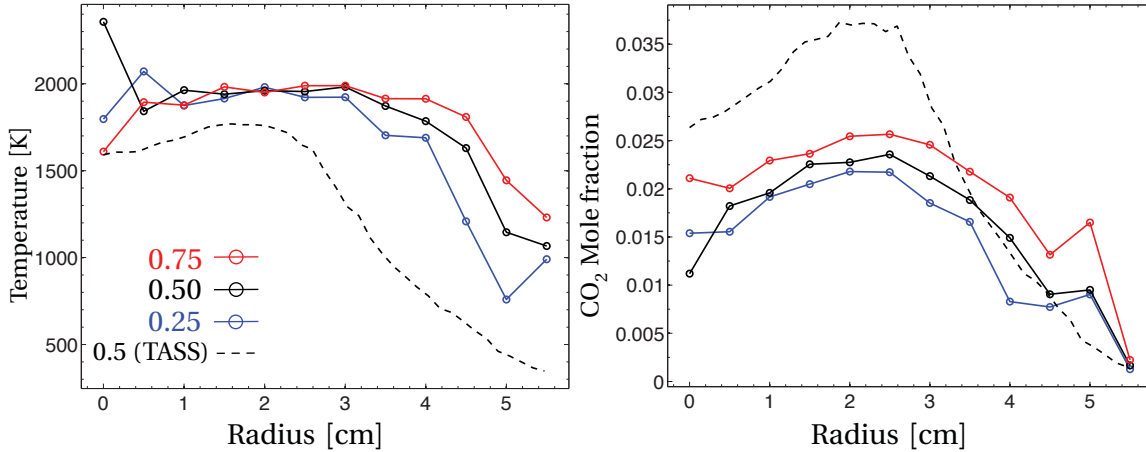
Figure 5.14: Retrieved temperature (left) and CO_2 quantiles at 40 D. The 0.50 TASS (- - -) profile is provided for reference.

the starting location of the fit. Early modeling efforts of the simulated data indicated similar behavior when the fit was not started at a radial location just beyond the flame edge.

The CO_2 profiles seen in Figure 5.14 (right) are an improvement over the temperature results. There is a general separation between quantiles across the profile, indicating the intensity sorting methodology holds for measured data. In the problematic region from center to $r = 3.6$ cm the retrieved CO_2 values drift well below the sorted TASS profile. This is perhaps to be expected considering the behavior of temperature in this same region and the correlation between the two scalars. In the remaining region from $r = 3.6$–5.5 cm the small sample of CO_2 retrieval points do indicate some promise. Initial estimates are high, again likely due to the nonoptimal starting location of the fit. Additional scalars and heights are not presented as they all suffer from the same systematic error and therefore retrieve similar profiles.

The impact of systematic error on these results has been emphasized, and it is likely an important factor in the poor performance of the model. In addition, the data sample size was more than 20 times below that of the simulated set. It is believed a larger dataset would

simultaneously increase the SNR across the spectrum and have the greatest mitigating effect toward the impact of the systematic error, and limit the inaccuracies due to finite sampling of quantiles. An improved SNR could improve retrievals near flame center by increasing the sensitivity of the model to changes in the H_2O spectrum near flame center, providing temperature information not available from the optically trapped CO_2 lines. As mentioned above, at flame edge the improved SNR would reduce the spectral effects due to the measurement and systematic error and likely improve fit results in that region. The SNR at flame edge could be improved further by collecting two sets of overlapping flame data at each height. At flame center, a set with low integration time and high optical attenuation would be taken, similar to the data in this work. At flame edge, an overlapping set with a higher integration time and little optical attenuation would capture high SNR spectra. These two sets could then be combined in post processing. Lastly, it is also possible the SNR could benefit from smoothing the LOS variation of each spectral channel.

In addition to an improved SNR, there are several other possible opportunities to improve retrieval results. One factor likely impacting results at flame edge—present in the data but not incorporated into the model—is background radiance. The pathlength behind the flame, particularly at the edges, would contribute to the radiance at the sensor. This was irrelevant when performing the fit under simulated conditions, as the background was absent in both the input and modeled spectra, but it could cause significant problems with the fit under the real physical conditions being input by the IFTS measured spectra. This is not an insurmountable problem and would require a modification to the developed model and additional testing under simulated conditions. Temperature estimates near flame center should benefit from the addition of high temperature CH_4 lines. This would minimize systematic errors in the CH_4 spectral region and should improve temperature estimates in the interior of the flame where CH_4 concentrations are large and the dominant CO_2 spectral feature is optically trapped. Finally, a more sophisticated retrieval algorithm,

which contains smoothing parameters and simultaneously fits scalars in multiple layers, may improve results in low SNR conditions. The results from the simple onion-peeling inspired method developed here would become starting input scalar parameters for the more sophisticated algorithm.

5.5   Conclusions

This chapter presented the results of several different inversion and retrieval scenarios. First, temperature and CO_2 profiles were retrieved for three stationary flame configurations. Results were excellent and demonstrated the inversion method developed for this work is well suited to the task. Although the initial intent was to employ a simple inversion algorithm with a focus on the quantile analysis, the robustness of this technique on the simulated data stands out as an achievement.

Spectral fit results and the retrieved profiles were also reported for simulated TNF spectra. Fits were excellent at all heights and radial locations, even well off axis where signal was low. In some low signal cases the relative RMS error was high, but within the CO_2 band the error was at or below 6 %. Subsequent simulation retrievals were excellent as well. The inversion algorithm proved susceptible to some problems estimating temperature at center. The simulations revealed the LOS intensity for the diametric path was more correlated with off axis LOS, and this proved accurate. This was most evident on the diametric path at 20 D, where the cooler flame center was dominated by the hotter outer layers along the LOS. The consistent overestimation of temperature along the profile is likely related to the averaging within the quantile bins and can be minimized with additional study of an ideal bin width. Retrieved CO_2 profiles were also acceptable. This is as expected, considering the strong correlation with temperature and the overwhelming presence of the species in the spectral band. Perhaps the most powerful demonstration of this technique was found in the radial plots of temperature standard deviation over the median temperature. The choice of 0.25 and 0.75 quantiles was arbitrary, and the two

were simply converted to a standard deviation of temperature at each point. Statistics of this type are not trivial and, considering they are being retrieved from 2D imagery and path-integrated spectra, are another significant achievement of this work.

The retrieved IFTS temperature and CO_2 profiles at 40 D are not ideal but do not invalidate the results put forth by the inversion of the simulated spectra. Analysis of the simulations indicated the algorithm was sensitive to both radial start location and initial spectral conditions. The high systematic error in the outer regions of the IFTS data imposed less than ideal fit conditions. In addition, the behavior of the dominant CO_2 feature from $r = 0$–3.6 cm further muddied the results. Despite these complications, the results did indicate the retrieval method was performing as desired in the $r = 3.6$–5.5 cm range. The proof of concept is demonstrated with the simulated data, and the question of whether IFTS data can be analyzed with respect to turbulence and quantiles has been answered there. It is believed a larger data sample set with higher signal to noise will demonstrate the method with measurements.

VI.   Conclusions

Pʀɪᴏʀ to this work, no IFTS measurements of turbulent flames existed. Due to the impact of the scene fluctuations on the formation of an interferogram, it may have even seemed counterintuitive to attempt such measurements—IFTS is designed to measure static scenes. The combination of high spectral and spatial resolution make IFTS particularly attractive for combustion diagnostics, since multiple species concentrations and the flow field temperature can in principle be discerned throughout the flame, artifacts from intensity fluctuations notwithstanding. This work demonstrates that IFTS is, in fact, a useful diagnostic for turbulent combustion. The simplest approach uses ensemble averaging to obtain spectral images free from fluctuation-induced artifacts. This is useful for qualitative assessment of flames, *e.g.* identifying where reactants and products are within the flame. This is also useful for quantitative comparison of time-averaged measurements with model predictions. This work showed favorable comparisons of IFTS mean measurements with TASS simulations, and this can easily be extended to spectral images produced from scalar fields generated by reactive-flow computational fluid dynamics. In fact, IFTS could be readily used to both benchmark numerical predictions and help identify specific improvements needed by these predictive codes.

While ensemble averaging yields useful flame spectral images, quantitative interpretation, *i.e.* inferring 3D scalar fields via direct inversion, is difficult if *a priori* knowledge of the scalar fields' probability distribution functions is unavailable. This is due to the highly nonlinear nature of radiative transfer. The most significant achievement of this work is the demonstration that the intensity fluctuations—previously viewed as a "noise term" to be averaged over—can be used to generate quantile spectra which contain information about the underlying scalar field fluctuation statistics. A quantile spectrum represents a conditional average over the limited set of scalar field configurations which produce a common

integrated intensity. This removes much of the nonlinear effects present in a standard ensemble average, and consequently makes spectral inversion less problematic in the absence of *a priori* scalar PDFs. In this work, an onion-peeling-like spectral inversion method was developed to estimate radial scalar distributions from each quantile spectrum. The accuracy of these retrievals is a function of several measurement parameters, including SNR, spectral resolution, optical thickness of the flame, and the presence of systematic errors. Inversions of TASS simulated quantile spectra yielded scalar estimates in good agreement with their underlying statistical distributions. For example, the non-dimensional RMS-to-mean temperature ratio estimated from retrievals from multiple quantile spectra was in good agreement with the underlying temperature statistics driving the TASS model. Spectral inversions were also performed on the Purdue Flame A measurements. A combination of systematic errors, insufficient SNR, and optical trapping within the strong CO_2 band made retrievals difficult near flame center. However, the qualitative behavior of temperature and CO_2 across quantiles was consistent with the elevated turbulence at the flame edge.

This work establishes IFTS as a combustion diagnostic which is complementary to myriad laser-based methods. Moreover, this work demonstrates the applicability of IFTS for estimating scalar fluctuation statistics in turbulent flames. Additional work is required to bring this capability to full fruition; however, this work justifies a substantial continued effort. Having summarized the significance of this work, a more detailed list of accomplishments is now documented.

1. Captured the highest spectral resolution ($0.25\,\text{cm}^{-1}$ across a wide channel band-pass) IFTS measurements of canonical flame (Purdue Flame A) at comparable spatial ($0.72\,\text{mm}$) and temporal ($5\,\text{kHz}$) resolutions of the best IR camera measurements to date.

(a) Provides the combustion and spectroscopic communities with high-resolution spectral data suitable for testing radiation models and assessing high temperature spectroscopy databases.

(b) Provides the computational fluid dynamics flame modeling community with highly-constraining measurements against which predictions from current and next-generation codes can be tested.

2. Validated both the spectral and imagery data regimes with previously acquired non-imaging spectral and narrowband IR measurements.

(a) Demonstrated that IFTS turbulent flame spectral measurements agree to within 10% of published FIAS measurements at 40 D and 60 D; comparison degraded to 20% at 20 D.

(b) Demonstrated that IFTS imagery measurements can be used to estimate turbulent integral time and length scales, intensity PDFs, and PSDs; integral length scales agree to within 14% at 20 D and 60 D; PDFs and PSDs exhibit nearly identical behavior.

3. Implemented stochastic TASS analysis to model instantaneous flame scalar profiles; developed a more robust approach to handling multiple species concentrations and their correlations with temperature.

4. Developed a multilayer spectral radiance model incorporating the latest high-temperature spectral databases suitable for modeling inhomogeneous axi-symmetric flames; coupled with TASS-generated stochastic scalar fields to simulate instantaneous flame spectra along arbitrary LOS.

5. Demonstrated good agreement between observed and simulated mean, diametric-path, high resolution ($0.25\,\mathrm{cm}^{-1}$) spectra at 20 D, 40 D and 60 D with RMS

fit errors between 13.5-18.6%; simultaneously validates the multi-layer radiative transfer model, extended TASS model, and sufficient quality of the high-temperature spectroscopy databases (excepting the methane line list).

6. Performed the first quantitative interpretation of quantile spectra for turbulent flames.

   (a) Demonstrated that quantile spectra can be used to estimate RMS spectra in turbulent flames due to the strong correlation which exists between integrated intensity and spectral channel intensity. Validated estimated RMS spectra against direct RMS measurements previously reported.

   (b) Compared measured and modeled quantile spectra at $20\,\mathrm{D}$, $40\,\mathrm{D}$ and $60\,\mathrm{D}$ for diametric and chord-like paths; observed decent agreement between measured and modeled diametric-path spectra; poor agreement observed for chord-like paths.

   (c) Demonstrated utility of quantile spectra for assessing how well stochastic time series analysis predicts TRI.

7. Developed a simple spectral fitting inversion method capable of retrieving scalar profiles in an inhomogeneous, axi-symmetric flame; motivation for novel approach stemmed from non-optically-thin nature of Flame A, which precluded many standard inversion techniques such as onion-peeling and Abel inversion.

   (a) Demonstrated good agreement between retrieved and known scalar profiles for stationary (i.e. non-turbulent) simulated spectra.

   (b) Parametric study with spectral resolution suggests only moderate resolution needed to retrieve temperature and species concentrations.

   (c) Showed that inversion method could be used to estimate scalar profiles for simulated turbulent quantile spectra.

(d) Established that fitted temperatures from TASS-simulated quantile spectra could be used to estimate a key, non-dimensional measure of turbulence, $T_{\text{std}}/T_{\text{med}}$, with a favorable comparison to the results from DLR Flame A data.

8. Presented a subset of these key results at a conference ([32]) and in the archival, peer-reviewed literature ([31, 59]).

Appendix A: Expanded experimental discussion and time-averaged analysis

THE four page maximum imposed by Optics Letters limited the number of figures and discussion which could be reasonably included for publication, therefore additional relevant details not included in Chapter 3 are found here. Details regarding the experimental measurements not pertinent for the Letter, but relevant to future IFTS TNF analysis, are discussed. Uncropped spectrally integrated imagery maps of the broadband and relevant species are presented. Additional high-resolution spectra (published only at 20 D on axis) are presented on and off axis with the approximate noise level of the instrument in each case. Finally, the low-resolution off axis spectral comparisons with data reported by Zheng *et al.* (previously compared only on center axis) are presented [81].

A.1 Experimental Measurements

The Purdue Flame A experiment was not originally intended to be the primary experiment in this dissertation. It was thought to be an excellent opportunity to acquire data comparable to the TNF workshop Flame A housed at the Sandia National Laboratories CRF in Livermore, California. Measurements from a future IFTS experiment on site at the CRF was expected to be the primary data analyzed in this work. Flame experiments of this sort had not been accomplished via the IFTS prior to this work, and any insight into ideal setup configuration, expected intensity values, optimal calibration points, etc. was welcome. The proximity of the Purdue laboratory also greatly simplified the logistics of the experiment (as compared to the cross-country shipment of the equipment to Sandia). This—coupled with the need to understand the many experimental unknowns—made it an obviously worthwhile endeavor.

The IFTS was originally developed for long-range (> km) remote sensing and has only recently been used for indoor, short-range (< m) experimental use. The minimum

unaltered focal distance is 3 m and not ideal for smaller laboratory settings. For this reason an external 0.25 X telescope was developed to expand the field-of-view and reduce the minimum working distance of the system to approximately 33 cm. The Purdue experiment was the first laboratory use of the IFTS with the fore-optic. The new estimated spatial resolution for the system calculated prior to the experiment was 0.88 mm/pix, which was off by nearly 20 % of the final post processing value of 0.72 mm/pix. This incorrect spatial resolution impacted the spacing of the imagery datasets as seen in the imagery analysis below.

The experimental setup is depicted in Figure A.1. The camera fore-optic was 50.8 cm from the center of the exit orifice providing a spatial resolution of approximately 0.25 mm^2 per pixel. The camera was mounted level to the optical bench on a computer controlled Gimbal mount. Preset swivel locations allowed for the camera to turn and face external blackbodies (for intermittent calibration points) while ensuring it always returned to the same center plume orientation. The close proximity of the 500 °C blackbody was problematic as the IFTS got extremely warm during the experiment. A spacer was placed between the two during data capture to alleviate some of the heat stress, but the combination of flame and blackbodies made heat mitigation an issue. Calibration points were taken often to account for the drift in FPA response under such conditions.

The flame under consideration was run with operating conditions designed to simulate Flame A from the International Workshop on Measurement and Computation of Turbulent Nonpremixed Flames. These conditions are described in Table A.1 and resemble those of Flame A established at the Turbulent Combustion Laboratory at Sandia National Laboratories with the exception of the slow co-flowing air. The flame tube was 480 mm long, mounted vertically, and moveable via unislide to allow for imaging of nearly the entire plume without camera tilt. The absence of the outer co-flowing air was not expected to have an impact on the IFTS experiment, nor was it expected to alter the footprint of Flame

A in any way. However, some differences between the Purdue Flame A and the Sandia CRF Flame A have been noticed and bear pointing out. IR imagery ($2.77\pm0.12\,\mu$m) comparisons made by Rankin between the Sandia and Purdue Flames showed a slightly larger spread in the Purdue Flame A. The entrainment boundary conditions differences, which can create changes in flame size and shape, were deemed a plausible cause [53]. This may partially explain the disagreement between off axis comparisons of IFTS and FIAS spectra as well as the off axis comparisons between IFTS and TASS modeled spectra.

Table A.1: Conditions for the Purdue laboratory non-premixed turbulent jet diffusion flame configured to closely resemble Flame A from the DLR TNF flame series (without the slow air coflow).

CH_4 [% by vol]	22
[mg/s]	313
H_2 [% by vol]	33
[mg/s]	59
N_2 [% by vol]	45
[mg/s]	1105
U_{exit} [m/s]	42.2
D_{exit} [mm]	8
Re_{exit}	15,200

Data was gathered over a two day period with relatively consistent atmospheric conditions. A Kestrel 4500 NV Weather Meter was used to intermittently capture ambient temperature, pressure, and humidity just behind the camera. It is likely the atmospheric

conditions along the pathlength between fore-optic and flame were different than those at the Kestrel. Day one had an average ambient temperature of 24.9°C, pressure of 990.18 hPa, and humidity of 46.9 %. Day two had averages of 23.8 °C, 989.51 hPa, and 45.4 %. During day one, high spectral resolution (0.25 cm^{-1}) datacubes were taken at 20, 40, and 60 diameters (D) above exit. The day two experiment was at a lower spectral resolution 16 cm^{-1} but a much larger window size (128 × 192 [H× W]) for increased spatial resolution. The goal was to individually image seven separate overlapping regions of the flame to allow for a final "stitched" image of the entire flame, however the miscalculated pixel resolution caused small gaps between final images. Despite the larger FOV, the lower spectral resolution of the spatial dataset greatly reduced the acquisition time per datacube 0.238 s and provided an excellent imaging frame rate of nearly 5 kHz. Integration time was set to 20 μs for all cases, and an optical filter (with ∼ 45% transmission in the 1.9 μm to 4.5 μm region) was in place to prevent saturation. Due to throughput complications between camera and PC controller, spatial resolution was partially sacrificed (8 × 192 [H×W]) to reduce file size, and the number of samples was reduced at each height. The 512 interferograms gathered at the higher spectral resolution were adequate for producing averaged spectra, but the same sample size on the low resolution sets intended for quantile analysis is unfortunate. Time constraints and the persistent throughput problem made this necessary, and it was thought much larger datasets would be acquired at Sandia.

Aside from the need to acquire a dataset devoid of the problematic behavior seen here, some lessons learned in the Purdue experiment would warrant changes to how future data is acquired. Certainly the window size must be chosen carefully. The sensitivity of the inversion algorithm to starting well outside the flame cannot be overstated. To prevent excessive data reduction issues (a relevant issue with IFTS data), the window width can likely be kept at or near the current (192 pixel) value, and the alignment of camera to flame can be adjusted. Capturing the full width of the flame would be ideal, but is not

necessary. Imaging a few centimeters beyond flame center (much in the same way the DLR data is reported) would allow for $r/x = 0$ to be located in post processing, and the majority of the FPA could be dedicated to providing ample space beyond flame edge for fitting. Comparisons between IFTS data and other sources, both measured and simulated, requires a precise understanding of flame location and alignment. It is paramount both the spatial resolution per pixel be as exact as possible, and the region of the flame being imaged is absolutely known. The Purdue experiment was the first experimental use of the external telescope, and some unknowns regarding spatial resolution existed prior to the experiment. This issue is mostly since resolved, but an imagery spatial reference before or after data capture is still recommended. To most accurately control flame behavior, it is recommended future experiments take place in a facility with a dedicated digital flame control setup of the type used at the Sandia CRF.

A.2   Imagery analysis

The left side of Figure A.2 contains the complete mean broadband image of the low-resolution data. The upper region has been cropped due to the large overlap caused by the bottoming out of the flame's unislide mount. The image is framed by the axes used in the published work, but the sides are now intentionally uncropped. Great care was taken in aligning and leveling both the unislide and the Gimbal mount, but the imagery suggests some misalignment still occurred. The shift between the bottom and top panels is obvious. Along center axis it appears the flame is not exactly axisymmetric, this is also likely due to the undetected tilt to the flame (or camera). The gaps between windows is necessary due to the incorrect pixel size estimated prior to data capture. During the experiment it was thought a 14 pixel overlap between windows would occur with each shift of the flame. The spacing between imagery was discovered during post processing. Fortunately, the gaps are small (less than the equivalent of 3 pixels) and do not overlap any of the heights of interest. The alignment and spacing determined using the broadband imagery was applied

to the remaining imagery figures. The right side of Figure A.2 is the complete map of the coefficient of variation (σ/μ). This imagery was combined with the integrated CH_4 species map in Figure 3.1 and not found in the Optics Letter submission, but nevertheless is presented here for a complete discussion of imagery. There is a noticeable disparity at the interface of the image windows between 40 D and 50 D at both flame center and the outer edge of the flame. It is unclear why this is so pronounced, but it does not appear in the mean integrated maps and is likely related to the standard deviation in this turbulent region of the flame.

The complete species integrated maps for H_2O (left), CH_4 (middle), and CO_2 (right) are presented in Figure A.3. Imagery is again presented with published axes but with no cropping of the edges. Unsurprisingly, the slight asymmetry to the center axis is seen in these figures as well. These are path averaged spectra, therefore color maps of radiance do not equate directly to species concentration, but there is still a qualitative usefulness to imagery of this type. A sense of the chemistry in the flame can certainly be gleaned from such qualitative analysis.

A.3   Spectral analysis

A.3.1   High-resolution mean spectra.

Spectra from the $0.25\,\mathrm{cm}^{-1}$ data set at 20 D are presented for $r/x = 0$ in Figure A.4 and for $r/x = 0.12$ in Figure A.5. These spectra (black) are across the entire band, and the imaginary component of the spectra (offset, gray) is included. The imaginary component is considered representative of the noise of the instrument. The RMS of the noise is reported in both cases. With respect to the mean of the spectrum, the RMS of the noise to the real spectra ($i_{\mathrm{RMS}}/L_{\mathrm{mean}}$) is 33 % at center and 28 % off axis. These are extremely high percentages, but nearly a third of the noise lies in the wings below $1900\,\mathrm{cm}^{-1}$ and above $4500\,\mathrm{cm}^{-1}$ where no spectral analysis was performed. The percentages of noise in the $1900\,\mathrm{cm}^{-1}$ to $4500\,\mathrm{cm}^{-1}$ range are 12 % at center and 10 % off axis. Spectra at 40 D are

presented in the same manner for $r/x = 0$ in Figure A.6 and for $r/x = 0.11$ in Figure A.7. Here, the RMS to mean across the entire band is 19 % at center and 24 % off axis. In the 1900 cm^{-1} to 4500 cm^{-1} range the percentages improve to 5 % at center and 8 % off axis. The final pair of high-resolution spectra at 60 D are presented for $r/x = 0$ in Figure A.8 and for $r/x = 0.11$ in Figure A.9. The RMS to mean across the entire band is 18 % at center and 32 % off axis. In the 1900 cm^{-1} to 4500 cm^{-1} range the percentages again improve to 6 % at center and 11 % off axis.

In the 1900 cm^{-1} to 4500 cm^{-1} spectral region of interest, the high-resolution spectra are excellent. It is worth pointing out the 20 D data has twice the percentage of noise as the remaining two heights at $r/x = 0$. This is likely due to the bleeding of the lower frequency turbulence into the spectral region of the IFTS. The topic is addressed further in the supplementary interferometric analysis in Appendix B.

A.3.2 *Low-resolution off axis spectral comparisons.*

The mean low-resolution spectra from chord-like paths at 20 D, 40 D and 60 D are compared with previous (non-imaged) LOS measurements of Flame A by Zheng *et al.* [78] in of Figure A.10. A spatial average over a 3×3 window was performed to approximate the 2 mm resolution of Zheng's data. The solid lines represent the apparent (i.e. at-sensor) radiance. Atmospheric correction and uncertainties were handled in the same manner as for the diametric comparison in Chapter 3. In contrast to the diametric spectra, agreement is not excellent at any height. This is likely due to a combination of factors. The pixel resolution of 0.72 mm/pix was used to determine the r/x locations. This resolution was chosen based on an analysis of imagery (measurement of flame exit tube exit width), a Zemax model estimate, and comparison between IFTS and narrow band IR axial integrated intensity profiles from Sandia Flame A. No pixel resolution gave a complete agreement between axial profiles at all heights (perhaps due to the lack of the outer co-flowing air), but 0.72 mm/pix gave the closest agreement and was used from that point forward. Any

error with the pixel resolution would impact the comparisons off axis. This is likely a minimal effect, especially considering the 3×3 averaging used for the IFTS spectra, but it is a possibility. Another likely contributor is the increase in flame spread due to the lack of co-flowing air. However, it would seem this would have greater impact further from the exit, and comparisons improve with height. Additional spectral and integrated intensity profile comparisons found in Appendix B explore this idea further.
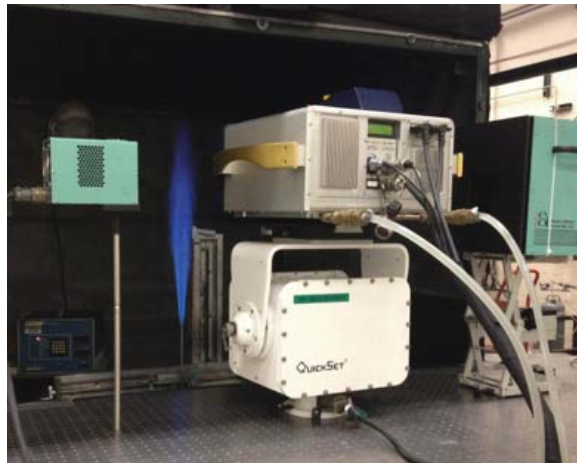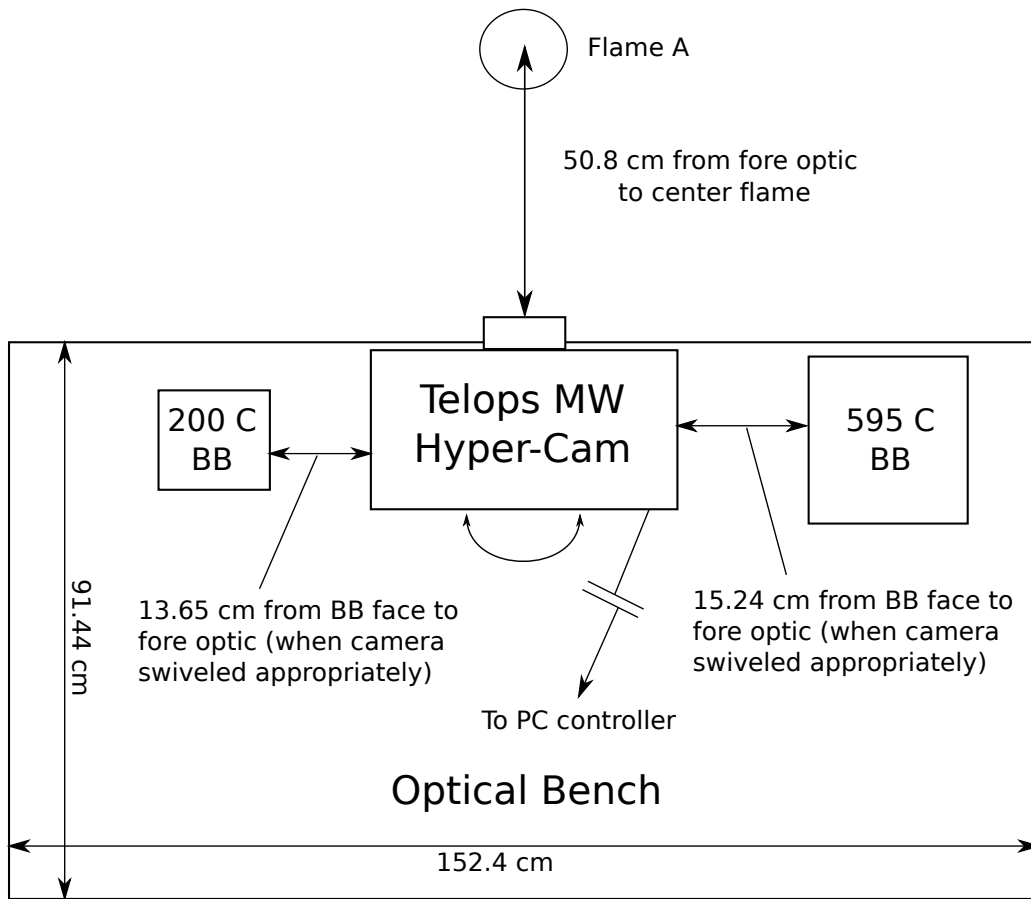
Figure A.1: *Top*: Overhead rendering of experimental setup. The IFTS was mounted to a PC controlled Gimbal mount and placed on a level optical bench with blackbodies mounted on either side for the capture of intermittent calibration data. *Bottom left*: Photo of the IFTS. *Bottom right*: Photo of the experiment as seen from the rear of the camera.
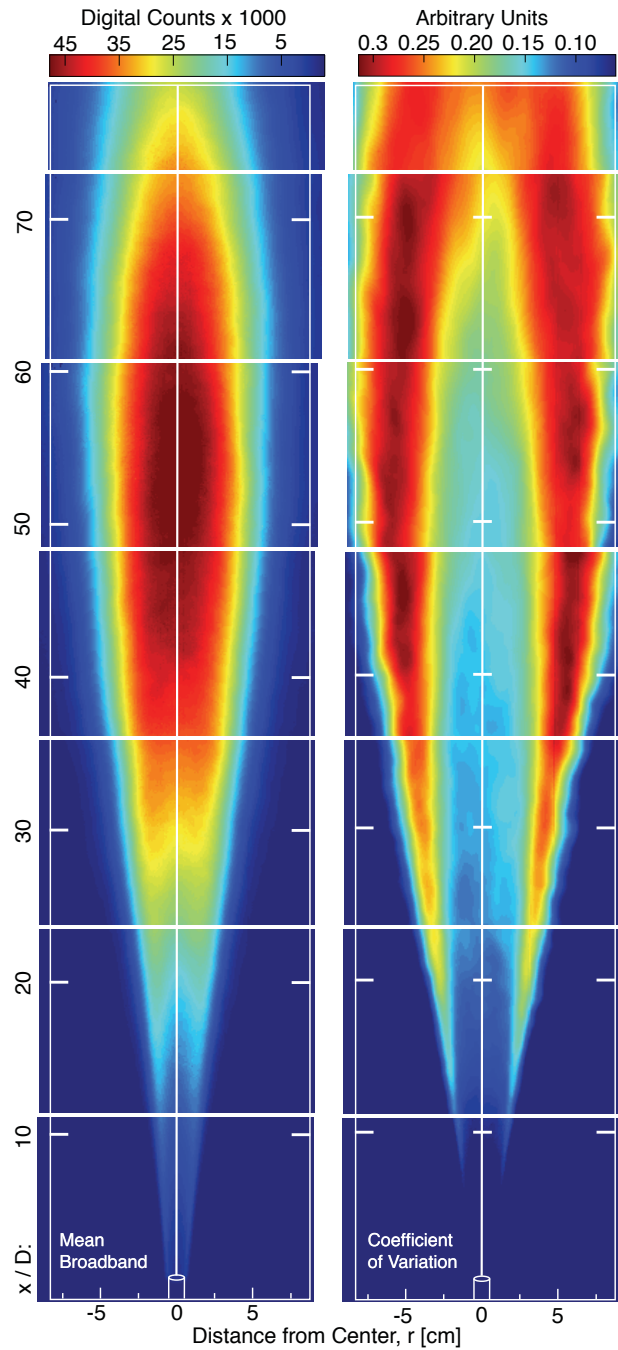
Figure A.2: Uncropped imagery. Mean broadband (left) and coefficient of variation (right). A slight shift is evident as the flame was lowered via unislide. White border represents the framing of the imagery as presented for publication. Upper segment has received a vertical crop to remove overlap with segment 6.
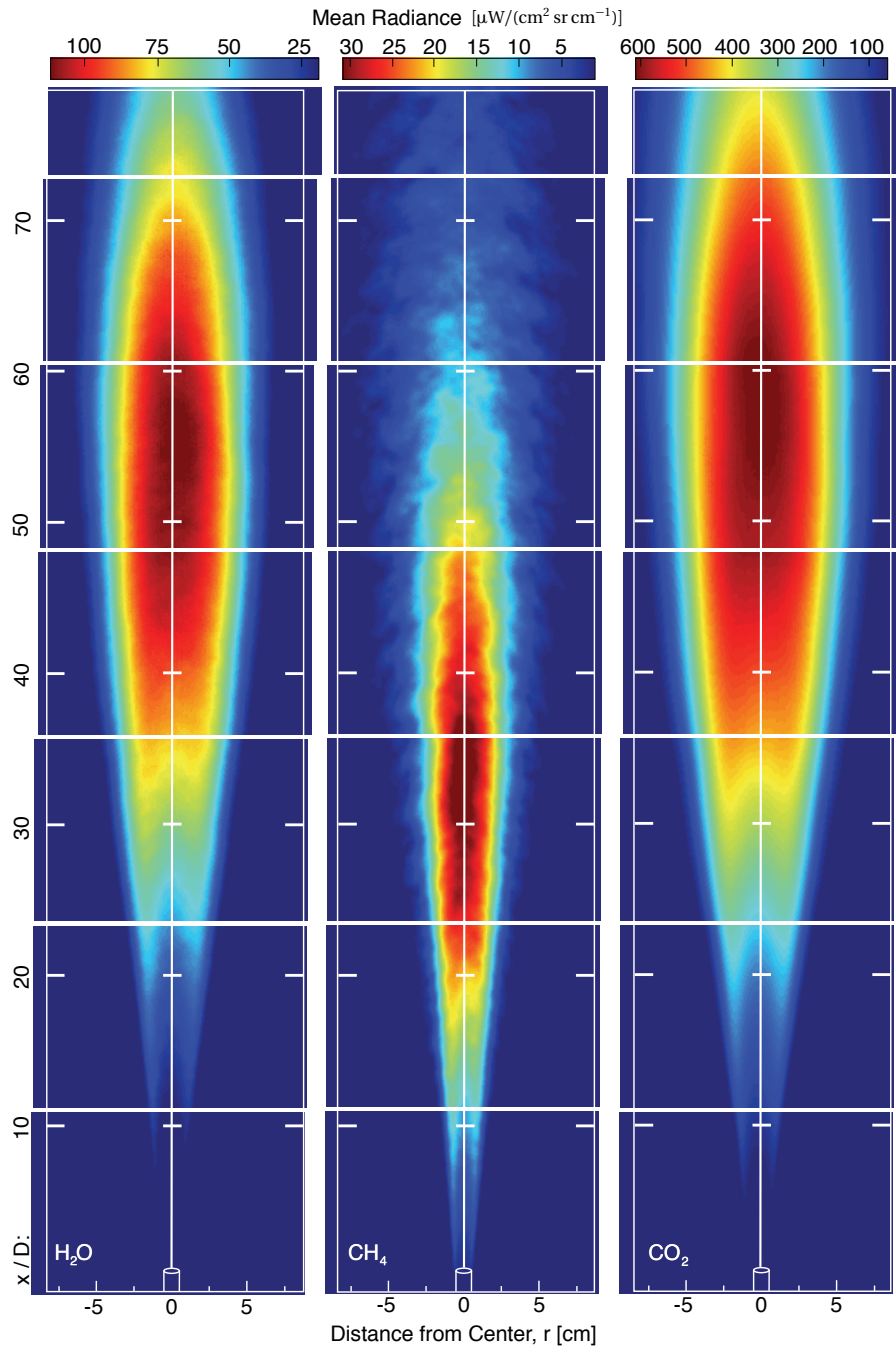
Figure A.3: Uncropped mean species imagery. H_2O (left), CH_4 (middle), and CO_2 (right).
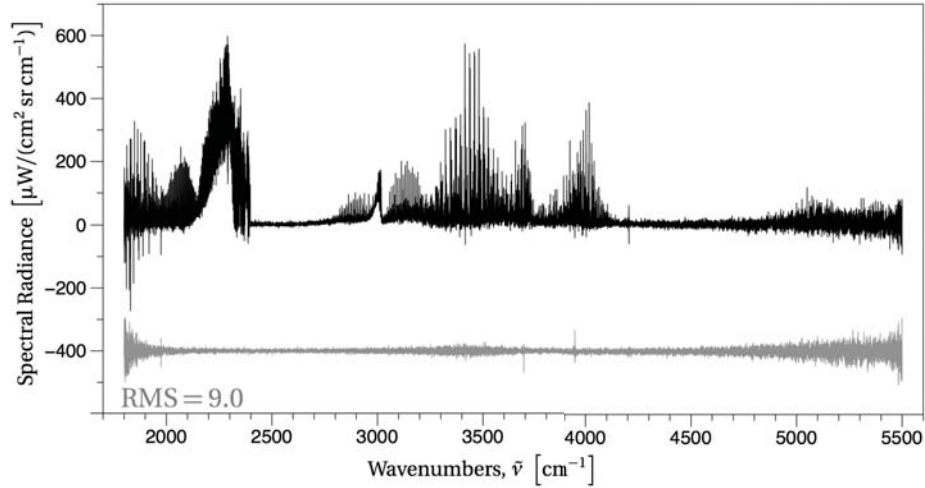
Figure A.4: High-resolution $0.25\,\mathrm{cm}^{-1}$ spectrum (black) at 20D through the diametric path at $r/x = 0$, center pixel $(4, 96)$. Imaginary component of the spectrum (gray), representative of the approximate noise level (offset for ease of interpretation, RMS in units of spectral radiance).
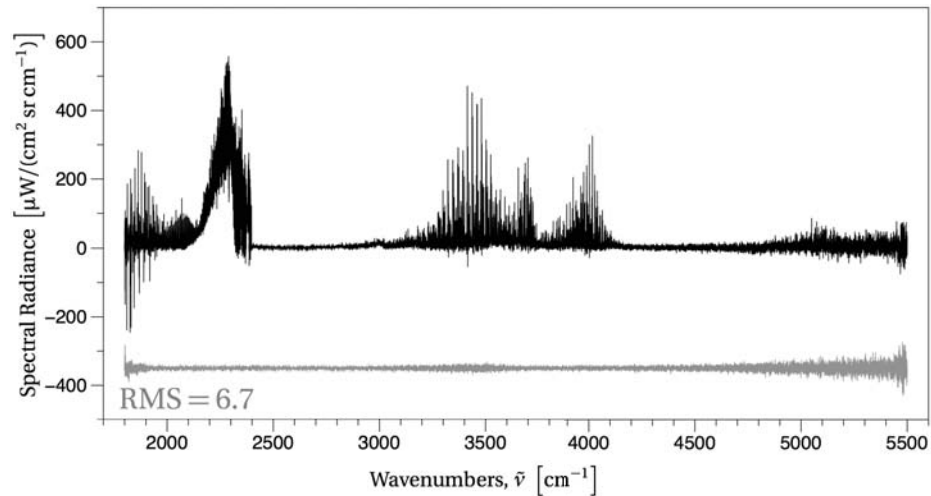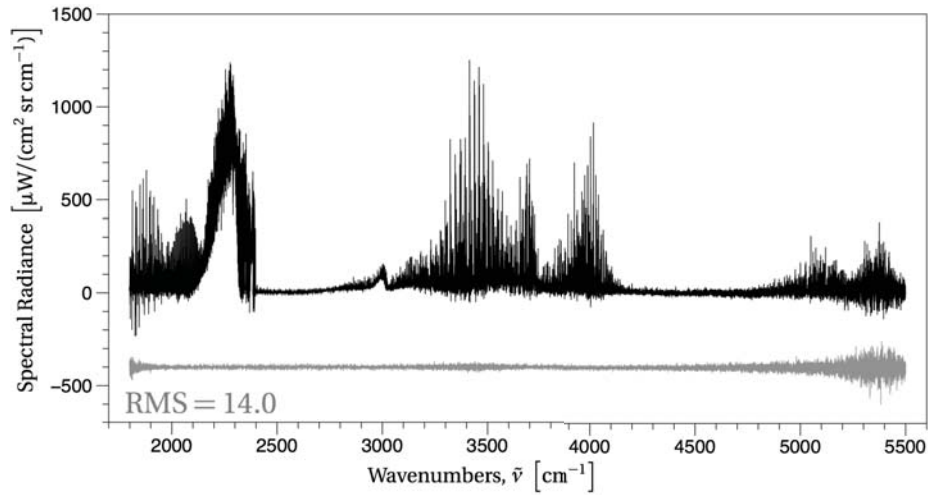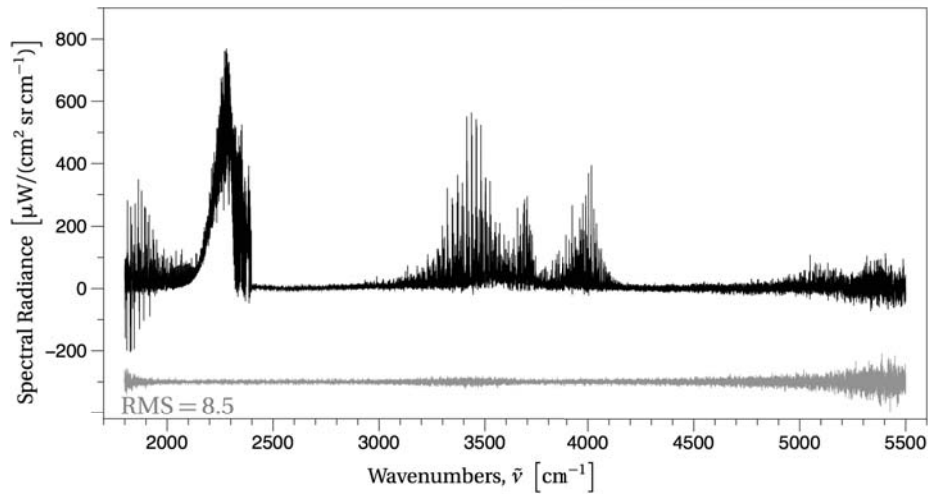

Figure A.5: High-resolution $0.25\,\mathrm{cm}^{-1}$ spectrum at 20D through the chord-like path at $r/x = 0.12$, pixel $(4, 123)$. Imaginary component of the spectrum (gray), representative of the instrument noise level (offset for ease of interpretation, RMS in units of spectral radiance).

Figure A.6: High-resolution $0.25\,\text{cm}^{-1}$ spectrum at 40D through the diametric path at $r/x = 0$, center pixel $(4, 96)$. Imaginary component of the spectrum (gray), representative of the approximate noise level (offset for ease of interpretation, RMS in units of spectral radiance).
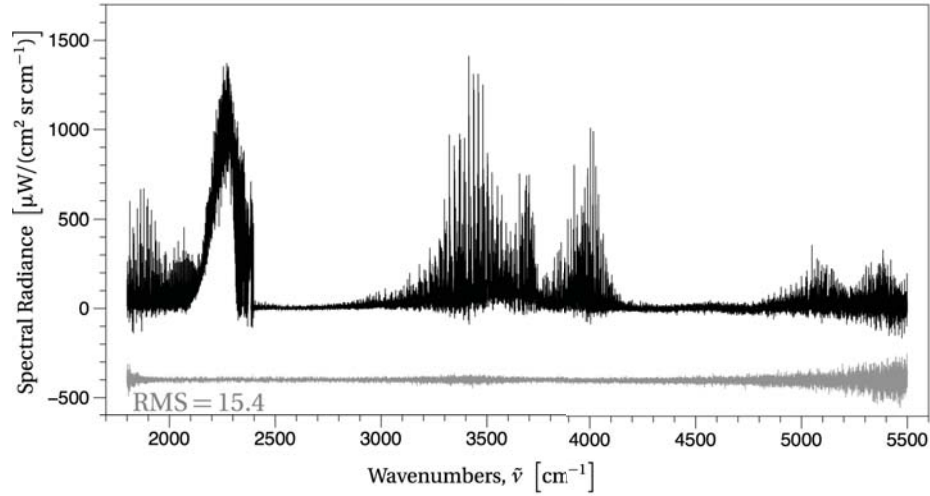

Figure A.7: High-resolution $0.25\,\text{cm}^{-1}$ spectrum at 40D through the chord-like path at $r/x = 0.11$, pixel $(4,145)$. Imaginary component of the spectrum (gray), representative of the approximate noise level (offset for ease of interpretation, RMS in units of spectral radiance).

Figure A.8: High-resolution $0.25\,\text{cm}^{-1}$ spectrum at 60D through the diametric path at $r/x = 0$, center pixel $(4, 96)$. Imaginary component of the spectrum (gray), representative of the approximate noise level (offset for ease of interpretation, RMS in units of spectral radiance).
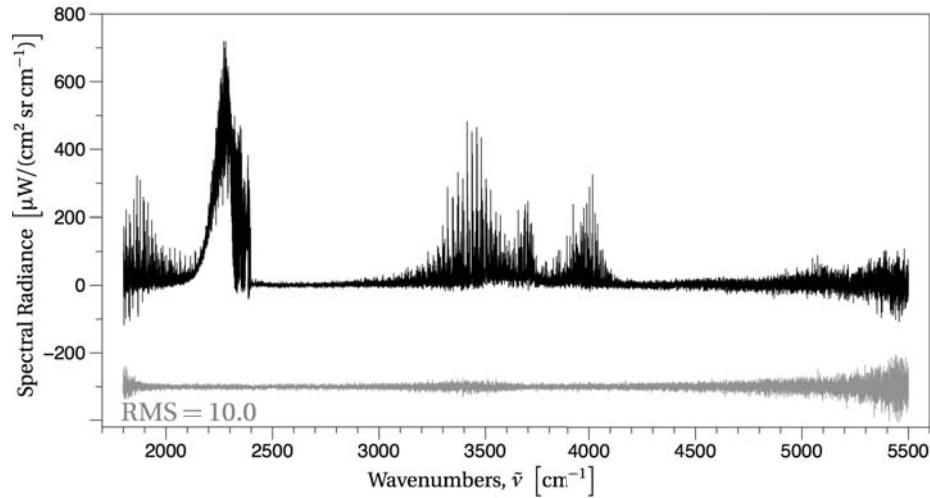

Figure A.9: High-resolution $0.25\,\text{cm}^{-1}$ spectrum at 60D through the chord-like path at $r/x = 0.09$, pixel $(4,56)$. Imaginary component of the spectrum (gray), representative of the approximate noise level (offset for ease of interpretation, RMS in units of spectral radiance).
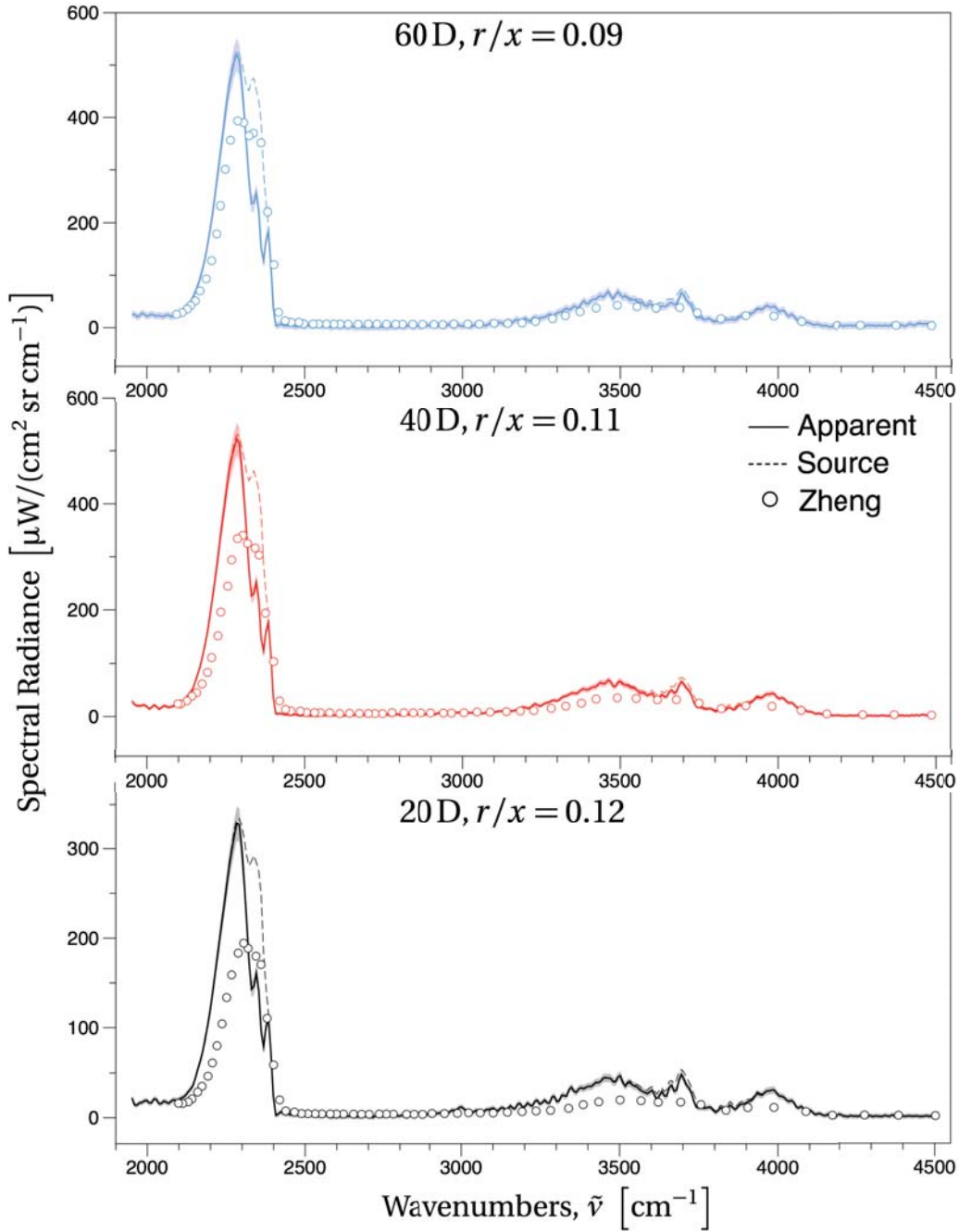
Figure A.10: Apparent (—) and atmospheric-corrected (⋯) low-resolution off axis flame spectra ($\delta\tilde{v}$ = $16\,\text{cm}^{-1}$) at $20\,\text{D}$, $40\,\text{D}$ and $60\,\text{D}$ (black, red, blue) compared with previous measurements (○). Radiance uncertainty (95% confidence interval) presented as a translucent band around each apparent spectrum.

Appendix B: Additional Flame A properties and TASS analysis

EXPANDED analysis of interferometric behavior, flame properties, and spectral comparisons from Chapter 4 is included in this appendix. In the interest of brevity, analysis and comparisons were made only at 60 D for the published work. The figures and discussion below include spectra from additional heights (diametric and chord-like), additional flame property figures at 20 D and 40 D, off axis high-resolution spectral comparisons between TASS and IFTS, off axis low-resolution quantile spectra comparisons between TASS and IFTS, and axial and radial integrated intensity profile comparisons between TASS, IFTS, and FIAS.

B.1 Interferometric behavior

Figures B.1–B.5 are additional comparisons of interferometric behavior in the presence of turbulence at 20 D, 40 D and 60 D for both diametric, $r/x = 0$, and chord-like, $r/x = 0.11$, paths. These figures are supplemental to Figure 3.1, where the behavior was examined at 60 D, $r/x = 0$. As described in Chapter 4, the lower frequency broadband intensity fluctuations due to turbulence at 60 D have mostly dissipated prior to any spectral response from the camera. Therefore, the turbulent effects are assumed isolated or removed via low pass filter (LPF) or high pass filter (HPF) respectively. These assumptions are correct at most heights and radial locations, but are not accurate at 20 D, $r/x = 0$. As seen in Figure B.1, the turbulence is at a slightly higher frequency at that height and has not yet fully dissipated prior to the spectral response near 1800 cm^{-1}. The off axis, $r/x = 0.11$, plot at that height in Figure B.2 shows that the turbulence does dissipate at—or just prior to—the camera response. The turbulence cutoff frequency is higher for all three heights at $r/x = 0$, but only overlaps spectral response at 20 D. The relative RMS error (12 %) at this

location was twice that of the error at the remaining two heights (5 % and 6 % at 40 D and 60 D, respectively). Figure B.1 indicates this was due to turbulence.

B.2 Flame properties

Measured Flame A integral time and length scales at 20 D, 40 D and 60 D were reported in Chapter 4, but the remaining properties were only reported at 40 D. Additional measurements at 20 D and 40 D are presented here in Figures B.6 and B.7, respectively. Rankin *et al.* report Flame A results at 20 D and 60 D (plume measurements at 100 D and 140 D are also reported, but those heights are not observed in this work), therefore only Figure B.6 contains comparisons with those narrow band results [54]. In both cases axial length scales could not be computed due to the windowing of the FPA at these two heights. The necessary number of pixels were not available to allow for correlation along center axis. However, the axial length scale reported at 60 D in Chapter 4 compared well with the reported data, demonstrating the IFTS capability.

The remaining comparisons at 20 D in Figure B.6 are in excellent agreement with the previously reported results. The normalized PDFs in Panel A compare well for both diametric ($r/x = 0$) and chord-like ($r/x = 0.08$) paths. The skewness is less pronounced as it is expected to increase with distance from flame time and with radius. The temporal autocorrelation functions in Panel B are also in good agreement, as are the broadband computed time scales reported in Table 4.1. The broadband PSD plots in Panel C have again been scaled to overlap the narrowband, allowing for a comparative emphasis on functional behavior. The shape of the plots agree well at this height as well, and the broadband PSD confirm the expected steady, break, and decay frequencies [51, 54]. Spatial autocorrelation plots are excellent, but the IFTS computed length scale in Table 4.1 is 14 % larger than the reported IR value. This may be due to the pixel scaling issue as spectral comparisons at this height have also not been ideal.

Calculated properties at 40 D are reported in Figure B.7 without comparisons. However, considering the excellent agreement at 20 D and 60 D these measurements are likely reliable. The increase in skewness with distance from flame exit and radius is evident in the PDFs, and the expected frequency behavior is found in the PSD plots.

B.3   Additional spectral comparisons

Comparisons between off axis high-resolution mean experimental (black) and TASS simulated (red) spectra through the off axis ($r/x = 0.11$) path at 20 D, 40 D and 60 D are found in Figures B.8–B.10. The residuals from data and model and the imaginary part of the data—representative of the instrument noise—are included at each height (gray). The results indicate the off axis spectra are not in as good agreement as the on axis comparisons. The mean relative error between data and simulation is 14.6 %, 43.2 % and 49.8 % at 20 D, 40 D and 60 D respectively. As with the center axis comparisons in Chapter 4, the error was computed using only lines at or above ten times the RMS of the instrument noise (at or above $50\,\mu W/(cm^2 srcm^{-1})$ in all three cases. The improved error from center to $r/x = 0.11$ at 20 D is partially due to the smaller CH_4 footprint off axis. Several factors likely contribute to the overall poor comparison at the three heights. First, there is again some structure in the CO_2 residuals near $2400\,cm^{-1}$ and throughout the H_2O region from $3300\,cm^{-1}$ to $4100\,cm^{-1}$ at all three heights, and this has been attributed to inaccuracies with the parameters used to compute the contribution from the atmospheric pathlength between sensor and flame. Second, the low-resolution comparisons between IFTS measurements of Purdue Flame A and FIAS measurements of Sandia Flame A had similar results. Considering the TASS model is driven by the DLR flame statistics, it should be expected the comparisons between IFTS measurements and TASS model indicate the same result.

The off axis low-resolution quantile comparisons between IFTS measurements and TASS simulations presented in Figures B.11–B.13 continue the trend seen in the off axis

high-resolution spectra. The quantile sorting has effectively generated unique spectra which are well separated from their data or simulation counterparts, but the comparisons between data and simulation at any given quantile is not ideal. This is certainly to be expected, considering the results of the off axis mean spectral comparisons between both IFTS and FIAS measurements and the IFTS measurements and TASS simulations.

B.4 Radial integrated intensity profiles

Radial integrated ($1950 \, \text{cm}^{-1}$ to $4500 \, \text{cm}^{-1}$) intensity profile comparisons between quantile sorted IFTS measurements and TASS simulations are presented in Figures B.14–B.16. In all cases the IFTS intensity falls off faster than the TASS simulation and—due to the results off axis spectral comparisons—this is expected. At $r/x = 0$, however, comparisons are also not ideal in some cases. The results at $20 \, \text{D}$ are expected. The impact of the missing high temperature CH_4 lines from the TASS simulation is going to be significant for the integrated intensity. This holds for the 0.25 and 0.50 quantiles, and at the 0.75 the simulation largely overpredicts the CO_2 peak near $2300 \, \text{cm}^{-1}$, dominating any problems with the CH_4 comparison. At $40 \, \text{D}$ the 0.75 and 0.50 quantiles compare reasonable well, but the 0.25 is much higher for the measured data across the entire profile. This is again likely due to the CH_4 comparison. The low-resolution spectral comparison at $r/x = 0$ in Chapter 4 shows a large gap between simulation and data from $2700 \, \text{cm}^{-1}$ to $3500 \, \text{cm}^{-1}$, where the CH_4 is still very present near center axis at that height. Little CH_4 remains in the spectrum at $60 \, \text{D}$, and the integrated intensity is largely dominated by the CO_2 peak seen in the spectral comparisons at all three quantiles. Unsurprisingly, the mean integrated intensity plot in Figure B.17 closely resemble the 0.50 quantiles at each height.
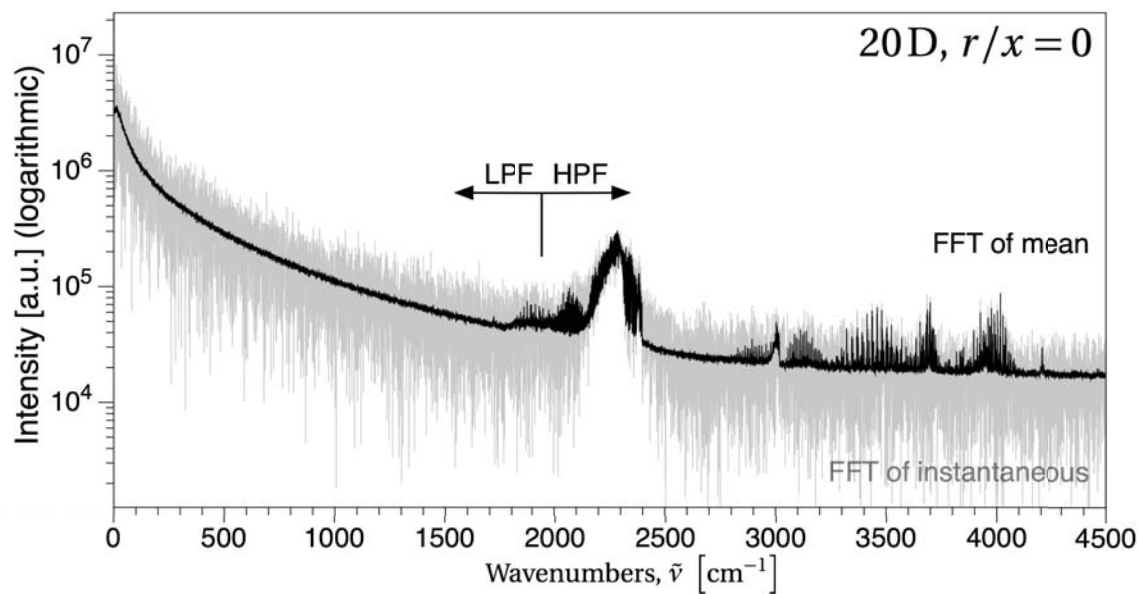
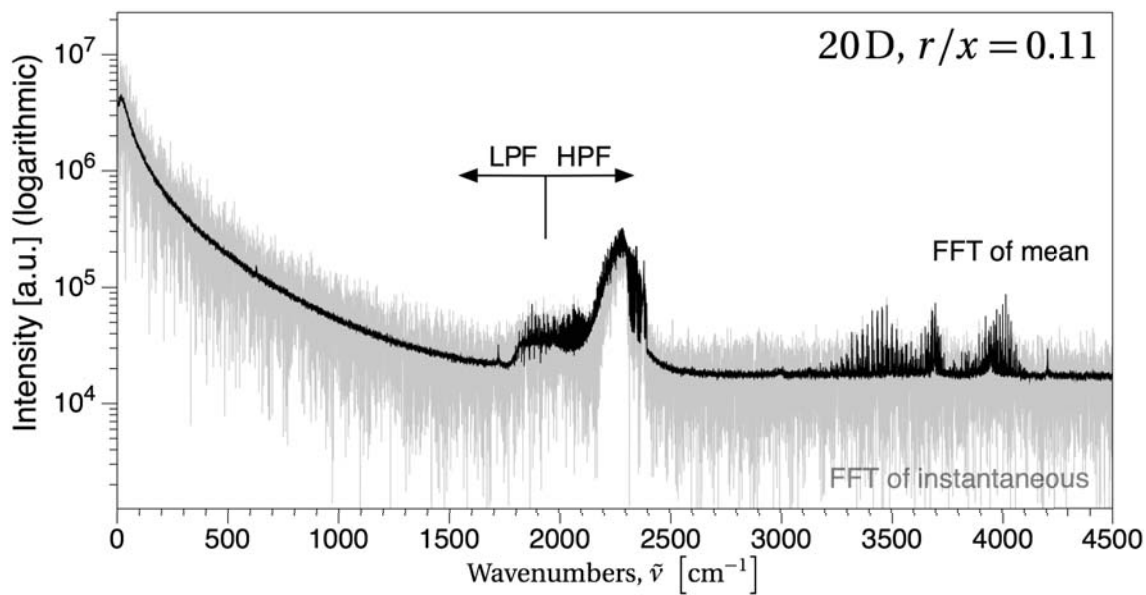Figure B.1: Interferometric behavior at 20 D, $r/x = 0$.

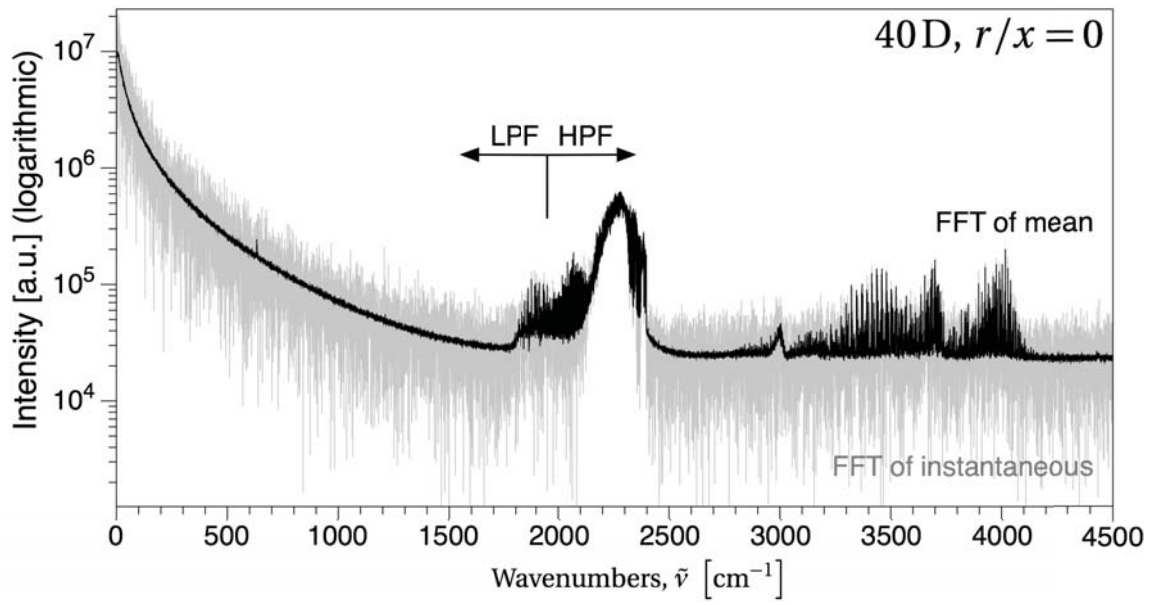Figure B.2: Interferometric behavior at 20 D, $r/x = 0.11$.

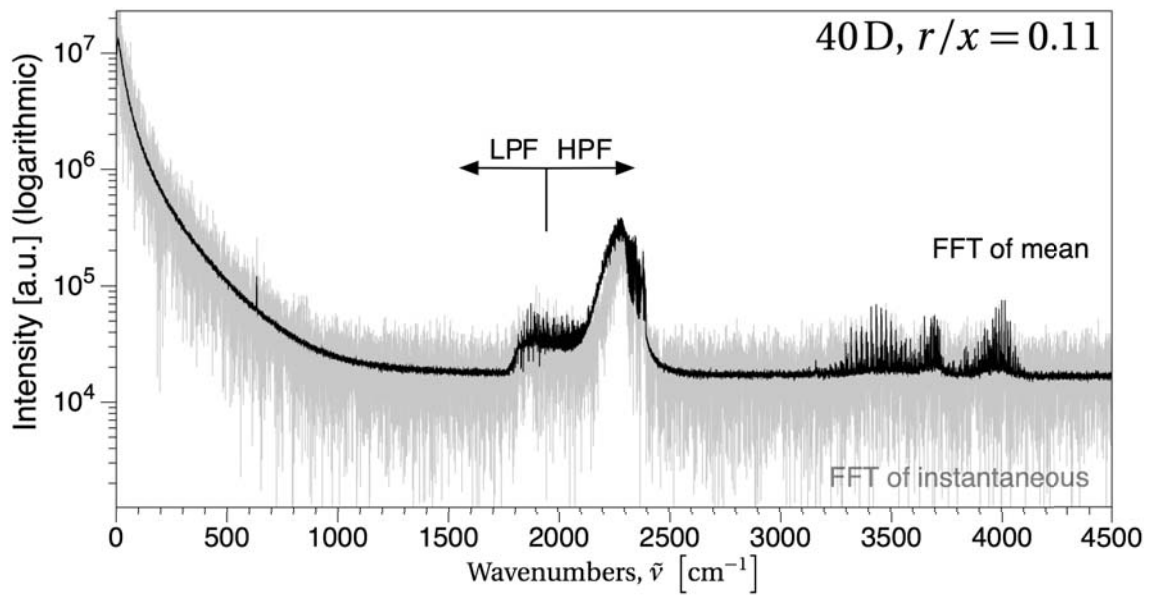Figure B.3: Interferometric behavior at 40 D, $r/x = 0$.

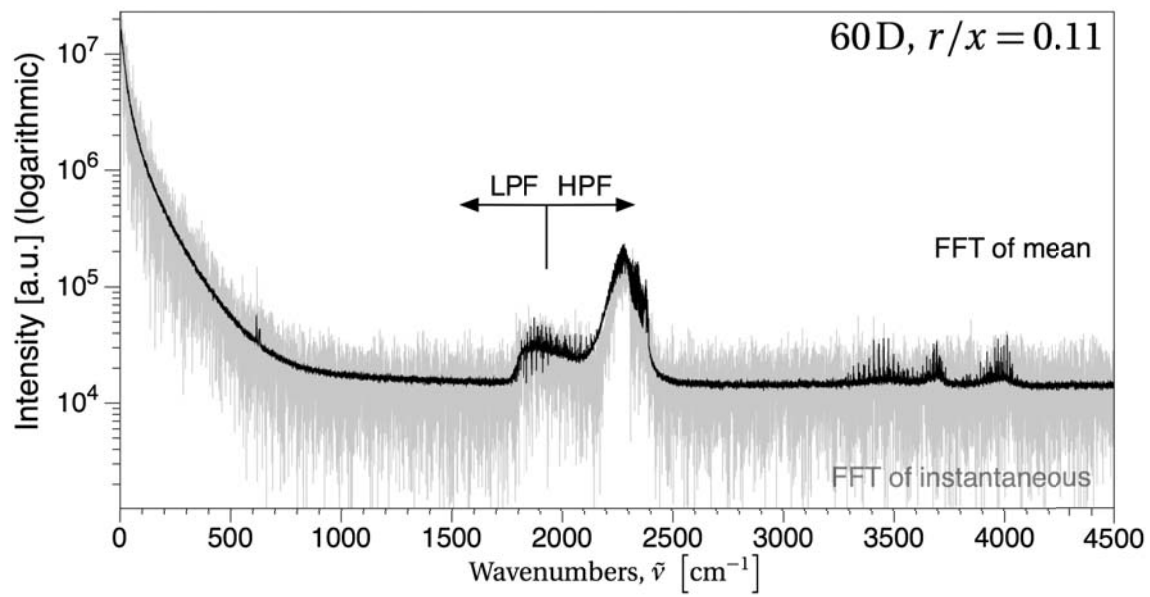Figure B.4: Interferometric behavior at 40 D, $r/x = 0.11$.

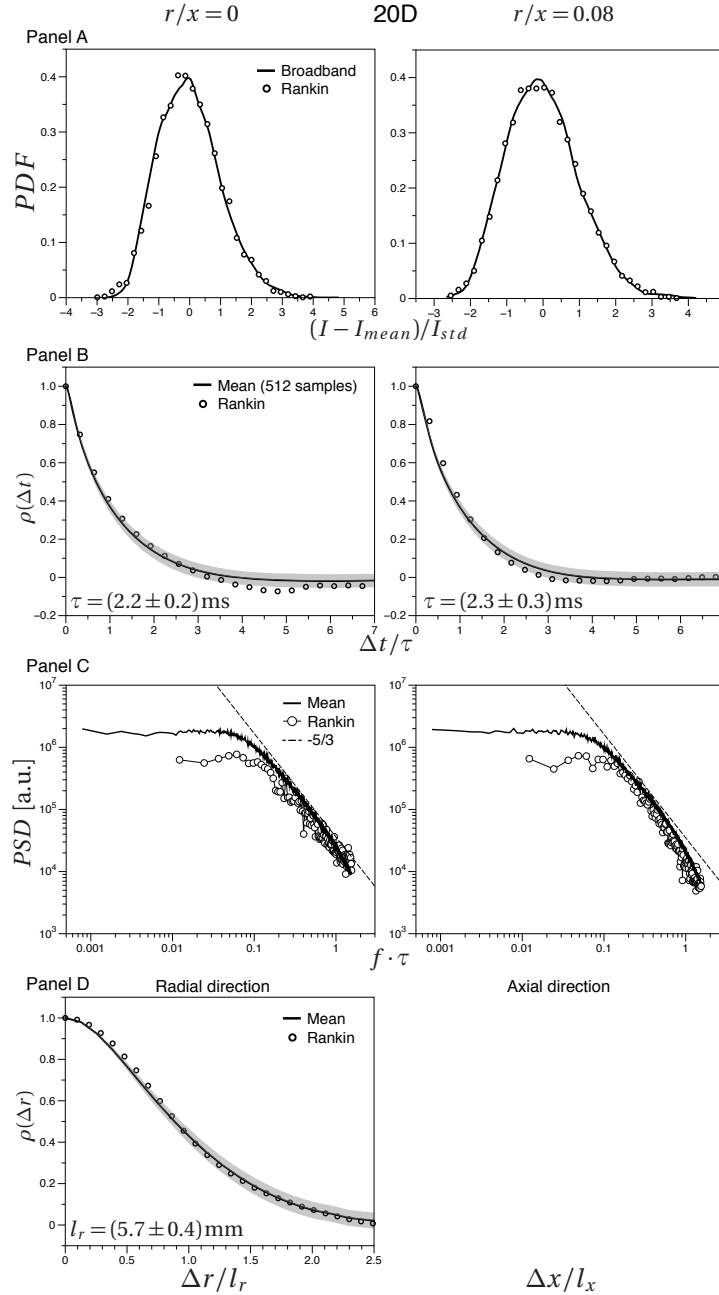Figure B.5: Interferometric behavior at 40 D, $r/x = 0.11$.

Figure B.6: Broadband (solid line) and narrowband (points) [54] flame property comparisons at 20 D for representative diametric ($r/x = 0$, left) and chord-like ($r/x = 0.08$, right) paths. *Panel A*: Probability density functions of the radiation intensity. *Panel B*: Temporal auto-correlation coefficients. *Panel C*: Power spectral density functions of the radiation intensity. *Panel D*: Spatial auto-correlation coefficients for the radial direction. Calculation of axial coefficients not possible due to window geometry at 20 D.

Figure B.7: Broadband generated flame properties at 40 D for representative diametric (r/x = 0, left) and chord-like (r/x = 0.08, right) paths. *Panel A*: Probability density functions of the radiation intensity. *Panel B*: Temporal auto-correlation coefficients. *Panel C*: Power spectral density functions of the radiation intensity. *Panel D*: Spatial auto-correlation coefficients for the radial direction. Calculation of axial coefficients not possible due to window geometry at 40 D.
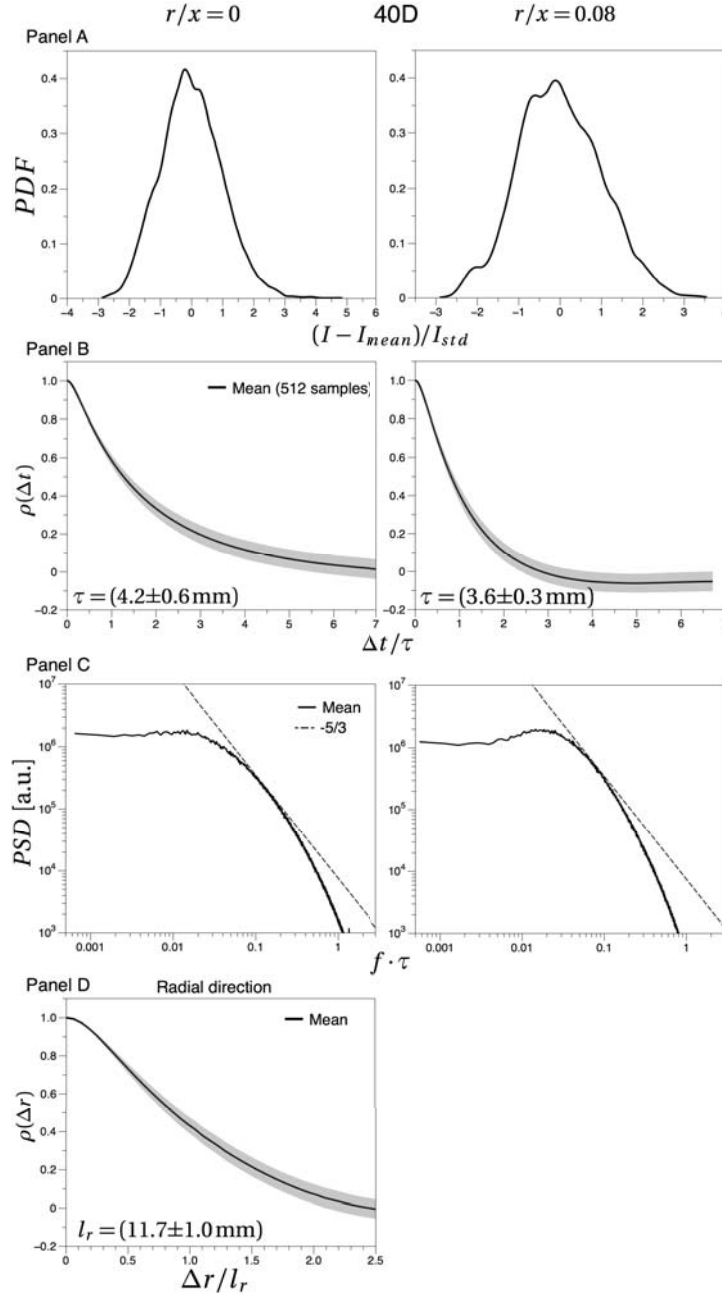
Figure B.8: High spectral resolution data (black) and TASS simulation (red) comparison with residuals (gray) at 20 D, $r/x = 0.11$.
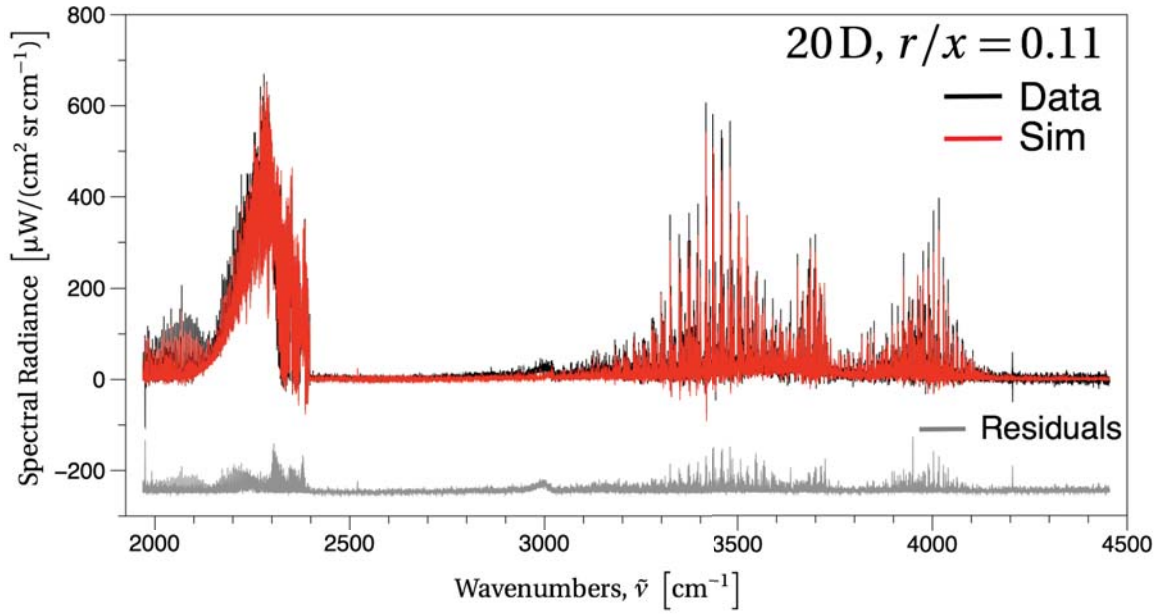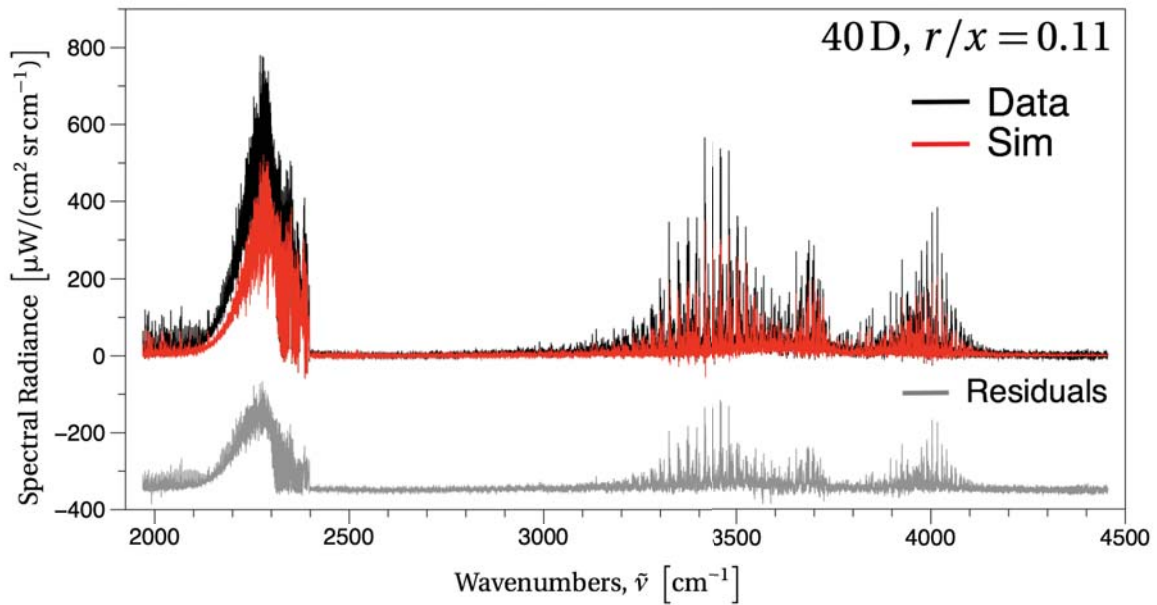

Figure B.9: High spectral resolution data (black) and TASS simulation (red) comparison with residuals (gray) at 40 D, $r/x = 0.11$.
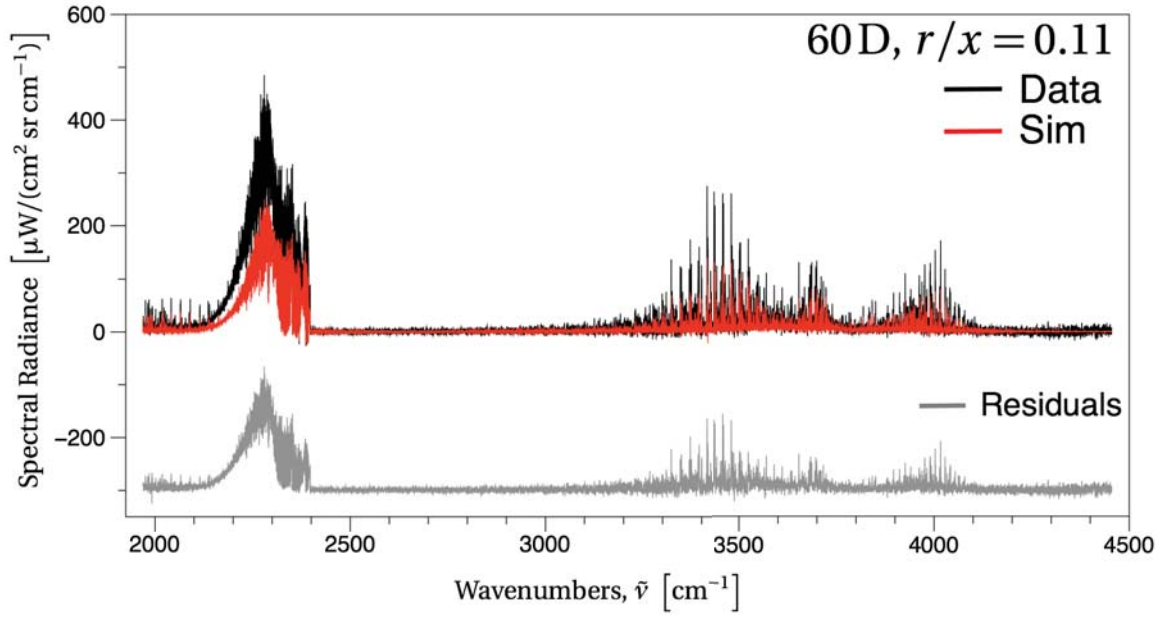
Figure B.10: High spectral resolution data (black) and TASS simulation (red) comparison with residuals (gray) at 60 D, $r/x = 0.11$.
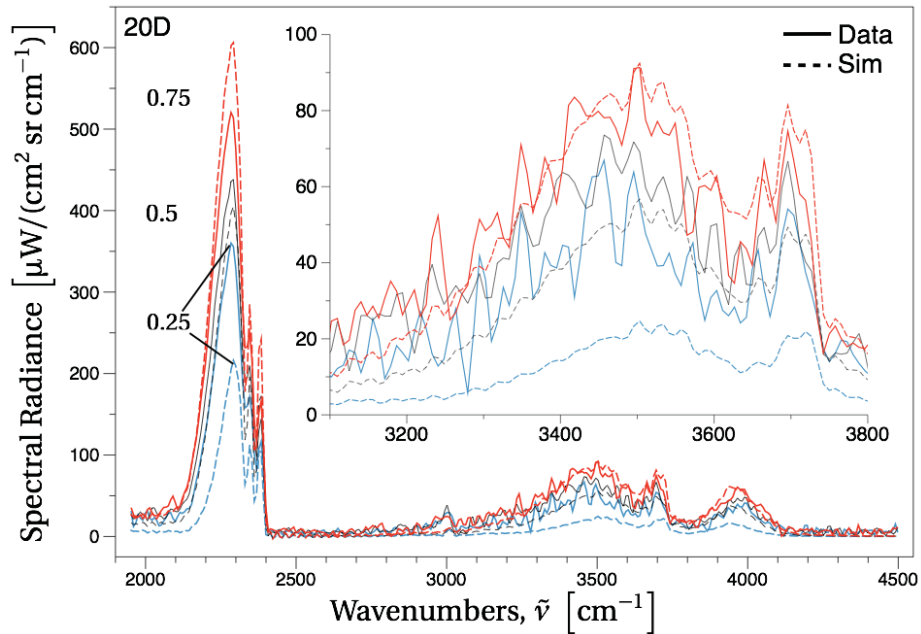
Figure B.11: Quartile sorted spectral comparison at 20 D, $r/x = 0.11$.
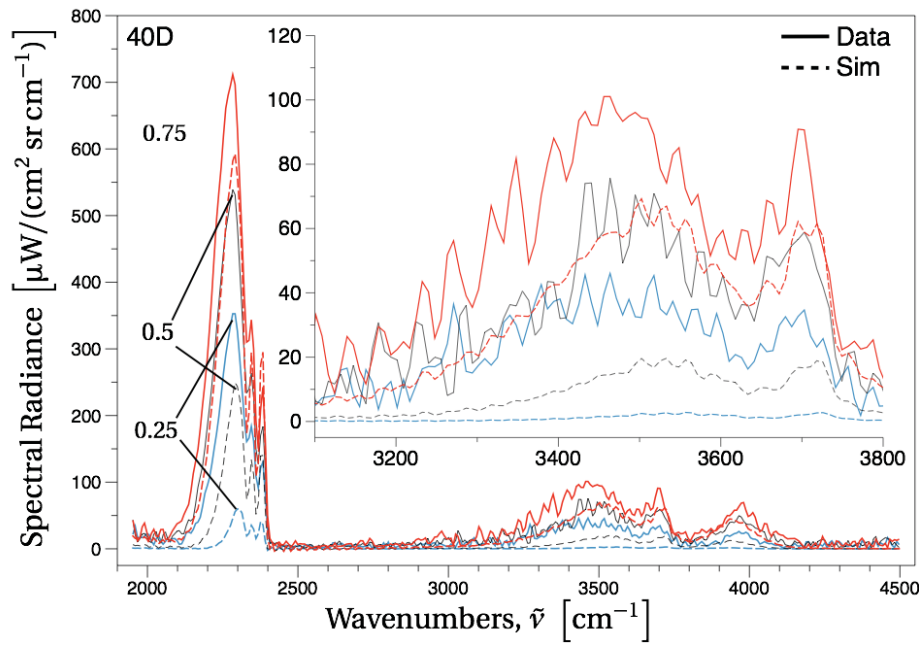
Figure B.12: Quartile sorted spectral comparison at 40 D, $r/x = 0.11$.

Figure B.13: Quartile sorted spectral comparison at 60 D, $r/x = 0.11$.

133

Figure B.14: Radial integrated intensity profile at 20 D.

Figure B.15: Radial integrated intensity profile at 40 D.

134

Figure B.16: Radial integrated intensity profile at 60 D.

Figure B.17: Mean radial integrated intensity profiles at 20 D, 40 D and 60 D.

135

Appendix C: Expanded analysis and results from scalar retrievals

THE analysis found in this appendix is supplemental to the retrieval results presented in Chapter 5. The remaining scalar profiles for both the s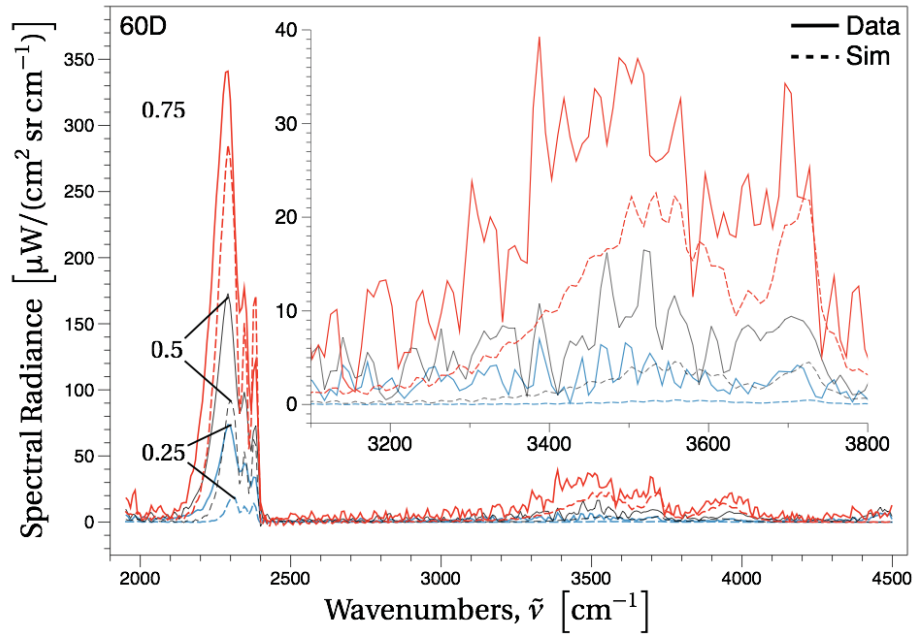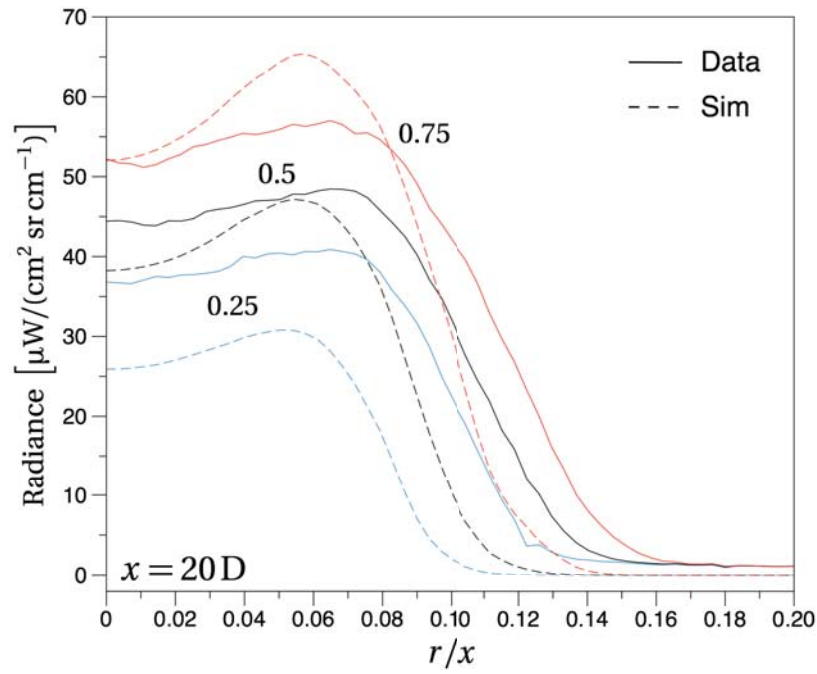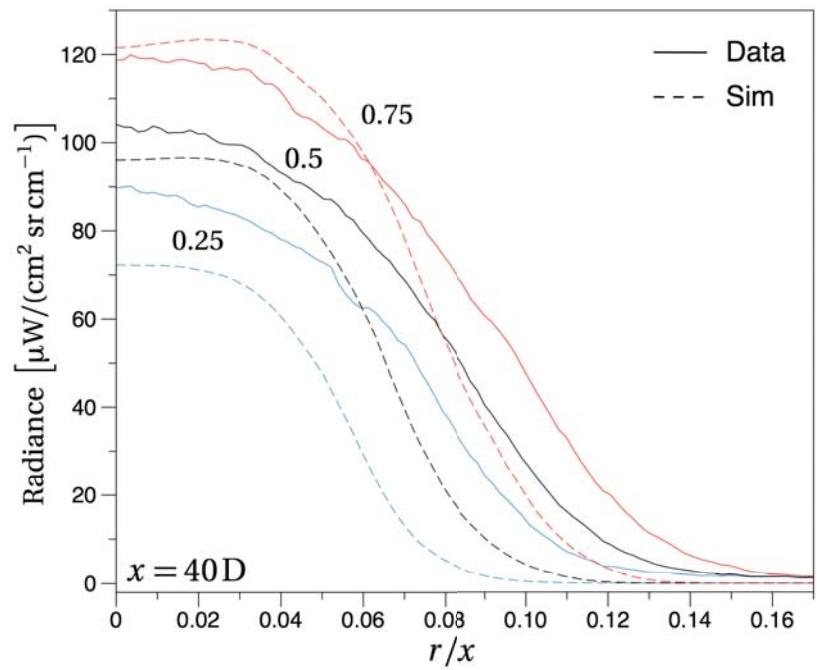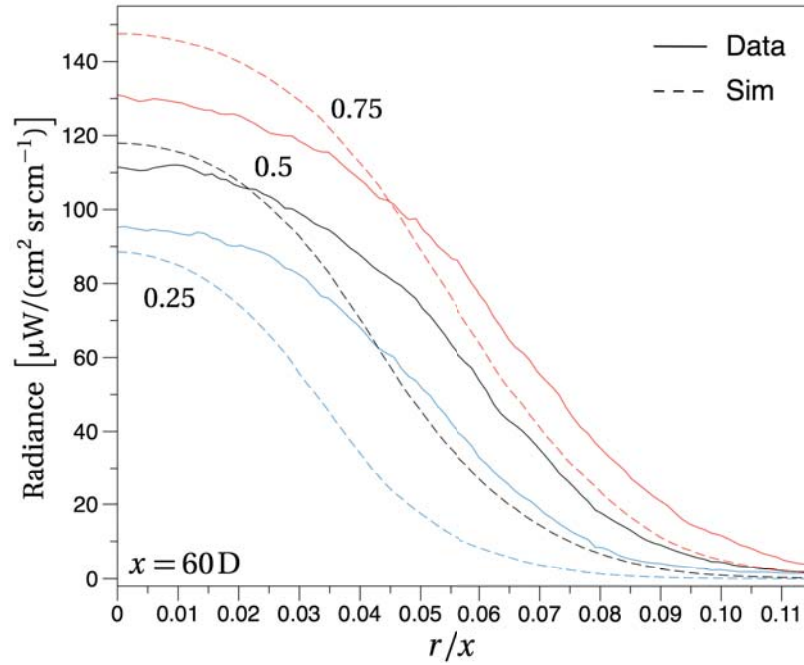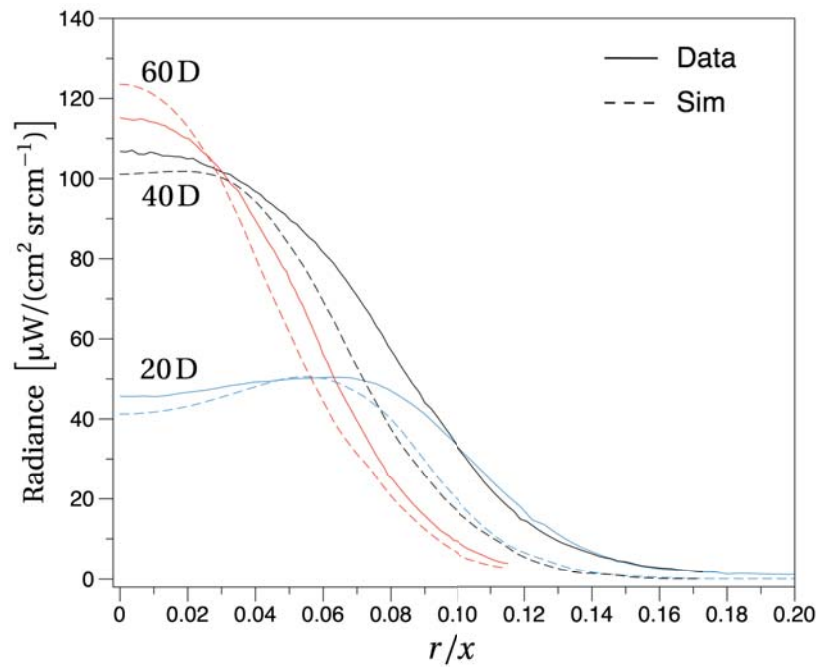tationary and turbulent spectra are presented as well as several brief parametric studies. As has been pointed out, the computational load for much of this work was significant, and any additional parametric studies which involved complete profile fits needed to be scoped very deliberately.

C.1 Additional stationary LOS scalar retrievals

The remaining scalars retrieved from the simulated stationary LOS spectra at $40\,D$ are presented in Figure C.1 (solid lines) and compared to the sorted TASS scalars (dashed lines). The strong spikes seen in the H_2O near the edges are not fully understood, but it is possible they are related to lower intensity at the edges. These results extend to $5\,cm$ for all three quantiles and were not specifically cropped at a unique temperature and intensity value. The improved results at $q = 0.75$ further establish this possibility. The erratic H_2O behavior does correspond to the same region where the CO_2 profile in Figure 5.3 displayed similar behavior and appears to be correlated. The profiles for CO—in regions with any appreciable concentration—match particularly well, with the exception of the disagreement at center of approximately for $q = 0.25$ and 0.50, respectively. The CH_4 displays odd behavior at $r = 0$, particularly for the 0.5 quantile where it drops to zero. This seems particularly odd considering the $r = 0$ spectrum at $40\,D$ has a very obvious CH_4 feature.

C.2 Additional quantile sorted scalar retrievals

The remaining scalars fit during the simulated turbulent quantile spectral retrievals are presented in Figures C.2–C.4 for $20\,D$, $40\,D$ and $60\,D$, respectively. Again, results (solid lines) are compared to the sorted TASS scalars (dashed lines). As with Figures 5.8 and 5.10, points below $500\,K$ and $1000\,\mu W/(cm^2 sr)$ were considered unreliable and omitted

from the plots. Results are generally not as good as those for temperature and CO_2, and this can be expected as those two scalars are the most correlated with LOS intensity.

In Figure C.2 (20 D), both H_2O and CO results are erratic at flame center and edge. This is consistent with the retrieved temperature and CO_2 estimates at this height, as seen in Figures 5.8 and 5.10. The behavior seen here is more erratic, where the scalars are less correlated with the LOS intensity. The retrieved CH_4 profiles are well below the known values from $r = 0$ to 1 cm at 20 D, where the feature is most prominent. It is known the CH_4 spectroscopic lines are not accurate for high temperatures in the model, but this is a model to model inversion and should not have an adverse effect on concentration estimates. It is possible these results are impacted by the 16 cm^{-1} resolution. The convolution of CH_4 and H_2O lines above 3000 cm^{-1} may have an adverse effect on fit results.

Results improve with height (an increase in signal), as seen in Figure C.3 (40 D). In all cases the fits have improved. H_2O again shows fluctuations near edge, but not to the degree seen at 20 D. The CO fits improve as well, with a drift upward near center, but again more accurate than the 20 D results. The fluctuations near edge are mostly in regions of little to no species concentration. The CH_4 results for $q = 0.25$ smoothly reproduce the curve of the data, even at center and edge. The $q = 0.50$ and 0.75 are not as accurate, but are both an improvement over the results at 20 D.

The retrieval results for H_2O seen in Figure C.4 (60 D) display similar behavior to that seen in the CO_2 profiles from Figure 5.10. The plots show the trends of the data, but oscillate about the dashed lines beyond approximately 2 cm. The addition of smoothing constraints to the retrieval algorithm could alleviate this behavior and further improve results. Aside from the excessive dip in concentration at $q = 0.5$, $r = 0$, the CO retrievals reproduce the data in regions where CO concentration is found. Considering the trace amounts of CH_4 found at this height and the 16 cm^{-1} spectral resolution, the retrieval results for the species can be considered reasonable.

C.3   Parametric studies

C.3.1   Spectral resolution effects.

A set of scalar profiles retrieved from $4.0\,\text{cm}^{-1}$ quantile spectra at 40 D are presented in Figure C.5. Considering the increase in processing time for this type of analysis, essentially equivalent to the factor increase in spectral resolution, careful consideration must be taken as to the most ideal spectral resolution. The temperature and CO_2 results are essentially equivalent to those seen in Figures 5.8 and 5.10. This is not surprising considering the dominant CO_2 feature is clearly resolved even at $16\,\text{cm}^{-1}$ and greatly influences those two scalar estimates. However, both H_2O and CO results are also largely unaffected by the improved spectral resolution. CO RMS values are identical to those found from the $16\,\text{cm}^{-1}$ results, and the H_2O RMS values only improve from 0.025, 0.018 and 0.023 to 0.020, 0.017 and 0.019 for $q = 0.25$, 0.50 and 0.75, respectively. The CH_4 results are improved for $q = 0.50$ and 0.75, with a factor of two improvement to the RMS values. But the $q = 0.25$ RMS actually increases from 0.004 to 0.006. Considering the increased processing time required for this higher spectral resolution, these results do not indicate the increased spectral resolution is warranted. Additional studies are likely needed to determine the optimal spectral resolution to return acceptable results in an acceptable time frame.

C.3.2   Noise effects.

To test the robustness of the algorithm under several noise conditions, another inversion study was performed on three spectral conditions. The spectra presented in Figure C.6 are samples of the fit spectra at $r/x = 0$, with RMS noise levels of 0 %, 5 % and 23 %. The same level of artificial noise was applied across a given set of spectra, from center to edge, in the manner described in Chapter 5. Temperature profile results of the inversions are presented in Figure C.7. The results are negatively impacted with the increase in artificial noise, but temperature profiles are retrieved in all cases. At all three quantiles there is an

average RMS increase of 28 % for the noise increase from 0 % to 5 %, and an average RMS increase of 92 % for the noise increase from 5 % to 23 %. Additional noise studies are needed to more completely test the algorithm, but these results indicate it can retrieve profiles under significant noise conditions.
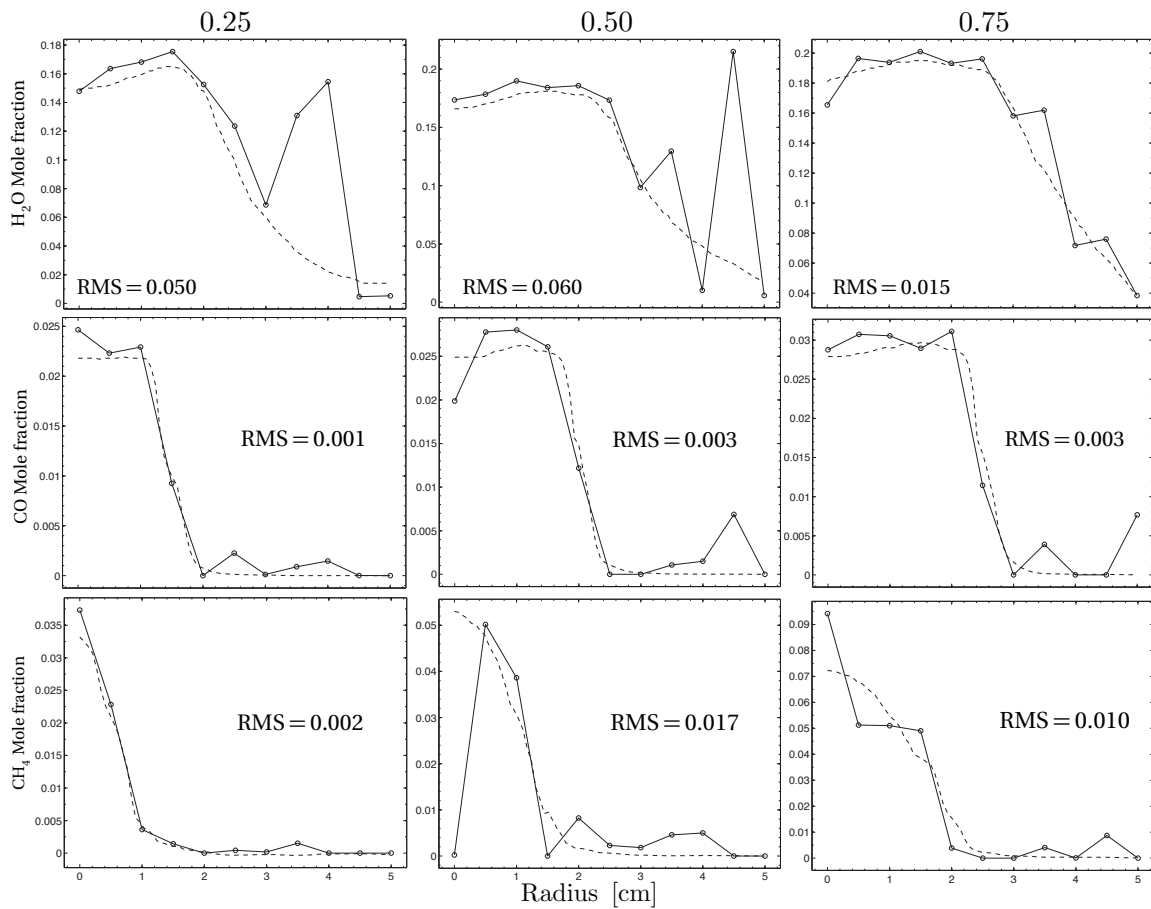
Figure C.1: Remaining scalar sort retrieval (stationary LOS) results at 40 D for the three quantiles. (RMS values in y axis units)
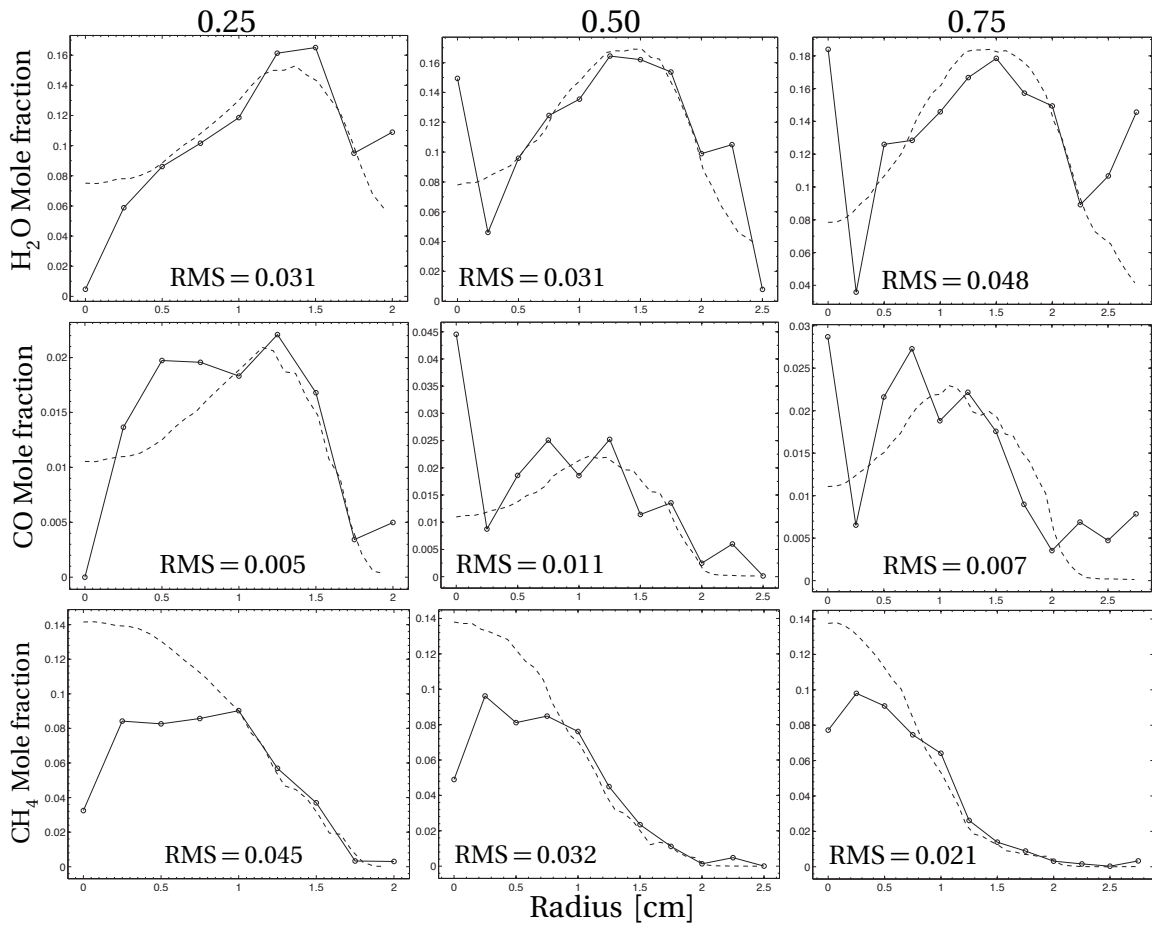
Figure C.2: Radial profiles of input (dashed) and retrieved (solid) turbulent quantile H_2O, CO, and CH_4 mole fractions at 20 D. (RMS values in y axis units)
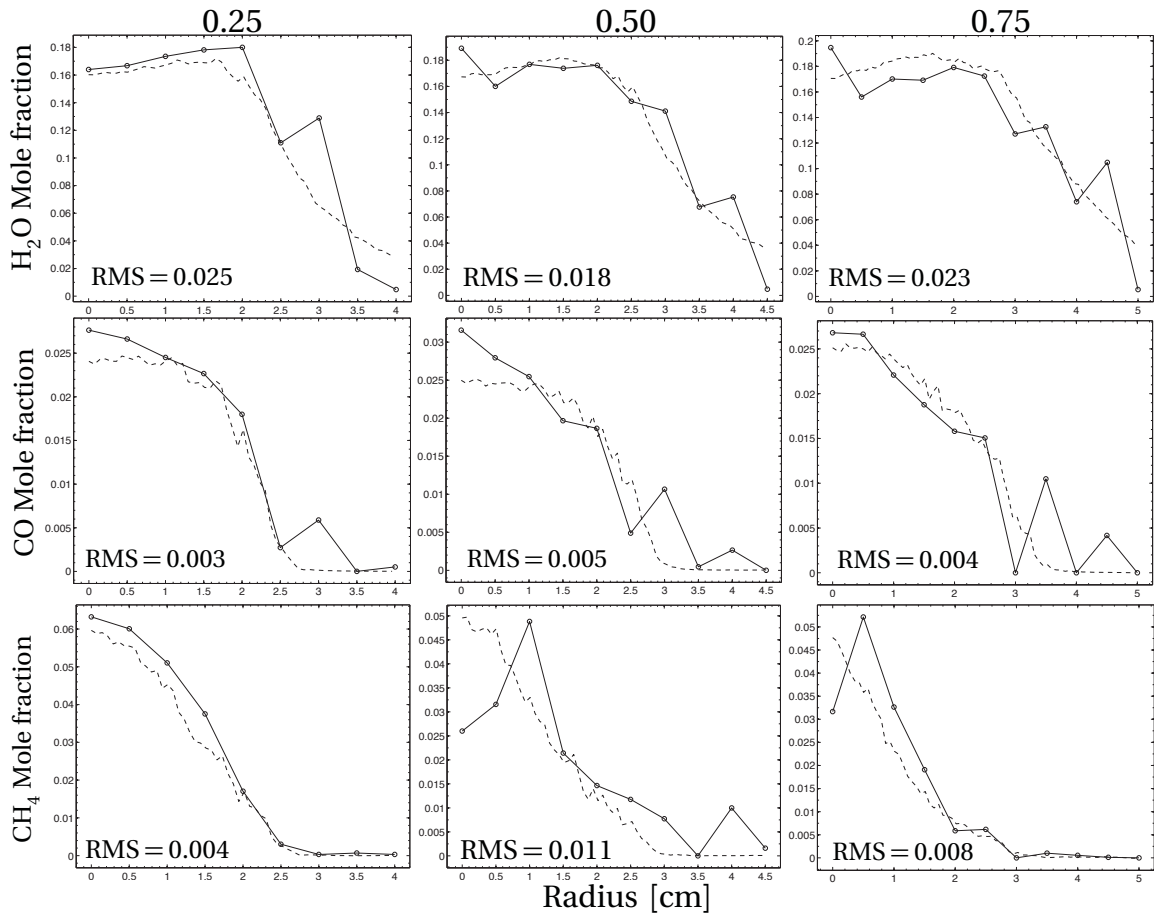
Figure C.3: Radial profiles of input (dashed) and retrieved (solid) turbulent quantile H_2O, CO, and CH_4 mole fractions at 40 D. (RMS values in y axis units)
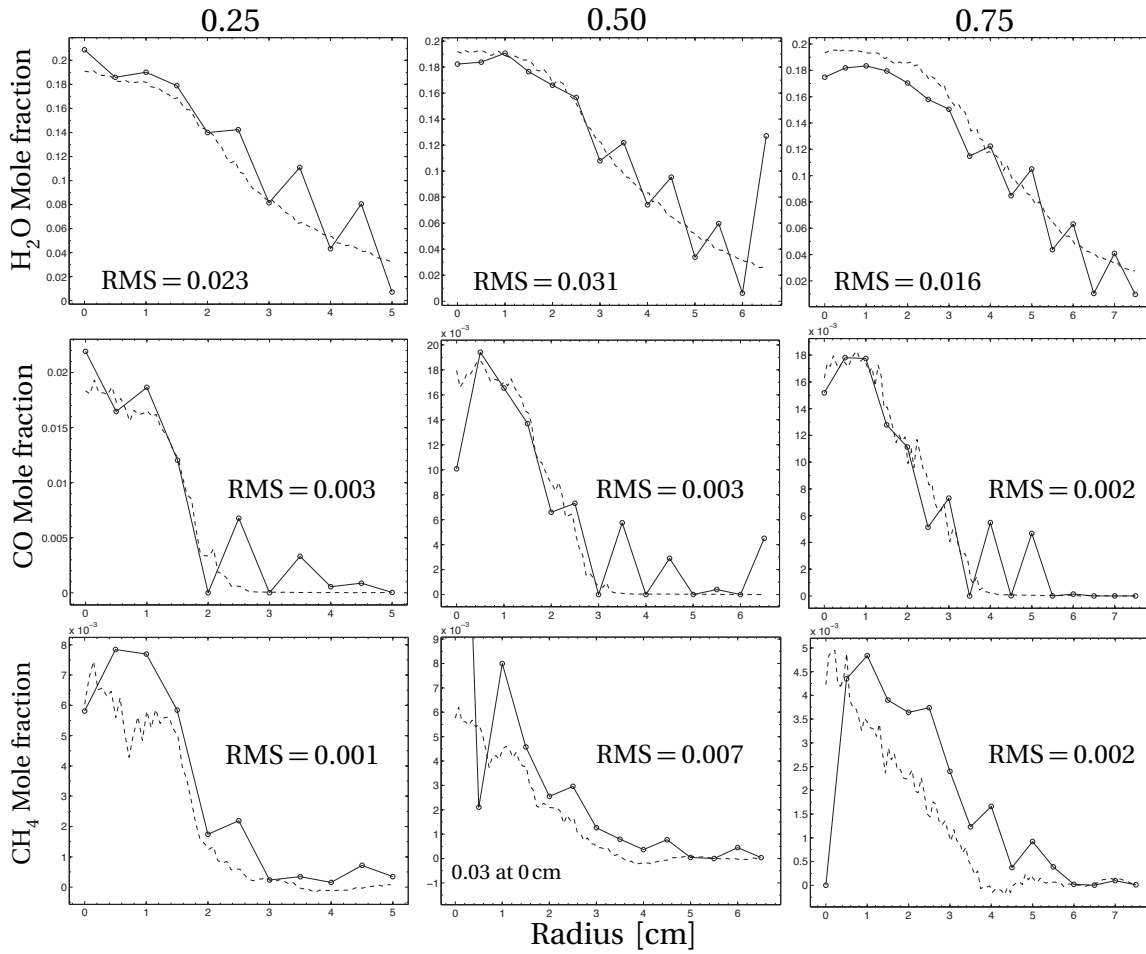
Figure C.4: Radial profiles of input (dashed) and retrieved (solid) turbulent quantile H_2O, CO, and CH_4 mole fractions at 60 D. (RMS values in y axis units)
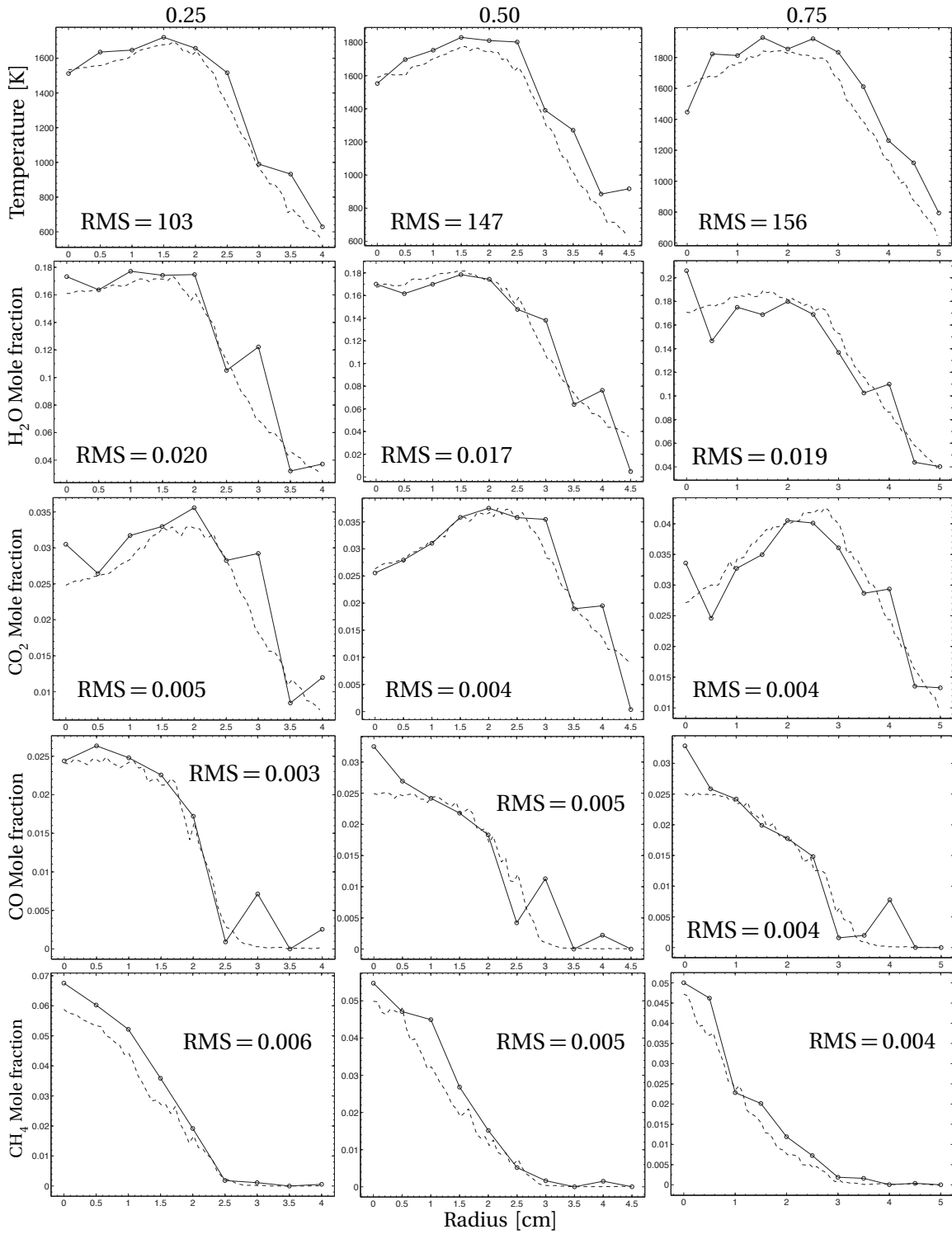
Figure C.5: Retrieved 0.25, 0.50, and 0.75 quantile scalars from simulated $4.0\,\mathrm{cm}^{-1}$ spectra at 40 D. (RMS values in y axis units)
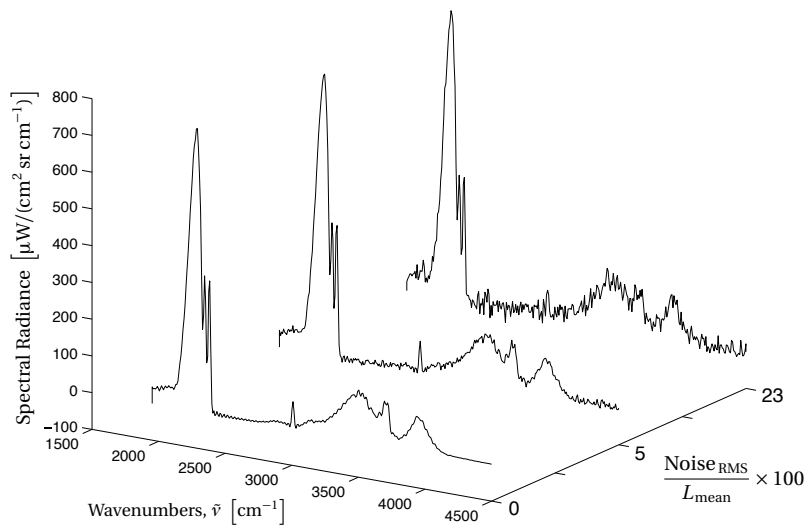
Figure C.6: Simulated spectra with various levels of artificial noise.
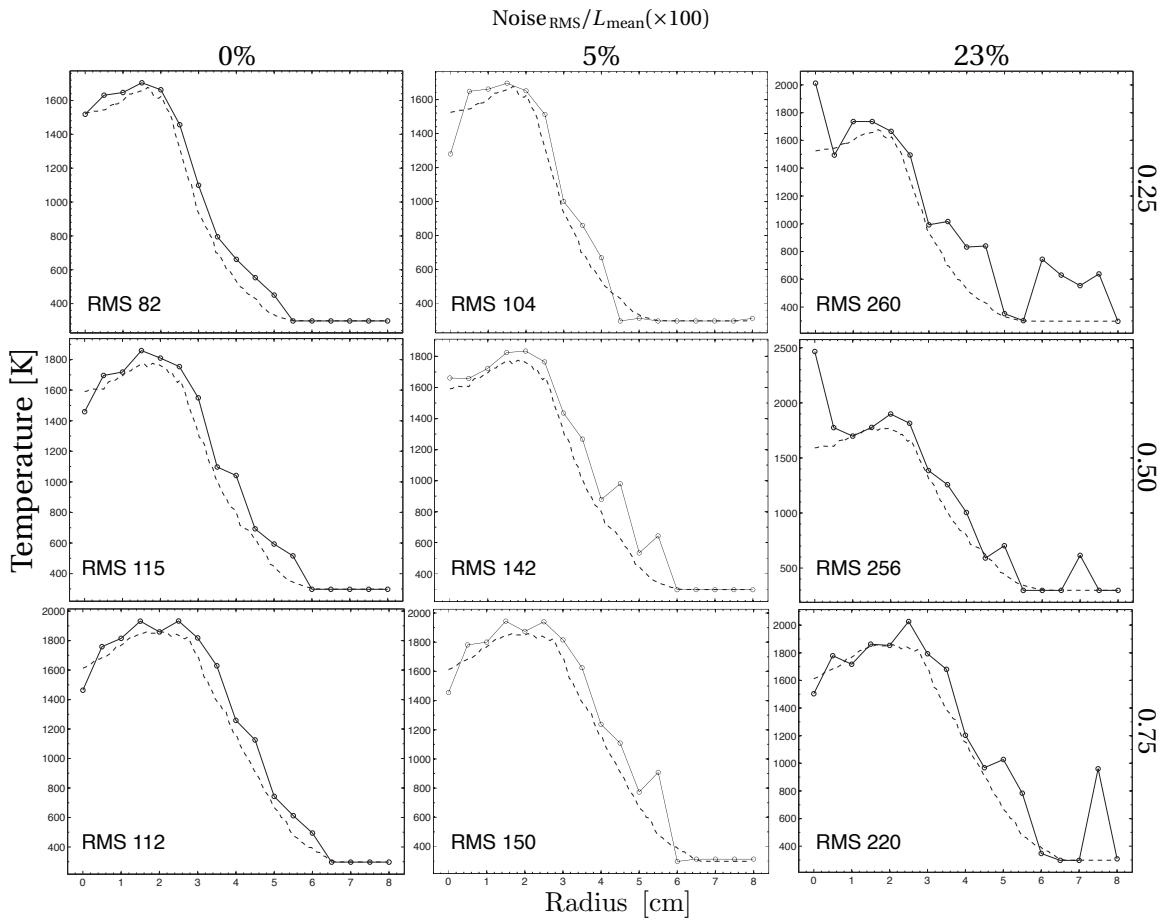
Figure C.7: Temperature retrievals under various spectral noise conditions. (RMS values in y axis units)

Appendix D: Imaging Fourier-transform spectrometry for plume diagnostics and code validation

THE following is a published, peer reviewed journal article from the International Journal of Energetic Materials and Chemical Propulsion presented in its entirety. As a coauthor for this paper I acted as an editor and contributed discussion, experimental data, and analysis. Specifically, I was responsible for the experiment and data capture used in the jet engine quantile discussion and the experiment, analysis, and discussion for the velocity feature tracking. This work explores some of the early analysis of radiative transfer and quantile interferogram analysis for turbulent flows.

D.1   Abstract

Laminar and turbulent flow fields found in smokestacks, flames, jet engine exhaust, and rocket plumes are of practical and academic interest and could greatly benefit from spatially-resolved spectral measurements. Key physical flow field parameters such as temperature and species concentrations can be extracted from spectral observations. Spectral images of flow fields produce rich information for plume diagnostics and could be used to validate next-generation plume codes. Laser-based diagnostics are typically used to measure temperatures, concentrations, and flow velocities. Unfortunately, these laser-based techniques are largely confined to a laboratory environment, and tracking multiple species concentrations is complicated due to the limited bandwidth of tunable laser sources. The advantage of a passive sensor with high resolution across a broad bandwidth would make an imaging Fourier-transform spectrometer (IFTS) an attractive instrument for flow diagnostics, particularly when the flow field of interest cannot be studied in a laboratory. In this paper, we present an overview of IFTS and its uses for flow visualization and

combustion diagnostics in various plumes. Examples from recent measurements of laminar flames and jet engine exhaust will be presented.

D.2 Introduction

Laminar and turbulent flow fields emanating from smokestacks, flames, jet engines, and rockets are of practical and academic interest and could benefit from spatially-resolved spectral measurements. Spectral emissions encode important flow field parameters such as temperature, density, and species concentrations. Laser-based diagnostics are typically used to measure these parameters [38]. However, such techniques are a challenge to set up and are limited to a laboratory environment. The limited bandwidth of tunable laser sources makes tracking multiple species concentrations difficult. The advantage of a passive sensor with high resolution across a broad bandwidth would make imaging Fourier-transform spectrometry (IFTS) an attractive instrument for flow diagnostics, particularly when the flow field of interest cannot be studied in a laboratory. In this paper, we present an overview of IFTS and its uses for flow visualization and combustion diagnostics in various plumes. Examples from recent measurements of a laminar flame [58] and jet engine exhaust [7, 9, 32, 49, 71] will be presented.

D.3 Instrumentation

We have looked at various high-temperature laminar and turbulent flow fields using a Telops Hyper-Cam interferometer [12, 23]. This IFTS features a high-speed 320 × 256 pixel InSb ($1.5-5.5\,\mu$m, 2 kHz full-frame) focal-plane array (FPA). Sequential scene imagery focused on the FPA is collected while looking through a scanning Michelson interferometer. The interferogram cube is thus a stack of broad-band infrared images collected at fixed optical path differences (OPDs). Acquisition rate depends on spectral resolution and mirror speed, which in turn is affected by spatial resolution and camera integration time.

147

An ideal Michelson-based IFTS produces (at each pixel) an interferogram $I(x)$ represented by

$$I(x) = \frac{1}{2} \int_0^\infty (1 + \cos(2\pi x\tilde{\nu})) G(\tilde{\nu}) (L_s(\tilde{\nu}) + L_i(\tilde{\nu})) \, d\tilde{\nu} = I_{DC} + I_{AC}(x)$$

where x is the optical path difference, $L_s(\tilde{\nu})$ is the scene spectrum, $L_i(\tilde{\nu})$ are spectral emissions from within the instrument, and $G(\tilde{\nu})$ is the spectral system response which includes the quantum efficiency of the detector. Here, I_{DC} represents the integrated intensity and $I_{AC}(x)$ is the cosine transform of the (uncalibrated or raw) spectrum. Fourier-transformation of $I(x) - I_{DC}$ yields the raw spectrum. This implicitly assumes the source spectrum is stationary over the course of the measurement. For laminar flow, this is typically true. However, the case of turbulent flow in which $L_s(\tilde{\nu})$ may rapidly and stochastically change throughout an interferometric measurement is addressed in Section D.4.2.

Two on-board blackbodies permit linear calibration to remove the effects of detector response $G(\tilde{\nu})$ and instrument self-emission $L_i(\tilde{\nu})$. A schematic of an IFTS is presented in Figure D.1. Also shown are an example interferogram for a single pixel and its corresponding spectrum upon Fourier-transformation.

D.4   Theory

D.4.1   Radiative transfer for ideal turbulent flow.

The spectral radiance $L(\tilde{\nu})$ from a non-scattering source in local thermodynamic equilibrium along a length l LOS can be expressed as [69]

$$L(\tilde{\nu}) = \int_0^l e^{-\tau(s)} \kappa(\tilde{\nu}, s) B(\tilde{\nu}, T(s)) \, ds \qquad (D.1)$$

where $\tau(s) = \int_s^l \kappa(\tilde{\nu}, s') \, ds'$ is the optical depth, $\kappa(\tilde{\nu}, s)$ is the absorption coefficient, and $B(\tilde{\nu}, T)$ is Planck's blackbody distribution at temperature T. The term $\kappa(\tilde{\nu}, s)B(\tilde{\nu}, T(s))$ accounts for photons "born" at the point s along the LOS, and $e^{-\tau(s)}$ accounts for the fraction of those photons absorbed as they travel through the remaining plume towards the source.
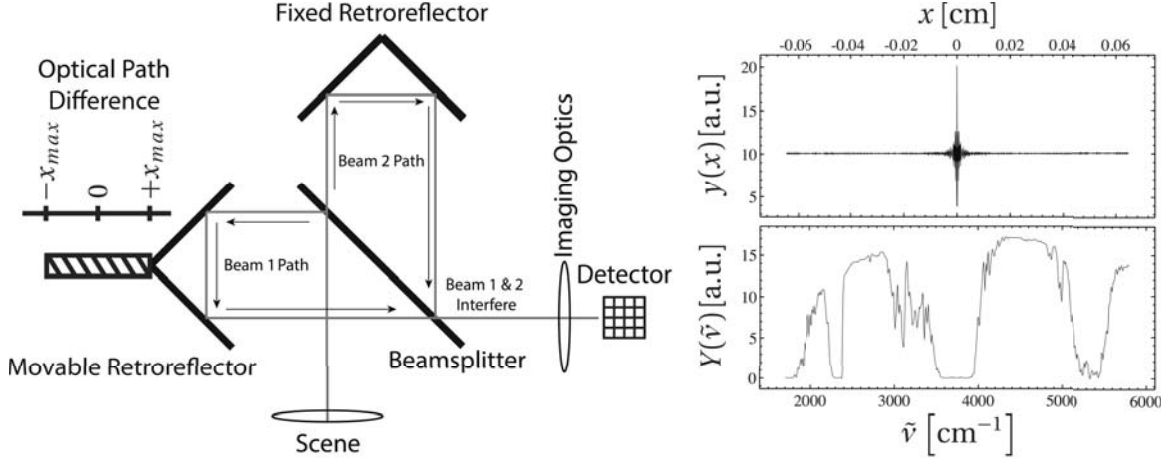
Figure D.1: *Left panel*: Schematic of an imaging Fourier-transform spectrometer. An interference pattern is measured at the focal-plane array detector by varying the phase between the two light beams via the movable retroreflector. *Right panel*: Illustration of an single-pixel interferogram (top) and its corresponding spectrum (bottom) upon Fourier-transformation.

The dependence of κ on both $T(s)$ and species concentrations $\vec{\xi}(s)$ was suppressed. For an ideal, high-temperature, two-dimensional flow field which is homogeneous along the LOS, Eq. D.1 can be approximated by

$$L(\tilde{v}, T) = \tau(\tilde{v})\varepsilon(\tilde{v}, \vec{\xi}, T)B(\tilde{v}, T) \qquad (D.2)$$

where the source emissivity ε is defined by $\varepsilon(\tilde{v}, \vec{\xi}, T) = 1 - e^{-\kappa(\tilde{v})l}$ and $\tau(\tilde{v})$ represents the transmittance of the material (atmosphere) between the source and instrument. This model assumes the plume radiance dominates all other sources (e.g., photons emitted behind or in front of the plume).

In this work, spectra are modeled using the Line-by-Line Radiative Transfer Model (LBLRTM) [14] in conjunction with the high-temperature extension (HITEMP [61]) to the HITRAN database [62] of spectroscopic line parameters.

Note that at all wavenumbers $\tilde{v}$, Planck's distribution $B(\tilde{v}, T)$ monotonically increases with temperature. Additionally, for many gas-phase systems in local thermodynamic equilibrium, this monotonicity is preserved, so we assume $T_2 > T_1$ implies $L(\tilde{v}, T_2) > L(\tilde{v}, T_1)$ for all $\tilde{v}$.

In a non-reactive turbulent flow field, the instantaneous temperature T fluctuates about a mean temperature $\langle T \rangle$ according to a probability distribution $P(T)$ [44]. Uncorrelated fluctuations in $\vec{\xi}$ may also occur, but are ignored[1]. For an ergodic flow field, the average of an ensemble of spectral measurements yields

$$\langle L(\tilde{v}, T) \rangle = \int L(\tilde{v}, T) \, P(T) \, \mathrm{d}T \neq L(\tilde{v}, \langle T \rangle) \tag{D.3}$$

where the non-equality arises due to the nonlinear dependence of L on T. To properly interpret $\langle L(\tilde{v}, T) \rangle$, *a priori* knowledge of $P(T)$ would be required and simply fitting a single-T model to it necessarily results in biased temperatures and species concentrations. To address this problem we now consider flow measurement made by an interferometer.

D.4.2 *Quantile interferogram analysis for a two-dimensional turbulent flow field* .

Dynamic scenes are often considered problematic for IFTS as changes in scene radiance during the interferometric scan produce scene-change artifacts (SCAs) in the spectrum. While time averaging can minimize the effects of this "source noise," an alternate method is presented which, in addition to minimizing SCAs, can provide additional information about the fluctuation statistics in the flow field. In the case of two dimensional turbulent flow which is dominated by temperature fluctuations and is homogeneous along the instrument's LOS, temperature fluctuation statistics can be recovered.

To simplify the presentation, we assume an instrument response of unity and ignore instrument self emission. Under these conditions, an ideal Michelson produces an

---

[1]If concentration fluctuations are significant, the one-to-one mapping of quantile spectra to unique temperatures to be described may not be valid. However, multiple quantile spectra do contain information complementary to and different from the mean spectrum.

interferogram $I(x_i, T_i)$ at each OPD x_i of the turbulent flow via

$$I(x_i, T_i) = \int \left(1 + \cos(2\pi x_i \tilde{\nu})\right) L(\tilde{\nu}, T_i) \, \mathrm{d}\tilde{\nu} \tag{D.4}$$

where T_i represents a random sample from $P(T)$ and is assumed constant over the short FPA integration time. With a FPA, the DC component is preserved, and this is key to the following development. Recall that $L(\tilde{\nu}, T)$ is a monotonic function of temperature at all $\tilde{\nu}$. Since $1 + \cos(2\pi x_i \tilde{\nu}) \geq 0$ for any x_i and all $\tilde{\nu}$, it follows that $T_2 > T_1 \rightarrow I(x_i, T_1) > I(x_i, T_2) \, \forall x_i$. If an ensemble of interferometric measurements of the ergodic flow field are captured, then at each x_i, a range of temperatures weighted by $P(T)$ will have been observed. As the chain of probabilities demonstrates, the monotonicity of $L(\tilde{\nu}, T)$ permits sorting the ensemble of measured $I(x_i)$'s into various quantiles

$$q = \mathbb{P}\left\{T \leq T_q\right\} = \mathbb{P}\left\{L(\tilde{\nu}, T) \leq L(\tilde{\nu}, T_q)\right\} = \mathbb{P}\left\{I(x_i, T) \leq I(x_i, T_q) \equiv I_q(x_i)\right\} \, \forall x_i \tag{D.5}$$

where T_q is the qth quantile, $\mathbb{P}\{\_\}$ denotes probability of the argument, and $I_q(x_i)$ defines the "quantile interferogram". So long as a sufficient number of measurements are made to enable robust quantile estimates, $I_q(x_i)$ is a valid interferogram corresponding to the spectrum $L_q(\tilde{\nu}) \equiv L(\tilde{\nu}, T_q)$.

The limitation to an unrealistic two-dimensional flow field may appear to limit the utility of this technique. However, the sorting of interferograms can still be performed to yield quantile spectra. These quantile spectra contain information which is complementary to and distinct from the mean spectrum. An example from an axi-symmetric jet is presented in Section D.5.2 and demonstrates this point.

D.4.3 *Extraction of moderate-speed imagery from interferometric measurements*

.

The Michelson interferometer encodes spectral information via intensity variations (as represented by the cosine term in Equation D.4). These variations occur at a frequency greater than $f = v_m \tilde{\nu}_d$ where v_m is the mirror scan velocity and $\tilde{\nu}_d$ is the lowest frequency

photon ($\tilde{\nu}_d \sim 1700\,\mathrm{cm}^{-1}$) that the camera detects. Thus, a temporal low-pass filter can be applied to the interferogram cube yielding moderate-speed imagery. Also, if there are broad regions in which no spectral emissions are observed, a temporal band-pass filter can be applied to recover imagery (with no DC level) at higher frame rates. The mirror scan velocity varies with spatial resolution and camera integration time.

A specific example illustrates the differences between camera and spectral image acquisition rates. For a window size of 48×156 pixels and an integration time of $5\,\mu s$, the camera in the IFTS acquires images at nearly $10\,\mathrm{kHz}$ as the Michelson assembly continuously varies the optical path difference (OPD) between interfering beams. Each image corresponds to a change in OPD of $632.816\,\mathrm{nm}$ [2], and in this instrument configuration, the mirror speed is $0.64\,\mathrm{cm \cdot s^{-1}}$. To achieve spectral images at $1.5\,\mathrm{cm}^{-1}$ between $1700\,\mathrm{cm}^{-1} < \tilde{\nu} < 6667\,\mathrm{cm}^{-1}$ requires approximately $12,500$ sequential images collected between $-0.4\,\mathrm{cm} < \mathrm{OPD} < 0.4\,\mathrm{cm}$. The spectral image is thus acquired at $0.8\,\mathrm{Hz}$. While the camera frames at $10\,\mathrm{kHz}$, intensity modulations at frequencies greater than $f = 1700\,\mathrm{cm}^{-1} \times 0.64\,\mathrm{cm \cdot s^{-1}} = 1088\,\mathrm{Hz}$ could occur due to the action of the Michelson, thus the effective frame rate after low-pass imagery is approximately $1\,\mathrm{kHz}$. Broadband infrared imagery at these rates permits characterization of many types of turbulent flow.

D.5   Results & Discussion

D.5.1   Laminar flame.

To demonstrate the utility of IFTS for combustion diagnostics, measurements of a Hencken burner were recently acquired [58] and the key results are summarized here. A Hencken burner produces a nearly ideal adiabatic flame and is routinely used as a calibration standard for testing new combustion diagnostics. In a series of experiments, an ethylene (C_2H_4) / air flame was produced at various equivalence ratios [3] (Φ). Total

---

[2] A HeNe reference laser is used to trigger the camera to capture images at regular OPD intervals.

[3] The equivalency ratio is defined by the actual fuel:air ratio relative to the stoichiometric fuel:air ratio.

volumetric flow rates were between 10.9 SLPM and 17.1 SLPM. The instrument collected 1000 spectral images at $1\,\mathrm{cm}^{-1}$ resolution on a 200×64 pixel array.

The observed spectra are dominated by broadband emission from CO_2 between $2150\,\mathrm{cm}^{-1}$ and $2400\,\mathrm{cm}^{-1}$. Emission from H_2O are spectrally structured and are found between $3000\,\mathrm{cm}^{-1}$ and $4200\,\mathrm{cm}^{-1}$; weaker emissions can be found below $2000\,\mathrm{cm}^{-1}$. Spectra from fuel-rich ($\Phi > 1$) flames exhibited CO emission lines on either side of the $2143\,\mathrm{cm}^{-1}$ band center. The CO line intensities increased with Φ. An example spectrum is presented in Figure D.2.
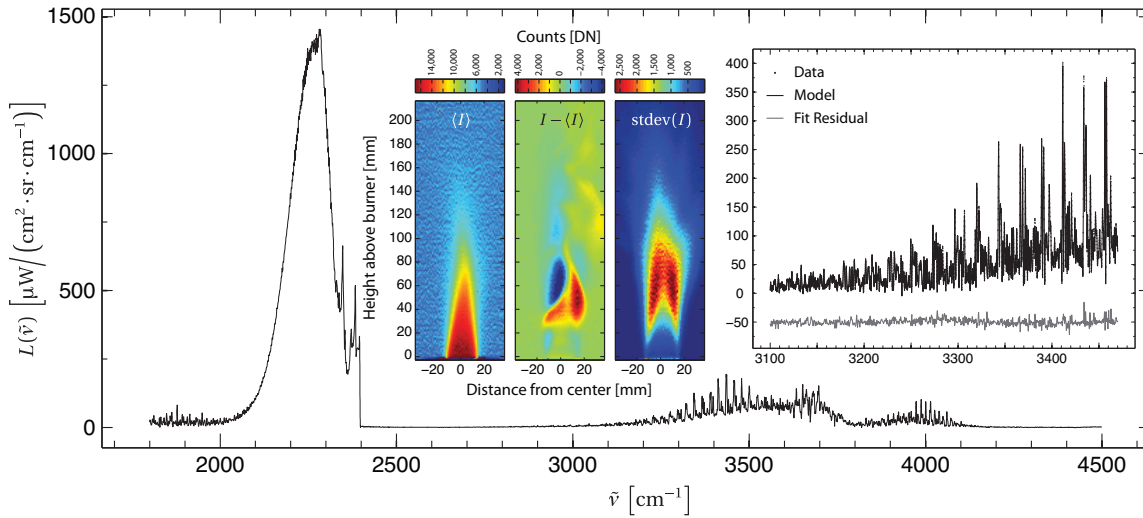
Figure D.2: Mean single-pixel spectrum of an ethylene flame centered 20 mm above the burner. The large peak at $2250\,\mathrm{cm}^{-1}$ is due to CO_2 and the structured emission between $3000\,\mathrm{cm}^{-1}$ and $4200\,\mathrm{cm}^{-1}$ is primarily due to H_2O. The inset color panels present (1) the time-averaged broadband infrared image (left), difference between an instantaneous and the mean flame image (middle), and the standard deviation of the flame intensity (right). The inset spectrum compares an ethylene center flame spectrum at 10 mm with a model fit. Fit quality can be judged by the residuals offset by $50\,\mu\mathrm{m}/\left(\mathrm{cm}^2 \cdot \mathrm{sr} \cdot \mathrm{cm}^{-1}\right)$.

High-speed imagery was extracted from the interferometric cubes (see Section D.4.3) and revealed that the flame was steady up to approximately 30 mm above the burner. Within this region, the flame is stable and nearly homogeneous with a very thin mixing layer. However, above 30 mm unsteady behavior was observed as revealed by the inset imagery in Figure D.2. The left panel provides the time-averaged flame intensity and characterizes the mean flow field. The middle panel shows the difference between an instantaneous flame intensity and the mean flame intensity. Variations up to 50% of the mean signal are evident. The standard deviation of each pixel's intensity are provided in the right panel.

Within this homogeneous portion of the flame, the radiative transfer model (Equation D.2) can be used to simultaneously retrieve temperature and species concentrations from the observed spectrum. To validate this approach, an ethylene flame measurement was taken corresponding to $\Phi = 0.91$ via fuel and air flow rates of 0.78 SLPM and 12.2 SLPM, respectively. This was to permit comparison with measurements of an identical flame studied using a tunable diode laser absorption[4] technique [47]. Flame temperature and mole fractions of H_2O and CO_2 were estimated by a nonlinear least-squares fit of Equation D.2 to the the IFTS spectrum at 10 mm above flame center. These fit parameters were adjusted using a Levenberg-Marquardt algorithm to minimize the sum of squared differences between the measured and model spectrum. The fit results were good as demonstrated in the inset spectrum of Figure D.2. The spectrally estimated temperature of $T = 2172 \pm 28$ K was in excellent agreement with the OH laser absorption temperature of $T = 2226 \pm 112$ K. Optimal concentrations for H_2O and CO_2 were $13.7 \pm 0.6\%$ and $15.5 \pm 0.8\%$, respectively, exceeding expected results by 20% according to equilibrium calculations. Relative line heights determine the gas temperature, whereas absolute line heights determine species concentrations. The good agreement in temperature suggest the relative instrument spec-

---

[4]The laser-based diagnostic measured the shape of a single hydroxy radical (OH) line to extract temperature

tral calibration is good. However, the poor agreement in concentration could be caused by a systematic error in the absolute calibration.

D.5.2 Jet engine .

Having demonstrated the applicability of IFTS to a laminar flame, we now consider the highly turbulent flow field produced by a jet engine. Rapid temperature fluctuations in the flow field produce substantial changes in the instantaneous scene spectrum during the course of an interferometric measurement. The SCAs associated with the spectrum from a single interferometric cube appear as noise. Time-averaging reduces this "source noise" and produces a recognizable spectrum. However, the quantile analysis discussed in Section D.4.2 is evaluated for its utility in reducing SCAs as well as providing information on temperature fluctuation statistics.

The exhaust plume from a Turbine Technologies SR-30 turbojet was imaged by the IFTS. The SR-30 is a small turbojet designed for educational laboratory work. A single-stage centrifugal compressor operating between 39,000–87,000 rpm delivers air to the 27 cm long × 17 cm diameter engine designed for combusting various fuels including Jet-A, JP-8, diesel, and kerosene. Maximum thrust of the SR-30 is approximately 178N with a nominal exhaust temperature of 720 °C. 800 spectra at 25 cm^{-1} were collected on a 48×156 pixel window.

The collection of interferometric measurements were sorted into quantiles $I_q(x_i)$ corresponding to $q \in \{0.159, 0.5, 0.841\}$. These quantiles correspond to the $m - \sigma$, median, and $m + \sigma$ of a normal distribution characterized by mean m and standard deviation σ. Quantile interferograms were converted to apparent radiance spectra. Plume spectra at all quantiles feature weak broadband emission between $2000-2800$ cm^{-1} with large emission features arising from thermally excited CO_2. A map of brightness temperature[5] $T_B(L_q(\tilde{v}))$ at $\tilde{v} = 2278$ cm^{-1} from the median quantile is presented in the top of Fig. D.3. The plume

---

[5]Brightness temperature is defined by $T_B(L(\tilde{v})) = c_2\tilde{v}/\log\left(1 + c_1\tilde{v}^3/L(\tilde{v})\right)$ where c_1 and c_2 are the first and second radiation constants.

155

appears fairly symmetric and spans nearly the full width of the FPA. The low-emissivity, polished metal engine appears substantially cooler. The median-quantile spectrum $L_{q=0.5}(\tilde{\nu})$ for a center pixel near the jet is also shown. The imaginary part of the spectrum is also provided and appears as noise, indicating SCAs have been minimized. (In a properly-calibrated FTS measurement of a stationary scene, the signal is contained in the real part and noise is equitably distributed among the real and imaginary parts. SCAs can be detected by examination of the imaginary part.) Kinetic temperatures could be retrieved from the spectrum using an appropriate radiative transfer model which properly accounts for the three-dimensional flow field.

At each pixel, the magnitude of temperature fluctuations can be characterized by estimating the standard deviation by differencing two brightness temperature quantiles, i.e. $\sigma_B^+(\tilde{\nu}) = T_B(L_{q=0.841}(\tilde{\nu})) - T_B(L_{q=0.5}(\tilde{\nu}))$. A map of $\sigma_B^+(\tilde{\nu})$ at $\tilde{\nu} = 2278 \, \mathrm{cm}^{-1}$ is provided in the bottom panel of Fig. D.3.

While the map represents fluctuations in brightness temperature and not the gas kinetic temperature, the two are connected through the effective spectral emissivity of the plume. Thus, this image indicates qualitatively the strength of temperature fluctuations throughout the plume and reveals asymmetry in the spatial distribution. The fluctuations are strongest at the shear layer where the hot exhaust gases turbulently mix with the cold ambient air. The wedge shaped core is also evident, and while turbulent, appears less so than at the shear layer as expected. While non-uniformities along the LOS complicate quantitative interpretation, we've demonstrated that IFTS can be used to study turbulent flows and have presented a novel method to estimate temperature fluctuation statistics.

Bulk flow field characterization is also possible as demonstrated in a separate experiment. Recently, exhaust from an F109 turbofan engine was imaged with the IFTS[32]. Examination of the time-averaged spectra from the exhaust plume indicated that the spectral region above $4200 \, \mathrm{cm}^{-1}$ was free of spectral emissions. Since the Michelson
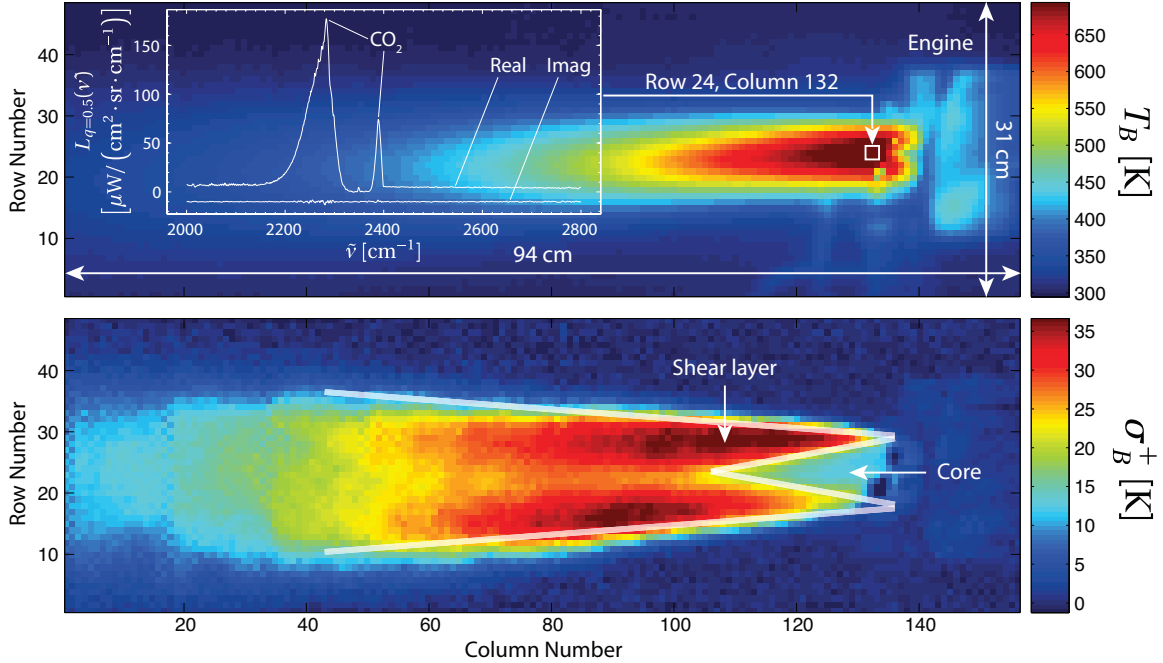
Figure D.3: *Top panel*: Brightness temperature T_B at $\tilde{\nu} = 2278\,\text{cm}^{-1}$ from the median quantile ($q = 0.5$) spectrum. The inset figure presents the spectrum for a center pixel at engine exit. *Bottom panel*: Brightness temperature standard deviation σ_B^+ estimated by differencing brightness temperatures from the $q = 0.841$ and $q = 0.5$ quantile spectra. Translucent lines are overlaid to distinguish the core and shear layers.

mirror was scanned at a speed of $0.18\,\text{cm}\cdot\text{s}^{-1}$ in this experiment, intensity variations at frequencies above $756\,\text{Hz}$ could be attributable to fluctuations in the flow field. A temporal high-pass filter (Butterworth, $756\,\text{Hz}$ cut-off) was applied to the stack of images comprising a single interferometric cube. A sequence of images is provided in Figure D.4 and reveals the dynamic flow. Turbulent eddies are observed to move down stream at a nearly constant velocity. Since the camera frame rate ($2860\,\text{Hz}$) and pixel dimensions ($0.26 \times 0.26\,\text{cm}^2$) are known, frame-by-frame tracking of one eddy provides a bulk flow velocity estimate of $181\,\text{m}\cdot\text{s}^{-1}$. This compares well to the exit velocity of $176\,\text{m}\cdot\text{s}^{-1}$ computed using measured

fuel/air mass flow rates and a thermocouple temperature measurement at the exhaust exit [32].

256 pixels, 0.26 cm/pixel   Camera frame rate: 2860 Hz
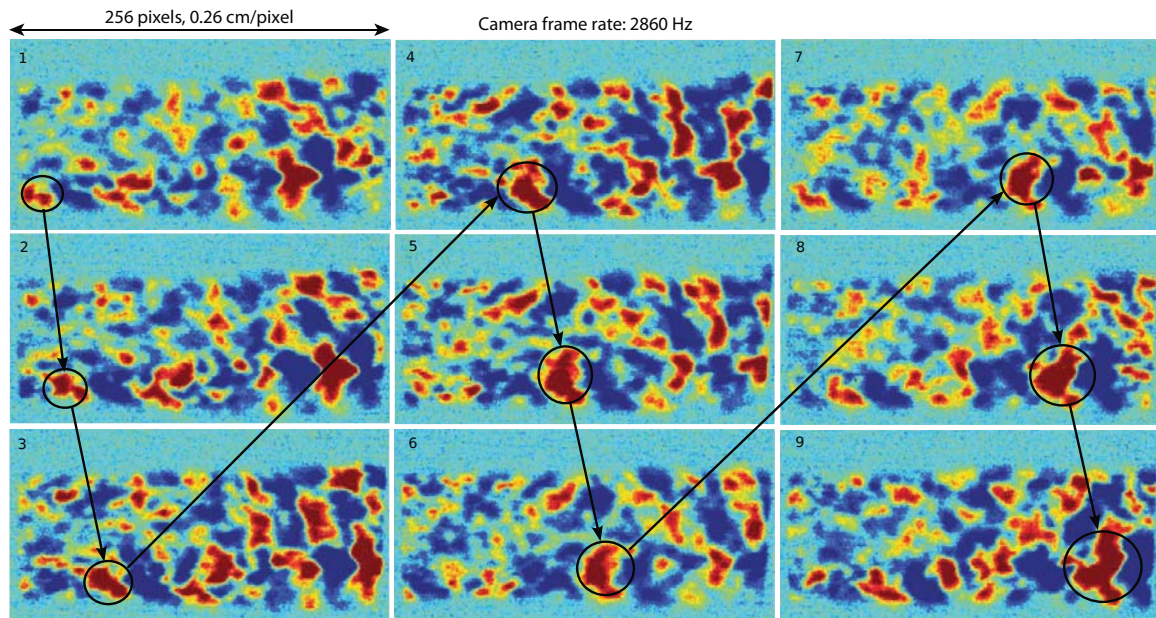
Figure D.4: Tracking turbulent eddies enables bulk flow velocity estimation as demonstrated in this sequential imagery of F109 engine exhaust. A Butterworth temporal high-pass filter with cut-off frequency of $756\,\text{Hz}$ was applied to the imagery.

D.6   Conclusions

In this paper, we've summarized recent efforts at developing IFTS for combustion and flow field diagnostics. The IFTS enables highly resolve spectra across a wide bandwidth to be captured at each pixel in an image. We've demonstrated how this enables simultaneous retrieval of temperature and multiple species concentrations. Moreover, the DC information captured by the focal-plane array in the IFTS yields high-speed, broad-band imagery "for free" enabling characterization of the bulk flow in a dynamic plume. This was used to successfully estimate bulk flow velocity from a jet engine. Additionally, the DC information permits the estimation of spectra at various total-intensity quantiles. These

quantile spectra complement the information found in the mean spectrum and enable qualitative estimates of temperature fluctuation statistics. The wealth of information that can be extracted from IFTS measurements of flow fields establishes it as a useful diagnostic tool. In particular, IFTS measurements could be used to validate predictions from next-generation plume codes.

Appendix E: Spatially resolved infrared spectra of jet exhaust from an F109 turbofan engine

Tʜɪs conference proceeding is presented in its entirety. It summarizes analysis of a turbofan engine exhaust via IFTS. The effort was an early attempt to demonstrate the feasability of IFTS as a combustion diagnostics tool. It presents temperature estimates and species volume mixing fractions (computed assuming a homogeneous flow) and leverages interferometric imagery to estimate the velocity of a turbulent feature.

E.1 Abstract

There is a strong interest in diagnosing engine performance problems and maintenance needs using optical techniques instead of expensive, time-consuming mechanical inspection. A Telops Hyper-Cam MWIR imaging Fourier-transform spectrometer collected spectrally-resolved images of jet exhaust from an F109 turbofan engine operating at 53 %, 82 %, and 88 % of maximum RPM. This work attempts to discern what information content about the turbulent jet flow field is revealed in the measured spectra. The spectrum is examined and simulated, a radial and axial temperature mapping of the plume is presented, and a turbulent temporal and spatial analysis method is demonstrated. Spectral simulation of a pixel centered at nozzle exit finds volume mixing fractions of 3.3 % H_2O and 2.8 % CO_2 and an exhaust temperature of 560 K with the engine at 82 %. A single, high frequency turbulent feature is mapped and tracked over several frames. Velocity of this feature, based on the 2.85 kHz camera frame rate and 0.067 cm^2 per pixel spatial resolution, is approximately 176 m/s and compares favorably with an estimate based on the measured mass flow rate. This effort is a proof of concept and intended to justify qualitative analysis of a more controlled and characterized turbulent source in future work.

E.2 Introduction

Combustion diagnostics can be useful in the development and maintenance of aircraft engines, but it can be difficult to accurately measure and determine the required parameters due to the harsh environment inherent in the very nature of combustion. Traditional invasive methods which involve direct measurement within the flow can be difficult, and sometimes a non-invasive approach may be preferred. Various applied combustion diagnostic techniques have been applied in this field [38], but due to its relatively recent maturation imaging Fourier-transform spectroscopy has not been attempted. Laser based remote methods have successfully been used to experimentally determine some of the most basic features such as temperature, concentrations, flow velocities, temporal and spatial fluctuations [38]. In separate instances, Imaging Fourier-transform spectroscopy (IFTS) has been shown to potentially have the capability to determine many of these basic features [28, 30, 43].

Due to its wide spectral band and high spectral resolution, Fourier-transform spectroscopy (FTS) has been employed as an optical remote sensing tool for quite some time [76]. With the recent advent of the imaging capability, IFTS can go beyond temperature and species identification (and concentration estimation) in a small subsection of a plume. The very nature of the focal plane array (FPA) provides a spatial facet which lends itself well to flow field analyis. The generation of an interferogram at every pixel on the array allows for analysis across a wide spectral band throughout a given exhaust plume. A spatial map of this sort can be used to examine temperature and species profiles as they evolve radially and axially. In addition, the combination of interferometer and IR imager allows for temporal examination of a plume, leading to velocity and turbulence analysis [73]. IFTS has been used to determine temperature, species concentrations, and flow velocity of industrial smokestack plumes[30, 72]. Additionally, spatial and

temporal fluctuations were analyzed and the potential for turbulence analysis via IFTS was demonstrated [28, 30, 43].

In this work, a Telops Hyper-Cam midwave infrared (MWIR) IFTS is used to observe the exhaust of an F109 turbofan jet engine at various operating speeds. The datasets are qualitatively analyzed to determine the feasability of IFTS as a comprehensive combustion diagnostic tool. Specifically, the data is examined for the possibilities of species identification and concentration estimation, temperature estimation and mapping, and turbulent temporal and spatial analysis. This work is intended solely as a proof of concept and lays the groundwork for future projects involving qualitative analysis of a much more characterized turbulent source.

E.3 Experimental

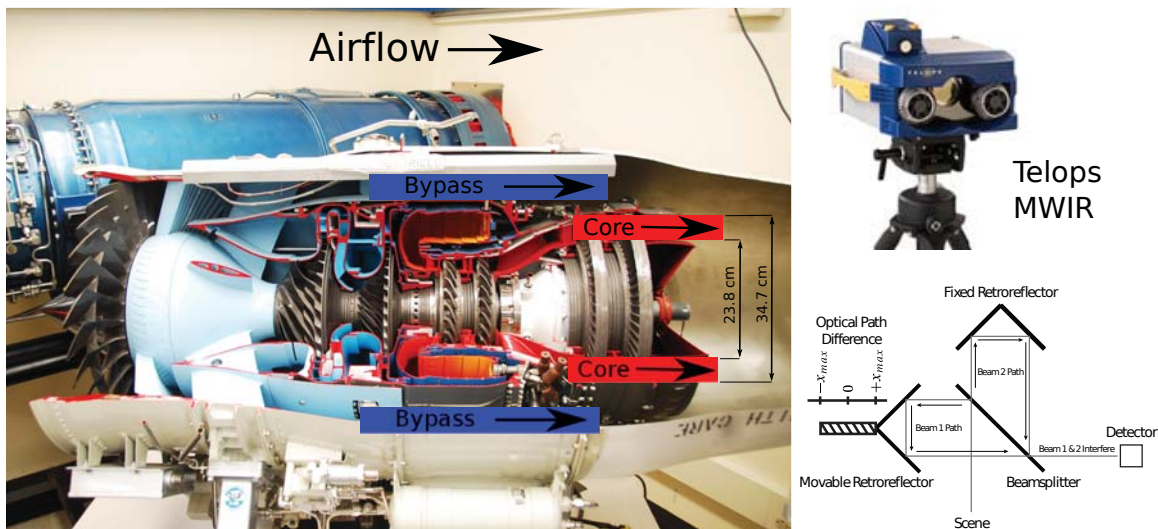### E.3.1 Equipment description..

Figure E.1: *Left*: Cutout display of the F109 Turbofan Engine. The cooler outer bypass air mixes with the hotter combustion core prior to entering the tapered exit nozzle. *Top right*: The Telops Hyper-Cam imaging Fourier-transform spectrometer. *Bottom right*: Diagram of a Michelson interferometer.

162

The Telops midwave Hyper-Cam (MWHC) is based on a traditional Michelson interferometer with an Indium Antimonide (InSb) focal plane array (FPA). For reference, the Hyper-Cam and a Michelson interferometer are depicted in Figure E.1 (right). The full 320×256 pixel set of the array can be windowed to enable faster acquisition rates. The spectral range covers $1800 \, \text{cm}^{-1}$ to $6667 \, \text{cm}^{-1}$ ($1.5 \, \mu\text{m}$ to $5.5 \, \mu\text{m}$), and the spectral resolution can be selected anywhere within the $0.25 \, \text{cm}^{-1}$ to $150 \, \text{cm}^{-1}$ range. Each pixel has a $0.35 \, \text{mrad}$ Instantaneous Field of View (IFOV). An interferogram is collected at each pixel, and a complete set of interferograms collected on the FPA is considered a single datacube. Fundamentally, the datacube is a sequence of broadband images of the scene as viewed through a Michelson interferometer. This interferometric datacube can be transformed into a hyperspectral image via Fourier-transformation of the individual interferograms at each pixel. The Telops LW Hyper-Cam (LWHC) is similar in construction and specifications to the MW, but has a Mercury Cadmium Telluride (HgCdTe) FPA with a spectral band of $870 \, \text{cm}^{-1}$ to $1299 \, \text{cm}^{-1}$ ($7.7 \, \mu\text{m}$ to $11.5 \, \mu\text{m}$).

The F109-GA-100 turbofan engine is housed and operated at the United States Air Force Academy (USAFA) Aeronautics Research Center (ARC). It is a dual-spool, centrifugal compressor, high-bypass (5:1) turbofan engine flat rated at 1330-pounds thrust at sea level static maximum power conditions. It was designed for very low fuel (JP8) consumption and high reliability to address Air Force training needs in the Fairchild T-46 trainer aircraft. The T-46 was cancelled in 1986, and the F109 engine was discontinued and now serves as a reliable test bed for turbofan engines. Figure E.1(a) shows a cutout of the engine's internals used for instruction at the ARC. The F109 resides in an engine test cell and is remotely monitored and controlled by a technician at a control consol in a separate room. Rakes with pressure and temperature probes are installed throughout the engine at various locations, allowing for these values to be remotely monitored and recorded throughout the various stages of combustion. Thrust and fuel flow is constantly

163

monitored at the console as well. The inner core is where combustion occurs, and both the inner core exit flow and outer bypass flow are labeled in Figure E.1 [17, 34, 42, 45]. The inner core creates an annular flow due to the solid center where the outlet is closed. The inner diameter of the core flow is 23.8 cm and the outer diameter is 34.7 cm, which nearly matches the final outer nozzle exit diameter of 36.3 cm.

Due to the complications provided by the test cell's dimensions and layout, a 76×51 cm (W × H) turning mirror was required. While the glass used in this collection was not of optical quality and has not been entirely characterized, it did provide moderate reflection in the midwave and was large enough to image the entire exhaust plume. To account for this mirror's involvement all radiance units are presented as arbitrary and peak normalized when possible.

E.3.2   *Laboratory measurements.*

Data was collected over a three day period in late September within the F109 engine test cell at the USAFA ARC in Colorado Springs. The room is 7.85 m long, 4.27 m wide, and 3.48 m high with solid concrete walls, floor, and ceiling. The exception is the wall on the intake side of the engine, which is actually a large door crafted out of baffles to allow proper air flow during engine operation. The wall at the exit nozzle side of the engine contains an outlet for gases to exhaust. While the room is ideal for contained engine performance testing, it provided complications for the placement and operation of the MWHC as depicted in Figure E.2. The dimensions of the laboratory made it necessary to use a turning mirror to image the plume and allow for the minimum focal distance of the MWHC. The mirror was placed approximately 1 m from the plume and the Hyper-Cam was nearly 6 m away on the inlet side of the engine. While this setup may not have been ideal, it did provide a complete view of the plume without adversely affecting the imagery and kept the camera outside of the engine intake airflow. The LWHC was on hand as well, but early in the process it was adversely affected by the vibrations in the room and the

164

data was not included in this work. The LWHC was not subject to the same minimal focal distance constraints as the MWHC and was placed much closer to the plume, this may have accounted for the increased response to the vibrations due to the engine.
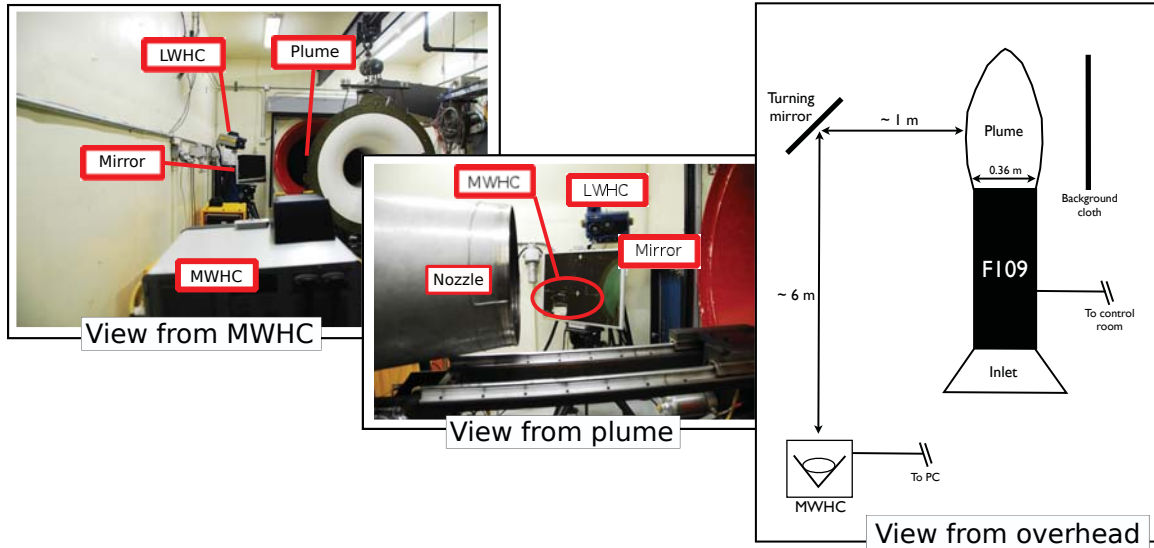
Figure E.2: Description of experimental setup. *Left*: View from the MW Hyper-Cam. The unit was positioned behind the engine and aimed at a turning mirror adjacent to the plume. This provided a complete reflected side view while allowing for the minimum focal distance of the camera. *Middle*: View from the plume. The Hyper-Cam can be seen reflected in the turning mirror. *Right*: Overhead rendering of setup.

As described above, data for this work was collected over several days, but all of the data in the analysis below came from the larger collection during day two. Collection began around 8:00 a.m. and went until approximately 2:00 p.m. with average atmospheric conditions of 14.20 °C (temperature), 37.90 % (humidity), and 786.05 hPa (pressure). Pressure varied little throughout the day, but temperature started as low as 10.3 °C and went as high as 19.2 °C. Humidity began near 50 % and dropped as low as 28.4 %. Collection was at several spectral resolutions and engine speeds with a constant spatial resolution of

0.067 cm^2 per pixel at the source. A 0.25 cm^{-1} resolution collect with a 70 μs integration time was windowed tightly to 8×256 [R × C] and centered at nozzle exit. This data was intended to gather higher resolution spectra of the type seen in Figure E.3, and fine spatial resolution was not necessary in this case. The data collected at a lower 32 cm^{-1} resolution and 70 μs integration time was windowed to 256×128 [R × C] and intended for imagery and spatial analysis of the type seen in Figure E.4. The entire exhaust plume is imaged at this configuration, and due to the lower spectral resolution higher frame rates were possible. Data was collected at these two camera settings for three engine speeds: 53 %, 82 % and 88 % (of the engine's maximum revolutions per minute (RPM)). Collections were attempted at 98 %, but room vibrations were too high and good data collection was not possible (and even proved detrimental in the case of the LWHC). A summary of the pertinent engine data is presented in Table E.1. These are the day two averages of the remotely monitored values for each engine speed. Notice the higher core temperature near 53 % (idle). The F109 is typically not considered to be running ideally, i.e. efficiently, until it is approaching approximately 70 % max RPM, so higher temperatures and fuel flow with little thrust is not surprising [66].

E.4 Methodology

E.4.1 Discerning the flow..

Interpreting and measuring the behavior of a three dimensional flow using two dimentional imagery introduces complications of its own [19, 24, 28, 30, 43]. The analysis in this work is complicated further by the layering effects that may be introduced by the cooler bypass air. As seen in the engine cutout depicted in Figure E.1 (left), the inner core is exhausted into the bypass stream prior to the entire flow being released into the quiescent air of the test chamber. In addition, after initial mixing the outer nozzle is tapered inward (nearly to the core diameter), likely increasing the mixing of core and bypass before exit.

Table E.1: Average monitored values for F109 engine data of interest during day two collection. The F109 is remotely monitored and controlled by a technician at a control consol in a separate room. Rakes with pressure and temperature probes are installed throughout the engine at various locations, allowing for these values to be remotely monitored and recorded.

Percent Max	53	82	88	98
Thrust [lbf]	34.7	387	558	1029
Core Fan [RPM × 1000]	24.1	37.1	39.7	44.3
Core Temperature [K]	729	675	708	815
Bypass Fan [RPM × 1000]	3.9	9.9	11.6	14.9
Bypass Temperature [K]	320	319	378	389

However, for the purposes of this work, the imaged core stream is going to be treated as unmixed at nozzle exit and the surrounding bypass flow is to be largely ignored. While this is a known oversimplification of the flow, it will allow for the simple comparison between this data and the behavior of a round turbulent jet penetrating a quiescent body of the same fluid [39, 51].

E.4.2 *Spectral modeling and simulation..*

As discussed above, a turning mirror with uncharacterized spectral reflectance $r(\tilde{v})$ complicates the ability to estimate temperature and concentrations. The radiance at a given pixel from the MWHC can be interpreted as

$$L(\tilde{v}) = \int \tau(\tilde{v}')\, r(\tilde{v}')\, \varepsilon(\tilde{v}')\, B(\tilde{v}', T)\, ILS(\tilde{v} - \tilde{v}')\, d\tilde{v}' \tag{E.1}$$

where τ is the LOS transmittance, ε the emissivity, B is Planck's blackbody radiation distribution, and *ILS* is the instrument's line shape function. Assuming LTE and ignoring scattering, background radiation, and atmospheric self-emission, the spectral emissivity

can be expressed as

$$\varepsilon(\tilde{v}) = 1 - exp\left(-\sum_i q_i N \sigma_i(\tilde{v}, T)\right)\tau_p. \tag{E.2}$$
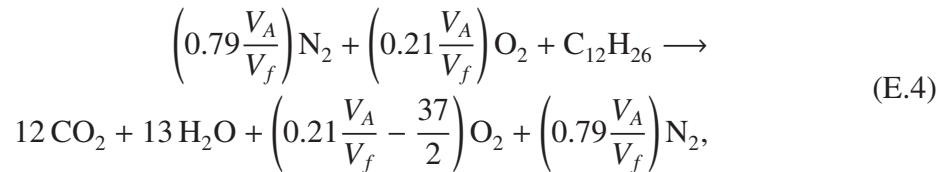
The factor q_i represents the fraction column density (a product of volume fraction and pathlength through the exhaust), N is the total gas density, σ_i is the absorption cross-section, and τ_p is the transmittance of the particulate. A complete explanation of the model can be found in the literature [28, 30, 43]. Radiance values based on this simple model will primarily drop with temperature, concentration, path length, or a combination of those factors.

E.4.3 *Expected mixing fractions..*

The volume mixing fractions of CO_2 and H_2O expected to be found in the exhaust can be estimated through analysis of the known combusted air and fuel flow rates. Treating the JP8 fuel as 100 % kerosene, the basic combustion process in this case can be expressed via the stoichiometric equation

$$\frac{37}{2}O_2 + C_{12}H_{26} \longrightarrow 12\,CO_2 + 13\,H_2O, \tag{E.3}$$

where the amounts of O_2 and $C_{12}H_{26}$ available will be driven by the air and fuel flow rates. The combusted air mass flow rate ($\dot{m}_A$) is one-fifth of the total air mass flow rate ($\dot{m}_0$) due to the bypass ratio, and 21 % of $\dot{m}_A$ is available as combustible O_2 (air is being simply considered as 79 % N_2 + 21 %O_2). Assuming excess oxygen and complete combustion, incorporation of air and fuel flow rates yields

$$\left(0.79\frac{V_A}{V_f}\right)N_2 + \left(0.21\frac{V_A}{V_f}\right)O_2 + C_{12}H_{26} \longrightarrow$$
$$12\,CO_2 + 13\,H_2O + \left(0.21\frac{V_A}{V_f} - \frac{37}{2}\right)O_2 + \left(0.79\frac{V_A}{V_f}\right)N_2, \tag{E.4}$$

where $V_{A,F} = \frac{\dot{m}_{A,F}}{\rho_{A,F}}$ is the known volume fraction of the air (or fuel). The gas density $\rho_{A,F}$ is a function of molecular mass and temperature, with pressure being treated as constant (altitude corrected atmospheric). Equation E.4 has been normalized by V_f to highlight the

$C_{12}H_{26} \longrightarrow 12\,CO_2 + 13\,H_2O$ relationship. Dividing the leading coefficients of CO_2 and H_2O by the coefficient total on the right side of the equation gives the expected volume mixing fractions. With the engine at 82 %, Equation E.4 predicts volume mixing fractions of 6.6 % and 7.2 % for CO_2 and H_2O respectively.

E.4.4 *Expected exhaust velocity..*

It is possible to estimate the exit velocity using physical quantities and monitored values. The law of mass conservation dictates $\dot{m}_{in} = \dot{m}_{out}$, and the conservation of mass equation at exhaust exit is expressed as

$$\dot{m}_{out} = \rho\,A\,v_e, \tag{E.5}$$

where ρ is again the (total) gas density, A is the area of the exit plane, and v_e is the exit velocity perpendicular to A [45]. Solving Equation E.5 for velocity and substituting $\dot{m}_{out} = \dot{m}_A + \dot{m}_F$ provides the means to determine an expected exhaust velocity. With the engine operating at 82 %, the measured flow rates and core flow exit temperature of 675 K lead to an expected exhaust velocity of 177 m/s. The area, $A = 0.23\,\mathrm{m}^2$, of the core flow was estimated via imagery by assuming a cylindrical geometry.

E.5 Results and Discussion

E.5.1 *Spectrum..*

The simulated spectrum presented in Figure E.3 is a result of employing the simple model from above to a pixel near stack exit. It is located at row 60, column 30, as indicated by the inset image within Figure E.5 (imagery analysis from section E.5.2 suggests a path length of 23.2 cm at this point). Ignoring the bypass air and treating the core flow as unmixed, the simulation corresponds to a flow temperature of 560 K and volume mixing fractions 3.3 % H_2O and 2.8 % CO_2. The CO_2 red and blue spikes are evident at 2280 cm^{-1} and 2380 cm^{-1} respectively, and the water lines can be seen from 1800 cm^{-1} to 2200 cm^{-1} as well. This simulated spectrum corresponds well to the actual time averaged spectrum
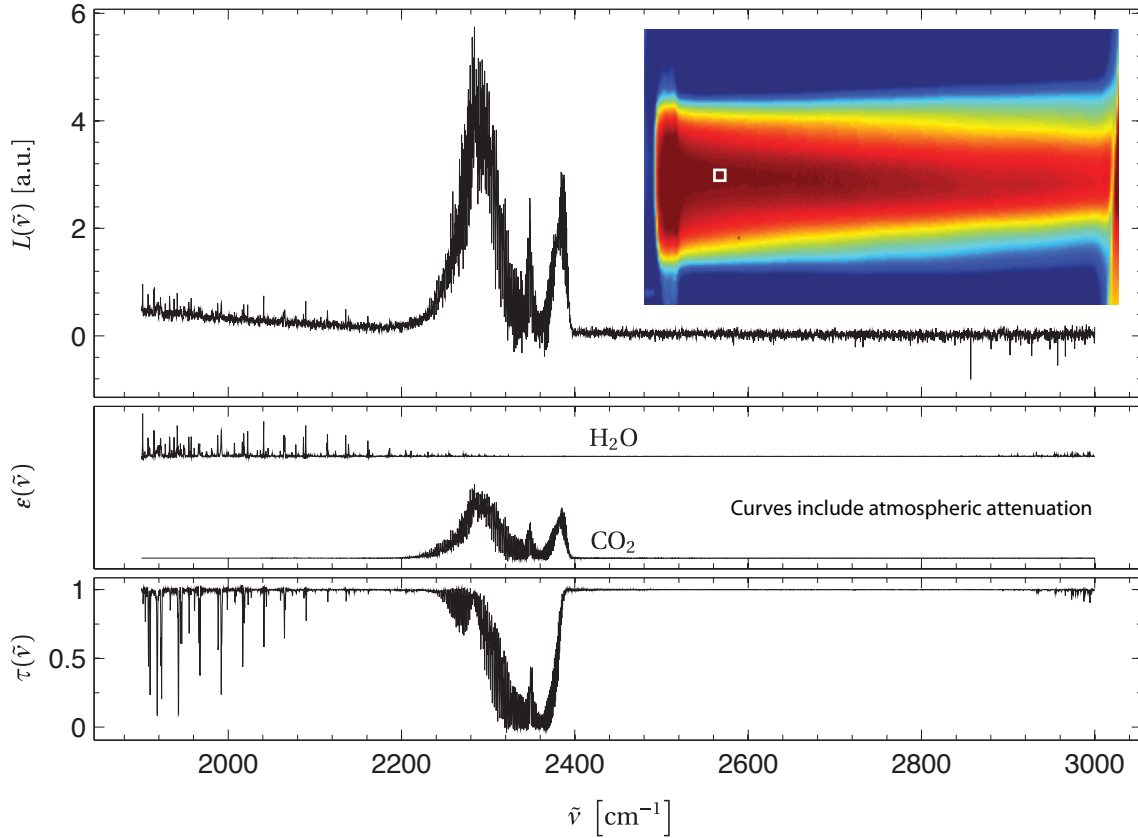
Figure E.3: *Top panel*: Apparent radiance spectrum of center plume pixel near nozzle exit. Mirror reflectivity not accounted for so units are arbitrary. White box in inset image indicates location of pixel in the plume (at 82 % engine speed). *Middle panel*: Emissivity curves for H_2O and CO_2, modified by atmospheric transmittance profile; H_2O emissivity has been increased by a factor of 5 for improved clarity. *Bottom panel*: Atmospheric transmittance profile for the 7 m path between the instrument and exhaust plume.

presented in Figure E.5, and the estimated temperature and mixing fractions are reasonable. At 82 % the measured core temperature is 674.6 K near core exit, which is located well within the nozzle. A cooler temperature further down stream is to be expected. The mixing fractions are roughly half the expected values computed in Section E.4.3, but those calculations assumed absolutely no mixing with the outer bypass stream, which is unlikely.

Additional mixing of the bypassed air would reduce both fractions and could easily account for the difference here.

The detection and estimation of these constituents indicates the feasability of the MWHC as a tool for the spectral analysis of combustion performance. While this paper is simply a cursory look at the data captured on the F109 turbofan, in future work a fit of the simple model to highly resolved spectra like the type seen in Figure E.5 could be used to achieve much more accurate estimations of volume mixing fractions and temperatures throughout the plume [28, 30, 43].

E.5.2 Temperature profiles..
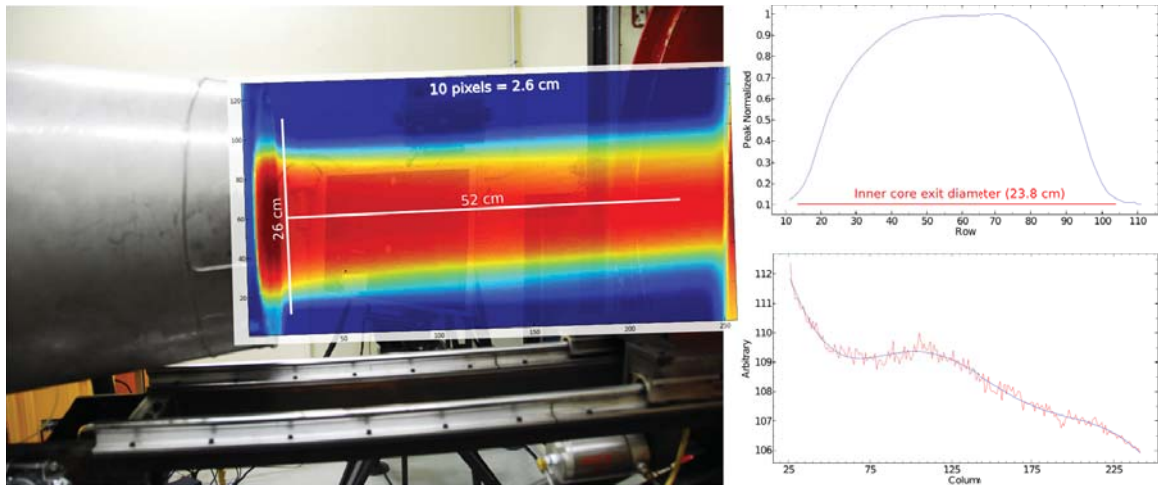
Figure E.4: *Left*: 82 % engine speed mean brightness image at the $2283\,cm^{-1}$ CO_2 red spike. The 128×256 (R×C) image has been angled and overlayed with an engine nozzle exhaust photo to demonstrate a sense of plume size. The axial and radial lines annotated correspond to the intensity plots right of the figure. *Top right*: Normalized peak radial intensity across the plume at column 25 near nozzle exit. *Bottom right*: Axial intensity along exhaust center at row 60; included in the plot is a simple fifth order polynomial fit to the intensity data.

171

Figure E.4 provides a 128×256 [R×C] mean brightness image at 2283 cm^{-1} (red spike) of the exhaust with the engine at 82 %. This image was generated by averaging each pixel's intensity over several hundred datacubes, with each datacube providing approximately 600 individual intensity values. This clean averaged image can be contrasted with the turbulence evident in a single frame snapshot of the type seen in Figure E.5. The brightness image has been overlayed with a nozzle exhaust photo and made slightly tranparent to provide an understanding of how this flow compares to the entire exhaust nozzle. Nozzle exit in Figure E.4 can be discerned on the left side of the figure, while on the right side of the figure the edge of the turning mirror can be seen near column 250. The actual engine exhaust was not angled and significant time was spent aligning camera and mirror in order to have the imaged flow as level as possible, nevertheless a slight upward tilt does seem evident. Only the 82 % results are presented here, but the spatial behavior was very similar in all three engine speed cases.

As can be seen in Figure E.4 center line axial intensity for CO_2 along row 60 drops with distance from nozzle exit. Examination of the geometry in this image indicates the pathlength through the plume is roughly the same, so intensity drop is likely due to a reduction in temperature and concentration. This is behavior typical of a turbulent jet. As the surrounding quiescent fluid is entrained into the exhaust flow due to the turbulence, a reduction in core temperature and center line concentration would be expected [51].

The plot of radial intensity at column 25 near nozzle exit is indicative of the response due to path length as described in Section E.4.2. The geometry of the exhaust plume core is evident in the plot as the intensity is lowest near the edges where the plume is thinnest (and little core path length is being integrated) and highest at center where the path length through the core is greatest. Due to both the nature of the turbofan (and the flow of bypassed air) and entrainment at the edges due to turbulence, temperature is no doubt a contributor to the intensity behavior as well. But the sharp radial intensity dropoff near rows 15 and

172

100 is likely dominated by plume geometry. These locations roughly correlate to the edges of the inner diameter of the hotter core flow.

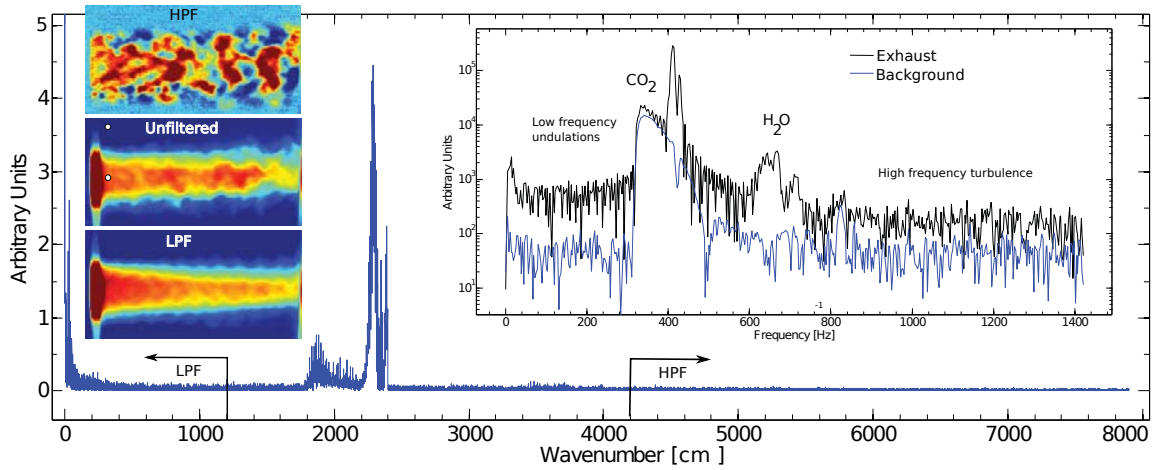### E.5.3   Turbulent behavior..

Figure E.5: Complete wavenumber spectrum from zero to Nyquist. The spectrum presented in Figure E.3 has been time averaged over several hundred interferogram cubes to reduce signal-to-noise ratio (SNR). The frequency spectrum inset is a product of Michelson mirror scan velocity and wavenumber and is presented on a log y scale. The spectral response of the camera is evident on both spectra. Low pass and high pass filters can be applied to remove the spectral response and allow imaging and frequency analysis of the underlying turbulent behavior of the plume.

The MWHC can be used to examine intensity fluctuations in the exhaust due to turbulent behavior through frequency analysis. The action of the Michelson interferometer records spectral information through variations in intensity. The frequency of these variations is a function of Michelson mirror scan velocity ($v \approx 0.18\,\mathrm{cm/s}$) and FPA response frequency ($1700\,\mathrm{cm^{-1}}$ to $6667\,\mathrm{cm^{-1}}$). Specifically, the intensity fluctuations resulting from the Michelson's action have a frequency, $f = v\,\tilde{\nu}$, between 305 and 1200 Hz.

Fluctuations below 305 Hz can be attributed to changes in broadband source intensity, brought about by, e.g., turbulence. Additionally, knowledge of the plume spectrum can be used to identify spectral regions in which radiant emissions are minimal. Thus, some frequencies within this range might be reasonably attributed to the source if corresponding spectral emissions are known to be absent or sufficiently weak.

As described above, an interferogram can be considered a sequential collection of 2D images. Inset within Figure E.5 (middle left) is a single 2D interferogram image (at $32\,\mathrm{cm}^{-1}$ resolution) of the engine exhaust running at 82 %. This is an unfiltered scene which contains the camera's complete intensity response. To bring out the lower frequency modulations in the image, and to ensure the spectral information is removed, a low pass filter (LPF) is applied to the data near $1250\,\mathrm{cm}^{-1}$. With a mirror velocity of 0.18 cm/s this will pass only the behavior below approximately 225 Hz. A corresponding single frame image of the lower frequency behavior is included in the figure (bottom left). The slowly undulating behavior of the steadier core is much more evident in this case. Note the lack of turbulent shedding around the edges of the plume under this filter choice. Contrasting this low frequency behavior is the image of the plume when a high pass filter (HPF) is applied (top left). To ensure the spectral water emission features near $3800\,\mathrm{cm}^{-1}$ were excluded, the HPF cutoff was set to $4200\,\mathrm{cm}^{-1}$. This corresponds to high frequency behavior from approximately 750 Hz to the Nyquist frequency of 1440 Hz. A single frame image is included in Figure E.5, and the high frequency turbulence is evident. A complete depiction of the high frequency behavior and an example of the tracking of a turbulent feature is depicted in Figure E.6. The spatial mapping of the high frequency

turbulence is a promising tool for analysis. The images in Figure E.6 are subsequent frames from a $32\,\mathrm{cm}^{-1}$ resolution interferogram after the application of a HPF. A single feature has been highlighted and tracked as it moves and evolves through the plume, but many such features reside in the images and could be monitored as well. The combination
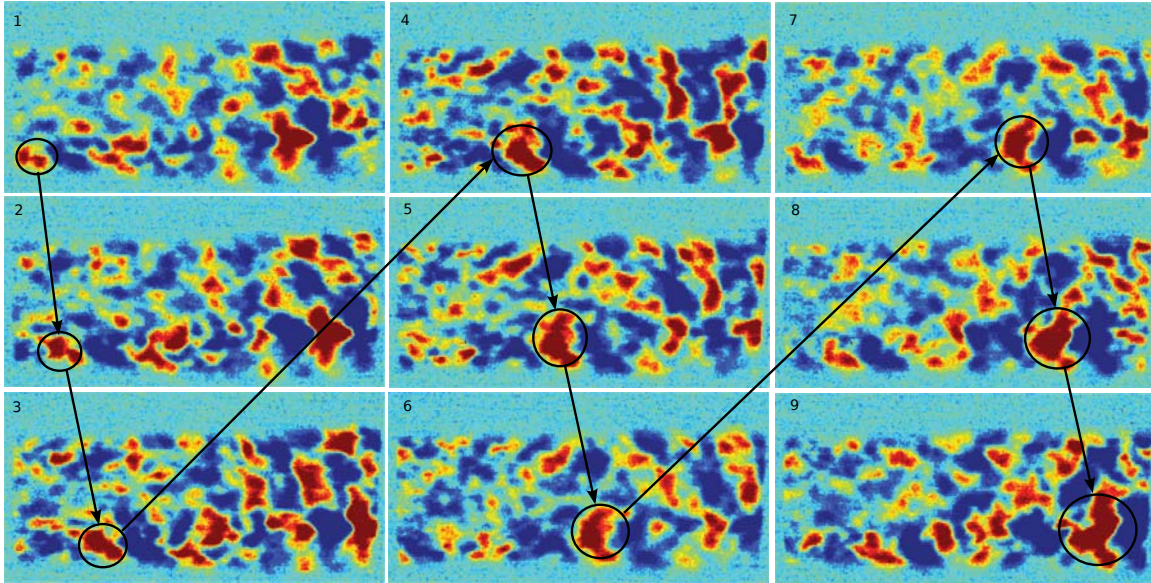
Figure E.6: Top to bottom, left to right: The tracking of a turbulent feature as it leaves the exhaust nozzle and evolves across the exhaust plume.

of spatial and temporal information provided by the MWHC as seen in Figure E.6 could lay a foundation for turbulent flow field analysis [36]. Each pixel's IFOV translates to a known distance across each image, and the camera frame rate provides a reliable time stamp between images, making estimation of characteristic turbulent length and time scales very possible. Velocity estimation has been accomplished with the MWHC in previous work with moderate success [30]. Typical velocity estimation of this data type would be accomplished with automated image correlation, but a simple manual estimate has been accomplished in this work to demonstrate the capability. For the $32\,\mathrm{cm}^{-1}$ resolution experiments each interferometric measurement was acquired in 0.21 s and consists of 594 images, resulting in a 2.86 kHz frame rate. The turbulent feature in Figure E.6 travels approximately 190 columns (49.2 cm) in 8 frames. This corresponds to an estimated velocity of 176 m/s, which is in excellent agreement with the 177 m/s perpendicular exit

velocity calculated above. Once again, the unknown impact of the bypass fan on the overall flow field cannot be understated, but these results certainly bode well for future analysis.

E.6 Conclusions

In this work a Telops MWHC IFTS was used to observe the exhaust of a F109-GA-100 turbofan engine at various engine speeds. The ultimate goal was to demonstrate the feasability of IFTS as a standoff combustion diagnostic tool. Temperature and concentration estimation have been accomplished in previous work, and it appears the same models and methods will apply to engine exhaust. Spectral filtering and frequency analysis of the type seen in Figures E.5 and E.6 seem to indicate the temporal and spatial turbulent characteristics can be quantified as well. Future effort will require a more controlled, characterized flow field ensuring analysis of the type performed in this work can be fully computed and vetted against *in situ* values. While the complicated task of examining a 3D flow field with 2D imagery was made more difficult with the bypass flow intrinsic to the turbofan engine, this qualitative examination of the data indicates IFTS can be successfully employed as a remote combustion and turbulence diagnostic tool.

E.7 Acknowledgements

Bibliography

[1] Acosta, Roberto I. *Imaging Fourier-transform spectroscopy of the boundary layer plume from laser irradiated polymers and carbon materials*. Ph.D. thesis, Air Force Institute of Technology (AU), Wright-Patterson AFB OH, March 2014.

[2] Bergmann, V., W. Meier, D. Wolff, and W. Stricker. "Application of spontaneous Raman and Rayleigh scattering and 2D LIF for the characterization of a turbulent CH4/H2/N2 jet diffusion flame". *Applied Physics B: Lasers and Optics*, 66(4):489–502, 1998.

[3] Bernath, Peter F. *Spectra of Atoms and Molecules*. Oxford University Press, 2005.

[4] Best, P. E., P. L. Chien, R. M. Carangelo, P. R. Solomon, M. Danchak, and I. Ilovici. "Tomographic reconstruction of FT-IR emission and transmission spectra in a sooting laminar diffusion flame: species concentrations and temperatures". *Combustion and Flame*, 85(3):309–318, 1991.

[5] Bharadwaj, S. P. *Medium Resolution Transmission Measurements of CO2 at High Temperature*. Master's thesis, The Pennsylvania State University, Department of Mechanical Engineering, University Park PA, 2000.

[6] Blunck, David, Sumit Basu, Yuan Zheng, Viswanath Katta, and Jay Gore. "Simultaneous water vapor concentration and temperature measurements in unsteady hydrogen flames". *Proceedings of the Combustion Institute*, 32(2):2527–2534, 2009.

[7] Bowen, Spencer J. *Hyperspectral imaging of a turbine engine exhaust plume to determine radiance, temperature, and concentration spatial distributions*. Master's thesis, Air Force Institute of Technology (AU), Wright-Patterson AFB OH, March 2009.

[8] Box, G. E. P., G. M. Jenkins, and G. C. Reinsel. *Time Series Analysis*. Prentice-Hall, Englewood Cliffs, NJ., 1994.

[9] Bradley, Kenneth C. *Midwave Infrared Imaging Fourier Transform Spectrometry of Combustion Plumes*. Ph.D. thesis, Air Force Institute of Technology (AU), Wright-Patterson AFB OH, September 2009.

[10] Bray, K. N. C. "The challenge of turbulent combustion". *Symposium (International) on Combustion*, 26(1):1–26, 1996.

[11] Brewer, L. E. and C. C. Limbaugh. "Infrared band model technique for combustion diagnostics". *Applied Optics*, 11(5):1200–1204, 1972.

177

[12] Chamberland, Martin, Vincent Farley, Alexandre Vallières, André Villemaire, Louis Belhumeur, Jean Giroux, and Jean-Francois Legault. "High-performance field-portable imaging radiometric spectrometer technology for hyperspectral imaging applications". *Proceedings of SPIE*, 5994:59940N, 2005.

[13] Chung, S. H. "Stabilization, propagation and instability of tribrachial triple flames". *Proceedings of the Combustion Institute*, 31(1):877–892, 2007.

[14] Clough, S. A., M. W. Shephard, E. J. Mlawer, J. S. Delamere, M. J. Iacono, K. Cady-Pereira, S. Boukabara, and P. D. Brown. "Atmospheric radiative transfer modeling: A summary of the AER codes". *Journal of Quantitative Spectroscopy and Radiative Transfer*, 91(2):233–244, 2005.

[15] Daily, John W. "Laser induced fluorescence spectroscopy in flames". *Progress in Energy and Combustion Science*, 23(2):133–199, 1997.

[16] Dasch, Cameron J. "One-dimensional tomography: a comparison of Abel, onion-peeling, and filtered backprojection methods". *Applied Optics*, 31(8):1146–1152, 1992.

[17] Davis, Milt, Dave Beale, Keith Boyer, and Devin O'Dowd. *An example for integrated gas turbine engine testing and analysis using modeling and simulation*. Technical report, DTIC Document, 2006.

[18] Denisova, Natalya, Pavel Tretyakov, and Andrey Tupikin. "Emission tomography in flame diagnostics". *Combustion and Flame*, 160(3):577–588, 2013.

[19] Duta, M. C. and M. B. Giles. "A three-dimensional hybrid finite element/spectral analysis of noise radiation from turbofan inlets". *Journal of Sound and Vibration*, 296(3):623–642, 2006.

[20] Eckbreth, Alan C. *Laser Diagnostics for Combustion Temperature and Species*. CRC Press, 1996.

[21] Eckbreth, Alan C. and Robert J. Hall. "CARS concentration sensitivity with and without nonresonant background suppression". *Combustion Science and Technology*, 25, 1981.

[22] Faeth, Gerard M., M. E. Kounalakis, and Y. R. Sivathanu. "Stochastic aspects of turbulent combustion processes". *Chemometrics and Intelligent Laboratory Systems*, 10(1):199–210, 1991.

[23] Farley, Vincent, Alexandre Vallières, Martin Chamberland, André Villemaire, and Jean-François F. Legault. "Performance of the FIRST: a long-wave infrared hyperspectral imaging sensor". *Optics/Photonics in Security and Defence*, 63980T–63980T. International Society for Optics and Photonics, 2006.

[24] Fleet, David and Yair Weiss. "Optical flow estimation". *Handbook of Mathematical Models in Computer Vision*, 237–257. Springer, 2006.

[25] Frank, J. H., R. S. Barlow, and C. Lundquist. "Radiation and nitric oxide formation in turbulent non-premixed jet flames". *Proceedings of the Combustion Institute*, 28(1):447–454, 2000.

[26] Goody, Richard M. *Atmospheric Radiation*. Oxford, Clarendon Press, 1964.

[27] Gross, Kevin C. *Phenomenological model for infrared emissions from high-explosive detonation fireballs*. Ph.D. thesis, Air Force Institute of Technology (AU), Wright-Patterson AFB OH, September 2007.

[28] Gross, Kevin C., Kenneth C. Bradley, and Glen P. Perram. "Remote identification and quantification of industrial smokestack effluents via imaging Fourier-transform spectroscopy". *Environmental Science & Technology*, 44(24):9390–9397, 2010.

[29] Hall, Robert J. and Paul A. Bonczyk. "Sooting flame thermometry using emission/absorption tomography". *Applied Optics*, 29(31):4590–4598, 1990.

[30] Harley, Jacob L. *Remote quantification of smokestack total effluent mass flow rates using imaging fourier-transform spectroscopy*. Master's thesis, Air Force Institute of Technology (AU), Wright-Patterson AFB OH, March 2011.

[31] Harley, Jacob L., Brent A. Rankin, David L. Blunck, Jay P. Gore, and Kevin C. Gross. "Imaging Fourier-transform spectrometer measurements of a turbulent nonpremixed jet flame". *Optics Letters*, 39(8):2350–2353, 2014.

[32] Harley, Jacob L., August J. Rolling, Charles F. Wisniewski, and Kevin C. Gross. "Spatially resolved infrared spectra of F109 turbofan exhaust". *Proceedings of SPIE*, 8354:83540H, 2012.

[33] Janacek, G. J. and A. L. Swift. "A class of models for non-normal time series". *Journal of Time Series Analysis*, 11(1):19–31, 1990.

[34] Jumper, Eric J. *Propagating potential disturbances in turbomachinery*. Technical report, DTIC Document, 2002.

[35] Katta, Viswanath R., William M. Roquemore, Scott Stouffer, and David Blunck. "Dynamic lifted flame in centerbody burner". *Proceedings of the Combustion Institute*, 33(1):1187–1194, 2011.

[36] Kerhervé, F. and J. Fitzpatrick. "Measurement and analysis of the turbulent length scales in jet flows". *Experiments in Fluids*, 50(3):637–651, 2011.

[37] Kohse-Höinghaus, Katharina. "Laser techniques for the quantitative detection of reactive intermediates in combustion systems". *Progress in Energy and Combustion Science*, 20(3):203–279, 1994.

[38] Kohse-Höinghaus, Katharina and Jay Barker Jeffries. *Applied Combustion Diagnostics*. Taylor & Francis, New York, 2002.

[39] List, E. J. "Turbulent jets and plumes". *Annual Review of Fluid Mechanics*, 14(1):189–212, 1982.

[40] Liu, L. H., H. P. Tan, and B. X. Li. "Influence of turbulent fluctuation on reconstruction of temperature profile in axisymmetric free flames". *Journal of Quantitative Spectroscopy and Radiative Transfer*, 73(6):641–648, 2002.

[41] Ma, Lin, Weiwei Cai, Andrew W. Caswell, Thilo Kraetschmer, Scott T. Sanders, Sukesh Roy, and James R. Gord. "Tomographic imaging of temperature and chemical species based on hyperspectral absorption spectroscopy." *Optics Express*, 17(10):8602–13, 5 2009.

[42] Maertins, Hans F., Kenneth W. Krieger, Jay D. Batson, and Mark A. Steele. *Design and development of the garrett F109 turbofan engine*. Technical report, SAE Technical Paper, 1989.

[43] Massman, Jennifer L. *Understanding the influence of turbulence in imaging Fourier-transform spectrometry of smokestack plumes*. Master's thesis, Air Force Institute of Technology (AU), Wright-Patterson AFB OH, March 2011.

[44] Mathieu, Jean and Julian Scott. *An Introduction to Turbulent Flow*. Cambridge University Press, 2000.

[45] Mattingly, Jack D. *Elements of Propulsion*. Department of Aeronautics, US Air Force Academy, 1989.

[46] Meier, W., R. S. Barlow, Y.-L. Chen, and J.-Y. Chen. "Raman/Rayleigh/LIF measurements in a turbulent CH4/H2/N2 jet diffusion flame: experimental techniques and turbulence–chemistry interaction". *Combustion and Flame*, 123(3):326–343, 2000.

[47] Meyer, Terrence R., Sukesh Roy, Thomas N. Anderson, Joseph D. Miller, Viswanath R. Katta, Robert P. Lucht, and James R. Gord. "Measurements of OH mole fraction and temperature up to 20 kHz by using a diode-laser-based UV absorption sensor". *Applied Optics*, 44(31):6729–6740, 2005.

[48] Modest, Michael F. *Radiative Heat Transfer*. Academic Press, 2013.

[49] Moore, Elizabeth A., Kevin C. Gross, Spencer J. Bowen, Glen P. Perram, Martin Chamberland, Vincent Farley, Jean-Philippe Gagnon, and André Villemaire. "Characterizing and overcoming spectral artifacts in imaging Fourier-transform spectroscopy of turbulent exhaust plumes". *Proceedings of SPIE*, 7304:730416, 2009.

[50] Perrin, Marie-Yvonne and Anouar Soufiani. "Approximate radiative properties of methane at high temperature". *Journal of Quantitative Spectroscopy and Radiative Transfer*, 103(1):3–13, 2007.

[51] Pope, S. B. *Turbulent Flows*. Cambridge University Press, New York, 2000.

[52] Posner, Jonathan D. and Derek Dunn-Rankin. "Temperature field measurements of small, nonpremixed flames with use of an Abel inversion of holographic interferograms". *Applied Optics*, 42(6):952–959, 2003.

[53] Rankin, Brent A. *Quantitative Experimental and Model-based Imaging of Infrared Radiation Intensity from Turbulent Reacting Flows*. Ph.D. thesis, Purdue University, West Lafayette IN, November 2012.

[54] Rankin, Brent A., David L. Blunck, and Jay P. Gore. "Infrared Imaging and Spatiotemporal Radiation Properties of a Turbulent Nonpremixed Jet Flame and Plume". *Journal of Heat Transfer*, 135(2):021201, 2012.

[55] Rankin, Brent A., David L. Blunck, Viswanath R. Katta, Scott D. Stouffer, and Jay P. Gore. "Experimental and computational infrared imaging of bluff body stabilized laminar diffusion flames". *Combustion and Flame*, 159(9):2841–2843, 2012.

[56] Rensberger, K. J., J. B. Jeffries, R. A. Copeland, K. Kohse-Höinghaus, M. L. Wise, and D. R. Crosley. "Laser-induced fluorescence determination of temperatures in low pressure flames." *Applied Optics*, 28(17):3556–66, 1989.

[57] Rhoby, Michael R., David L. Blunck, and Kevin C. Gross. "Mid-IR hyperspectral imaging of laminar flames for 2-D scalar values". *Optics Express*, 22(18):21600–21617, 2014.

[58] Rhoby, Michael R. and Kevin C. Gross. "Mid-wave IFTS measurements of a laboratory-scale laminar flame". *Proceedings of SPIE*, 8390:83900E, 2012.

[59] Rhoby, Michael R., Jacob L. Harley, Kevin C. Gross, Pierre Tremblay, and Martin Chamberland. "Imaging Fourier-transform spectrometry for plume diagnostics and code validation". *International Journal of Energetic Materials and Chemical Propulsion*, 12(1), 2013.

[60] Rothman, L. S., I. E. Gordon, Y. Babikov, A. Barbe, Chris D. Benner, P. F. Bernath, M. Birk, L. Bizzocchi, V. Boudon, L. R. Brown, A. Campargue, K. Chance, E. A. Cohen, L. H. Coudert, V. M. Devi, B. J. Drouin, A. Fayt, J.-M. Flaud, R. R. Gamache, J. J. Harrison, J.-M. Hartmann, C. Hill, J. T. Hodges, D. Jacquemart, A. Jolly, J. Lamouroux, R. J. Le Roy, G. Li, D. A. Long, O. M. Lyulin, C. J. Mackie, S. T. Massie, S. Mikhailenko, H. S. P. Müller, O. V. Naumenko, A. V. Nikitin, J. Orphal, V. Perevalov, A. Perrin, E. R. Polovtseva, C. Richard, M. A. H. Smith, E. Starikova, K. Sung, S. Tashkun, J. Tennyson, G. C. Toon, Vl. G Tyuterev, and G. Wagner. "The HITRAN2012 molecular spectroscopic database". *Journal of Quantitative Spectroscopy and Radiative Transfer*, 130:4–50, 11 2013.

[61] Rothman, L. S., I. E. Gordon, R. J. Barber, H. Dothe, R. R. Gamache, A. Goldman, V. I. Perevalov, S. A. Tashkun, and J. Tennyson. "HITEMP, the high-temperature molecular spectroscopic database". *Journal of Quantitative Spectroscopy and Radiative Transfer*, 111(15):2139–2150, 2010.

[62] Rothman, Laurence S., Louli E. Gordon, Alain Barbe, D. Chris Benner, Peter F. Bernath, Manfred Birk, Vincent Boudon, Linda R. Brown, Alain Campargue, and J.-P. Champion. "The HITRAN 2008 molecular spectroscopic database". *Journal of Quantitative Spectroscopy and Radiative Transfer*, 110(9):533–572, 2009.

[63] Rothman, Laurence S., C. P. Rinsland, A. Goldman, S. T. Massie, D. P. Edwards, J. M. Flaud, A. Perrin, C. Camy-Peyret, V. Dana, and J.-Y. Mandin. "The HITRAN molecular spectroscopic database and HAWKS (HITRAN Atmospheric Workstation): 1996 edition". *Journal of Quantitative Spectroscopy and Radiative Transfer*, 60(5):665–710, 1998.

[64] Schneider, Ch., A. Dreizler, J. Janicka, and E. P. Hassel. "Flow field measurements of stable and locally extinguishing hydrocarbon-fuelled jet flames". *Combustion and Flame*, 135(1-2):185–190, 2003.

[65] Solomon, Peter R., Philip E. Best, Robert M. Carangelo, James R. Markham, Po-Liang Chien, Robert J. Santoro, and Hratch G. Semerjian. "FT-IR emission/transmission spectroscopy for in situ combustion diagnostics". *Symposium (International) on Combustion*, 21(1):1763–1771, 1988.

[66] Stermer, Jerry. Department of Aeronautics, US Air Force Academy. Telephone Interview, September 2012.

[67] Tashkun, S. A. and V. I. Perevalov. "CDSD-4000: High-resolution, high-temperature carbon dioxide spectroscopic databank". *Journal of Quantitative Spectroscopy and Radiative Transfer*, 112(9):1403–1410, 2011.

[68] Tashkun, Sergey A., Valery I. Perevalov, Jean-Luc Teffo, Alexander D. Bykov, and N. N. Lavrentieva. "CDSD-1000, the high-temperature carbon dioxide spectroscopic databank". *Journal of Quantitative Spectroscopy and Radiative Transfer*, 82(1):165–196, 2003.

[69] Thomas, Gary E. and Knut Stamnes. *Radiative Transfer in the Atmosphere and Ocean*. Cambridge University Press, 2002.

[70] Tilotta, David C., Kenneth W. Busch, and Marianna A. Busch. "Fourier transform flame infrared emission spectroscopy". *Applied Spectroscopy*, 43(4):704–709, 1989.

[71] Tremblay, Pierre, Kevin C. Gross, Vincent Farley, Martin Chamberland, André Villemaire, and Glen P. Perram. "Understanding and overcoming scene-change artifacts in imaging Fourier-transform spectroscopy of turbulent jet engine exhaust". *SPIE Optical Engineering+ Applications*, 74570F–74570F. International Society for Optics and Photonics, 2009.

[72] Tremblay, Pierre, Simon Savary, Matthias Rolland, André Villemaire, Martin Chamberland, Vincent Farley, Louis Brault, Jean Giroux, Jean-Luc Allard, Éric Dupuis, and Tiarles Padia. "Standoff gas identification and quantification from turbulent stack plumes with an imaging Fourier-transform spectrometer". *SPIE Defense, Security, and Sensing*, 76730H–76730H. International Society for Optics and Photonics, 2010.

[73] Weibring, Petter, M. Andersson, Hans Edner, and Sune Svanberg. "Remote monitoring of industrial emissions by combination of lidar and plume velocity measurements". *Applied Physics B: Lasers and Optics*, 66(3):383–388, 1998.

[74] Wolfrum, Jürgen. "Lasers in combustion: from basic theory to practical devices". *Symposium (International) on Combustion*, 27(1):1–41, 1998.

[75] "TNF Workshop Abstract", (n.d.). URL http://www.sandia.gov/TNF/abstract.html.

[76] Wormhoudt, Joda. *Infrared Methods for Gaseous Measurements: Theory and Practice*. CRC Press, 1985.

[77] "Radiant Zemax", (n.d.). URL http://radiantzemax.com.

[78] Zheng, Yuan, R. S. Barlow, and Jay P. Gore. "Measurements and calculations of spectral radiation intensities for turbulent non-premixed and partially premixed flames". *Journal of Heat Transfer*, 125(4):678–686, 2003.

[79] Zheng, Yuan, R. S. Barlow, and Jay P. Gore. "Spectral radiation properties of partially premixed turbulent flames". *Journal of Heat Transfer*, 125(6):1065–1073, 2003.

[80] Zheng, Yuan and Jay P. Gore. "Measurements and inverse calculations of spectral radiation intensities of a turbulent ethylene/air jet flame". *Proceedings of the Combustion Institute*, 30(1):727–734, 2005.

[81] Zheng, Yuan, Yudaya R. Sivathanu, and Jay P. Gore. "Measurements and stochastic time and space series simulations of spectral radiation in a turbulent non-premixed flame". *Proceedings of the Combustion Institute*, 29(2):1957–1963, 2002.

REPORT DOCUMENTATION PAGE

The public reporting burden for this collection of information is estimated to average 1 hour per response, including the time for reviewing instructions, searching existing data sources, gathering and maintaining the data needed, and completing and reviewing the collection of information. Send comments regarding this burden estimate or any other aspect of this collection of information, including suggestions for reducing the burden, to the Department of Defense, Executive Service Directorate (0704-0188). Respondents should be aware that notwithstanding any other provision of law, no person shall be subject to any penalty for failing to comply with a collection of information if it does not display a currently valid OMB control number.

PLEASE DO NOT RETURN YOUR FORM TO THE ABOVE ORGANIZATION.

1. REPORT DATE (DD-MM-YYYY)	2. REPORT TYPE	3. DATES COVERED (From - To)
18-09-2014	Doctoral Dissertation	Oct 2011-Sep 2014

4. TITLE AND SUBTITLE

DEVELOPMENT OF IMAGING FOURIER-TRANSFORM SPECTROSCOPY FOR THE CHARACTERIZATION OF TURBULENT JET FLAMES

5a. CONTRACT NUMBER

5b. GRANT NUMBER

5c. PROGRAM ELEMENT NUMBER

6. AUTHOR(S)

Harley, Jacob L., Captain, USAF

5d. PROJECT NUMBER

5e. TASK NUMBER

5f. WORK UNIT NUMBER

7. PERFORMING ORGANIZATION NAME(S) AND ADDRESS(ES)

Air Force Institute of Technology
Graduate School of Engineering and Management (AFIT/EN)
2950 Hobson Way
WPAFB, OH 45433-7765

8. PERFORMING ORGANIZATION REPORT NUMBER

AFIT-ENP-DS-14-S-13

9. SPONSORING/MONITORING AGENCY NAME(S) AND ADDRESS(ES)

Dr. James Gord (james.gord@us.af.mil)
AFRL/RQ
WPAFB, OH 45433-7765

10. SPONSOR/MONITOR'S ACRONYM(S)

11. SPONSOR/MONITOR'S REPORT NUMBER(S)

12. DISTRIBUTION/AVAILABILITY STATEMENT

DISTRIBUTION STATEMENT A: APPROVED FOR PUBLIC RELEASE; DISTRIBUTION UNLIMITED.

13. SUPPLEMENTARY NOTES

This material is declared a work of the U. S. Government and is not subject to copyright protection in the United States.

14. ABSTRACT

Recent advances in computational models to simulate turbulent, reactive flow fields have outpaced the ability to collect highly constraining data—throughout the entire flow field—for validating and improving such models. In particular, the ability to quantify in three dimensions both the mean scalar fields (i.e. temperature & species concentrations) and their respective fluctuation statistics via hyperspectral imaging would be a game-changing advancement in combustion diagnostics, with high impact in both validation and improvement efforts for computational combustion models. This research effort establishes imaging Fourier-transform spectrometry (IFTS) as a valuable tool (which complements laser diagnostics) for the study of turbulent combustion. Specifically, this effort (1) demonstrates that IFTS can be used to quantitatively measure spatially resolved spectra from a canonical turbulent flame; (2) establishes the utility of quantile spectra in first-ever quantitative comparisons between measured and modeled turbulent radiation interaction (TRI); (3) develops a simple onion-peeling-like spectral inversion methodology suitable for estimating radial scalar distributions in axisymmetric, optically-thick flames; (4) builds understanding of quantile spectra and demonstrates proof of concept for their use in estimating scalar fluctuation statistics.

15. SUBJECT TERMS

Imaging Fourier-transform spectrometry; hyperspectral imaging; combustion diagnostics; turbulence; infrared spectroscopy

16. SECURITY CLASSIFICATION OF:			17. LIMITATION OF ABSTRACT	18. NUMBER OF PAGES	19a. NAME OF RESPONSIBLE PERSON
a. REPORT	b. ABSTRACT	c. THIS PAGE			Dr. Kevin C. Gross, AFIT/ENP
U	U	U	UU	205	19b. TELEPHONE NUMBER (Include area code) (937) 255-3636 x4558, kevin.gross@afit.edu